EXPERIMENTAL AND SIMULATION RESEARCH ON NUCLEAR REACTOR THERMAL-HYDRAULICS

EDITED BY: Liangming Pan, Luteng Zhang, Jun Wang and Wei Ding
PUBLISHED IN: Frontiers in Energy Research

frontiers Research Topics

ISSN 1664-8714
ISBN 978-2-83250-424-6
DOI 10.3389/978-2-83250-424-6

About Frontiers

Frontiers is more than just an open-access publisher of scholarly articles: it is a pioneering approach to the world of academia, radically improving the way scholarly research is managed. The grand vision of Frontiers is a world where all people have an equal opportunity to seek, share and generate knowledge. Frontiers provides immediate and permanent online open access to all its publications, but this alone is not enough to realize our grand goals.

Frontiers Journal Series

The Frontiers Journal Series is a multi-tier and interdisciplinary set of open-access, online journals, promising a paradigm shift from the current review, selection and dissemination processes in academic publishing. All Frontiers journals are driven by researchers for researchers; therefore, they constitute a service to the scholarly community. At the same time, the Frontiers Journal Series operates on a revolutionary invention, the tiered publishing system, initially addressing specific communities of scholars, and gradually climbing up to broader public understanding, thus serving the interests of the lay society, too.

Dedication to Quality

Each Frontiers article is a landmark of the highest quality, thanks to genuinely collaborative interactions between authors and review editors, who include some of the world's best academicians. Research must be certified by peers before entering a stream of knowledge that may eventually reach the public - and shape society; therefore, Frontiers only applies the most rigorous and unbiased reviews.
Frontiers revolutionizes research publishing by freely delivering the most outstanding research, evaluated with no bias from both the academic and social point of view. By applying the most advanced information technologies, Frontiers is catapulting scholarly publishing into a new generation.

What are Frontiers Research Topics?

Frontiers Research Topics are very popular trademarks of the Frontiers Journals Series: they are collections of at least ten articles, all centered on a particular subject. With their unique mix of varied contributions from Original Research to Review Articles, Frontiers Research Topics unify the most influential researchers, the latest key findings and historical advances in a hot research area! Find out more on how to host your own Frontiers Research Topic or contribute to one as an author by contacting the Frontiers Editorial Office: frontiersin.org/about/contact

EXPERIMENTAL AND SIMULATION RESEARCH ON NUCLEAR REACTOR THERMAL-HYDRAULICS

Topic Editors:
Liangming Pan, Chongqing University, China
Luteng Zhang, Chongqing University, China
Jun Wang, University of Wisconsin-Madison, United States
Wei Ding, Helmholtz Center Dresden-Rossendorf, Helmholtz Association of German Research Centres (HZ), Germany

Citation: Pan, L., Zhang, L., Wang, J., Ding, W., eds. (2022). Experimental and Simulation Research on Nuclear Reactor Thermal-Hydraulics.
Lausanne: Frontiers Media SA. doi: 10.3389/978-2-83250-424-6

Table of Contents

frontiers | Frontiers in Energy Research

TYPE Editorial
PUBLISHED 23 September 2022
DOI 10.3389/fenrg.2022.1028698

OPEN ACCESS

EDITED AND REVIEWED BY
Shripad T. Revankar,
Purdue University, United States

*CORRESPONDENCE
Luteng Zhang,
ltzhang@cqu.edu.cn
Liangming Pan,
cneng@cqu.edu.cn

SPECIALTY SECTION
This article was submitted to Nuclear Energy, a section of the journal Frontiers in Energy Research

RECEIVED 26 August 2022
ACCEPTED 06 September 2022
PUBLISHED 23 September 2022

CITATION
Zhang L, Pan L, Wang J and Ding W (2022), Editorial: Experimental and simulation research on nuclear reactor thermal-hydraulics.
Front. Energy Res. 10:1028698.
doi: 10.3389/fenrg.2022.1028698

Editorial: Experimental and simulation research on nuclear reactor thermal-hydraulics

Luteng Zhang[1]*, Liangming Pan[1]*, Jun Wang[2] and Wei Ding[3]

[1]Department of Nuclear Engineering and Technology, School of Energy and Power Engineering, Chongqing University, Chongqing, China, [2]Department of Engineering Physics, University of Wisconsin-Madison, Madison, WI, United States, [3]Helmholtz-Zentrum Dresden-Rossendorf, Dresden, Germany

KEYWORDS

nuclear reactor, thermal, hydraulics, experiments, simulation

Editorial on the Research Topic
Experimental and simulation research on nuclear reactor thermal-hydraulics

The researches on nuclear reactor thermal-hydraulics have achieved outstanding progresses in the past decades. In recent years, basic research on multiphase flow dynamics and corresponding measurement technology, as well as preliminary research on Gen IV reactors based on experiments and simulations are attracting more and more attention. However, the inside complicated physics and outside extreme conditions will also bring risks and challenges to the development of nuclear industry.

Prof. Liangming Pan from Chongqing University held the first annual academic meeting of the branch of Nuclear Reactor Thermal-Hydraulics and Fluid Mechanics of Chinese Nuclear Society in October 2021. Several high-quality papers were selected from this conference. Therefore, Prof. Pan proposed the Research Topic "*Experimental and Simulation Research on Nuclear Reactor Thermal-Hydraulics*" in the journal *Frontiers in Energy Research*. This research topic aims to promote the novel experimental and numerical investigations on relevant issues refer to nuclear reactor thermal-hydraulics, which is of great significance to the system optimization and safety evaluation of nuclear power plants. Finally, 14 articles were collected and published in this topic, covering the experimental and numerical research of thermal hydraulic problems in light water reactors to supercritical coolant reactors.

Most papers are relevant to the thermal hydraulic problems in light water reactors. Li et al. have contributed an article: "*Research on Countercurrent Flow Limitation in Reactor Hot Leg at the Loss of Coolant Accident-Thermal hydraulic Calculation with System Code RELAP5*". Meng et al. have presented an article entitled: "*Research of Thermal Hydraulic Conditions Effect on PWR CIPS Risk*". Yu et al. have presented an article: "*An Innovative Investigation on Fluid-to-Fluid Modeling of Post-Dryout Heat Transfer in Thermal Energy Systems*". Zhu et al. have contributed an article: "*Comparison of Intergroup Mass Transfer Coefficient Correlations in Two-Group IATE for Subcooled Boiling Flow*". Ding et al. have contributed their research relevant to: "*Experimental Research of Flow Distribution at Reactor Core Inlet of ACP100*". Li et al. have presented article in title of "*Experimental Study on Stratification Morphology of the Molten Pool during Severe Accident*".

Several research papers are about the supercritical coolant. Zhang et al. have contributed an article: "*Experimental Study on Prototype of Printed Circuit Heat Exchanger*". Zhu et al. have presented an article entitled: "*Dynamic Characteristic Study of Supercritical CO_2 Recompression Brayton Cycle System*". Min et al. have presented their research article of: "*Study of Supercritical CO_2 Physical Property Calculation Models*".

Several articles are related to the high temperature gas-cooled reactor. Qin et al. have presented an article entitled: "*Numerical Investigation of Hot Helium Flow Homogenizer on Inter-Unit Flow Rate Uniformity of HTGR Once through Steam Generator*". Qu et al. have contributed an article: "*Characteristics Analysis of Combined Cycle Coupled With High Temperature Gas-Cooled Reactor Based on Progressive Optimization*".

Meanwhile, there are several articles about other issues. Wang et al. have contributed the research paper of: "*Neutronics and Thermal Hydraulics Coupling Analysis on Novel Organic Cooled Reactor Based on Single-Channel Model*". Fang et al. have contributed an article: "*Numerical Study on Heat Transfer and Enhancement Mechanism in PCM-Filled Shell-and-Tube Heat Exchangers*". Su et al. have contributed an article entitled: "*Development and Assessment of an Isotropic Four-Equation Model for Heat Transfer of Low Prandtl Number Fluids*".

Through revision and update for almost 1 year, this topic finally closed with above 14 papers published in the journal Frontiers in Energy Research. This topic presents a chance to public to follow these high-quality papers selected from this conference. The journal *Frontiers* in Energy Research will always open to accept more papers from international conferences. All the editors are welcomed to contact the journal for further information.

Author contributions

LZ is the leading author. LP is the corresponding author. JW and WD contribute the review. All authors approved the submitted version.

Conflict of interest

The authors declare that the research was conducted in the absence of any commercial or financial relationships that could be construed as a potential conflict of interest.

Publisher's note

frontiers in Energy Research

ORIGINAL RESEARCH
published: 24 December 2021
doi: 10.3389/fenrg.2021.813298

Experimental Study on Stratification Morphology of the Molten Pool During Severe Accident

Yang Li, Houjun Gong*, Yunwen Hu, Shengxing Yang, Yong Li and Yuanfeng Zan

CNNC Key Laboratory on Nuclear Reactor Thermal Hydraulics Technology, Nuclear Power Institute of China, Chengdu, China

Stratification morphology of a molten pool under severe reactor accident was investigated by the CESEF experimental facility. The experimental scale was 5,000 g, the atomic ratio of U/Zr was 1.5, the content of stainless steel was 10%, and the oxidation degree of Zr was 40–100%. It was shown that the molten pool was obviously stratified within the range of experimental parameters; one was a metal layer, and the other was an oxide layer. The layered morphology of the molten pool was different with the composition of different corium. With the decrease in the Zr oxidation degree, the metal layer moved downward in the molten pool, and the molten pool would overturn. The main elements in the oxide layer were U, Zr, and O, and the content of stainless steel was low. The main element in the metal layer was stainless steel and contained a certain amount of U and Zr.

Keywords: stratification morphology, prototype material, molten pool, severe accident, experimental

Edited by:
Luteng Zhang,
Chongqing University, China

Reviewed by:
Yapei Zhang,
Xi'an Jiaotong University, China
Yan Xiang,
Royal Institute of Technology, Sweden

****Correspondence:***
Houjun Gong
ghjtsing@126.com

Specialty section:
This article was submitted to Nuclear Energy, a section of the journal Frontiers in Energy Research

Received: *11 November 2021*
Accepted: *23 November 2021*
Published: *24 December 2021*

Citation:
Li Y, Gong H, Hu Y, Yang S, Li Y and Zan Y (2021) Experimental Study on Stratification Morphology of the Molten Pool During Severe Accident. Front. Energy Res. 9:813298. doi: 10.3389/fenrg.2021.813298

INTRODUCTION

In the severe accident of a nuclear reactor, such as the Fukushima Daiichi NPP (nuclear power plant), the fuel and structural materials in the core had been melted (Report of Japanese Government to the IAEA Ministerial Conference on Nuclear Safety, 2011). The molten materials (UO_2, Zr, ZrO_2, stainless steel, etc.) were heated up and melted by decay heat as the coolant in the pressure vessel was depleted. Finally, a molten pool with U-Zr-Fe-O as the main element is formed. The configuration of the molten pool, so called corium, as it affects the failure mechanism of the pressure vessel. The thermodynamic properties of the melt determine that the molten pool will be stratified at the lower head of the pressure vessel, and the stratification morphology of the molten pool determines the heat distribution of the lower head, which is one of the key factors of IVR (retention in the melt stack) strategy. For a long time, the stratification form of the molten pool has been a hot and difficult point in the field of severe accidents at home and abroad.

It was suggested that the compositions of the molten pool formed at the late phase of a severe accident would be in the domain of the miscibility gap of the U-Zr-Fe-O phase diagram, and two immiscible liquid phases will be formed (Theofanous et al., 1997). Edwards (Edwards and Martin, 1966), Hirotomo (Ikeuchi et al., 2020), Guéneau (Guéneau et al., 1998), Bakardjieva (Bakardjieva et al., 2010), Pierre Yves (Chevalier et al., 2004), and Pascal Piluso (Pascal et al., 2005) found that the U-O binary system will be divided into two layers, and Guéneau (Guéneau et al., 1998), Jinho Song (Song et al., 2020), and Bechta (Bechta and Granovsky, 2008) found that the U-Zr-O ternary system will also be divided into two layers. The thermodynamic database of the U-Zr-Fe-O-B-C-FPs complex system is established by the SGTE (scientific group thermodata Europe) database (Fukasawa et al., 2005), and the calculated results are consistent with the experimental data of MASCA (Fukasawa and Shigeyuki, 2012). Bechta (Bechta et al., 2005) supplemented and revised the European nuclear database (NUCLEA) with the help of the experimental data of CORPHAD and METCOR projects, providing a more accurate model for the thermodynamic calculation of the melt.

The RASPLAV project (Asmolov and Behbahani, 2000; Bechta and Khabensky, 2001; Bechta and Khabensky, 2006) carried out experimental research with prototype melt materials and found that the bottom of the molten pool was rich in U and the top was rich in Zr. In the MASCA project (Asmolov, 2004; Tsurikov et al., 2007), three different melting pool stratification forms were found, namely, the molten pool with the metal layer above and the oxide layer below, the molten pool with the metal layer below and the oxide layer above, and the molten pool with the metal layer suspended in the oxide layer. The South Korea COSMOS project (Kang and Park, 2014) found that the molten pool presents a three-layered structure, with a metal layer in the upper part and an oxide layer and some heavy metals in the lower part. The EU IVMR project (Almjashev et al., 2018) studied the layered inversion phenomenon of the molten pool and also found the stratification morphology of the three-layered molten pool. Masahide Takano (Takano et al., 2014) and other experiments on the Fukushima Daiichi nuclear accident show that the molten pool is divided into a metal layer (Fe-Cr-Ni-U-B-C) and an oxide layer (U-Zr-O). Sang Mo (Sang et al., 2016) also carried out experimental research on the prototype melt materials for the Fukushima Daiichi nuclear accident and found that the molten pool was divided into two layers, with a metal layer at the top and an oxide layer at the bottom.

In this study, the configuration of the molten pool for a typical Hualong nuclear reactor composition was investigated by a melting and solidification experiment using an induction heating technique in a cold crucible. The physical and chemical analyses were conducted for the samples taken from the solidified corium ingot to investigate the morphology and chemical composition at each position.

EXPERIMENTAL METHODS

Experimental Setup

The CESEF facility is designed to investigate the stratification of the molten pool at the lower head of the pressure vessel under severe accident, which adopts an electromagnetic induction heating technique with a cold crucible. This technique has been optimized for melting of various reactor materials ranging from a metallic mixture of Zr and stainless steel to an oxidic mixture of UO_2 and ZrO_2, which are the prototypic reactor materials (Sang et al., 2016). The cold crucible consists of a copper plate and an induction coil. The copper plate is forced to circulate to provide cooling. The induction coil is located to provide induction heating by using a high frequency generator. A high frequency generator was designed to supply power up to 400 kW with 100 kHz. However, the frequency could change depending on several factors, such as crucible dimensions, induction coil turns, and melting materials, and so on (Sang et al., 2016). The cold crucible is installed in the inerting chamber and has a diameter of 110 mm and a height of 170 mm. A schematic diagram of the facility is given in **Figure 1**. There is a window at the top of the inerting chamber to measure the temperature of the molten pool, which adopts two-color infrared. The temperature measurement rang of two-color infrared is 1,500–3,500°C, and the measurement accuracy is ± 1.5%. Argon gas is purged into the inerting chamber through a tube at the bottom of the inerting chamber.

Figure 2 shows the melt generation behavior along with the supplied voltage. The voltage increased by 10–20 V every 2 minutes. When the voltage was about 140–160 V, the Zr ring started to light up. After 200 V, the molten pool started to melt, the current decreased, and the power decreased. It was held for 2 h, and the experiment was ended.

Experimental Materials

The cold crucible was filled with a mixture of UO_2 pellets, ZrO_2 powder, Zr pellets, and stainless steel pellets. The composition of the prototype material is usually defined by the atomic molar ratio ($R_{U/Zr}$) of U and Zr, the oxidation ratio (Cn) of Zr, and the mass ratio (X_{SS}) of stainless steel to the prototype material. Assuming that the mass of each component in the prototype material is m_i, i = UO_2, ZrO_2, Zr, and SS (stainless steel), the calculation method of each parameter is as follows:

$$R_{U/Zr} = \frac{m_{UO_2}/271}{m_{ZrO_2}/123 + m_{Zr}/91}, \tag{1}$$

$$C_n = \frac{m_{ZrO_2}/123}{m_{ZrO_2}/123 + m_{Zr}/91}, \tag{2}$$

$$X_{SS} = \frac{m_{SS}}{m_{UO_2} + m_{ZrO_2} + m_{Zr} + m_{SS}}. \tag{3}$$

The experimental scale is 5,000 g, the $R_{u/Zr}$ is 1.5, the X_{SS} is 10%, and the Cn is 40–100% experimental conditions are shown in **Table 1**. Cn of condition one is 100%, Cn of condition two is 80%, and Cn of condition three is 40%. The loading process is as follows: first, a layer of ZrO_2 was laid at the bottom of the crucible to protect the crucible during the melting process. Then, UO_2 pellets and ZrO_2 powder were added into the crucible; stainless steel was placed in the middle of the crucible to prevent direct contact between stainless steel and the crucible wall. It was allowed to flatten and compact; then, a layer of ring composed of Zr pellets was laid on the upper part as an initiator for induction heating, and finally, a layer of ZrO_2 powder was laid on the upper part to reduce heat loss from the melt to the environment. Some holes were initially made by the stainless steel wire for gas venting.

Chemical Analysis

After the experiment, the molten ingot was cut from the middle by using a wire cutting machine and then sampled at different positions by using a tungsten cobalt hollow drill. The samples are used to analyze the chemical composition and structure, which was obtained from X-ray fluorescence (XRF) and a scanning electron microscope/energy dispersive spectrometer (SEM/EDS). The XRF equipment is S8 TIGER, a wavelength-dispersive X-ray fluorescence spectrometer produced by the BROOKE Company, with a maximum excitation current of 170 mA and a maximum excitation point of 60 kV. The SEM equipment is Gemini SEM, a fully functional emission scanning electron microscope produced

FIGURE 1 | Schematic diagram of the CESEF facility.

FIGURE 2 | Morphology of the corium ingot after the experiment (2).

by the Zeiss Company, and equipped with two Oxford X-ray spectrometers, which can be widely used for micro area morphology and composition analysis.

RESULTS AND DISCUSSION

Morphology of Corium Ingot

Figure 2 shows the morphology of the corium ingot after the experiment. It is shown that the corium ingot consists of six parts; the upper crust, upper cavity, metal-rich layer, oxide-rich layer, side crust, and lower unmelted part. The upper crust is mainly unmelted ZrO_2 and sintered melt during the melting process (Sang et al., 2016) because the top layer is exposed to the atmosphere and cooled by radiating heat to the inerting chamber, so that the top layer has been cooled before reaching the melting temperature. Some amount of the unmelted layer was observed at the bottom and side of the corium ingot. A large cavity is formed between the upper crust and the molten ingot, which is formed due to the volume reduction of molten particles after melting and the downward collapse of the molten pool (Song et al., 2018). A lump of the corium ingot below the cavity was found; the metal layer and oxide layer are easy to distinguish after cut from the middle by the wire-cutting machine. The metal layer is bright, and the oxide layer is dark. After separating the metal layer and oxide layer, it is found that the metal layer is very hard and the oxide layer is brittle. It can be considered that liquid phase separation occurs in the melting process because phase separation will not be so complete if it occurs in the solidification process (Sang et al., 2016). The density of the metal layer and oxide layer is different so as to form a different morphology of the molten pool. We found three different molten pool stratification: the molten pool with a metal layer above and an oxide layer below, the molten pool with a metal layer below and an oxide layer above, and the molten pool with the metal layer suspended in the oxide layer, which is similar to the experimental results of the MASCA project (Asmolov, 2004; Tsurikov et al., 2007). A side crust with a thickness of about 2 mm is formed between the ingot and crucible. The crust isolates the internal 2,800°C high-temperature melt from the cold crucible, which shows that the thermal conductivity of the crust of the melt is very small.

Stratification Morphology of the Molten Pool

Figure 3 is a longitudinal sectional view of the corium ingot. The metal layer and oxide layer in the ingot are very easy to distinguish. The metal layer is bright, and the oxide layer is dark. In working condition 1, the melt composition is mainly oxide and Zr metal is completely oxidized. No obvious stratification is found in the molten pool formed by this melt

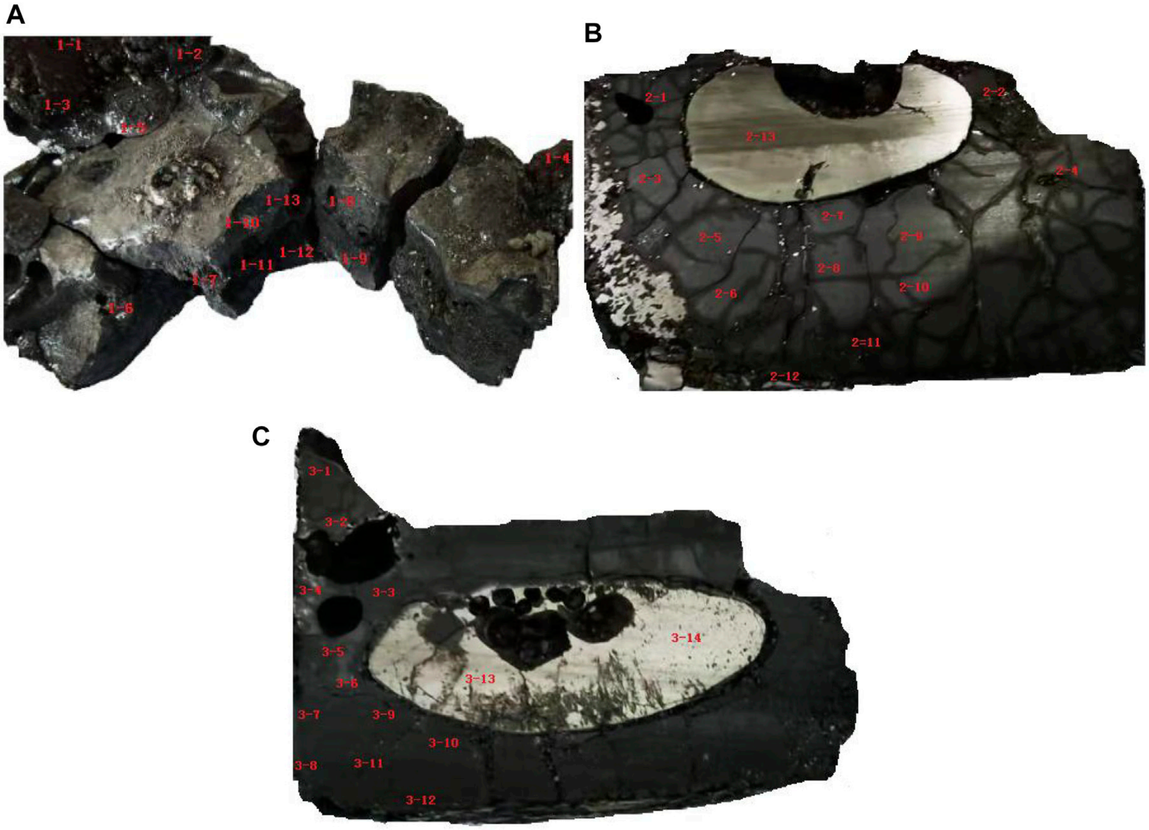

FIGURE 3 | Longitudinal sectional view of the corium ingot **(A)** 1, **(B)** 2, **(C)** 3.

composition, and only a metal ball with a diameter of about 10 mm is formed at the top of the molten pool. With the decrease in the Zr oxidation degree, obvious stratification began to appear in the molten pool, forming a bright metal layer and dark oxide layer. In working condition 2, the formed metal layer is located in the upper part of the molten pool, and the oxide layer is located in the lower part of the molten pool. The metal layer formed in working condition three is located in the middle of the molten pool; the oxide layer wraps the metal layer, and the approximate metal layer is suspended in the middle of the molten pool. The MA experiment in the MASCA project also found three-layered molten pools (Tsurikov et al., 2007).It is found that the metal ball in condition one is mainly composed of stainless steel, which will be described in detail in section 3.3 composition analysis. The density of stainless steel is lower than that of the oxide layer, and it floats on the upper part of the oxide layer. As the oxidation degree of Zr decreases, more U and Zr elements enter the metal layer, the density of the metal layer gradually increases, and the metal layer begins to migrate downward. By working condition 3, the density of the metal layer has been equivalent to that of the oxide layer. The metal layer is suspended in the oxide layer.

Composition Analysis

The corium ingot is cut axially, and then, a small part of the ingot was sampled at different positions, including the upper crust, around the cavity, side crust, lower crust, metal layer, and oxide layer, as shown in **Figure 4**.

Elemental compositions of the samples taken from the different positions of the corium ingot are shown in **Table 2**. **Table 2** only shows the XRF analysis results of condition 1. Total concentrations of U, Zr, Fe, Ni, and Cr in the samples were less than 100%, which implies that the samples contain other elements such as oxygen that are not measurable by XRF. In condition 1, 1-1 to 1–5 are the sampling points of the upper crust. It is found that the content of elements in different positions of the upper crust varies greatly, mainly because on the one hand, the top melt is not completely melted and is only sintered together, so it is difficult for mass transfer in the crust. On the other hand, after the upper crust is formed, it is quickly separated from the lower molten pool, forming a large cavity, and then, mass transfer will not occur with the molten pool. On the other hand, at high temperature, some elements will escape from the molten pool and then be adsorbed on the upper crust. Three reasons lead to great differences in the distribution of elements at different positions of the upper crust, and other conditions also have similar characteristics.

The main elements of the oxide layer are U and Zr in condition 1; the content of U is about 62.64%, Zr is about 15.1%, and stainless steel is very low, less than 5%. Similar results are obtained in conditions 2and 3. The main elements in the

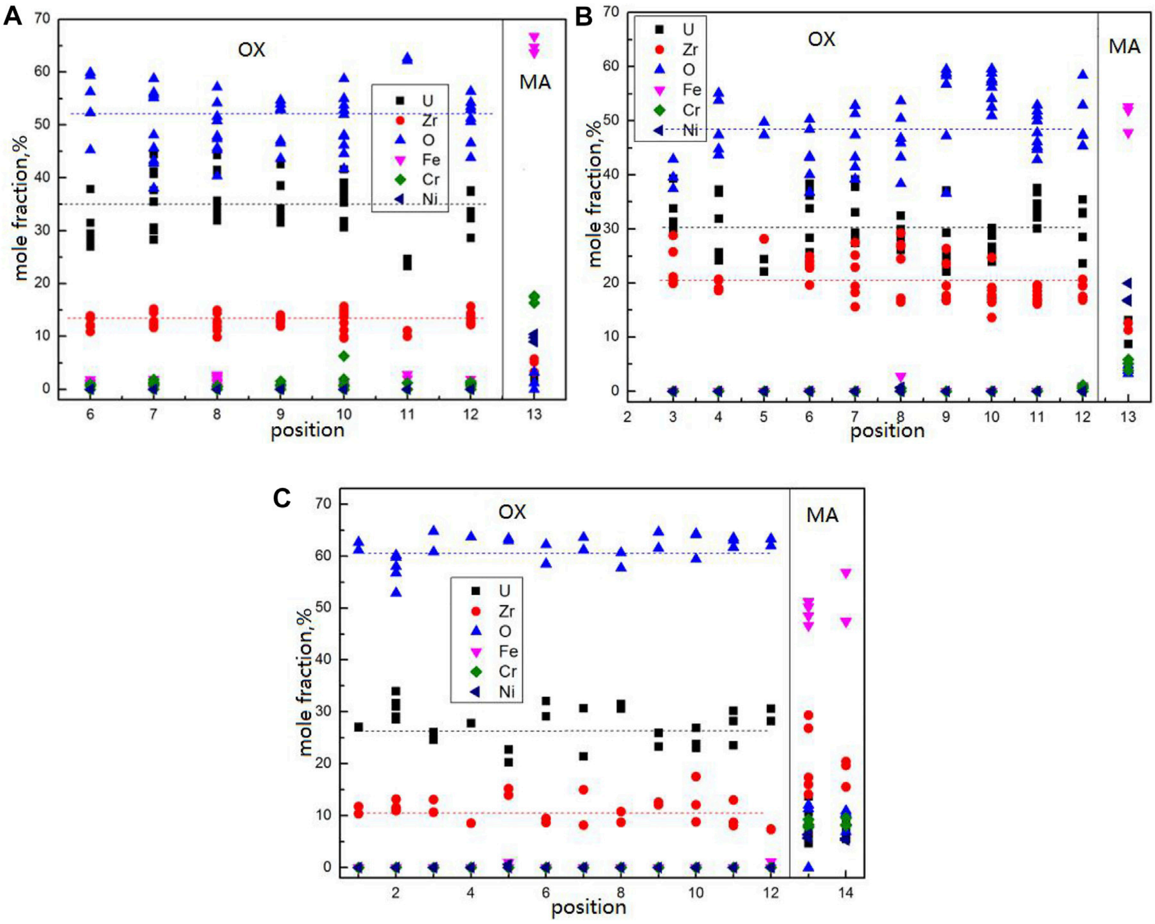

FIGURE 4 | Element distribution characteristics of the molten pool **(A)** 1, **(B)** 2, **(C)** 3.

TABLE 1 | Experimental condition.

Condition	U/Zr	C_n(%)	X_{ss} (%)	Total(g)
1	1.5	100	10	5,000
2	1.5	80	10	5,000
3	1.5	40	10	5,000

metal layer are stainless steel, Fe, Cr, and Ni; the content of Fe in the metal ball in condition one is as high as 62.2%, and the contents of U and Zr are very low. With the decrease of C_n, the Fe content in the metal layer decreases, and the contents of U and Zr increase. Under condition 3, the Fe content in the metal layer is about 34%, while U is about 21% and Zr is about 19.5%. The increase of U and Zr contents in the metal layer will increase the density of the metal layer, and the metal layer begins to move to the lower part of the molten pool.

Figure 4 shows the SEM/EDS test results of the experimental sample. It can be found that the elements of the oxide layer are mainly U, Zr, and O, and there are certain differences in the content of elements at different positions. This may be that during the cooling process of the molten pool, the temperature gradient in the molten pool is large and segregation occurs, resulting in certain differences in the contents of U and Zr at different positions. Under condition 1, the average content of U in the oxide layer is about 35%, the average content of Zr is about 14%, and the average content of O is about 52%, forming the oxide (U, Zr)$O_{1.3}$. The content of stainless steel in the oxide layer is very low, basically below 3%. Under condition 2, the average content of U in the oxide layer is about 32%, the average content of Zr is about 20%, and the average content of O is about 50%. The oxide (U, Zr)O_1 is formed. The oxide layer contains very little stainless steel, and the content is less than 2%. Under condition 3, the average content of U in the oxide layer is about 26%, the average content of Zr is about 10%, and the average content of O is about 60%, forming the oxide (U, Zr)$O_{1.7}$. The composition of stainless steel is not measured.

The metal ball has great hardness in condition 1, and the main component is stainless steel (Fe, Cr, and Ni), in which the content of Fe reaches about 65%, and the content of O in the metal ball is very low, less than 3%. In condition 2, the main elements in the metal layer are also stainless steel (Fe, Cr, and Ni) and some U and Zr, in which the content of Fe is about 50%, the content of Ni is about 18%, the content of Cr is about 5%, the content of U is about 10%, the content of Zr is about 12%, and the content of O is about 4%. In condition 3, the metal layer is mainly composed of

TABLE 2 | Elemental compositions of the corium samples measured using XRF (condition 1).

Sample No	U (wt%)	Zr (wt%)	Fe (wt%)	Cr (wt%)	Ni(wt%)	Total (at%)	U/Zr
1–1	0.17	56.40	7.50	7.60	0.34	72.03	0.00
1–2	20.30	54.50	0.62	1.00	0	76.39	0.14
1–3	42.90	2.50	25.30	6.10	1.70	78.50	6.56
1–4	74.60	4.70	3.00	2.60	0.13	85.07	6.07
1–5	15.20	59.90	0.57	0.64	0.05	76.31	0.10
1–6	57.00	17.10	4.80	3.40	0.12	82.43	1.27
1–7	63.20	14.70	3.50	1.70	0.13	83.16	1.64
1–8	60.50	16.40	4.30	1.30	0.61	83.09	1.41
1–9	63.90	15.40	2.70	1.50	0.12	83.67	1.59
1–10	64.00	13.50	3.90	2.00	0.30	83.69	1.81
1–11	63.00	16.40	2.40	1.60	0.16	83.45	1.47
1–12	66.90	12.20	3.40	1.70	0.13	84.31	2.10
1–13	5.60	1.30	62.20	2.50	12.60	84.20	1.65

stainless steel, in which the content of Fe is about 48%, the content of Cr is about 9%, the content of Ni is about 5%, the content of U is about 8%, the content of Zr is about 20%, and the content of O is about 7.5%.

It can be found from conditions 1, 2, and 3 that when the $R_{U/Zr}$ is unchanged and the stainless steel content is low, C_n is the key factor for the stratification of the molten pool. When C_n reaches 100%, the molten pool will form a single layer of the oxide layer. With the reduction of C_n, the molten pool begins to appear in stratification, the area occupied by the metal layer increases, and the U and Zr contents in the metal layer increase, resulting in the increase of the density of the metal layer, and the metal layer begins to sink. The molten pool is turned from a metal layer on the upper oxide layer to a metal layer on the lower oxide layer.

CONCLUSION

In this study, the prototype materials are used to study the stratification morphology of the molten pool, and the following conclusions are obtained:

1) After the experiment, a complete corium ingot was formed. The molten corium mainly includes the upper crust, upper cavity, metal-rich layer, oxide-rich layer, side crust, and lower unmelted part;
2) With different melt composition, the layered structure of the molten pool is different. An obvious layered structure of the molten pool is observed. One layer is the bright layer, and the other is the dark layer;
3) The main elements in the oxidation layer of the molten pool are U, Zr, and O, and the content of stainless steel is low. The main elements in the metal layer are stainless steel and contain a certain amount of U and Zr at the same time;
4) With the decrease in the Zr oxidation degree, the contents of U and Zr in the metal layer of the molten pool increase, the density of the metal layer increases, and the molten pool will turn over.

DATA AVAILABILITY STATEMENT

The raw data supporting the conclusion of this article will be made available by the authors, without undue reservation.

AUTHOR CONTRIBUTIONS

YaL is responsible for experiment and data processing. HG is responsible for experimental design. YH is responsible for experimental operation. SY is responsible for sample testing. YoL is responsible for providing overall ideas. YZ is responsible for providing overall ideas.

FUNDING

This work was supported by the National Key Research and Development Program of China (2018YFB1900104). A part of this work was also supported by the China National Nuclear Corporation.

REFERENCES

Almjashev, V. I., Granovsky, V. S., and Khabensk, V. B. (2018). Experimental Study of Transient Phenomena in the Three-Liquid Oxidic-Metallic Corium Pool[J]. *Nucl. Eng. Des.* 332, 31–37. doi:10.1016/j.nucengdes.2018.03.004

Asmolov, V., and Behbahani, A. (2000). *CSNI/NEA RASPLAV Seminar, 14-15 November 2000*. Munich, Germany.

Asmolov, V. G. (2004). in *Main Results of the First Phase of MASCA Project* (France: RRC Kurchatov Institute). *Integrated Report.*

Bakardjieva, S., Barrachin, M., and Bechta, S. (2010). Improvement of the European Thermodynamic Database NUCLEA [J]. *Prog. Nucl. Energ.*, 52 (1), 84–96. doi:10.1016/j.pnucene.2009.09.014

Bechta, S. V., and Khabensky, V. B. (2006). Corrosion of Vessel Steel during its Interaction with Molten Corium Part 2: Model Development. *Nucl. Eng. Des.* 236, 1362–1370. doi:10.1016/j.nucengdes.2005.12.008

Bechta, S. V., and Khabensky, V. B. (2001). Experimental Studies of Oxidic Molten Corium–Vessel Steel Interaction. *Nucl. Eng. Des.* 210, 193–224. doi:10.1016/s0029-5493(01)00377-6

Bechta, S. V., Khabensky, V. B., and Granovsky, V. S. (2005). *CORPHAD and METCOR ISTC projects[A]. The First European Review Meeting on Severe Accident Research [C]*. France.

Bechta, S. V., and Granovsky, V. S. (2008). Corium Phase Equilibria Based on MASCA, METCOR and CORPHAD Results. *Nucl. Eng. Des.* 238, 2761–2771. doi:10.1016/j.nucengdes.2008.04.018

Chevalier, P-Y., Fischer, E., and Bertrand, C. (2004). Progress in the Thermodynamic Modelling of the O–U–Zr Ternary System[J]. *ScienceDirect* 28, 15–40. doi:10.1016/j.calphad.2004.03.005

Edwards, R. K., and Martin, A. E. (1966). Phase Relation in the Uranium–Uranium Dioxide System at High Temperature. *Thermodynamics* 69 (5), 2423.

Fukasawa, M., Shigeyuki, T., and Mitsuhiro, H. (2005). Development of Thermodynamic Database for U–Zr–Fe–O–B–C–FPs System[J]. *Nuclear Science Technology* 42 (8), 706–716. doi:10.1080/18811248.2004.9726440

Fukasawa, M., and Shigeyuki, T. (2012). Thermodynamic Analysis for Molten Corium Stratification Test MASCA with Ionic Liquid U-Zr-Fe-O-B-C-FPs Database[J]. *Nucl. Sci. Techn.* 44 (9), 1210–1219. doi:10.1080/18811248.2007.9711364

Guéneau, C., Dauvois, V., Pérodeaud, P., Gonella, C., and Dugne, O. (1998). Liquid Immiscibility in a (O,U,Zr) Model Corium. *J. Nucl. Mater.* 254, 158–174. doi:10.1016/s0022-3115(98)00002-6

Ikeuchi, H., Yano, K., and Washiya, T. (2020). Chemical Forms of Uranium Evaluated by Thermodynamic Calculation Associated with Distribution of Core Materials in the Damaged Reactor Pressure Vessel. *J. Nucl. Sci. Techn.* 57, 704–718. doi:10.1080/00223131.2020.1720844

Kang, K-H., and Park, R-J. (2014). An Experimental Study on Layer Inversion in the Corium Pool during Asevere Accident. *Nucl. Eng. Des.* 278, 163–170. doi:10.1016/j.nucengdes.2014.07.005

Pascal, P., Trillon, G. T., and Journeau, C. (2005). The UO_2-ZrO_2 System at High Temperature(T > 2000 K):importance of the Meta-Stable Phases under Severe Accident Conditions[J]. *ScienceDirect* 344, 259–264. doi:10.1016/j.jnucmat.2005.04.052

Report of Japanese Government to the IAEA Ministerial Conference on Nuclear Safety (2011). *The Accident at TEPCO's Fukushima Nuclear Power Stations – Jun(), Nuclear Emergency Response Headquarters*. Vienna: Government of Japan.

Sang, M. A., Song, J. H., and Kim, J-Y. (2016). Experimental Investigation on Molten Pool Representing Corium Composition at Fukushima Daiichi Nuclear Power Plant[J]. *J. Nucl. Mater.* 478, 164–171. doi:10.1016/j.jnucmat.2016.06.011

Song, J., An, S., and Kim, J-Y. (2020). Morphology and Phase Distributions of Molten Core in a Reactor Vessel[J]. *Nucl. Mater.* 542 (15), 542. doi:10.1016/j.jnucmat.2020.152471

Song, J., Min, B., and Hong, S. (2018). An Investigation on the Physical and Chemical Behaviors of Fuel Debris during Severe Accident Progression[J]. *Prog. Nucl. Energ.* 106, 345–356. doi:10.1016/j.pnucene.2018.02.028

Takano, M., Nishi, T., and Shirasu, N. (2014). Characterization of Solidified Melt Among Materials of UO_2 Fuel and B_4C Control Blade[J]. *J. Nucl. Sci. Techn.* 51 (7-8), 859–875. doi:10.1080/00223131.2014.912567

Theofanous, T. G., Liu, C., Additon, S., Angelini, S., Kymäläinen, O., and Salmassi, T. (1997). In-vessel Coolability and Retention of a Core Melt. *Nucl. Eng. Des.* 169, 1–48. doi:10.1016/s0029-5493(97)00009-5

Tsurikov, D. F., Strizhov, V. F., and Bechta, S. V. (2007). *Integrated Report Main Resultsof the MASCA1 and 2 Projects* (France: RRC Kurchatov Institute, Organization for Economic Cooperation and Development).

Conflict of Interest: The authors declare that the research was conducted in the absence of any commercial or financial relationships that could be construed as a potential conflict of interest.

frontiers
in Energy Research

ORIGINAL RESEARCH
published: 27 January 2022
doi: 10.3389/fenrg.2021.817373

Characteristics Analysis of Combined Cycle Coupled With High Temperature Gas-Cooled Reactor Based on Progressive Optimization

Xinhe Qu[1,2], *Xiaoyong Yang*[1,2]* *and Jie Wang*[1,2]

[1]Institute of Nuclear and New Energy Technology, Advanced Nuclear Energy Technology Cooperation Innovation Center, Key Laboratory of Advanced Nuclear Engineering and Safety, Ministry of Education, Tsinghua University, Beijing, China, [2]Tsinghua University-Zhang Jiagang Joint Institute for Hydrogen Energy and Lithium-Ion Battery Technology, Tsinghua University, Beijing, China

Owing to the current serious environmental and climate problems, the energy industry must focus on the problem of energy utilization rates. High-temperature gas-cooled reactors (HTGRs) are fourth-generation reactors, characterized by high outlet temperatures. The combined cycle is composed of the gas turbine and steam turbine cycles, and it can realize the cascade utilization of high-quality energy. It is a highly competitive power conversion scheme for HTGRs. In this study, the matching characteristics of the combined cycle coupled with HTGRs are revealed through the progressive optimization method. In the combined cycle coupled with HTGRs, the topping and bottoming cycle are both closed cycles, therefore, the optimization for cycle efficiency is to match the topping and bottoming cycles. For a combined cycle with subcritical steam parameters, there are two extreme values of the combined cycle efficiency that have different power ratios. The characteristics revealed in this study are unique to closed combined cycle coupled with HTGRs.

Keywords: high temperature gas-cooled reactor, power conversion unit, combined cycle, matching characteristics, progressive optimization

OPEN ACCESS

Edited by:
Jun Wang,
University of Wisconsin-Madison,
United States

Reviewed by:
Karl Verfondern,
Max Planck Institute for Solid State
Research, Germany
Adil Malik,
Harbin Engineering University, China

****Correspondence:***
Xiaoyong Yang
xy-yang@tsinghua.edu.cn

Specialty section:
This article was submitted to
Nuclear Energy,
a section of the journal
Frontiers in Energy Research

Received: *18 November 2021*
Accepted: *24 December 2021*
Published: *27 January 2022*

Citation:
Qu X, Yang X and Wang J (2022)
Characteristics Analysis of Combined
Cycle Coupled With High Temperature
Gas-Cooled Reactor Based on
Progressive Optimization.
Front. Energy Res. 9:817373.
doi: 10.3389/fenrg.2021.817373

INTRODUCTION

High-temperature gas-cooled reactors (HTGRs) have experienced a long and tortuous development since the middle of the previous century. The final technical route focuses on small modular HTGRs with inherent safety (Kugeler et al., 2019). HTGRs use helium as the cooling medium, and its reactor outlet temperature (ROT) can reach 700–950 C (shown in **Table 1**). Compared with HTGRs, the outlet temperature of very-high-temperature gas-cooled reactors (VHTRs) is higher and can exceed 1,000 C. In addition, it can realize a wide range of applications, including the combined cycle and nuclear hydrogen production (Sun et al., 2020; International Atomic Energy Agency, 2012).

There are two types of power generation systems for HTGRs: the steam turbine cycle power generation system and helium turbine cycle power generation system. The HTGR projects that use the steam cycle for the power generation system are listed in **Table 1** (Simnad, 1991; Frutschi, 2005; McDonald, 2012; Olumayegun et al., 2016). These mainly include the Dragon in the United Kingdom and the AVR in Germany, which started operation as early as the 1960s; the HTTR in Japan and the HTR-10 in China, which are currently in operation; and the demonstration reactor HTR-PM in China, which is currently under construction. The HTGR design projects that use a helium turbine as the power generation system mainly include the GTHTR300 in Japan, the HTGR-GT (Bardia, 1980; McDonald et al., 1981) in the

TABLE 1 | Representative HTGRs in different development stages, and their main technical parameters.

Plants **In early operation**	**Country**	**Power (MW)**	**ROT (°C)**	**Heat application**
Dragon	United Kingdom	20	750	Steam turbine cycle power generation
AVR	Germany	46	950	Steam turbine cycle power generation
Peach Bottom	United States	115	728	Steam turbine cycle power generation
Fort St. Vrain	United States	840	785	Steam turbine cycle power generation
THTR	Germany	750	750	Steam turbine cycle power generation
In operation				
HTTR	Japan	30	850/950	Test
HTR-10	China	10	700	Steam turbine cycle power generation
In construction				
HTR-PM	China	2 × 250	750	Grid connected power generation
Early design projects				
HTR-Module	Germany	200	700	Steam turbine cycle cogeneration
HTR 100	Germany	250	750	Steam turbine cycle cogeneration
HTR 500	Germany	1,250	750	Steam turbine cycle power generation
HHT	Germany	1,500	850	Helium turbine power generation
PNP 500	Germany	500	950	Steam turbine cycle cogeneration
PBMR	South Africa	200/450	700/900	Steam turbine cycle cogeneration/helium turbine power generation
HTGR-GT	United States	400 × 3/600 × 2	850	Helium turbine power generation
MHTGR	United States	350/450	687/850	Steam turbine cycle cogeneration/helium turbine power generation
ANTARES	France	600	850	Combined cycle power generation/hydrogen production
INCOGEN	Netherlands	40	800	Steam turbine cycle cogeneration
ACACIA	Netherlands	60	900	Steam turbine cycle cogeneration
Current design projects				
GT-MHR	United States/Russia	600	850	Helium turbine power generation/hydrogen production
GTHTR300	Japan	600	850	Helium turbine power generation/hydrogen production
HTR-10GT	China	10	750	Helium turbine power generation
NGTCC	United States	350	950	Helium/steam turbine combined cycle

United States, the GT-MHR in the United States and Russia cooperation, the HTR-10GT in China, and the PBMR in South Africa.

The theoretical basis of the steam turbine cycle power generation system is the Rankine cycle. Its cycle efficiency increases with an increase in the pressure and temperature of the main steam. Theoretically, the maximum temperature of the main steam can reach 500 C or even 600°C; however, the temperature difference between the main steam and helium from the reactor outlet is large for HTGRs, and the loss of work capacity is large.

Because the pressure vessel of the steam generator in HTGRs is not suitable for penetration by the reheating steam pipeline, the pressure of the main steam cannot be too high, and it is suitable for subcritical pressure (Zhang et al., 2006; Zhang et al., 2009). Therefore, the technical scheme for the steam turbine cycle power generation cannot provide the full high-temperature advantage of HTGRs.

The efficiency of the helium turbine power generation mainly depends on the gas temperature at the turbine inlet; it increases with an increase in the gas temperature. For the blade without cooling, the inlet temperature of the helium turbine can reach 850°C; for the blade with cooling, the temperature can exceed 1,000 C (Baxi et al., 2008; McDonald, 2014). Therefore, the technical solution for helium turbine power generation is to make full use of the high-grade heat source of HTGRs, thereby providing the high-temperature advantages of HTGRs. This is suitable for the future power generation program of VHTRs.

There are two types of helium turbine power generation: the direct turbine cycle and combined cycle. The direct helium turbine cycle usually adopts the Brayton cycle with precooling, intercooling, and recuperating (Baxi et al., 2008; Wang et al., 2004; Wang et al., 2018). For the direct helium turbine cycle, when the ROT is high, the reactor inlet temperature is also high owing to recuperation. This is limited by the material of the reactor pressure vessel (RPV), and the inner wall of the RPV should be cooled, which increases the system complexity (Kim et al., 2006; Natesan et al., 2007; Demick, 2012). The combined cycle, in which the topping cycle is the simple Brayton cycle, can make maximal use of the high-grade heat from HTGRs; the RPV in this case is not limited by the materials. Research on the combined cycle coupled with HTGRs (CC-HTGRs) is represented by the ANTARES (Gauthier et al., 2006; Gomez et al., 2010) in France and the NGTCC (McDonald, 2014 and 2010) in the United States.

The CC-HTGRs have the same principle as the gas–steam combined cycle (Duan, 2010). This is a cycle form that is based on the principle of energy cascade utilization (Jin, 2008); however, the two are significantly different. The main differences are as follows:

(1) The topping cycle of CC-HTGRs is a closed cycle, and its minimum cycle temperature is affected by the bottoming cycle.
(2) The heat recovery steam generator (HRSG) in CC-HTGRs is a once-through steam generator, including the preheating section, evaporation section, and superheating section, but excluding the steam drum.

(3) Because the heat source of CC-HTGRs is the reactor, some cycle parameters (such as reactor inlet temperature and compression ratio) need to meet certain constraints (Qu et al., 2020).

Presently, there are a limited number of studies that focus on CC-HTGRs, which are far from adequate. McDonald (2010) and McDonald (2014) proposed a combined cycle scheme coupled with an HTGR with a ROT of 950 C to generate power and provide district heating. The thermal power of the reactor is 350 MW, the power distribution is 50 MW in the topping cycle and 130 MW in the bottoming cycle, and the plant efficiency can reach 51.5%. Gomez et al. (2009) and Gomez et al. (2010) conducted optimization studies on the CC-HTGRs, which mainly focused on the optimization method, and research on the system characteristics that were lacking. Jaszczur et al. (2018) and Jaszczur et al. (2020) carried out thermodynamic analyses and compared the characteristics of CC-HTGRs coupled with single-pressure, double-pressure, three-pressure, interstage superheating, and reheating HRSGs. The authors and their research team of this study conducted studies on CC-HTGRs, including comparisons of the different cycle schemes (Wang et al., 2015; Wang et al., 2016), cycle characteristic analyses (Chen, 2001), cycle optimization (Yang et al., 2020), and off-design performance analysis (Qu et al., 2019).

Before this study, the authors used a genetic algorithm to optimize the combined cycle efficiency of a CC-HTGR model and found that the optimal value alternated between two groups of parameters, which did not conform to the expected trend, the authors used a genetic algorithm to optimize the combined cycle efficiency of a CC-HTGR model and found that the optimal value alternated between two groups of parameters, which did not conform to the expected trend. To further explore the internal reasons, the authors chose the most basic CC-HTGR model to perform this research and reveal the reasons of the above discrepancy.

CALCULATION MODEL AND METHOD

According to the authors' previous analysis, the CC-HTGR comprising a simple Brayton cycle and a reheating and multistage regenerative Rankine cycle is more competitive (Chen, 2001; Jin et al., 2008). Because this article is a theoretical study on the characteristics of the CC-HTGRs and the purpose is to reveal the internal relationship between the cycle parameters, the bottoming cycle is simplified and the combined cycle shown in **Figure 1** is used as the analysis model, and no control components are added. This study is based on the cycle model shown in **Figure 1**. **Figure 2** is the corresponding temperature–entropy diagram. The combined cycle consists of the topping cycle, bottoming cycle, and HRSG. The topping cycle in **Figure 1** is a simple Brayton cycle. After the helium is heated in the reactor (2–3), it directly enters the helium turbine for expansion (3–4). The temperature of the expanded helium is still high. It enters the HRSG to transfer the heat to the feed water (4–1) of the bottoming cycle. After the heat is released, the helium enters the compressor so it can be compressed (1–2), and then it returns to the reactor to complete the cycle.

The bottoming cycle in **Figure 1** is a subcritical Rankine cycle without reheat, which contains one stage of regeneration (the deaerator). The feed water absorbs the heat (11–12) in the HRSG to reach an overheated state, and then it enters the steam turbine to expand (12–14). The exhaust steam from the steam turbine is condensed into saturated water in the condenser. Then, it successively flows through the condensation pump, deaerator, and feed water pump. After these processes, the feed water returns to the HRSG. The heat source of the deaerator is extracted from the steam turbine.

The thermodynamic model of the CC-HTGR is presented in **Table 2**, which includes the momentum, energy, and isentropic equations of the 11 subprocesses.

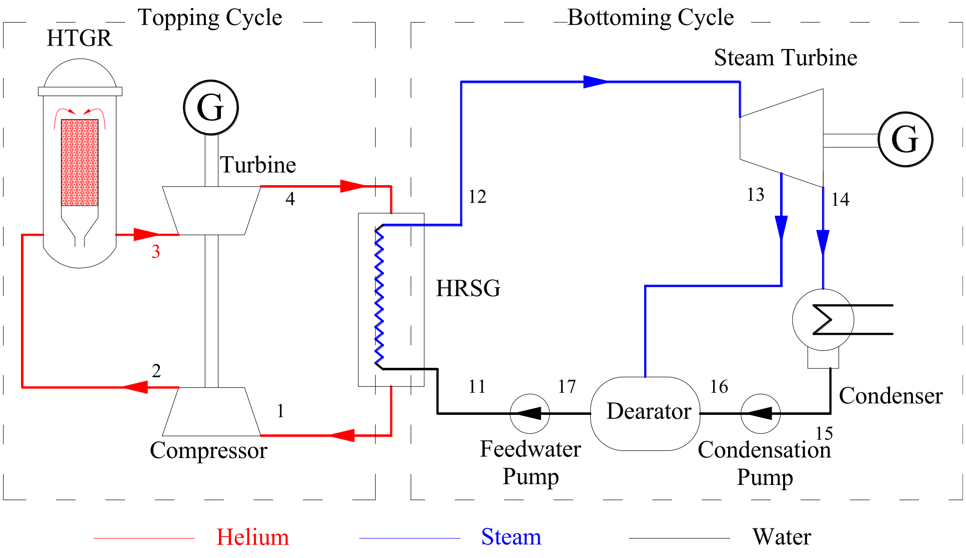

FIGURE 1 | Flow sheet of the CC-HTGR.

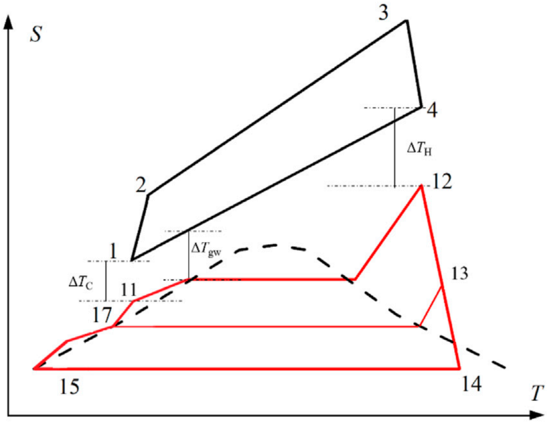

FIGURE 2 | Temperature-entropy diagram of the CC-HTGR.

Assumptions and calculation conditions used in this study:

1) For steady-state analysis, the resistance recovery coefficient, ξ_{cc}, and isentropic efficiency, η_{cc_tur}, of the components in the cycle were not used as the analysis variables, and their values are as follows: $\eta_C = 0.88, \eta_T = 0.89, \eta_{ST} = 0.88, \eta_{con} = 0.85, \eta_F = 0.85$.
2) The condensation temperature, T_{15}, depends on the environmental conditions and was not used as the analysis variable, and its value is 33 C ($P_{15} = 5$ kPa).
3) According to a previous analysis (Yang et al., 2020), the ROT, T_3, is a monotonically increasing function of the combined cycle efficiency; therefore, T_3 was not used as the analysis variable. Only the ROT of 950 C was considered.
4) Similarly, the main steam pressure, P_{12}, is also a monotonically increasing function of the combined cycle efficiency, and P_{12} was not used as the main analysis variable. The subcritical steam pressures of 16, 18, and 20 MPa were analyzed and compared.

Under the above conditions, the combined cycle efficiency can be expressed as follows:

$$\eta_{CC} = \eta_{CC}(\gamma, \Delta T_C, T_{12}, P_{12}, P_{13}) \tag{1}$$

The calculation and analysis methods are shown in **Figure 3**. The calculation includes four levels: the first level searched for the best extraction pressure, P_{13}; the second level searched for the best main steam temperature, T_{12}; the third level observed the influence of the temperature difference at the cold end of HRSG, ΔT_C, on cycle efficiency; and the forth level observed the influence of the compression ratio, γ, on cycle efficiency.

RESULT ANALYSIS

First Level Optimization

According to the analysis method shown in **Figure 3**, the extraction pressure, P_{13}, and main steam temperature, T_{12}, are optimized. The combined cycle efficiency shown in **Eq. 1** can be expressed as follows:

TABLE 2 | Thermodynamic model of the combined cycle.

No.	Sub processes	Momentum equation	Energy equation	Isentropic equation
1	1–2	$\frac{P_2}{P_1} = \gamma$	$\frac{T_{2s}-T_1}{T_2-T_1} = \eta_C$	$\frac{T_{2s}}{T_1} = (\frac{P_2}{P_1})^{\frac{k-1}{k}}$
2	2–3	$\frac{P_3}{P_2} = \xi_{2-3}$	$c_p(T_3 - T_2) = \dot{q}_{core}$	
3	3–4	$\frac{P_3}{P_4} = \pi_T$	$\frac{T_3-T_4}{T_3-T_{4s}} = \eta_T$	$\frac{T_3}{T_{4s}} = (\frac{P_3}{P_4})^{\frac{k-1}{k}}$
4	4–1	$\frac{P_1}{P_4} = \xi_{4-1}$	$\frac{Q_{4-1}}{Q_{11-12}} = \eta_{HRSG}$	
5	11–12	$\frac{P_{12}}{P_{11}} = \xi_{11-12}$		
6	12–14		$\frac{\dot{h}_{12}-\dot{h}_{14}}{\dot{h}_{12}-\dot{h}_{14s}} = \eta_{ST}$	$\dot{s}_{14s} = \dot{s}_{12}$
7	14–15	$\frac{P_{15}}{P_{14}} = \xi_{14-15}$	$T_{14} = T_{15}$	
8	15–16		$\frac{\dot{h}_{16s}-\dot{h}_{15}}{\dot{h}_{16}-\dot{h}_{15}} = \eta_{CON}$	$\dot{s}_{16s} = \dot{s}_{15}$
9	16–17	$\frac{P_{17}}{P_{16}} = \xi_{16-17}$	$Q_{16-17} = Q_{13-17}$	
10	13–17	$\frac{P_{17}}{P_{13}} = \xi_{13-17}$	$\dot{h}_{17} = \dot{h}_{satw}(P_{13})$	
11	17–11		$\frac{\dot{h}_{11s}-\dot{h}_{17}}{\dot{h}_{11}-\dot{h}_{17}} = \eta_F$	$\dot{s}_{11s} = \dot{s}_{17}$
Efficiency of the topping cycle			$\eta_{gt} = \frac{\dot{w}_T-\dot{w}_C}{\dot{q}_{core}}$ $\eta_{gt} = \eta_{gt}(T_1, T_3, \gamma, \xi_{top}, \eta_{top\_tur})$	$\xi_{top} = [\xi_{2-3}, \xi_{1-4}]$ $\eta_{top\_tur} = [\eta_C, \eta_T]$
Efficiency of the bottoming cycle			$\eta_{st} = \frac{W_{ST}-W_{CON}-W_F}{Q_{11-12}}$ $\eta_{st} = \eta_{st}(T_{12}, P_{12}, P_{13}, T_{15}, \xi_{bot}, \eta_{bot\_tur})$	$\xi_{bot} = [\xi_{11-12}, \xi_{14-15}, \xi_{16-17}, \xi_{13-17}]$ $\eta_{bot\_tur} = [\eta_{CT}, \eta_{CON}, \eta_F]$
Efficiency of the combined cycle			$\eta_{CC} = \eta_{gt} + \eta_{st} - \eta_{gt}\eta_{st}$	$\eta_{CC} = \eta_{CC}(T_1, \gamma, \Delta T_C, T_{12}, P_{12}, P_{13}, T_{15}, \xi_{CC}, \eta_{CC\_tur})$ $\xi_{CC} = [\xi_{top}, \xi_{bot}]$ $\eta_{CC\_tur} = [\eta_{top\_tur}, \boldsymbol{\eta}_{bot\_tur}]$
Constrains			$\Delta T_C \geq 30℃, \Delta T_H \geq 30℃, \Delta T_{gw} \geq 15℃$	

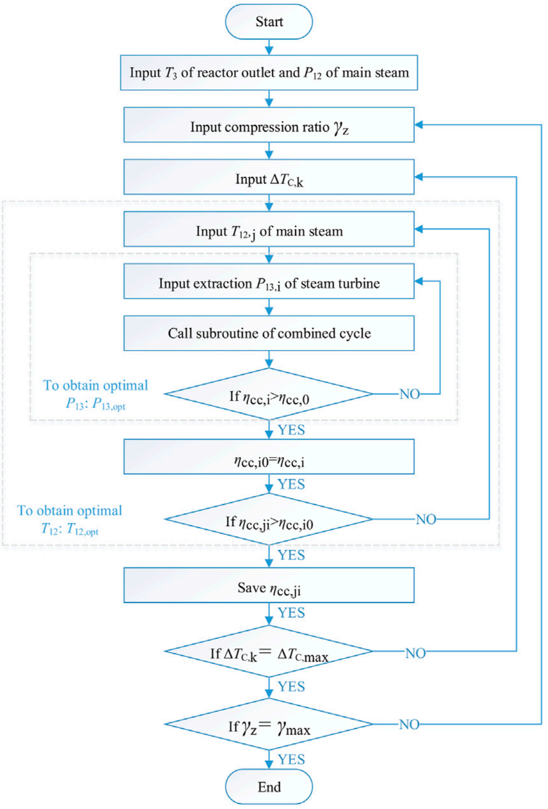

FIGURE 3 | Calculation and analysis methods.

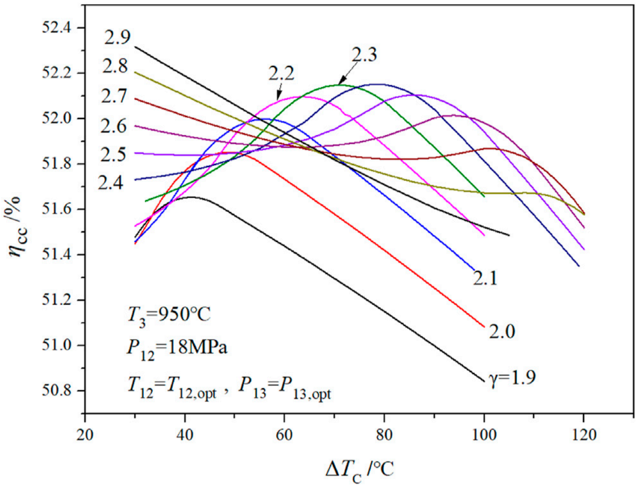

FIGURE 4 | Relationship curves of combined cycle efficiency with cold end temperature difference and compression ratio.

$$\begin{cases} \eta_{CC,opt} = \eta_{CC}\left(\gamma, \Delta T_C, , P_{12}\right) \\ T_{12} = T_{12,opt} \\ P_{13} = P_{13,opt} \end{cases} \tag{2}$$

The effects of the other two parameters (ΔT_C and γ) on the combined cycle efficiency are presented in **Figure 3**. **Figure 5** shows the optimized value of steam turbine extraction pressure, $P_{13,opt}$, corresponding to **Figure 4**. **Figure 6** indicates the optimized value of the main steam temperature, $T_{12,opt}$, corresponding to **Figure 4**.

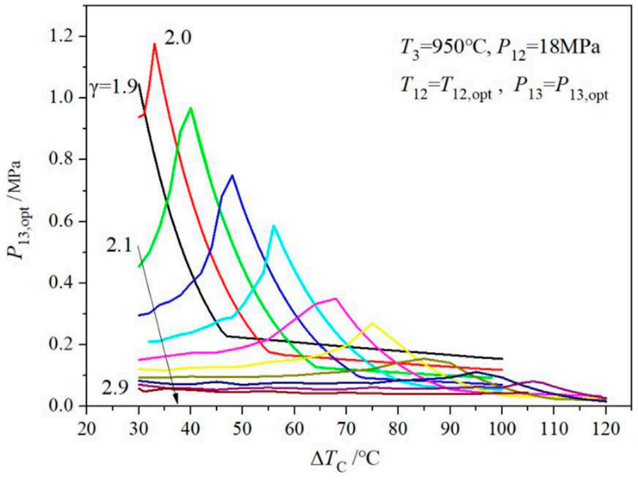

FIGURE 5 | Corresponding optimized value of steam turbine extraction pressure.

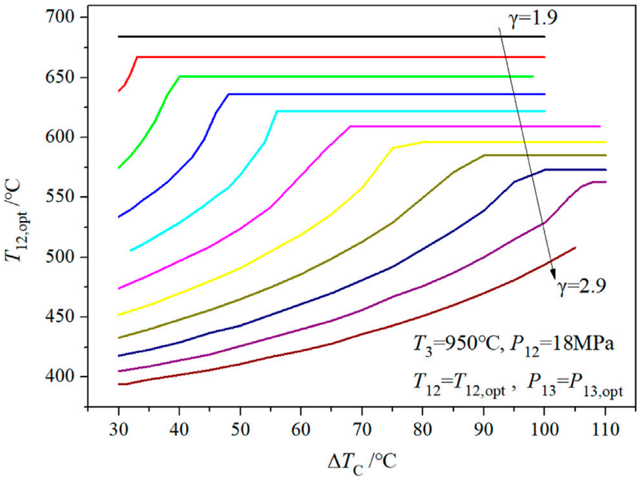

FIGURE 6 | Corresponding optimal value of main steam temperature.

When the compression ratio changes from 1.9 to 2.9, the combined cycle efficiency shows one extreme point, then two extreme points, and finally one extreme point (as shown in **Figure 4**). During the change of the compression ratio, the optimal value of the main steam temperature, $T_{12,opt}$, gradually decreases; it also varies with the temperature difference at the cold end, ΔT_C (as shown in **Figure 6**). When ΔT_C is large, $T_{12,opt}$ is at the maximum point of the main steam temperature (that is, the minimum point of the temperature difference at the hot end ΔT_H); when ΔT_C is small, $T_{12,opt}$ decreases (ΔT_H increases accordingly). $T_{12,opt}$ also affects the optimized value of the

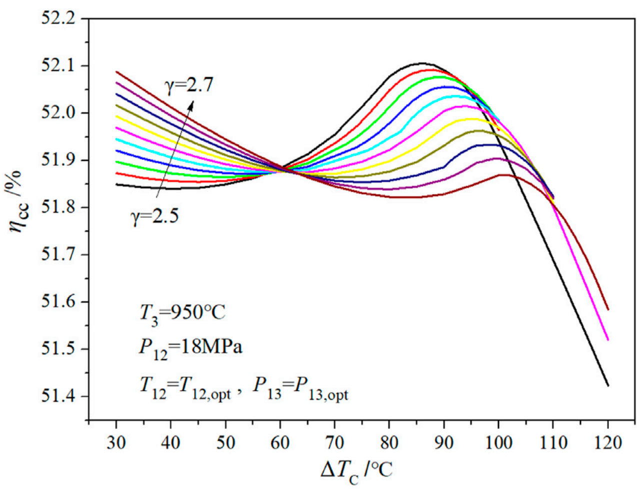

FIGURE 7 | Relationship between combined cycle efficiency and cold end temperature difference in the local compression ratio range.

steam turbine extraction pressure, $P_{12,\mathrm{opt}}$ (as shown in **Figure 5**). When the compression ratio increases from 1.9 to 2.0, $P_{12,\mathrm{opt}}$ decreases gradually. When ΔT_{C} increases, $P_{12,\mathrm{opt}}$ increases first, then decreases, and finally reaches an optimal value.

Furthermore, the interval between two extreme points (γ = 2.5–2.7), shown in **Figure 4**, was calculated. The results are shown in **Figure 7** and **Table 3**. When the compression ratio is 2.5, the extreme value of cycle efficiency on the right side of **Figure 7** is greater than that on the left side. When the compression ratio is 2.7, the extreme value of the left side is greater than that of the right side. When the compression ratio is 2.62 (as shown in bold in **Table 3**), the extreme values of the two cycle efficiencies are equal, the corresponding ΔT_{C} values are 30°C and 95°C, and the optimized main steam temperatures are 430°C and 582°C, respectively.

Figure 8 further reveals the difference between the temperature–entropy diagrams of the combined cycle under two extreme conditions. The essence of efficiency optimization for CC-HTGRs is to match the topping cycle with the bottoming cycle. In **Figure 8**, the area of the topping cycle at the first extreme point is larger than that at the second extreme point; by contrast, the area of the bottoming cycle at the first extreme point is smaller than that at the second extreme point. A variable called the power ratio (PR) is defined to reflect the matching characteristics of the topping cycle and the bottoming cycle in the combined cycle. The PR is defined as the ratio of the output power of the topping cycle to the total output power of the combined cycle, as shown in **Eq. 2**. The PR at the first extreme point is 0.388, and at the second extreme point is 0.330.

$$\text{Power ratio} = \frac{W_{gt}}{W_{gt} + W_{st}} \tag{3}$$

Second Level Optimization

Based on **Eq. 3**, the expression of the combined cycle efficiency shown in **Eq. 4** can be obtained by further optimizing ΔT_{C}. The extreme values of cycle efficiency, corresponding main steam temperatures, and PRs at different compression ratios were extracted, and the results are shown in **Figures 9–11**, and **Figure 9**. shows that as the compression ratio increases, the main steam temperature corresponding to the extreme point of cycle efficiency decreases. It is clear that there are two extreme values (EVs) in a given compression ratio range (the first EV in the figures is the maximum value of cycle efficiency). As the compression ratio increases, the PR increases; that is, the proportion of the output power from the topping cycle increases.

$$\begin{cases} \eta_{CC,opt} = \eta_{CC}(\gamma, P_{12}) \\ T_{12} = T_{12,opt} \\ P_{13} = P_{13,opt} \\ \Delta T_C = \Delta T_{C,opt} \end{cases} \tag{4}$$

The main steam pressures of 16, 18, and 20 MPa are shown in **Figure 11** to compare and verify the conclusions. The calculation

TABLE 3 | Results of the compression ratio in the range of 2.5–2.7.

Calculation conditions: ROT, 950°C; P_{12}, 18 MPa; $\Delta T_C = \Delta T_{C,opt}$; $T_{12} = T_{12,opt}$; $P_{13} = P_{13,opt}$; 1 EV is at the maximum value of combined cycle efficiency; 2 EV is at the second extreme value of combined cycle efficiency

γ	ΔT_C/°C		T_{12}/°C		P_{13}/MPa		T_{11}/°C		η_{CC}/%		η_{gt}/η_{st}/%		PR	
	1 EV	**2 EV**	**1 EV**	**2 EV**	**1 EV**	**2 EV**	**1 EV**	**2 EV**	**1 EV**	**2 EV**	**1 EV**	**2 EV**	**1 EV**	**2 EV**
2.50	86	30	596	452	0.127	0.121	108.5	107.0	52.11	51.85	16.90/42.37	19.26/40.37	0.324	0.371
2.52	88	30	594	448	0.119	0.115	106.5	105.6	52.09	51.87	16.97/42.30	19.42/40.28	0.326	0.374
2.54	90	30	592	444	0.111	0.109	104.5	104.0	52.08	51.90	17.04/42.24	19.59/40.18	0.327	0.377
2.56	90	30	589	440	0.119	0.101	106.5	101.9	52.06	51.92	17.00/42.24	19.77/40.08	0.327	0.381
2.58	92	30	587	437	0.111	0.103	104.5	102.5	52.04	51.95	17.06/42.17	19.85/40.04	0.328	0.382
2.60	94	30	585	433	0.103	0.093	102.3	99.6	52.02	51.97	17.13/42.10	20.06/39.91	0.329	0.386
2.62	**30**	**95**	**430**	**582**	**0.093**	**0.102**	**99.6**	**102.1**	**51.99**	**51.99**	**20.17/39.87**	**17.15/42.05**	**0.388**	**0.330**
2.64	30	97	426	580	0.081	0.094	95.8	99.9	52.02	51.96	20.41/39.71	17.21/41.98	0.392	0.331
2.66	30	98	423	578	0.079	0.095	95.1	100.2	52.04	51.93	20.54/39.64	17.19/41.96	0.395	0.331
2.68	30	100	420	576	0.076	0.088	93.9	98.1	52.07	51.90	20.69/39.56	17.24/41.88	0.397	0.332
2.70	30	102	418	573	0.083	0.080	96.5	95.4	52.09	51.87	20.69/39.59	17.32/41.78	0.397	0.334

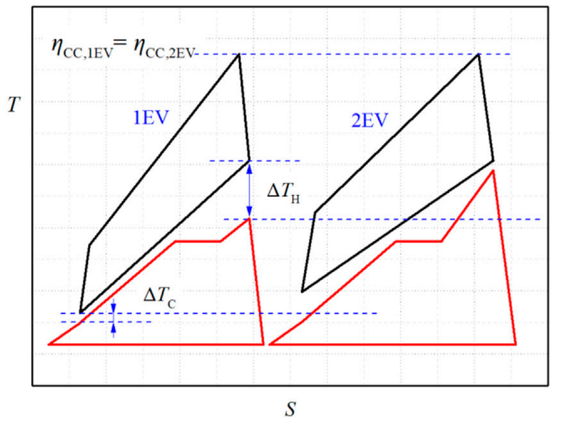

FIGURE 8 | Temperature-entropy diagram of two combined cycles with equal extreme efficiency values.

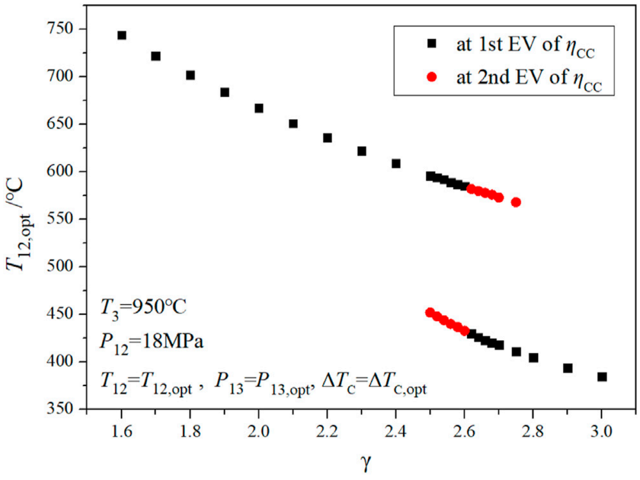

FIGURE 9 | Main steam temperatures corresponding to the extreme values of combined cycle efficiency.

results of the three main steam pressures shown in the figure are consistent. For each main steam pressure, curve γ-$\eta_{CC,opt}$ consists of two different curves. The two curves intersect at a compression ratio, γ_E. Near the intersection point, γ_E, a compression ratio corresponds to two $\eta_{CC,opt}$, which is the result of the first step optimization. The results of the second step optimization can be obtained by extracting the upper half part of the two γ-$\eta_{CC,opt}$ curves. The left half of the new curve is approximately parabolic, and the right half is approximately linear. Therefore, there are still two extreme points of cycle efficiency. The compression ratio corresponding to the two extreme values are 2.3 and 3.0, and the PRs are 0.31 and 0.43, respectively. In the engineering design, the compression ratio is limited by the engineering conditions, generally less than 3.0; therefore, there are two optimization points for the cycle efficiency of CC-HTGR.

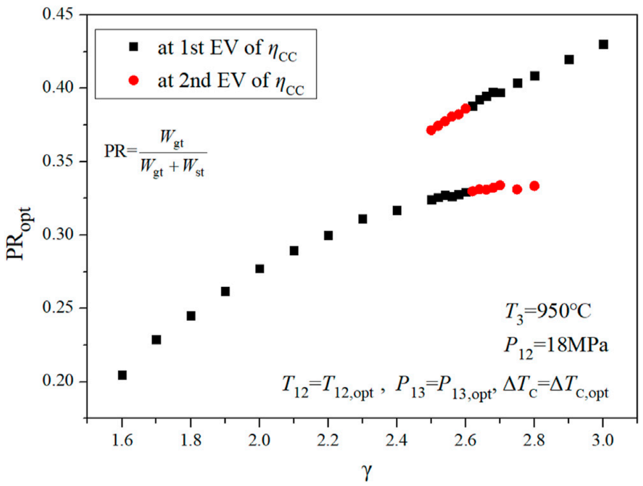

FIGURE 10 | Power ratios corresponding to the extreme values of combined cycle efficiency.

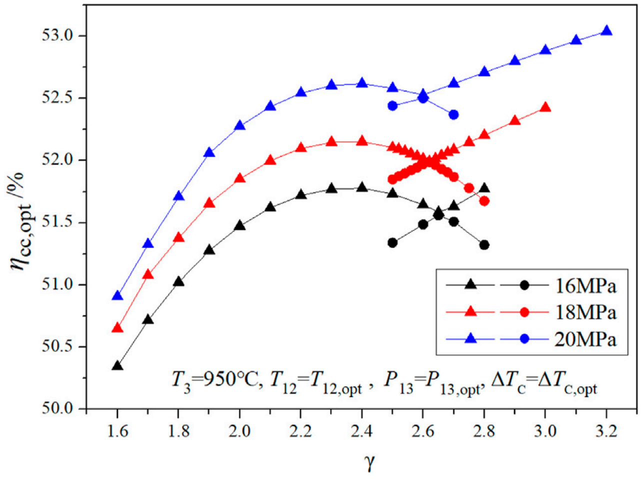

FIGURE 11 | Extreme efficiency values of the combined cycle under different main steam pressures.

CONCLUSION

Facing the current climate problem, nuclear energy can play a big role. High-temperature gas-cooled reactor is a new generation of inherent safety reactor with great potential, which is characterized by high temperature. The world's first HTGR demonstration plant (HTR-PM) has reached the critical point and connected to the grid for power generation in China. The next development will further improve the reactor outlet temperature. When the reactor outlet temperature is high, the steam cycle cannot fully show the advantages of the high-temperature reactor, and the combined cycle is a highly competitive power conversion scheme for HTGRs. Because the topping cycle and bottoming cycle are closed cycles, the combined cycle coupled with HTGRs has some characteristics different from the conventional combined cycle. In this study, the matching characteristics of the topping and bottoming cycles of the combined cycle coupled with HTGRs under subcritical steam parameters were studied. The derived thermodynamic model showed that the combined cycle efficiency has four main optimization variables: compression ratio, temperature difference at the cold end, main steam temperature, and steam turbine extraction pressure. Based on a progressive optimization method, the steam turbine extraction pressure and main steam temperature were first analyzed and optimized. After the temperature difference at the cold end was analyzed in the second level optimization, the compression ratio–cycle efficiency curve was obtained. The compression ratio–cycle efficiency curve consists of two curves with different shapes, which makes the combined cycle efficiency have two extreme values in the domain of definition. In CC-HTGRs, the topping and bottoming cycles are both closed cycles; therefore, the optimization for the combined cycle efficiency is to match the topping and bottoming cycles. The optimization of the combined cycle efficiency is to maximize the area of the topping and bottoming cycles in the temperature–entropy diagram, which is to optimize the cycle PR. Under the reactor outlet temperature of 950°C and main steam pressure of 18 MPa, the compression ratios of the two extreme values are 2.3 and 3.0, and the PRs are 0.31 and 0.43, respectively. This study is helpful to understand the CC-HTGR and improve the energy efficiency.

DATA AVAILABILITY STATEMENT

The raw data supporting the conclusions of this article will be made available by the authors, without undue reservation.

AUTHOR CONTRIBUTIONS

XQ is the main finisher of the manuscript. XY provided guidance and suggestions for the overall thinking of the manuscript. JW provided guidance and suggestions for the thermodynamic model of the manuscript.

FUNDING

This work was supported by the National Key R&D Program of China (Grant No. 2018YFB1900500), the National Science and Technology Major Project (Grant No. ZX069), and the Youth Talent Project of China National Nuclear Corporation.

REFERENCES

Bardia, A. (1980). *Dynamics and Control Modeling of the Closed-Cycle Gas Turbine (GT-HTGR) Power Plant*. California: General Atomic Co. GA-A 15677.

Baxi, C. B., Shenoy, A., Kostin, V. I., Kodochigov, N. G., Vasyaev, A. V., Belov, S. E., et al. (2008). Evaluation of Alternate Power Conversion Unit Designs for the GT-MHR. *Nucl. Eng. Des.* 238, 2995–3001. doi:10.1016/j.nucengdes.2007.12.021

Chen, Y. H. (2001). Study on Potentiality of High Temperature Gas-Cooled Reactor-Combined Cycle System. *Nucl. Power Eng.* 22, 475–480.

Demick, L. (2012). *Using SA508/533 for the HTGR Vessel Material*. Idaho: Idaho National Laboratory (INL.

Duan, Q. S. (2010). *Theory and Calculation of thermal Performance Analysis of Gas-Steam Combined Cycle Power Plant*. Beijing: Tsinghua Univ. Press.

Frutschi, H. U. (2005). *Closed-cycle Gas Turbines: Operating Experience and Future Potential*. New York: ASME Press.

Gauthier, J.-C., Brinkmann, G., Copsey, B., and Lecomte, M. (2006). ANTARES: The HTR/VHTR Project at Framatome ANP. *Nucl. Eng. Des.* 236, 526–533. doi:10.1016/j.nucengdes.2005.10.030

Gomez, A., Azzaro-Pantel, C., Pibouleau, L., Domenech, S., Latgé, C., Dumaz, P., et al. (2009). A MultiObjective Genetic Algorithm Framework for Electricity/Hydrogen Co-production from Generation IV Nuclear Energy Systems. *Comput.-Aided Chem. Eng.* 26, 1263–1268. doi:10.1016/s1570-7946(09)70210-x

Gomez, A., Pibouleau, L., Azzaro-Pantel, C., Domenech, S., Latgé, C., and Haubensack, D. (2010). Multiobjective Genetic Algorithm Strategies for Electricity Production from Generation IV Nuclear Technology. *Energ. Convers. Manag.* 51, 859–871. doi:10.1016/j.enconman.2009.11.022

International Atomic Energy Agency (2012). *Hydrogen Production Using Nuclear Energy*. Vienna: Nuclear Energy Series.

Jaszczur, M., Dudek, M., and Kolenda, Z. (2020). Thermodynamic Analysis of Advanced Gas Turbine Combined Cycle Integration with a High-Temperature Nuclear Reactor and Cogeneration Unit. *Energies* 13, 400. doi:10.3390/en13020400

Jaszczur, M., Dudek, M., Śliwa, T., and Kolenda, Z. (2018). An Analysis of High-Temperature Nuclear Reactor Coupled with Gas Turbine Combined Cycle. *MATEC Web Conf.* 240, 05010. doi:10.1051/matecconf/201824005010

Jin, H. G., and Lin, N. M. (2008). *Comprehensive cascade Utilization of Energy and Total Energy System of Gas Turbine*. Beijing: Science press.

Kim, M. H., and Lee, W. J. (2006). "Survey on Cooled-Vessel Designs in High Temperature Gas-Cooled Reactors," in *Transactions of the Korean Nuclear Society Autumn Meeting Gyeongju*.

Kugeler, K., and Zhang, X. Y. (2019). *Modular High-Temperature Gas-Cooled Reactor Power Plant. Berlin*. Springer.

McDonald, C. F. (2012). Helium Turbomachinery Operating Experience from Gas Turbine Power Plants and Test Facilities. *Appl. Therm. Eng.* 44, 108–142. doi:10.1016/j.applthermaleng.2012.02.041

McDonald, C. F. (2014). Power Conversion System Considerations for a High Efficiency Small Modular Nuclear Gas Turbine Combined Cycle Power Plant Concept (NGTCC). *Appl. Therm. Eng.* 73, 82–103. doi:10.1016/j.applthermaleng.2014.07.011

McDonald, C. F., and Smith, M. J. (1981). *Turbomachinery Design Considerations for the Nuclear HTGR-GT Power Plant*. South Windsor: General Atomic Co. GA-A 15614.

McDonald, C. G. (2010). Power Conversion System Considerations for an Advanced Nuclear Gas Turbine (GT-VHTR) CHHP Demonstration Plant Concept. *Int. J. Turbo Jet Engines* 27, 179–217. doi:10.1515/tjj.2010.27.3-4.179

Natesan, K., Majumdar, S., Shankar, P. S., and Shah, V. N. (2007). *Preliminary Materials Selection Issues for the Next Generation Nuclear Plant Reactor Pressure Vessel*. Oak Ridge: Argonne National Laboratory.

Olumayegun, O., Wang, M., and Kelsall, G. (2016). Closed-cycle Gas Turbine for Power Generation: A State-Of-The-Art Review. *Fuel* 180, 694–717. doi:10.1016/j.fuel.2016.04.074

Qu, X. H., Yang, X. Y., and Wang, J. (2020). Combined Cycles-Coupled High-Temperature and Very High-Temperature Gas-Cooled Reactors: Part II–Engineering Design. *Ann. Nucl. Energy*. doi:10.1016/j.anucene.2019.106953

Qu, X., Yang, X., and Wang, J. (2019). Off-design Performance and Power-Control Strategy for Combined Cycle Coupled with High-Temperature Gas-Cooled Reactor. *Ann. Nucl. Energ.* 130, 338–346. doi:10.1016/j.anucene.2019.03.009

Simnad, M. T. (1991). The Early History of High-Temperature Helium Gas-Cooled Nuclear Power Reactors. *Energy* 16, 25–32. doi:10.1016/0360-5442(91)90084-Y

Sun, Q., Gao, Q., Zhang, P., Peng, W., and Chen, S. (2020). Modeling Sulfuric Acid Decomposition in a Bayonet Heat Exchanger in the Iodine-Sulfur Cycle for

Hydrogen Production. *Appl. Energ.* 277, 115611. doi:10.1016/j.apenergy.2020.115611

Wang, J., Cao, X., Meng, Z., and Ding, M. (2018). A Hybrid Semi-implicit Method of 1D Transient Compressible Flow for thermal-hydraulic Analysis of (V) HTR Gas Turbine Systems. *Front. Energ. Res.* 6, 1–11. doi:10.3389/fenrg.2018.00044

Wang, J., Ding, M., Yang, X. Y., and Wang, J. (2016). Performance Comparison and Optimization of Two Configurations of (Very) High Temperature Gas-Cooled Reactors Combined Cycles. *Ann. Nucl. Energ.* 94, 279–287. doi:10.1016/j.anucene.2016.03.009

Wang, J., Ding, M., Yang, X. Y., and Wang, J. (2015). Study on Compound Combined Cycle of High Temperature Gas-Cooled Reactor. *At. Energ. Sci. Technol.* 49, 616–622.

Wang, J., Huang, Z. Y., Zhu, S. T., and Yu, S. Y. (2004). "Design Features of Gas Turbine Power Conversion System for HTR-10GT," in *2nd International Topical Meeting on High Temperature Reactor Technology*.

Yang, X. Y., Qu, X. H., and Wang, J. (2020). Combined Cycle-Coupled High-Temperature and Very High-Temperature Gas-Cooled Reactors: Part I—Cycle Optimization. *Ann. Nucl. Energ.* 134, 193–204. doi:10.1016/j.anucene.2019.06.018

Zhang, Z., Wu, Z., Sun, Y., and Li, F. (2006). Design Aspects of the Chinese Modular High-Temperature Gas-Cooled Reactor HTR-PM. *Nucl. Eng. Des.* 236, 485–490. doi:10.1016/j.nucengdes.2005.11.024

Zhang, Z., Wu, Z., Wang, D., Xu, Y., Sun, Y., Li, F., et al. (2009). Current Status and Technical Description of Chinese 2×250MWth HTR-PM Demonstration Plant. *Nucl. Eng. Des.* 239, 1212–1219. doi:10.1016/j.nucengdes.2009.02.023

Conflict of Interest: This study received funding from China National Nuclear Corporation. The funder was not involved in the study design, collection, analysis, interpretation of data, the writing of this article, or the decision to submit it for publication.

The authors declare that the research was conducted in the absence of any commercial or financial relationships that could be construed as a potential conflict of interest.

NOMENCLATURE

$\boldsymbol{k}$ isentropic exponent

$\dot{h}$ specific enthalpy (kJ kg^{-1})

$\boldsymbol{P}$ pressure (MPa)

$\dot{q}$ specific heat (MW kg^{-1})

$\boldsymbol{Q}$ heat (MW)

$\dot{s}$ specific entropy (kg kg^{-1} K^{-1})

$\boldsymbol{T}$ temperature (k)helium turbine

$\dot{w}$ specific work (MW/kg)

$\boldsymbol{W}$ work (MW)

$\boldsymbol{\Delta T_{C}}$ temperature difference at cold end of HRSG

$\boldsymbol{\Delta T_{H}}$ temperature difference at hot end of HRSG

$\boldsymbol{\Delta T_{gw}}$ temperature difference at pinch point of HRSG

Acronym

CC-HTGR combined cycle coupled with HTGR

EV extreme value

HRSG heat recovery steam generator

HTGR high-temperature gas-cooled reactor

PR power ratio

ROT reactor outlet temperature

VHTR very-high-temperature gas-cooled reactor

Greek

$\boldsymbol{\beta}$ cooling flow for helium turbine

$\boldsymbol{\gamma}$ compression ratio

$\boldsymbol{\eta}$ efficiency

$\boldsymbol{\xi}$ pressure recovery coefficient

$\boldsymbol{\pi}$ expansion ratio

Subscripts

CC combined cycle

C helium compressor

CON condenser

EV extreme value

F feedwater pump

gt gas turbine cycle

opt optimal value

st steam turbine cycle

satw saturated water

T temperature (k)helium turbine

tur turbomachinery

frontiers
in Energy Research

ORIGINAL RESEARCH
published: 28 January 2022
doi: 10.3389/fenrg.2021.819060

An Innovative Investigation on Fluid-to-Fluid Modeling of Post-Dryout Heat Transfer in Thermal Energy Systems

Dali Yu[1,2*†], *Chi Xu*[1,3], *Chongju Hu*[1,3] and *Yijiang Fan*[1,3]

[1] *Institute of Nuclear Energy Safety Technology, Hefei Institutes of Physical Science, Chinese Academy of Sciences, Hefei, China,*
[2] *Key Laboratory of Advanced Reactor Engineering and Safety, Ministry of Education, Tsinghua University, Beijing, China,*
[3] *University of Science and Technology of China, Hefei, China*

Post-dryout heat transfer is an important thermal hydraulics phenomenon happening in the loss-of-coolant accident of water-cooled nuclear reactors and the off-design conditions of water-cooled ceramic breeder blanket in fusion reactors. It is necessary to research the flow and heat transfer mechanisms of post-dryout. To economically and comprehensively study on the post-dryout heat transfer characteristics, this work conducted fluid-to-fluid modeling research on water and R-134a data banks by using Buckingham dimensional analysis methodology. In addition, a new interpolation method was developed and verified to make the scaling between the two data banks possible. Finally, a scaling method of post-dryout heat transfer was proposed and assessed by using experimental data. The results showed that the obtained scaling method is reliable in certain conditions.

Keywords: post-dryout, LOCA, fluid-to-fluid modeling, dimensional analysis, thermal hydraulics

Edited by:
Luteng Zhang,
Chongqing University, China

Reviewed by:
Wan Sun,
Chongqing University, China
Wei Ding,
Helmholtz Association of German Research Centres (HZ), Germany

Correspondence:
Dali Yu
dlyu@inest.cas.cn

†ORCID:
Dali Yu
orcid.org/0000-0002-3637-9599

Specialty section:
This article was submitted to Nuclear Energy, a section of the journal Frontiers in Energy Research

Received: *20 November 2021*
Accepted: *31 December 2021*
Published: *28 January 2022*

Citation:
Yu D, Xu C, Hu C and Fan Y (2022) An Innovative Investigation on Fluid-to-Fluid Modeling of Post-Dryout Heat Transfer in Thermal Energy Systems. Front. Energy Res. 9:819060. doi: 10.3389/fenrg.2021.819060

1 INTRODUCTION

1.1 Background

Post-dryout heat transfer phenomenon widely exists in both the loss-of-coolant accident (LOCA) of a pressurized water reactor (Yoo et al., 2020) and the off-design conditions of water-cooled ceramic breeder blanket in the Chinese Fusion Engineering Test Reactor (Cheng et al., 2020). A post-dryout heat transfer region can be encountered once the contact between the liquid film and the heated surface cannot be maintained due to continuous liquid film depletion, and the liquid phase is only in the form of dispersed droplets or small fragments, which usually occurs at a void fraction greater than 80% (Groeneveld, 1973). As shown in **Figure 1**, a post-dryout region consists of a developing region (unstable film boiling) and a fully developed region (stable film boiling) (Yu et al., 2018). The developing region is defined as an unstable region with wet contact heat transfer occurring between the wall and droplets. The heat transfer coefficient in this region reduces significantly, with an accompanying steep temperature rise on the wall surface. While the direct wall–droplets contact becomes less frequent, the vapor temperature and velocity structures and the droplets distribution over the cross-section of the flow are well rearranged, finally the flow develops into a relatively stable state, which is called fully developed post-dryout region, characterized by a stable mist flow pattern and no wall–droplets wet contact. Heat transfer in the full-range post-dryout regime involves various heat exchange paths among the vapor phase, droplets, and the heated wall, including 1) convective heat transfer from wall to vapor; 2) interfacial heat transfer from vapor to droplets; 3) contact heat

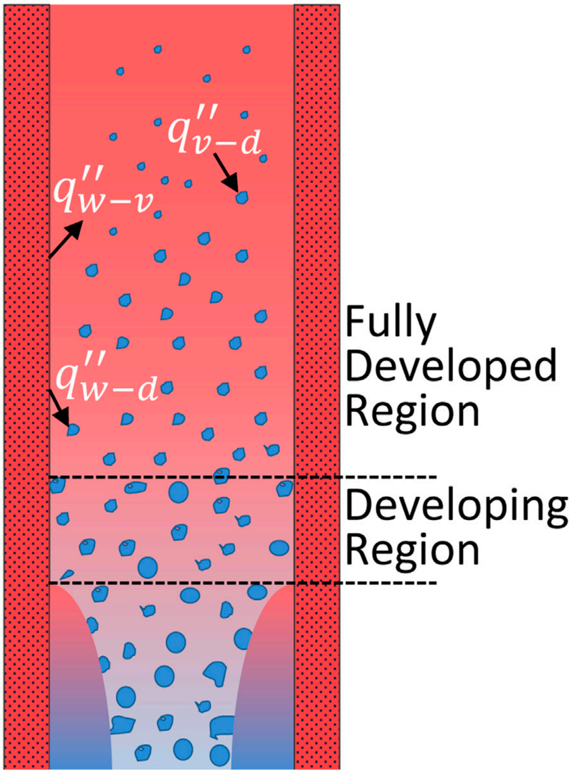

FIGURE 1 | Typical flow and heat transfer patterns in the post-dryout region; q''_{w-v}: convective and radiative heat transfer between wall and vapor, q''_{w-d}: contact and radiative heat transfer between wall and droplet, q''_{v-d}: interfacial and radiative heat transfer between vapor and droplet.

transfer between wall and droplets; 4) radiative heat transfer from wall to droplets; 5) radiative heat transfer from vapor to droplets; and 6) radiative heat transfer from wall to vapor.

A very significant thermal nonequilibrium of several hundred degrees can be generated in the post-dryout region, which has been confirmed by some experiments with water at low to moderate pressures in a tube (Nijhawan et al., 1980; Evans et al., 1983; Gottula et al., 1985). According to this fact, both the experimental studies and the predicting methods of post-dryout heat transfer have been conducted for over 60 years, ranging from wall temperature data in various fluids and various flow conditions to subtopics such as the influence of droplet hydrodynamics on both the convective heat transfer between wall and vapor and the interfacial heat transfer between vapor and droplets. However, the reliable prediction methods for post-dryout heat transfer are still missing due to the complexity of processes involved, especially due to the difficulties in the prediction of thermal nonequilibrium.

1.2 State of the Art of Experiments, Theoretical Models, and Fluid-to-Fluid Modeling

An experimental study of post-dryout heat transfer was performed at the KIT Model Fluid Facility (KIMOF) by using refrigerant R-134a as the working fluid (Köckert et al., 2018; Köckert et al., 2021). Tests were conducted in a uniformly heated tube (inside diameter: 10 *mm*, heated length: 3,100 *mm*) at pressures of 11.1, 16, and 28 *bar*, with varying mass flux in the range of 300–1,500 $\mathrm{kg}/(m^2s)$. Wall temperature distributions were obtained and used to verify the developed KIT Mechanistic Model (Yu et al., 2018; Yu, 2019). As to further verify and possibly improve the predictions, additional experimental information about the droplet behavior and vapor temperature distributions are required. Köckert et al. (2021) integrated a visualizable annular test section into the KIMOF test facility in order to measure the droplet distribution, size distribution, and velocities using a high-speed camera through 32 bull's-eye–shaped windows on the test section. Liu et al. (2021) performed post-dryout heat transfer experiments in a vertical tubular test section using water as the working fluid. The heat transfer characteristics during the formation, growth, and propagation of dry patches were analyzed based on the measured outer surface temperature. Jin and Shirvan (2021) experimentally investigated on the two-phase flow interface behavior during film boiling in quench transients using image processing.

Different types of theoretical models and correlations have been developed and were applied with varying degrees of success. An analytic model was developed for the whole post-dryout region by the authors (Yu et al., 2018; Yu, 2019; Köckert et al., 2021) and was verified by plenty of data bank including both water and R-134a experiments. Cheng et al. (2018) developed a mechanistic model to predict the post-dryout heat transfer and rewetting. Based on the treatment of direct contact heat transfer between the wall and droplets, the hysteresis phenomenon of the flow boiling curve was obtained and explained by the Leidenfrost effect. In addition to these modeling works, Li and Anglart (2016), Shi et al. (2017), and Fan et al. (2020) simulated some interesting features of post-dryout heat and mass transfer (e.g., vapor temperature and velocity profile, droplet behaviors) through the CFD approach. However, this kind of approach is computationally expensive, and the models applied in the CFD still need quite extensive knowledge of the physical phenomena to improve the prediction.

Massive data are required to reveal the flow and heat transfer mechanisms of post-dryout with water, as well as validating the theoretical models and CFD approaches. In order to reduce the cost and technical difficulties of the water-based post-dryout experiments, Freon family fluids have been frequently used as the model fluid because of their lower latent heat of vaporization and lower critical pressure. Groeneveld et al. (1997) indicated that in the fluid-to-fluid modeling of post-dryout heat transfer, geometric and dynamic similarities must be satisfied. Equal equilibrium qualities were utilized to achieve thermodynamic similarity. For hydrodynamic similarity, equal density ratios (ρ_v/ρ_d) in both fluids were required. As for the dimensionless number $\Psi(G)$ involving mass flux, it is important to apply compensated distortion coefficients to make it appropriate for the studied phenomena. Groeneveld et al. (1997) suggested the use of $Re_v\,\mathrm{Pr}^{0.5}$ as the dimensionless number $\Psi(G)$ through the concluding research results of Hammouda et al. (1996), in which the post-dryout heat transfer was studied in three different Freons.

1.3 Objectives

In this study, the work started from deriving dimensionless numbers and then selecting dimensionless numbers by their significance to post-dryout heat transfer. Five different forms of the scaling methods were obtained and evaluated through an optimization procedure, for which a new interpolation method was developed. The optimized scaling methods were eventually assessed by some experimental tests.

2 METHODS

2.1 Derivation of Dimensionless Numbers

Based on the experience of theoretical investigations on post-dryout heat transfer, the independent variables that determine the wall temperature in a post-dryout flow in a round tube can be described as below:

The system describing variables: P, G, $q_w^{''}$, Δi, L_T, D_T, and g,where P is the system pressure; G is the inlet mass flux; $q_w^{''}$ is the wall heat flux; Δi is the subcooling of the inlet flow and equals the enthalpy difference of the saturation liquid and the flow at inlet; L_T is the heated length of the tube, D_T is the inner diameter of the tube; and g is gravitational acceleration.

The detailed analyses usually take into account the pressure P via the saturation temperature T_s, or via the physical properties that are evaluated at the saturation temperature. The primary properties that would be used in the derivation of the dimensionless numbers are listed as below:

The properties describing variables: i_{v-d}, ρ_d, ρ_v, μ_d, μ_v, $C_{p,d}$, $C_{p,v}$, k_d, k_v, and $\sigma$where i_{v-d} is the latent heat of evaporation; ρ_d and ρ_v are the droplet and vapor densities at the saturation temperature individually; μ_d and μ_v are the droplet and vapor viscosities at the saturation temperature individually; $C_{p,d}$ and $C_{p,v}$ are the droplet and vapor specific heat capacities at constant pressure individually; k_d and k_v are the droplet and vapor thermal conductivities at saturation temperature individually; and σ is the surface tension.

With all the possibly relevant variables obtained, the most interesting variable, which is the wall inner surface superheat $T_w - T_s$, can be described as a function of these variables:

$$T_w - T_s = \mathrm{F}\left(G, q_w^{''}, \Delta i, L_T, D_T, g, i_{v-d}, \rho_d, \rho_v, \mu_d, \mu_v, C_{p,d}, C_{p,v}, k_d, k_v, \sigma\right) \quad (1)$$

According to the Buckingham Pi-theorem in the form of one possible set of π terms, the function in **Eq. 1** can be transformed as below:

$$\pi_1 = \mathrm{F}(\pi_2, \pi_3, \pi_4, \ldots, \pi_{13}) \quad (2)$$

where the π terms are expressed as below:

$\pi_1 =$	$\frac{q_w^{''} D_T}{k_v (T_w - T_s)}$	Nusselt number	$\pi_2 =$	$\frac{q_w^{''}}{G i_{v-d}}$	Boiling number
$\pi_3 =$	$\frac{G D_T}{\mu_v}$	Reynolds number	$\pi_4 =$	$\frac{G^2 D_T}{\rho_d \sigma}$	Weber number
$\pi_5 =$	$\frac{\mu_v C_{p,v}}{k_v}$	Prandtl number	$\pi_6 =$	$\frac{G}{\rho_d \sqrt{g D_T}}$	Froude number
$\pi_7 =$	$\frac{\Delta i}{i_{v-d}}$	Subcooling number	$\pi_8 =$	$\frac{L_T}{D_T}$	Geometric similarity
$\pi_9 =$	$\frac{\rho_d}{\rho_v}$	Density ratio	$\pi_{10} =$	$\frac{k_d}{k_v}$	Thermal conductivity ratio
$\pi_{11} =$	$\frac{\mu_d}{\mu_v}$	Viscosity ratio	$\pi_{12} =$	$\frac{C_{p,d}}{C_{p,v}}$	Specific heat capacity ratio
$\pi_{13} =$	$\frac{G}{\rho_d \sqrt{i_{v-d}}}$	Velocity ratio			

In the above dimensionless numbers, π_1 is the dependent dimensionless number that includes the variable of interest $T_w - T_s$, and the remaining are called independent dimensionless numbers formed by independent variables. Though there are many different complete sets of dimensionless numbers that can be formed, in the current work, the above group of dimensionless number is chosen on the basis of the following considerations:

- Except the one chosen dependent dimensionless number π_1—the Nusselt number, each independent dimensionless number to the greatest extent includes only one independent variable that can be regulated experimentally. This allows the maximum amount of experimental control over the dimensionless numbers.
- Most of the dimensionless numbers are expressed as classic numbers (e.g., Reynolds, Prandtl, and Weber), especially while the numbers have their physical significance in post-dryout flow.
- For the properties used in the dimensionless numbers, all are evaluated at the saturation temperature, and which phase's properties are used (since they have the same dimensions) depends on the dimensionless number's physical meaning. For example, the Reynolds number relates to the intensity of flow, and the vapor properties are used because the vapor is the continuous phase with more than 80% volume fraction in the flow.

Strictly speaking, the fluid-to-fluid modeling of post-dryout heat transfer should keep the inlet subcooling number equal in both the model and prototype facilities since the inlet flow conditions can influence droplets generation upstream of the dryout. However, this kind of scaling from case to case is quite expensive due to which the inlet conditions can vary from using different scaling methods and is not suitable to massively evaluate different scaling methods through this way. In the current work, scaling was performed from point to point between the water-based Becker and R-134a-based KIT experiments, and the variables were derived from

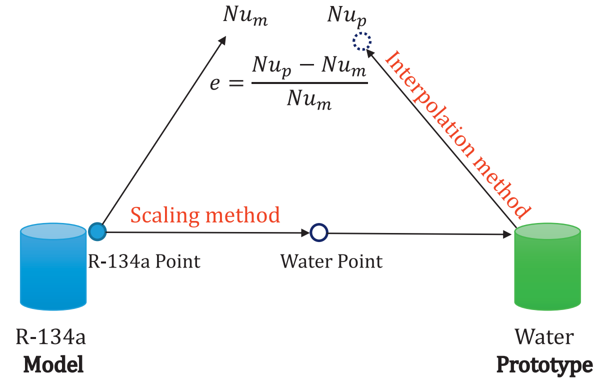

FIGURE 2 | Scaling methods optimization procedure.

the local flow conditions. The geometric similarity is kept by using identical tubes as suggested by Groeneveld et al. (1997) to eliminate the geometric effect. The thermodynamic similarity is kept by using equivalent equilibrium quality x_e and boiling number Bo. As for the hydrodynamic similarity, the pressure is controlled by using the density ratio π_9, and a dimensionless number $\Psi(G)$ involving mass flux can be derived by applying the compensated distortion technique by using the other considered dimensionless numbers, including π_3, π_4, π_5, and π_{11}. Thus, the scaling method can be written as below:

$$\frac{q_w'' D_T}{k_v (T_w - T_s)} = \mathrm{F}\left(\Psi(G), \frac{q_w''}{Gi_{v-d}}, x_e, \frac{\rho_d}{\rho_v}\right) \tag{3}$$

where, five different forms of $\Psi(G)$, including $\pi_3\pi_4^n$, $\pi_3\pi_5^n$, $\pi_3\pi_{11}^n$, $\pi_4\pi_5^n$, and $\pi_4\pi_{11}^n$, are investigated in the current work to obtain the best-fitted constant exponent n for each form.

2.2 Scaling Methods Optimization Procedure

To obtain the best-fitted scaling method, an optimization procedure is used as shown in **Figure 2**. Scaling is performed from point to point by using the method given in **Eq. 3** with different forms of $\Psi(G)$. The details are as follows:

First, the Model data bank comes from the R-134a–based KIT experiment (Köckert et al., 2018). Each data point is obtained in the fully developed post-dryout region with a selection criterion of dryout void fraction $\alpha_{do} > 0.8$. The Prototype data bank comes from the water-based Becker experiment (Becker et al., 1983). Each data point is also obtained in the fully developed post-dryout region with a selection criterion of dryout void fraction $\alpha_{do} > 0.8$. Then, the parameters of the selected data points are listed in **Table 1**.

Secondly, five different forms of $\Psi(G)$, including $\pi_3\pi_4^n$, $\pi_3\pi_5^n$, $\pi_3\pi_{11}^n$, $\pi_4\pi_5^n$, and $\pi_4\pi_{11}^n$, are used to scale the mass flux separately. For each form of $\Psi(G)$, the constant exponent n is tested from −2 to 2 with an interval of 0.1. For each constant exponent n, **Eq. 3** can be fixed as one scaling method. For each scaling method, every data point in the Model data bank is scaled through this method to water conditions. The Nu_m is the dependent Pi term π_1 of the data point in the Model data bank. Since the water data point obtained through the scaling method cannot be well matched in the Prototype data bank, an interpolation method should be used to determine its actual dependent Pi term π_1, which is named Nu_p.

Lastly, an error e is defined as $e = (Nu_p - Nu_m)/Nu_m$, representing the accuracy of the scaling. The average e and RMS e of all the data points can be used to evaluate the applied scaling method, under the circumstance that the interpolation method can provide an accurate value of Nu_p.

2.3 Interpolation Method

To massively evaluate the fluid-to-fluid scaling methods, an interpolation method is required to make the optimization procedure possible. The sparsity of the data bank and performance of the interpolation method determine the quality of the evaluation of the scaling methods. In the current work, the interpolation is performed with Becker data bank, in which the flow parameter (e.g., mass flux, heat flux, pressure) intervals are not small. Thus, an effective interpolation method is required to give an accurate prediction of Nu_p.

Badea et al. (2018) developed a procedure to assess the intrinsic consistency of the experimental information (values of Nusselt number at the bulk Nu_{vb}) contained in the data bank for supercritical water in circular tubes. The procedure was based on the assumption that the ratio of the Nusselt number value at point *i* to the value calculated by the local optimal correlation is equal to that ratio which is obtained from its neighboring data point *j*. The relation can be described as below:

$$\frac{Nu_i}{Nu_{i,oc}} = \frac{Nu_j}{Nu_{j,oc}} \tag{4}$$

where, Nu_i and Nu_j are the values of the Nusselt number at points *i* and *j*, respectively; $Nu_{i,oc}$ and $Nu_{j,oc}$ are the values of the

TABLE 1 | Information of data bank used in optimizing scaling method.

Data bank	D_T *[mm]*	Parameters				Points number
		Pressure *[MPa]*	Mass flux *[kg/(m²s)]*	Heat flux *[kW/m²]*	Quality [–]	
KIT	10	1.1, 1.6, 2.8	300–1,500	30–140	0.28–1.76	1820
Becker	10, 14.9	3–16	500–3,100	147–1,295	0.3–1.35	2930

TABLE 2 | Information of the scaling methods optimizing matrix.

Name	SM1	SM2	SM3	SM4	SM5
$\Psi(G)$	$(\frac{GD_T}{\mu_v})(\frac{G^2D_T}{\rho_d\sigma})^n$	$(\frac{GD_T}{\mu_v})(\frac{\mu_v C_{p,v}}{k_v})^n$	$(\frac{GD_T}{\mu_v})(\frac{\mu_d}{\mu_v})^n$	$(\frac{G^2D_T}{\rho_d\sigma})(\frac{\mu_v C_{p,v}}{k_v})^n$	$(\frac{G^2D_T}{\rho_d\sigma})(\frac{\mu_d}{\mu_v})^n$

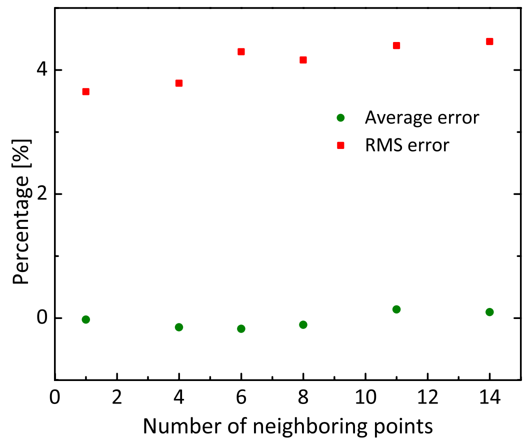

FIGURE 3 | Assessment results versus the number of neighboring points *n*.

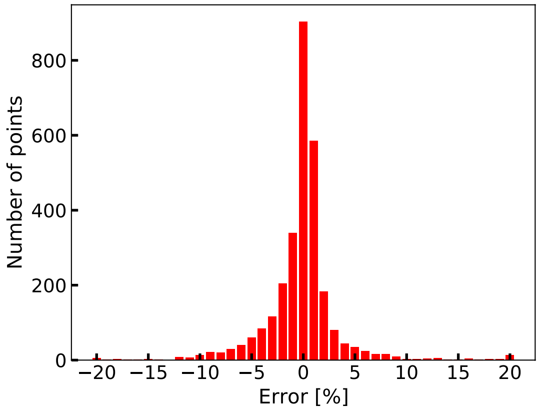

FIGURE 4 | Error distribution of the assessment with *n* is 4.

Nusselt number at points *i* and *j*, which are calculated by the local optimal correlation, respectively.

Based on this assumption, the interpolation method used for post-dryout heat transfer data bank is developed with the following procedures:

2.3.1 Determination of Neighboring Data Points

The data points in post-dryout heat transfer can be considered as neighboring points if the differences of all the parameters are within a small range receptively. In the current work, the tube diameter D_T and the local flow parameters including pressure P, mass flux G, wall heat flux q''_w, and equilibrium quality x_e are used to define a data point. Therefore, for the data point i, the criteria to determine its neighboring data points are proposed as below:

$$
\begin{aligned}
|D_{T,i} - D_{T,j}| &\leq C \cdot 6\ [mm] \\
|P_i - P_j| &\leq C \cdot 0.5\ [MPa] \\
|G_i - G_j| &\leq C \cdot 250\ [kg/(m^2 s)] \\
|q''_{w,i} - q''_{w,j}| &\leq C \cdot 100\ [kW/m^2] \\
|x_{e,i} - x_{e,j}| &\leq C \cdot 0.05\ [-]
\end{aligned}
$$

For this interpretation method, if a data point is closer to the data point of interest, the assumption in **Eq. 4** is more likely to be correct. However, if only one data point is selected to speculate the actual Nu_i of the data point of interest, the systematic error that is caused by this assumption cannot be compensated. Thus, a coefficient C is applied, decreasing it from 1 to 0 until around n neighboring points are found. In the current work, the number n is chosen to be equal to 4.

2.3.2 Calculating Nusselt Number

While the neighboring points are found, two post-dryout heat transfer models including the KIT Mechanistic Model (Yu et al., 2018; Yu, 2019) and the Local Condition Solution (LCS) (Yoder and Rohsenow, 1983; Varone and Rohsenow, 1986) can be used to calculate the predicted $Nu_{j,oc}$ of each neighboring point. The prediction error by the model is defined as below:

$$e_j = \frac{Nu_{j,oc} - Nu_j}{Nu_j}; \quad j = 1, 2, 3, 4, \cdots n \tag{5}$$

where, n is the number of the found neighboring data points. Comparing the two root-mean-square (RMS) errors which were individually calculated by the proposed model and the LCS, the model that has smaller RMS error is considered as the local optimal correlation.

Finally, a mean value of the Nusselt number $\overline{Nu_i}$ can be obtained as follows:

$$\overline{Nu_i} = \frac{\sum_{j=1}^{n} Nu_j \frac{Nu_{i,oc}}{Nu_{j,oc}}}{n} \tag{6}$$

The mean value $\overline{Nu_i}$ is considered as the actual Nusselt number of the interested point i.

To assess this interpolation method, each data point in the Prototype data bank is selected and calculated by applying this interpolation method on the remaining data points. A sensitivity study is implemented on the influence of the utilized number of neighboring data points n on the accuracy of the interpolation method. As shown in **Figure 3**, the assessment results are plotted against the number of neighboring points n. The value of n varies from 1 to 14, the average error remains close to 0, and the RMS error increases slightly but is less than 5%. Finally, n is chosen equal to 4 in the current work. The assessment shows that the average error is −0.149% and the RMS error is 3.786%. As shown in **Figure 4**, the accuracy of most of the data points are within a range of ±3%.

Though this assessment only guarantees the accuracy of the interpolation method that was used in the flow conditions of the

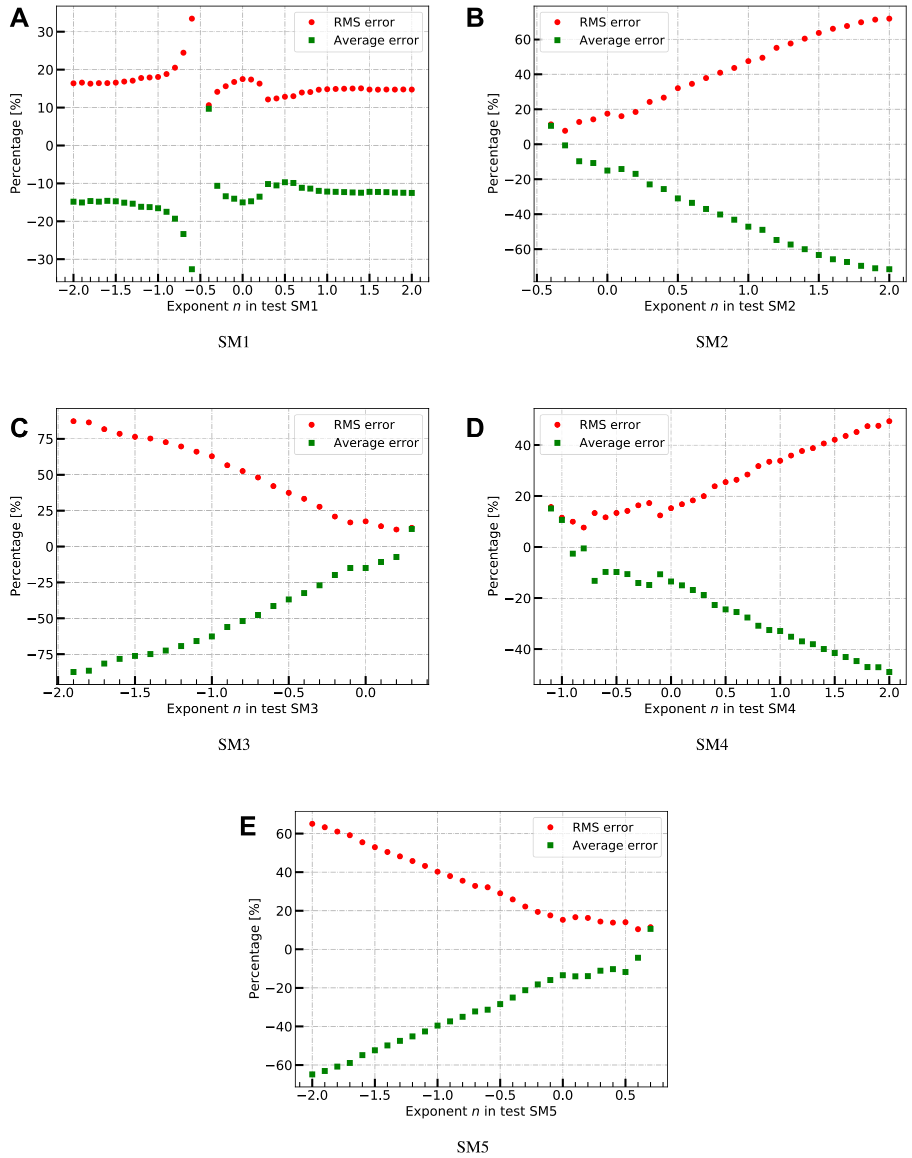

SM1

SM2

SM3

SM4

SM5

FIGURE 5 | Optimization results of each form of the scaling methods.

TABLE 3 | Results of the average and RMS errors of each form of the scaling methods with fitted *n*.

Name	Ψ(G)	Fitted n	Average error	RMS error
SM1	$(\frac{GD_T}{\mu_v})(\frac{G^2D_T}{\rho_d\sigma})^n$	0.4	–0.105	0.124
SM2	$(\frac{GD_T}{\mu_v})(\frac{\mu_vC_{p,v}}{k_v})^n$	–0.3	–0.006	0.077
SM3	$(\frac{GD_T}{\mu_v})(\frac{\mu_d}{\mu_v})^n$	0.2	–0.073	0.118
SM4	$(\frac{G^2D_T}{\rho_d\sigma})(\frac{\mu_vC_{p,v}}{k_v})^n$	–0.8	–0.005	0.077
SM5	$(\frac{G^2D_T}{\rho_d\sigma})(\frac{\mu_d}{\mu_v})^n$	0.6	–0.044	0.104

Prototype data bank, it can generally reflect the reliability while the method is applied within the whole range of the flow conditions. By increasing the density of the points in the data bank, this assessment would be more credible to testify the accuracy of the interpolation method in the optimization procedure.

2.4 Scaling Methods Optimization Results

As described in **Section 2.2**, the scaling methods optimization procedure is performed from point to point by using the method in **Eq. 3** with five different forms of $\Psi(G)$. The optimizing matrix is shown in **Table 2**.

For each form of the scaling methods, the constant exponent n is tested from −2 to 2 with an interval of 0.1. The optimization results are shown in **Figure 5**, where the error is defined as $e = (Nu_p - Nu_m)/Nu_m$. For form SM1, the RMS error varies very fast, while n is close to the value of –0.5, which would vanish the mass flux G in the dimensionless number $\Psi(G)$. The best-fitted value of

TABLE 4 | Scaling ratios R_S of heat flux, mass flux, and pressure for each form of the scaling methods.

Name	Heat flux R_S	Mass flux R_S	Pressure R_S
SM1	0.072	0.682	0.16
SM2	0.060	0.566	0.16
SM3	0.058	0.553	0.16
SM4	0.060	0.567	0.16
SM5	0.056	0.532	0.16

n can be selected as 0.4, where the RMS error is nearly the smallest and the value is not sensitive when n is around 0.4. For form SM2, after each data point in the Model data bank scaled by the scaling method with n is less than −0.4, no neighboring data points can be found in the Prototype data bank. The best-fitted value of n for SM2 can be selected as −0.3. For form SM3, while n is more than 0.3, no neighboring data points can be found. The best fitted n for SM3 can be selected as 0.2. For form SM4, while n is less than −1.1, no neighboring data points can be found. The best fitted n for SM4 can be selected as −0.8. For form SM5, while n is greater than 0.7, no neighboring data points can be found. The best fitted n for SM5 can be selected as 0.6. The average and RMS errors of each form of the scaling methods with fitted values of n are listed in **Table 3**. If merely based on the RMS errors, the optimized SM2 and SM4 perform the best, and SM1 performs the worst.

A flow condition in Prototype is chosen as pressure $P = 7\ MPa$, mass flux $G = 2{,}600\ kg/(m^2 s)$, heat flux $q''_w = 1500\ kW/m^2$, and diameter $D_T = 12.6\ mm$ to investigate the scaling ratio R_S of each form of the scaling methods. R_S is defined as below:

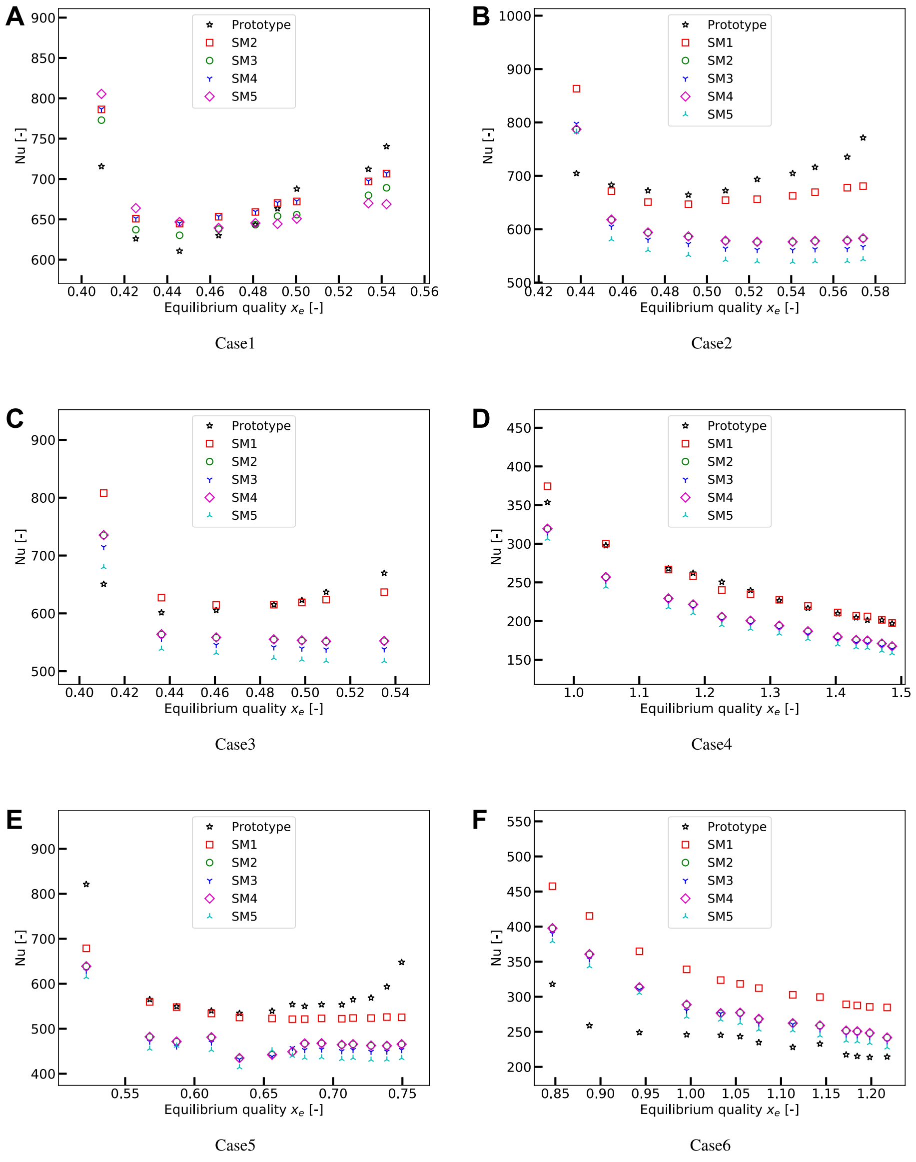

Case1

Case2

Case3

Case4

Case5

Case6

FIGURE 6 | Assessments of the optimized scaling methods with Prototype data from Bennett et al. (1968).

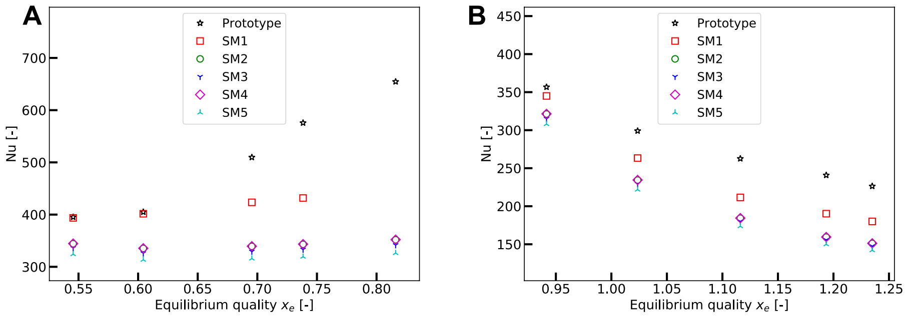

Case7 Case8

FIGURE 7 | Assessments of the optimized scaling methods with Prototype data from Era et al. (1966).

TABLE 5 | Parameters of tests for assessment of the optimized scaling methods.

Test Id	Data bank	Tube diameter [*mm*]	Pressure [*MPa*]	Mass flux [*kg*/(*m*^{2}*s*)]	Heat flux [*kW*/*m*^{2}]
Case1	Bennett et al. (1968)	12.6	7.0	2,600	1,500
Case2	Bennett et al. (1968)	12.6	7.0	2000	1,100
Case3	Bennett et al. (1968)	12.6	7.0	1950	1,500
Case4	Bennett et al. (1968)	12.6	7.0	394	545
Case5	Bennett et al. (1968)	12.6	7.0	1,360	970
Case6	Bennett et al. (1968)	12.6	7.0	650	582
Case7	Era et al. (1966)	6.0	7.0	2,200	1,100
Case8	Era et al. (1966)	6.0	7.0	1,100	500

$$R_S = \frac{value\ in\,\mathbf{Model}}{value\ in\,\mathbf{Prototype}} \tag{7}$$

The results are listed in **Table 4**, and the optimized SM5 scaling method has the best scaling ratio, which can reduce the cost and technical difficulties of implementing the post-dryout experiments.

3 ASSESSMENT OF THE OPTIMIZED SCALING METHODS

Assessments of each form of the optimized scaling methods are performed point-to-point from the Prototype data to the Model data. **Figures 6**, **7** show the assessment results by using six cases from Bennett et al. (1968) and two cases from Era et al. (1966), respectively. The cases are scaled by each scaling method point-to-point to R-134a conditions, and the Nusselt number in Model Nu_m is obtained by using the proposed interpolation method with the KIT data bank. Information of each case is listed in **Table 5**.

In Case1 as shown in **Figure 6A**, there are no neighboring points found in the KIT data bank for the scaling by using method SM1. The results show the optimized methods SM2 and SM4 perform the best in this case, and their predictions are almost the same. For Case2, Case3, Case4, and Case5, method SM1 performs the best and has excellent agreement with the Prototype data. For Case6, methods SM2, SM3, SM4, and SM5 predict very similar results, and SM1 performs obviously worse than the others. For Case7 and Case8, method SM1 predicts better than the others, and assessments in these two cases show worse accuracy of the scaling methods than the six cases from Bennett et al. (1968).

To sum up, though very limited cases are used to assess the optimized scaling methods, the results show that the optimized methods SM2 and SM4 always give very similar predictions. In most cases, SM1 can have a better agreement with the Prototype data than the other scaling methods, but in some particular cases, it can also have worse predictions than the other methods. All methods give worse predictions for Era (Era et al., 1966) than for Bennett (Bennett et al., 1968) under similar flow conditions. This could be because the tube diameter in the Era experiment is small, the scaling or the interpolation method is not effective, while the diameter is far from that of the data bank, which in these assessment tests is 10 *mm* for the KIT data bank.

4 CONCLUSION AND OUTLOOK

In this study, fluid-to-fluid modeling of the post-dryout heat transfer between R-134a and water is studied. The scaling methods are developed based on dimensional analyses by using the Buckingham Pi-theorem. The work starts from deriving dimensionless numbers, selecting dimensionless numbers by their significance to post-dryout heat transfer, and then evaluating five different forms of scaling methods through an optimization procedure, in which a proposed interpolation method is used. The interpolation method is necessary for such massive scaling between two data banks and is assessed by verifying the data in the Prototype data bank itself. Finally, for each form of the scaling methods, a fitted dimensionless number $\Psi(G)$ involving mass flux can be obtained. For each form of the scaling methods with fitted $\Psi(G)$, assessments are implemented point-to-point from the Prototype data to Model data. The prototype data makes use of six cases from Bennett et al. (1968) and two cases from Era et al. (1966). The Model data makes use of the KIT data bank from Köckert et al. (2018).

Merely from the obtained results in the current work, the optimized SM1 can be selected as the best scaling method, which in final form can be expressed as:

$$\frac{q_w'' D_T}{k_v (T_w - T_s)} = \mathrm{F}\left(\left(\frac{G D_T}{\mu_v}\right) \cdot \left(\frac{G^2 D_T}{\rho_d \sigma}\right)^{0.4}, \frac{q_w''}{G i_{v-d}}, x_e, \frac{\rho_d}{\rho_v}\right) \tag{8}$$

All the properties are evaluated at saturation temperature, and its application range should be kept the same as the flow conditions of KIT and Becker data banks, as shown in **Table 1**.

It is worth noting that this scaling method is not verified under a wide range of flow conditions since sometimes no neighboring data points can be found by using this scaling method. The accuracy of the interpolation method during the optimizing of the scaling methods is also not directly assessed. Besides, as indicated at the beginning, the near-wall fluid properties cannot be taken into consideration in the scaling method because the heat flux controlled system is being focused on in this study, and this could probably lead the scaling method SM1 into a limited application range, where the wall superheat cannot be too high. Therefore, the accuracy of the scaling method SM1 is only guaranteed to be reliable in certain conditions so far, until further work can be implemented through the same optimization procedure but by using data points that are generated in two identical tubes and in a wide range of flow conditions for both R-134a and water experiments. Meanwhile, another approach for scaling can be carried out in future work, in which the wall temperature is considered as a controlled variable since properties variation over the cross-section of the flow influences post-dryout heat transfer greatly.

DATA AVAILABILITY STATEMENT

The raw data supporting the conclusions of this article will be made available by the authors without undue reservation.

AUTHOR CONTRIBUTIONS

DY: Conceptualization, methodology, software, validation, formal analysis, investigation, and writing. CX: Methodology, software, and editing. CH: Methodology, software, and editing. YF: Methodology, software, and editing.

FUNDING

This work was supported by the experimental data from the Institute for Applied Thermofluidics (IATF) of KIT, the assistance from Ludwig Köckert, and the supervision from Prof. Xu Cheng. DY is grateful for the support from the Ministry of Education Key Laboratory of Advanced Reactor Engineering and Safety Project (ARES-2020-04) and the CASHIPS Director's Fund (YZJJ2021QN36).

REFERENCES

Badea, A. F., Zhao, M., Cheng, X., Feuerstein, F., and Liu, X. (2018). Consistency Considerations on a Large Databank and Wide Range Heat Transfer Prediction for Supercritical Water in Circular Tubes. *Nucl. Eng. Des.* 335, 178–185. doi:10.1016/j.nucengdes.2018.05.015

Becker, K., Ling, C., Hedberg, S., and Strand, G. (1983). *An Experimental Investigation of post Dryout Heat Transfer*. Stockholm: Tech. Rep. KTH-NEL-33, Royal Inst. of Tech.

Bennett, A., Hewitt, G., Kearsey, H., and Keeys, R. (1968). *Heat Transfer to Steam–Water Mixtures Flowing in Uniformly Heated Tubes in Which the Critical Heat Flux Has Been Exceeded*. Harwell: Tech. Rep. REP/AERE-R-5373, Atomic Energy Research Establishment, Harwell, Eng.

Cheng, X., Feuerstein, F., Klingel, D., and Yu, D. L. (2018). Mechanistic Prediction of post Dryout Heat Transfer and Rewetting. *Kerntechnik* 83 (3), 203–207. doi:10.3139/124.110872

Cheng, X., Ma, X., Lu, P., Wang, W., and Liu, S. (2020). Thermal Dynamic Analyses of the Primary Heat Transfer System for the Wccb Blanket of Cfetr. *Fusion Eng. Des.* 161, 112067. doi:10.1016/j.fusengdes.2020.112067

Era, A., Gaspari, G., Hassid, A., Milani, A., and Zavattarelli, R. (1966). *Heat Transfer Data in the Liquid Deficient Region for Steam-Water Mixtures at 70* Kg/cm^2 *Flowing in Tubular and Annular Conduits*. Italy: Tech. Rep. No. 11, Centro Informazioni Studi Esperienze.

Evans, D., Webb, S., and Chen, J. (1983). *Measurements of Axially Varying Non-equilibrium in post Critical-Heat-Flux Boiling in a Vertical Tube*. United States: Tech. Rep. NUREG/CR-3363, Lehigh Univ., USA. Inst. of Thermo-Fluid Engineering and Science.

Fan, W., Li, H., and Anglart, H. (2020). A Study of Rewetting and Conjugate Heat Transfer Influence on Dryout and post-dryout Phenomena with a Multi-Domain Coupled Cfd Approach. *Int. J. Heat Mass Transfer* 163, 120503. doi:10.1016/j.ijheatmasstransfer.2020.120503

Gottula, R., Condie, K., Sundaram, R., Neti, S., Chen, J., and Nelson, R. (1985). *Forced Convective, Nonequilibrium, post-chf Heat Transfer experiment Data and Correlation Comparison*. United States: Tech. Rep. NUREG/CR-3193, NASA.

Groeneveld, D., Doeffler, S., Tain, R., Hammouda, N., and Cheng, S. (1997). "Fluid-to-fluid Modelling of the Critical Heat Flux and post-dryout Heat Transfer," in *Proceedings of the Experimental Heat Transfer* (Brussels: Fluid Mechanics and Thermodynamics), 859–866.

Groeneveld, D. (1973). *Post-dryout Heat Transfer at Reactor Operating Conditions*. Ontario: Tech. Rep. AECL-4513, Atomic Energy of Canada Ltd.

Hammouda, N., Groeneveld, D. C., and Cheng, S. C. (1996). An Experimental Study of Subcooled Film Boiling of Refrigerants in Vertical Up-Flow. *Int. J. Heat mass transfer* 39 (18), 3799–3812. doi:10.1016/0017-9310(96)00062-2

Jin, Y., and Shirvan, K. (2021). Study of the Film Boiling Heat Transfer and Two-phase Flow Interface Behavior Using Image Processing. *Int. J. Heat Mass Transfer* 177, 121517. doi:10.1016/j.ijheatmasstransfer.2021.121517

Köckert, L., Badea, A. F., Cheng, X., Yu, D., and Klingel, D. (2021). Studies on post-dryout Heat Transfer in R-134a Vertical Flow. *Int. J. Adv. Nucl. Reactor Des. Tech.* 3, 44–53. doi:10.1016/j.jandt.2021.05.001

Köckert, L., Feuerstein, F., Yu, D., Klingel, D., and Cheng, X. (2018). "Experimental Study of post-dryout Heat Transfer and Rewetting in a R- 134a Cooled Vertical Tube at Comparable Water Cooled Reactor Pressure Conditions," in *The 12th International Topical Meeting on Reactor Thermal-Hydraulics, Operation, and Safety (NUTHOS-12)* (Qingdao (China): Chinese Nuclear Society).

Li, H., and Anglart, H. (2016). Prediction of Dryout and post-dryout Heat Transfer Using a Two-phase Cfd Model. *Int. J. Heat Mass Transfer* 99, 839–850. doi:10.1016/j.ijheatmasstransfer.2016.04.021

Liu, Q., Sun, H., Liu, Y., Kelly, J., and Sun, X. (2021). Experimental Study of post-chf Heat Transfer in a Vertical Tubular Test Section. *Int. J. Heat Mass Transfer* 166, 120697. doi:10.1016/j.ijheatmasstransfer.2020.120697

Nijhawan, S., Chen, J. C., Sundaram, R. K., and London, E. J. (1980). Measurement of Vapor Superheat in post-critical-heat-flux Boiling. *J. Heat Transfer* 102 (3), 465–470. doi:10.1115/1.3244324

Shi, J., Sun, B., Yu, X., Zhang, P., and Song, F. (2017). Modeling the Full-Range thermal-hydraulic Characteristics and post-dryout Deviation from Thermodynamic Equilibrium in Once-Through Steam Generators. *Int. J. Heat Mass Transfer* 109, 266–277. doi:10.1016/j.ijheatmasstransfer.2017.02.007

Varone, A. F., and Rohsenow, W. M. (1986). Post Dryout Heat Transfer Prediction. *Nucl. Eng. Des.* 95, 315–327. doi:10.1016/0029-5493(86)90057-9

Yoder, G. L., and Rohsenow, W. M. (1983). A Solution for Dispersed Flow Heat Transfer Using Equilibrium Fluid Conditions. *J. Heat Transfer* 105 (1), 10–17. doi:10.1115/1.3245528

Yoo, J. M., Yun, B. J., Yoon, H. Y., and Jeong, J. J. (2020). Modeling of the Droplet Entrainment Rate in the post-dryout Regime for the Analysis of a Reflood Phase. *Ann. Nucl. Energ.* 148, 107757. doi:10.1016/j.anucene.2020.107757

Yu, D. (2019). *Analysis and Modelling of Full-Range post-dryout Heat Transfer in Vertical Tubes*. Karlsruhe: Karlsruhe Institute of Technology. Ph.D. thesis. doi:10.5445/IR/1000098370

Yu, D., Feuerstein, F., Koeckert, L., and Cheng, X. (2018). Analysis and Modeling of post-dryout Heat Transfer in Upward Vertical Flow. *Ann. Nucl. Energ.* 115, 186–194. doi:10.1016/j.anucene.2018.01.026

Conflict of Interest: The authors declare that the research was conducted in the absence of any commercial or financial relationships that could be construed as a potential conflict of interest.

frontiers
in Energy Research

ORIGINAL RESEARCH
published: 08 February 2022
doi: 10.3389/fenrg.2022.816560

Development and Assessment of an Isotropic Four-Equation Model for Heat Transfer of Low Prandtl Number Fluids

Xingkang Su[1,2], Xianwen Li[1,2], Xiangyang Wang[3], Yang Liu[3], Qijian Chen[3], Qianwan Shi[3], Xin Sheng[1,2] and Long Gu[1,2,3]*

[1]Institute of Modern Physics, Chinese Academy of Sciences, Lanzhou, China, [2]School of Nuclear Science and Technology, University of Chinese Academy of Sciences, Beijing, China, [3]School of Nuclear Science and Technology, Lanzhou University, Lanzhou, China

In the simple gradient diffusion hypothesis, the turbulent Prandtl number (Pr_t) with a constant of 0.85 is difficult to accurately predict for liquid metals having low Prandtl numbers (Pr), while a four-equation model can improve this solution by introducing the turbulence time-scale into the calculation of turbulent thermal diffusivity. However, the four-equation model's transport form and numerical stability are so complex that suitable commercial code is lacking. Therefore, an isotropic four-equation model with simple Dirichlet wall boundary conditions is built in the present work. Based on the open-source computational fluid dynamics program OpenFOAM, the fully developed velocity, temperature, Reynolds stress, and heat flux of low Pr fluids (Pr = 0.01–0.05) in the parallel plane are obtained by numerical simulation. The results show that the time-average statistics predicted using the present four-equation model are in good agreement with the direct numerical simulation data. Then, the isotropic four-equation model is used to analyze the flow and heat of liquid metal (Pr = 0.01) in a quadrilateral infinite rod bundle. The numerical results are compared with the various and available experimental relationships. The Nusselt numbers calculated using the isotropic four-equation model are betweenness the available correlations, while the turbulent Prandtl number model using a constant of 0.85 over predicts heat transfer. More detailed local heat transfer phenomena and distribution of low Pr fluids are obtained using the present isotropic four-equation model.

Keywords: low Pr fluid, four-equation, OpenFOAM, heat transfer, liquid metal

Edited by:
Wei Ding,
Helmholtz Association of German Research Centres (HZ), Germany

Reviewed by:
Yacine Addad,
Khalifa University, United Arab Emirates
Luteng Zhang,
Chongqing University, China

***Correspondence:**
Long Gu
gulong@impcas.ac.cn

Specialty section:
This article was submitted to Nuclear Energy, a section of the journal Frontiers in Energy Research

Received: *16 November 2021*
Accepted: *14 January 2022*
Published: *08 February 2022*

Citation:
Su X, Li X, Wang X, Liu Y, Chen Q, Shi Q, Sheng X and Gu L (2022) Development and Assessment of an Isotropic Four-Equation Model for Heat Transfer of Low Prandtl Number Fluids. Front. Energy Res. 10:816560. doi: 10.3389/fenrg.2022.816560

1 INTRODUCTION

Liquid metals are widely considered coolants with good thermal-hydraulic characteristics for many energy systems, such as fast reactors and subcritical reactors (Gu and su, 2021; Wang et al., 2021). However, liquid metals' low molecular Prandtl number Pr leads to special heat transfer compared to traditional fluids. Typically, the Pr of lead-bismuth is 0.03–0.01 and that of sodium is 0.01–0.006 (Vià et al., 2020). It is significant to study liquid metals' turbulent heat transfer characteristics, which will affect the economy and security of the energy system.

It is difficult, dangerous, and costly to experiment with liquid metals (Schroer et al., 2012; Ejenstam and Szakálos, 2015), while the computational fluid dynamics (CFD) method is more commonly applied to investigate the thermal-hydraulic properties of these liquids. However, in CFD, the computing cost required by the direct numerical simulation (DNS) method and the large eddy simulations (LES) method is too high to rely on this technique for a quick and economic calculation of heat transfer in complex geometries (Kawamura et al., 1999), while the Reynolds Averaged Navier–Stokes (RANS) method can be promoted. The velocity boundary layer and the temperature layer of traditional fluid ($Pr \approx 1$) are generally considered to be similar in the RANS framework. In this way, one can obtain a constant turbulent Prandtl number Pr_t to simplify the calculation of the energy equation after using the simple gradient diffusion hypothesis (SGDH) (Groetzbach, 2013). However, it is invalid for low Pr fluids (Reynolds, 1975).

In the SGDH framework, Cheng (Cheng and Tak, 2006) derived a Pr_t correlation through employing global Reynolds numbers, while Kays (Kays, 1994) introduced the local turbulence effect into the Pr_t relation. These nonlinear Pr_t relations can effectively improve this problem in some simple geometries. However, these relations still need to be further verified in complex geometries (Duponcheel et al., 2014). Unlike the SGDH method, the differential or algebraic heat flux model (D/AHFM) establishes differential or algebraic transport equations to consider the dissimilarity between velocity and the temperature field to improve the heat transfer accuracy of liquid metals. Assessment and calibration results of D/AHFM models for low Pr fluids completed in some simple geometries show that the heat transport of second-moment closure is very sensitive to the model coefficients and functions (Lai and So, 1990; Shikazono and Kasagi, 1996; Choi and Kim, 2007; Shams et al., 2019).

Another popular model in the SGDH work, called the four-equation k-ε-k_θ-ε_θ turbulent heat transfer model, is introduced into turbulent and thermal time-scales for the simulation of the explicit first-order turbulent heat diffusivity. The literature (Nagano and Kim, 1988; Abe et al., 1995; Nagano and Shimada. 1996) has contributed extensively to near-wall model closure and thermal turbulence effect for a four-equation model. In recent years, Manservisi (Manservisi and Menghini, 2014a) improved the four-equation k-ε-k_θ-ε_θ model proposed by Abe and Nagano. The model predicted the heat transfer process of the plane, circular tube, triangular rod bundles, and quadrilateral rod bundles for $Pr = 0.025$ fluids (Manservisi and Menghini, 2014b; Manservisi and Menghini, 2015). However, the numerical stability of the four-equation model is affected by its near-wall boundary conditions. To improve the problem, a four-equation k-ω-k_θ-ω_θ model with the specific dissipation rates $\omega = \varepsilon/(C_\mu k)$ and $\omega_\theta = \varepsilon_\theta/(C_\mu k_\theta)$ was developed based on Manservisi's k-ε-k_θ-ε_θ model (Cerroni et al., 2015). Then by the following work of the literatures (Vià et al., 2016; Chierici et al., 2019; Vià and Manservivi, 2019), logarithmic specific dissipation rates of ω and ω_θ, that is, $\Omega = \ln(\omega)$ and $\Omega_\theta = \ln(\omega_\theta)$, have been used to simplify the near-wall boundary conditions and have been introduced into the logarithmic four-equation k-Ω-k_θ-Ω_θ model. Other state variables as proposed by Youssef (Youssef, 2006) are the velocity $\tau_u = k/\varepsilon$ and temperature time-scale $\tau_\theta = k_\theta/\varepsilon_\theta$ to improve its numerical stability. The proposed k_θ-τ_θ model does not suffer from numerical stiffness problems since natural boundary conditions for the variables k_θ and τ_θ are used ($k_\theta = \tau_\theta = 0$, at walls). In addition, the static variables $\tilde{\varepsilon}$ and $\widetilde{\varepsilon_\theta}$, called the isotropic dissipation rates, which are linked to the "true" dissipation rates ε and ε_θ, can also provide Dirichlet wall boundary conditions and simpler transport modes than the k_θ-τ_θ modes (Nagano and Shimada, 1996; Nagano et al., 1997).

However, the application codes of an isotropic four-equation model in complex geometries are still lacking for liquid metals, and its reliability needs to be further verified and evaluated. So, in the present work, the four-equation model in an isotropic dissipation rate $k - \tilde{\varepsilon} - k_\theta - \widetilde{\varepsilon_\theta}$ formulation for liquid metals to improve its numerical robustness was presented by Taylor series expansion and near-wall turbulence analysis based on Abe's model and Manservisi's model. The turbulent heat transfer process of $Pr = 0.01 \sim 0.05$ fluids in parallel planes is numerically studied based on the finite volume method and the open-source CFD program OpenFOAM. The validity of the present four-equation model was verified by DNS data. To evaluate the present model's applicability in complex geometries, the turbulent heat transfer of $Pr = 0.01$ fluids in a bare quadrilateral infinite rod bundle with different pitch-to-diameter ratios is predicted on the present isotropic four-equation model. The numerical results obtained from two SGDH options, the $Pr_t = 0.85$ model and the present isotropic $k - \tilde{\varepsilon} - k_\theta - \widetilde{\varepsilon_\theta}$ model, are compared and analyzed with the available experimental relations and CFD results. The local distributions of dimensionless temperature, temperature fluctuation, turbulent heat diffusivity, and turbulent Prandtl numbers are analyzed.

2 MATHEMATICAL MODEL

2.1 Isotropic Four-Equation Turbulence Model

The incompressible RANS equations with no gravity and constant physical properties for the calculation of velocity, pressure, and temperature fields are considered as follows:

$$\frac{\partial u_i}{\partial x_i} = 0 \tag{1}$$

$$\frac{\partial u_i}{\partial t} + u_j \frac{\partial u_i}{\partial x_j} = --\frac{1}{\rho}\frac{\partial P}{\partial x_i} + \frac{\partial}{\partial x_j}\left(\nu \frac{\partial u_i}{\partial x_j}\right) - \frac{\partial}{\partial x_j}\overline{u_i' u_j'} \tag{2}$$

$$\frac{\partial T}{\partial t} + u_j \frac{\partial T}{\partial x_j} = \frac{\partial}{\partial x_j}\left(\alpha \frac{\partial T}{\partial x_j}\right) - \frac{\partial}{\partial x_j}\overline{u_j' T'} \tag{3}$$

where u_i, P, and T are the RANS velocities, pressure, and temperature fields. ν, ρ, and α are the molecular viscosity, density, and molecular thermal diffusivity, respectively. The Reynolds stress $\overline{u_i' u_j'}$ using the Boussinesq hypothesis and Reynolds flux $\overline{u_j' T'}$ using the SGDH are set as follows:

$$\overline{u_i' u_j'} = -\nu_t \left(\frac{\partial u_i}{\partial x_j} + \frac{\partial u_j}{\partial x_i} \right) + \frac{2k}{3} \delta_{ij} \tag{4}$$

$$\overline{u_j' T'} = -\alpha_t \frac{\partial T}{\partial x_j} \tag{5}$$

The turbulent viscosity ν_t can be solved using two-equation $k-\varepsilon$ or $k-\omega$ models, while the turbulent thermal diffusivity α_t is considered as follows:

$$\alpha_t = \frac{\nu_t}{Pr_t} \tag{6}$$

Due to low Pr fluids' physical properties, there are great differences between the momentum and heat. A constant $Pr_t \approx 0.85–0.9$ cannot give acceptable results for liquid metals. It is possible to consider α_t as a function of the turbulence variables, such as two-equation $k_\theta - \varepsilon_\theta$ or $k_\theta - \omega_\theta$ analogy to dynamic two-equation $k-\varepsilon$ or $k-\omega$. To smooth the isotropic variables at the wall, when one makes $\tilde{\varepsilon}$ and $\widetilde{\varepsilon_\theta}$ zero at the wall, an isotropic four-equation $k - \tilde{\varepsilon} - k_\theta - \widetilde{\varepsilon_\theta}$ model can be written using the Taylor series expansion as follows:

$$\tilde{\varepsilon} = \varepsilon - 2\nu \left(\sqrt{k}_{,2} \right)^2 \tag{7}$$

$$\widetilde{\varepsilon_\theta} = \varepsilon_\theta - 2\alpha \left(\sqrt{k_{\theta,2}} \right)^2 \tag{8}$$

$$\frac{\partial k}{\partial t} + u_j \frac{\partial k}{\partial x_j} = \frac{\partial}{\partial x_j} \left[\left(\nu + \frac{\nu_t}{\sigma_k} \right) \frac{\partial k}{\partial x_j} \right] + P_k - \tilde{\varepsilon} - 2\nu \left(\frac{\partial \sqrt{k}}{\partial x_j} \right)^2 \tag{9}$$

$$\frac{\partial \tilde{\varepsilon}}{\partial t} + u_j \frac{\partial \tilde{\varepsilon}}{\partial x_j} = \frac{\partial}{\partial x_j} \left[\left(\nu + \frac{\nu_t}{\sigma_\varepsilon} \right) \frac{\partial \tilde{\varepsilon}}{\partial x_j} \right] + C_{\epsilon 1} \frac{\tilde{\varepsilon}}{k} P_k - C_{\epsilon 2} f_\varepsilon \frac{\tilde{\varepsilon}^2}{k} + \nu \nu_t (1 - f_w) \left(\frac{\partial^2 u_i}{\partial x_j x_k} \right)^2 \tag{10}$$

$$\frac{\partial k_\theta}{\partial t} + u_j \frac{\partial k_\theta}{\partial x_j} = \frac{\partial}{\partial x_j} \left[\left(\alpha + \frac{\alpha_t}{\sigma_{k\theta}} \right) \frac{\partial k_\theta}{\partial x_j} \right] + P_{k\theta} - \widetilde{\varepsilon_\theta} - 2\alpha \left(\frac{\partial \sqrt{k_\theta}}{\partial x_j} \right)^2 \tag{11}$$

$$\frac{\partial \widetilde{\varepsilon_\theta}}{\partial t} + u_j \frac{\partial \widetilde{\varepsilon_\theta}}{\partial x_j} = \frac{\partial}{\partial x_j} \left[\left(\alpha + \frac{\alpha_t}{\sigma_{\varepsilon\theta}} \right) \frac{\partial \widetilde{\varepsilon_\theta}}{\partial x_j} \right] + C_{p1} \frac{\widetilde{\varepsilon_\theta}}{k_\theta} P_{k\theta} + C_{p2} \frac{\widetilde{\varepsilon_\theta}}{k} P_k - C_{d1} \frac{\widetilde{\varepsilon_\theta}}{k_\theta} \widetilde{\varepsilon_\theta} - C_{d2} f_{d2} \frac{\widetilde{\varepsilon_\theta}}{k} \tilde{\varepsilon} + \alpha \alpha_t (1 - f_{w\theta}) \left(\frac{\partial^2 T}{\partial x_j x_k} \right)^2 \tag{12}$$

$$P_k = -\overline{u_i' u_j'} \frac{\partial u_i}{\partial x_j}, P_{k\theta} = -\overline{u_j' T'} \frac{\partial T}{\partial x_j} \tag{13}$$

$$f_\varepsilon = \left\{ 1 - 0.3\, exp\left[-\left(R_t / 6.5 \right)^2 \right] \right\} \tag{14}$$

$$f_w = \left(1 - exp\left(-R_\varepsilon / 19 \right) \right)^2 \tag{15}$$

$$f_{d2} = 1/C_{d2} \left(C_{\varepsilon 2} f_\varepsilon - 1 \right) \left[1 - exp\left(-R_\varepsilon / 5.7 \right) \right]^2 \tag{16}$$

$$f_{w\theta} = \left(1 - exp\left(-R_\varepsilon \sqrt{Pr} / 19 \right) \right)^2 \tag{17}$$

where $\tilde{\varepsilon}$ and $\widetilde{\varepsilon_\theta}$ call the isotropic dissipation rate. ε and ε_θ are the "true" dissipation rate, respectively. f_ε, f_w, f_{d2}, and $f_{w\theta}$ are wall-proximity effect functions. Based on the analysis of the literature and the DNS database (Abe et al., 1995; Kawamura et al., 1998; Manservisi and Menghini, 2014a), the isotropic four-equation model coefficients for liquid metals are used and corrected as shown in **Table 1**. Here, the $k - \tilde{\varepsilon} - k_\theta - \widetilde{\varepsilon_\theta}$ model functions and constants recommended in this study, such as f_ε, f_w, f_{d2}, $f_{w\theta}$, and C_{d1}, are different from the $k - \varepsilon - k_\theta - \varepsilon_\theta$ model values of Manservisi (Manservisi and Menghini, 2014b). It is noted that $P_{k\theta}$ is the production term of temperature fluctuations k_θ, which represents the energy transferred to the turbulent flux by the average temperature change rate of the RANS flow. That is, the temperature fluctuations k_θ is the result of the combined action of the average temperature change rate and Reynolds heat flux. Through the transport of **Eq. 11**, after the temperature fluctuation occurs, it will experience convection, molecular diffusion, and turbulent diffusion until it is dissipated.

TABLE 1 | Values for the $k - \tilde{\varepsilon} - k_\theta - \widetilde{\varepsilon_\theta}$ model constants in **Eqs 9–12**.

$C_{\epsilon 1}$	$C_{\epsilon 2}$	σ_k	σ_ε	C_{p1}	C_{p2}	C_{d1}	C_{d2}	$\sigma_{k\theta}$	$\sigma_{\varepsilon\theta}$
1.5	1.9	1.4	1.4	0.925	0.9	1.1	0.9	1.4	1.4

Both the turbulent Reynolds number $R_t = k^2/\nu\varepsilon$ and R_ε are introduced into the isotropic model. Let δ be the wall distance. R_ε can be recommended by Abe et al. (Abe et al., 1995), as follows:

$$R_\varepsilon = \delta / \eta \tag{18}$$

where $\eta = (\nu^3/\varepsilon)^{1/4}$ is the Kolmogorov length scale which can calculate the separated flow well. When isotropic variables are used, R_t and R_ε in **Eqs 14–17** should become the following:

$$R_t = k^2 / \nu\tilde{\varepsilon}, R_\varepsilon = \delta / \eta \text{ where } \eta = \left(\nu^3 / \tilde{\varepsilon} \right)^{1/4} \tag{19}$$

2.2 Turbulent Viscosity and Turbulent Thermal Diffusivity

Some dynamic and thermal time-scales should be applied to calculate the turbulent viscosity ν_t and turbulent thermal diffusivity α_t. Using dynamic and thermal time-scales, that is, $\tau_u = k/\varepsilon$ and $\tau_\theta = k_\theta/\varepsilon_\theta$, turbulent viscosity and turbulent thermal diffusivity can be defined (Abe et al., 1995; Manservisi and Menghini, 2015) as follows:

$$\nu_t = C_u f_u k \tau_u \tag{20}$$

where

$$f_u = \left\{ 1 - \exp\left(-\frac{R_\varepsilon}{14} \right) \right\}^2 \left(1 + \frac{5}{R_t^{3/4}} f_d \right) \tag{21}$$

and

$$f_d = \exp^{-\left(R_t / 200 \right)^2} \tag{22}$$

$$\alpha_t = C_\lambda f_\lambda k \tau_u \tag{23}$$

where

$$f_\lambda = \left\{ 1 - \exp\left(-\frac{R_\varepsilon}{14} \right) \right\} \left\{ 1 - \exp\left(-\frac{R_\varepsilon \sqrt{Pr}}{19} \right) \right\} \left(Pr_{t\infty} + \frac{2R}{C_m + R} f_{\theta 1} + \frac{\sqrt{2R}}{Pr} \frac{1.3}{R_t^{3/4}} f_{\theta 2} \right) \tag{24}$$

$$f_{\theta 1} = \exp^{-\left(R_t / 500 \right)^2} \tag{25}$$

and

TABLE 2 | Series expansion near the wall.

Mean parameter	Fluctuating parameter
$u = A_1\delta + A_2\delta^2 + A_3\delta^3 + \ldots$	$u' = a_1\delta + a_2\delta^2 + a_3\delta^3 + \ldots$
$v = B_2\delta^2 + B_3\delta^3 + \ldots$	$v' = b_2\delta^2 + b_3\delta^3 + \ldots$
$w = C_1\delta + C_2\delta^2 + C_3\delta^3 + \ldots$	$w' = c_1\delta + c_2\delta^2 + c_3\delta^3 + \ldots$
$T = D_1\delta + D_2\delta^2 + D_3\delta^3 + \ldots$	$T' = d_1\delta + d_2\delta^2 + d_3\delta^3 + \ldots$

$$f_{\theta 2} = \exp^{-(R_t/200)^2} \tag{26}$$

The above model has been proved to be effective in producing correct turbulence behavior of liquid metal, which draws into the mixing time-scale $\tau_m = \tau_u R/(C_m + R)$ and the ratio of the velocity time-scale to the thermal time-scale $R = \tau_\theta/\tau_u$ (Abe et al., 1995). The values of $Pr_{t\infty} = 0.9$ and $C_m = 0.3$ are recommended for liquid metals (Manservisi and Menghini, 2015). In order to establish a complete isotropic four-equation turbulent heat transfer model $k - \tilde{\varepsilon} - k_\theta - \widetilde{\varepsilon_\theta}$, we used the isotropic variables $\tilde{\varepsilon}$ and $\widetilde{\varepsilon_\theta}$ in **Eqs 20–26** instead of the "true" variables ε and ε_θ.

2.3 Wall Boundary Conditions for Turbulence Models

Appropriate boundary conditions should be applied to solve the four-equation turbulent models without the available wall functions. By using series expansions as shown in **Table 2**, the near-wall behaviors of dynamical and thermal turbulence variables k, ε, k_θ, and ε_θ can be obtained (Deng et al., 2001) as follows:

$$\begin{aligned} k &= \frac{1}{2}\overline{u_i' u_i'} = \frac{1}{2}\overline{(a_1^2 + c_1^2)}\delta^2 + \ldots \\ \varepsilon &= \nu\overline{\frac{\partial u_i'}{\partial x_j}\frac{\partial u_i'}{\partial x_j}} = \nu\left(\overline{a_1^2 + c_1^2}\right) + \ldots = 2\nu\left(\sqrt{k}_{,2}\right)^2 + \ldots \\ k_\theta &= \frac{1}{2}\overline{T'T'} = \frac{1}{2}\left(\overline{d_1^2}\right)\delta^2 + \ldots \\ \varepsilon_\theta &= \alpha\overline{\frac{\partial T'}{\partial x_j}\frac{\partial T'}{\partial x_j}} = \alpha\overline{d_1^2} + \ldots = 2\alpha\left(\sqrt{k_\theta}_{,2}\right)^2 + \ldots \end{aligned} \tag{27}$$

According to the definitions of **Eqs 7**, **8**, when δ tends to zero, k, $\tilde{\varepsilon}$, k_θ, and $\widetilde{\varepsilon_\theta}$ tend to zero. Thus, the simple Dirichlet wall boundary conditions with the isotropic $k - \tilde{\varepsilon} - k_\theta - \widetilde{\varepsilon_\theta}$ model can be imposed.

2.4 Modified Navier–Stokes Equations for Periodic Boundary Conditions

For a fully developed turbulent field, the pressure gradient term in **Eq. 2** is divided into the mean of the pressure gradient dP_f/dz which is constant along the flow direction z and the fluctuating pressure gradient $\partial P/\partial x_i$. The mean term of the pressure gradient is given as the known power source term.

$$\frac{\partial u_i}{\partial t} + u_j\frac{\partial u_i}{\partial x_j} = -\frac{1}{\rho}\frac{\partial P}{\partial x_i} + \frac{1}{\rho}\frac{dP_f}{dz} + \frac{\partial}{\partial x_j}\left(\nu\frac{\partial u_i}{\partial x_j}\right) - \frac{\partial}{\partial x_j}\overline{u_i' u_j'} \tag{28}$$

TABLE 3 | Physical properties for Pr = 0.01, 0.025, and 0.05

Parameter	Value	Unit	Symbol	Pr
Dynamic viscosity	0.00181	Pa·s	μ	—
Density	10,340	kg/m^3	ρ	—
Specific heat capacity	145.75	J/(kg · K)	Cp	—
Thermal conductivity	5.27615	W/(m · K)	λ	0.05
	10.5523	—	—	0.025
	26.38075	—	—	0.01

For a fully developed temperature field, temperature T is written as follows:

$$\theta(x, y) = T_{in} + z\Delta T_b - T(x, y, z) \tag{29}$$

where T_{in} is the inlet temperature, and ΔT_b is a constant wall temperature gradient, while θ satisfies periodic boundary conditions along the flow direction. According to the energy conservation for thermal fully developed flow with a wall flux q_w, ΔT_b can be set as $4q_w/(\rho C_p u_b D_h)$, where u_b is average velocity, and D_h is an equivalent diameter. After introducing periodic temperature θ, **Eq. 3** can be written as follows:

$$\frac{\partial \theta}{\partial t} + u_j\frac{\partial \theta}{\partial x_j} = \frac{\partial}{\partial x_j}\left(\alpha\frac{\partial \theta}{\partial x_j}\right) - \frac{\partial}{\partial x_j}\overline{u_j'\theta'} + u_z\Delta T_b \tag{30}$$

3 NUMERICAL RESULTS AND ANALYSIS

3.1 Numerical Solver of the Isotropic Four-Equation Model

For the modified RANS system and the isotropic four-equation $k - \tilde{\varepsilon} - k_\theta - \widetilde{\varepsilon_\theta}$ model in **Section 2**, the appropriate discrete format could be selected according to the needs. Here, the convection term adopts the Gauss upwind format, the diffusion term uses the Gauss linear format, and the time term uses the steady-state format. The SIMPLE algorithm solves the continuity and momentum simultaneously, and coupled multigrid iteration is used for the matrix solution. The convergence conditions of residual error are as follows:

$$Max\left|\frac{Q^{i+1}}{Q^i} - 1\right| < 10^{-9} \tag{31}$$

where Q stands for u_i, θ, k, $\tilde{\varepsilon}$, k_θ and $\widetilde{\varepsilon_\theta}$. The index i denotes the steps of calculation. All calculations were realized on OpenFOAM (Weller et al., 1998; Moukalled et al., 2016). The detailed analysis of the four-equation model solver by Gu and Su (Gu and su, 2021) based on OpenFOAM can be further referred to. The height of the grid point closest to the wall is approximately 10^{-3} mm to meet the requirements of the isotropic four-equation model ($y^+ < 1$).

3.2 Numerical Verification of the Plane

The full development process of different Pr fluids in a constant heat flow heated plane was studied using DNS (Kawamura et al., 1998; Kawamura et al., 1999; Tiselj and Cizelj, 2012). This study compares the DNS data with Pr = 0.01 ~ 0.05. The plane geometry and mesh parameters are

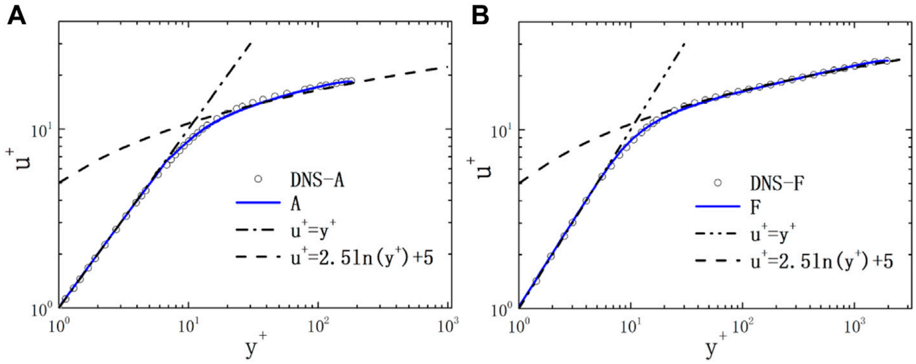

FIGURE 1 | Non-dimensional velocity of the plane. **(A)** case A; **(B)** case F.

consistent with those in the literature (Su et al., 2021; Su and Gu, 2021). Here, the three-dimensional parallel plane with a flow length of 6.4 h, a spanwise width of 3.2 h, and a plane height of 2 h were selected as the calculation domain, where *h* is the half-height of the plane, 30.25 mm. The wall heat flux is set as $q_w = 360\,\mathrm{kW/m^2}$. Finally, 80, 50, and 100 nodes are divided into three directions, respectively: Flow direction, span direction, and height. Due to the symmetry of the plane, half of the plane is taken as the calculation domain, and the structured grid is used. The grid height of the first boundary layer is set to 3×10^{-6} m to meet the requirements of the low Reynolds number turbulence model, $y^+ < 1$. The physical properties of $Pr = 0.01$–0.05 are reported in **Table 3**. The friction Reynolds number $Re_\tau = u_\tau h/\nu$ is taken as the calculation conditions: 180 (A), 395 (B), 590 (C), 640 (D), 950 (E), 2000 (F), and 4,400 (G), where u_τ is the friction velocity on the wall side, *h* is the half-height of the plane, and the numbers A ~ G represent different Reynolds number calculation conditions. For the convenience of analysis, u_τ and the friction temperature T_τ are taken as the dimensionless reference quantity, where T_τ is set as $q_w\rho^{-1}Cp^{-1}u_\tau^{-1}$, and q_w is the wall heat flux.

3.2.1 Velocity Field Verification

The dimensionless velocity $u^+ = u/u_\tau$ distribution of cases A and F along the dimensionless wall-normal distance $y^+ = yu_\tau/\nu$ is shown in **Figure 1**. At a low Reynolds number and a high Reynolds number, the velocity distribution predicted by the present isotropic four-equation model is in good agreement with the DNS results, and the velocity distribution meets $u^+ = y^+$ in the linear region ($u^+ = y^+$) while it meets $u^+ = 2.5\ln y^+ + 5$ in the logarithmic rate region ($y^+ > 30$).

The distribution of dimensionless Reynolds stress $\tau_R^+ = \overline{uv}u_\tau^{-2}$ and total shear stress $\tau_{total}^+ = \tau_R^+ + \nu v_{,y}u_\tau^{-2}$ along y^+ under cases A and F is shown in **Figure 2**. The stress calculation results are in good agreement with DNS results. In the near-wall region ($1 < y^+ < 7$), this study predicted τ_R^+ to be lower than the DNS value. However, it has little effect on the calculation results of the velocity field in the linear region, mainly because the molecular diffusion is dominant in the near-wall region. With the increase in wall distance, the turbulent diffusion effect increases gradually. When $y^+ > 30$, the total shear stress coincides with the Reynolds stress curve.

3.2.2 Temperature Field Verification

1) $Pr = 0.01$

The dimensionless temperature $\theta^+ = \theta/T_\tau$ distribution of the $Pr = 0.01$ fluid along y^+ is shown in **Figure 3A**. Cases A, B, and C agree with DNS and meet $\theta^+ = Pry^+$ in the linear region ($1 < y^+ < 40$).

The distribution of dimensionless Reynolds heat flux $q_R^+ = -\alpha_t\theta_{,y}u_\tau^{-1}T_\tau^{-1}$ and total heat flux $q_{total}^+ = -(\alpha_t + \alpha)\theta_{,y}u_\tau^{-1}T_\tau^{-1}$ along y^+ is shown in **Figures 3B–D**. The heat flux calculation results of cases A–C are in good agreement with DNS results. Due to the thick thermal boundary layer and strong molecular heat conduction of low *Pr* fluid, although the predicted Reynolds heat flux deviates from the DNS results at $1 < y^+ < 30$, it does not affect the linear distribution of the temperature field in this region. With the increase in wall distance, although the effect of turbulent heat diffusion is gradually increasing, there is still a difference between the total heat flow and Reynolds heat flux, mainly caused by the strong molecular heat conduction of low *Pr* fluid.

2) $Pr = 0.025$

The distribution of θ^+/Pr of the $Pr = 0.025$ fluid along y^+ is shown in **Figure 4A**. Cases A, B, and C are in good agreement with DNS. The peak value of θ^+/Pr increases with the increase in the Reynolds number. The distribution of q_R^+ along y^+ is shown in **Figure 4B**. Cases A and B agree with DNS. With the increase in *Re*, the q_R^+ peak increases and moves to the turbulent core.

3) Pr=0.05

As shown in **Figure 5A**, the dimensionless temperature θ^+ of case A of $Pr = 0.05$ fluid is in good agreement with the DNS results. At the same Reynolds number, with the decrease in *Pr*, the molecular thermal conductivity increases and the average θ^+ decreases. As shown in **Figure 5B**, the dimensionless Reynolds

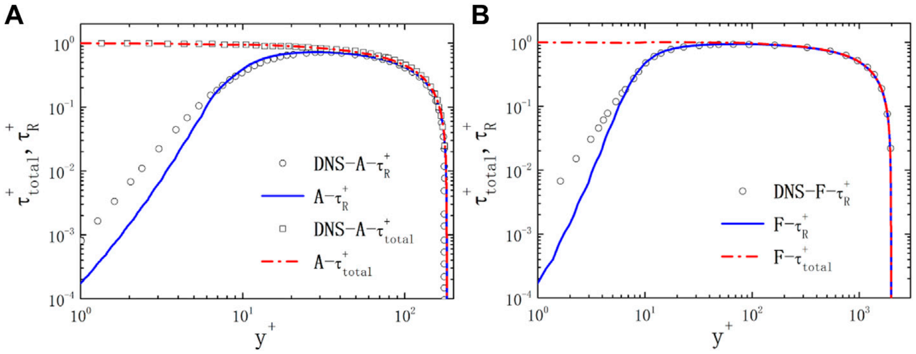

FIGURE 2 | Non-dimensional stress of the plane. **(A)** case A; **(B)** case F.

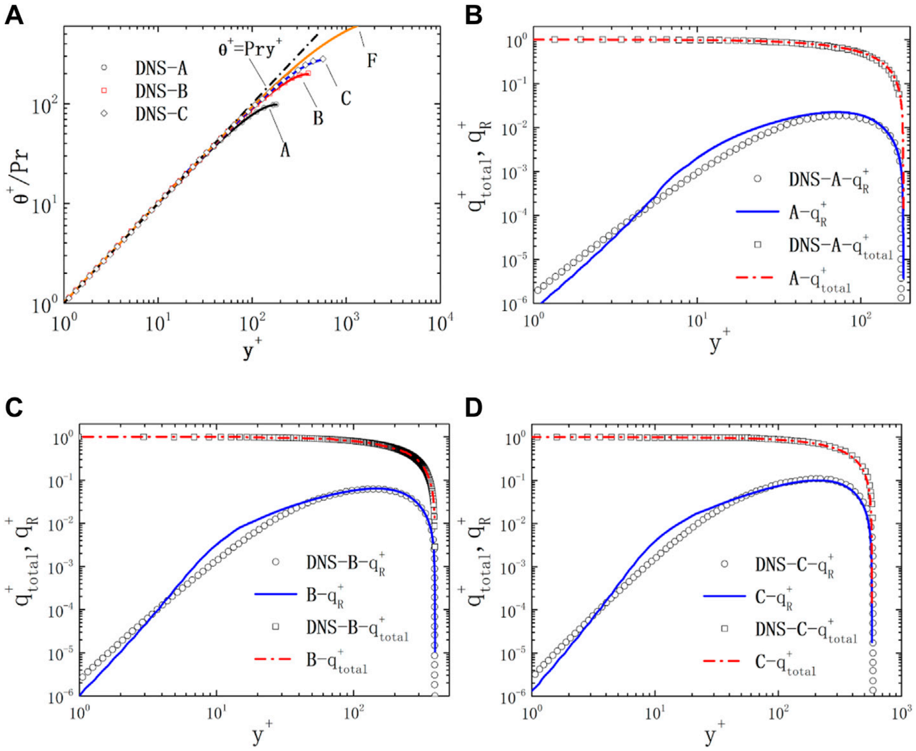

FIGURE 3 | Non-dimensional temperature and heat flux of the plane for $Pr = 0.01$. **(A)** temperature; **(B)** heat flux of case A; **(C)** heat flux of case B; **(D)** heat flux of case C.

heat flux of case A of $Pr = 0.05$ fluid is in good agreement with the DNS results.

3.3 Numerical Analysis of the Square Bundle

To further analyze the applicability of the current isotropic four-equation model in complex geometries, the flow and heat of liquid metal with a Prandtl value of 0.01 in the quadrilateral infinite rod bundle were studied. **Figure 6** shows the schematic diagram of the computational domain and local hexahedral mesh of the quadrilateral infinite rod bundle. Lines ab, bo, oc, and arc ca are the local distributions to be analyzed next. The flow parameters are reported in **Table 4**. The surfaces of rods in contact with the fluids are heated by uniform wall fluxes q_w. Symmetry condition is applied on other faces to simulate the infinite rod bundle region with a quadrilateral arrangement. The heat fully developed flow length L_z is set to $10D_h$ (Ge et al., 2017). The rod diameter D and $X = P/D$ ratio are the same as in Zhukov's experiment (Zhukov et al., 2002).

3.3.1 Heat Transfer Evaluation and Analysis

In **Table 5**, a few important heat transfer correlations of Nusselt number Nu are available for the quadrilateral infinite rod bundle,

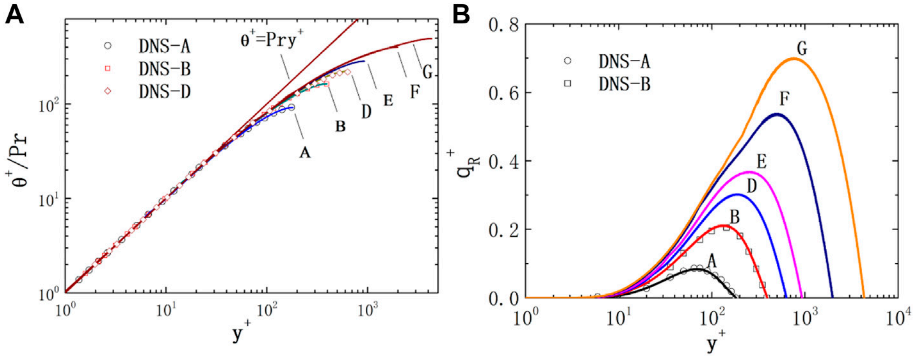

FIGURE 4 | Non-dimensional temperature and heat flux of the plane for *Pr* = 0.025. **(A)** temperature; **(B)** heat flux.

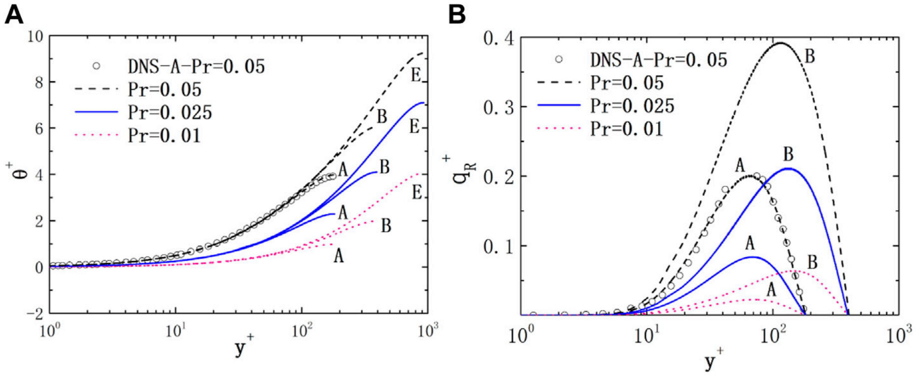

FIGURE 5 | Non-dimensional temperature and heat flux of the plane for different *Pr* fluids. **(A)** temperature; **(B)** heat flux.

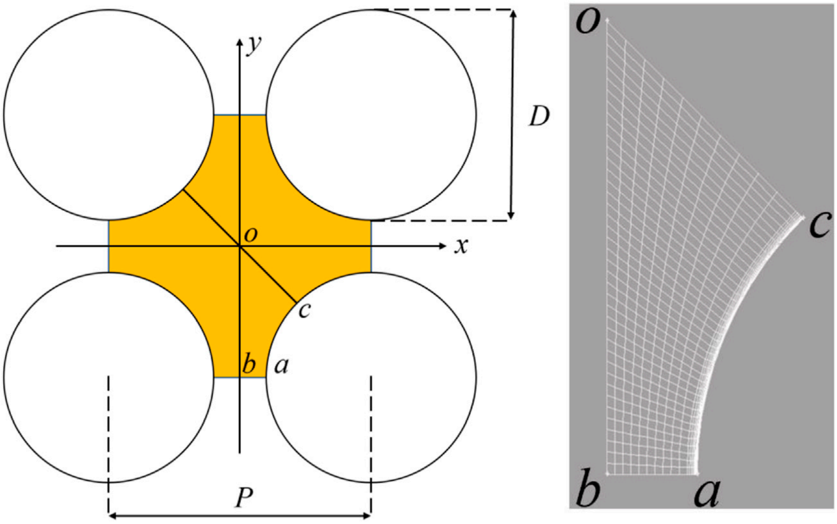

FIGURE 6 | Schematic diagram of the quadrilateral infinite rod bundle. **(A)** flow area; **(B)** local mesh.

TABLE 4 | Flow parameters.

Parameter	Symbol	Value	Unit
Prandtl numbers	*Pr*	0.01	—
Rod diameter	*D*	12	mm
P/D ratios	*X*	1.25, 1.34, 1.46	—
Peclet numbers	*Pe*	250–4,000	—
Reynolds numbers	*Re*	25,000–400,000	—

reviewed in the study by (Mikityuk 2009). Zhukov (Zhukov et al., 2002) obtained 36 $Nu(Pe)$ data from the heat transfer experiment of 22%Na–78%K in a quadrilateral rod bundle. The correlations obtained by Subbotin (Subbotin et al., 1965) and BREST (Adamov 2001) were derived from triangular bundles, while Mikityuk, from a wide database, conducted experimental results of liquid metals (Mikityuk 2009). It is worth noting that there are no more available experimental data. The correlations should be used with care and be paid more attention to for analysis of the reliability. The Nu can be calculated as follows:

$$Nu = \frac{q_w D_h}{\lambda (T_{wm} - T_b)}, T_b = \frac{\int_A u_i n_i T dA}{\int_A u_i n_i dA}, T_{wm} = \frac{\int_{\Gamma_w} T ds}{\int_{\Gamma_w} ds} \tag{32}$$

where n_i is a vector of a unit perpendicular to a sliced face.

First, the simulations for $Pr = 0.01$ are characterized by $X = 1.25$, 1.34, and 1.46 with a corresponding hydraulic diameter D_h of 11.87, 15.43, and 20.57 mm. Nine simulations with bulk Reynolds numbers of 250–400,000 were operated. The corresponding Peclet number is approximately 250–4,000. **Figure 7** shows the Nusselt number results for $X = 1.25$ -1.46 cases. In **Figure 7**, Subbotin and Mikityuk correlations overestimated the Nusselt number compared with the conservative result of Zhukov and BREST. The correlation

TABLE 5 | Correlations of Nusselt number for the square bundle.

Investigator	Correlation	*X*	*Pe*
Zhukov et al.	$Nu = 7.55X - 14X^{-5} + 0.007Pe^{0.64+0.246X}$	1.25–1.46	60–2000
Subbotin et al.	$Nu = 0.58\left(\frac{4}{\pi}X^2 - 1\right)^{0.55}Pe^{0.45}$	1.1–1.5	80–4,000
BREST	$Nu = 7.55X - 20X^{-5} + \frac{0.0354}{X^2}Pe^{0.56+0.204X}$	1.28–1.46	100–1,600
Mikityuk	$Nu = 0.047\left(1 - \exp^{-3.8(X-1)}\right)\left(Pe^{0.77} + 250\right)$	1.1–1.95	30–5,000

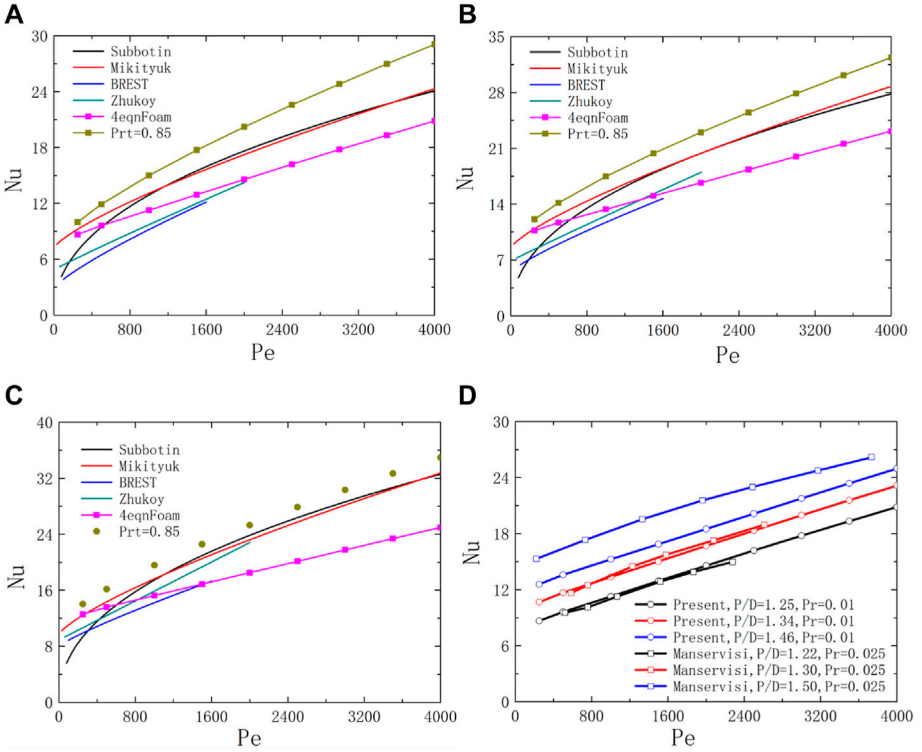

FIGURE 7 | Schematic diagram of Nusselt number for the square bundle. **(A)** $X = 1.25$; **(B)** $X = 1.34$; **(C)** $X = 1.46$; **(D)** $X = 1.22$–1.5.

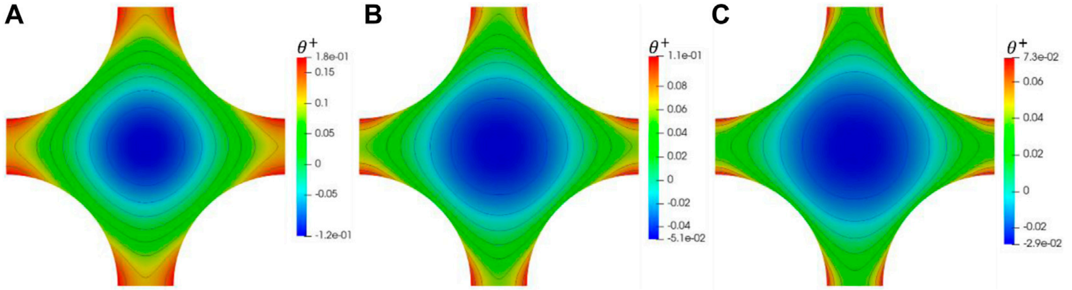

FIGURE 8 | Schematic diagram of dimensionless temperature on a slice for square lattice $X = 1.25$. **(A)** $Pe = 250$; **(B)** $Pe = 2000$; **(C)** $Pe = 4000$.

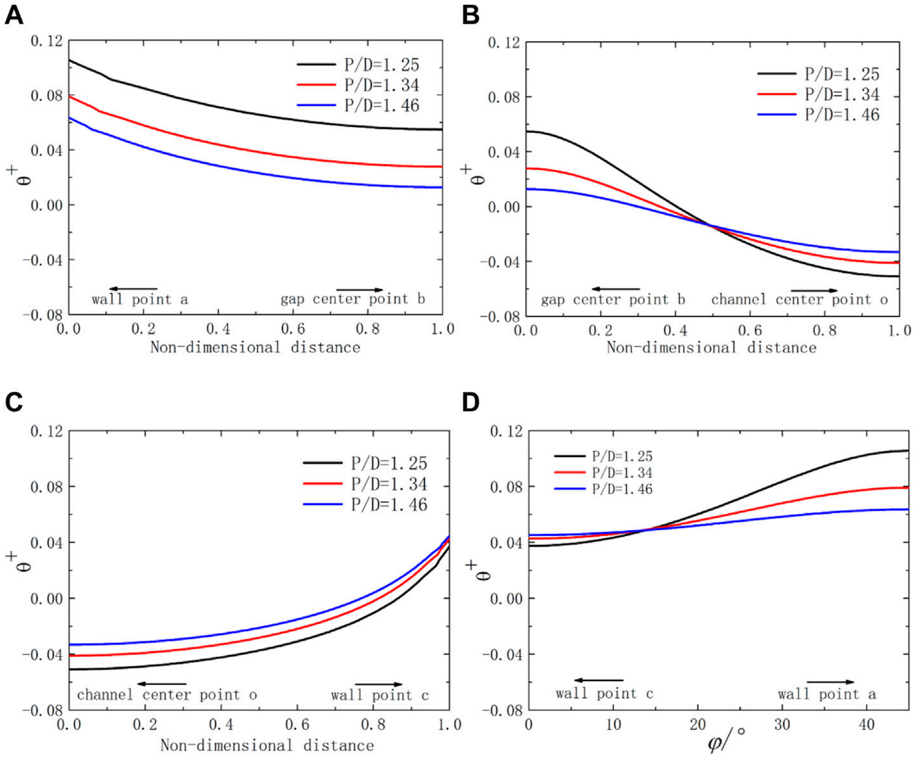

FIGURE 9 | Schematic diagram of dimensionless temperature over lines for the square lattice at $Pe = 2000$ with different P/D ratios. **(A)** line ab; **(B)** line bo; **(C)** line oc; **(D)** arc ca.

between these empirical relations is too poor to relate because these relationships have very different slopes.

In **Figures 7A–C**, the prediction Nu of the isotropic $k - \tilde{\varepsilon} - k_\theta - \tilde{\varepsilon_\theta}$ model almost lies between the experimental relationship. The prediction of the $Pr_t = 0.85$ model is higher than Subbotin and Mikityuk correlations. At low Peclet numbers, the Nu results having a special slope predicted using the isotropic four-equation model is closer to the Subbotin and Mikityuk correlations, while the calculation results at high Pe are conservative, similar to the Zhukov and BREST correlations. The overall numerical Nu seems to be more conservative than these experimental correlations. Poor experimental relevance makes this problem's numerical verification difficult to go on.

As shown in **Figure 7D**, the numerical slope in the $Nu(Pe)$ line obtained using the $k - \tilde{\varepsilon} - k_\theta - \tilde{\varepsilon_\theta}$ model is very similar to that predicted using Manservisi's $k - \varepsilon - k_\theta - \varepsilon_\theta$ model, which has successfully predicted heat transfer calculation for $Pr = 0.025$ fluids and can provide an additional CFD relationship reference. Therefore, we still use the present isotropic four-equation model for thermal analysis and local temperature calculations.

This present work focuses on the comparison of the effects of two turbulent thermal diffusion models (the $Pr_t = 0.85$ model and the present isotropic $k - \tilde{\varepsilon} - k_\theta - \tilde{\varepsilon_\theta}$ model) on the temperature field, without considering the influence of different RANS turbulence $k - \varepsilon$ or $k - w$ models. The detailed

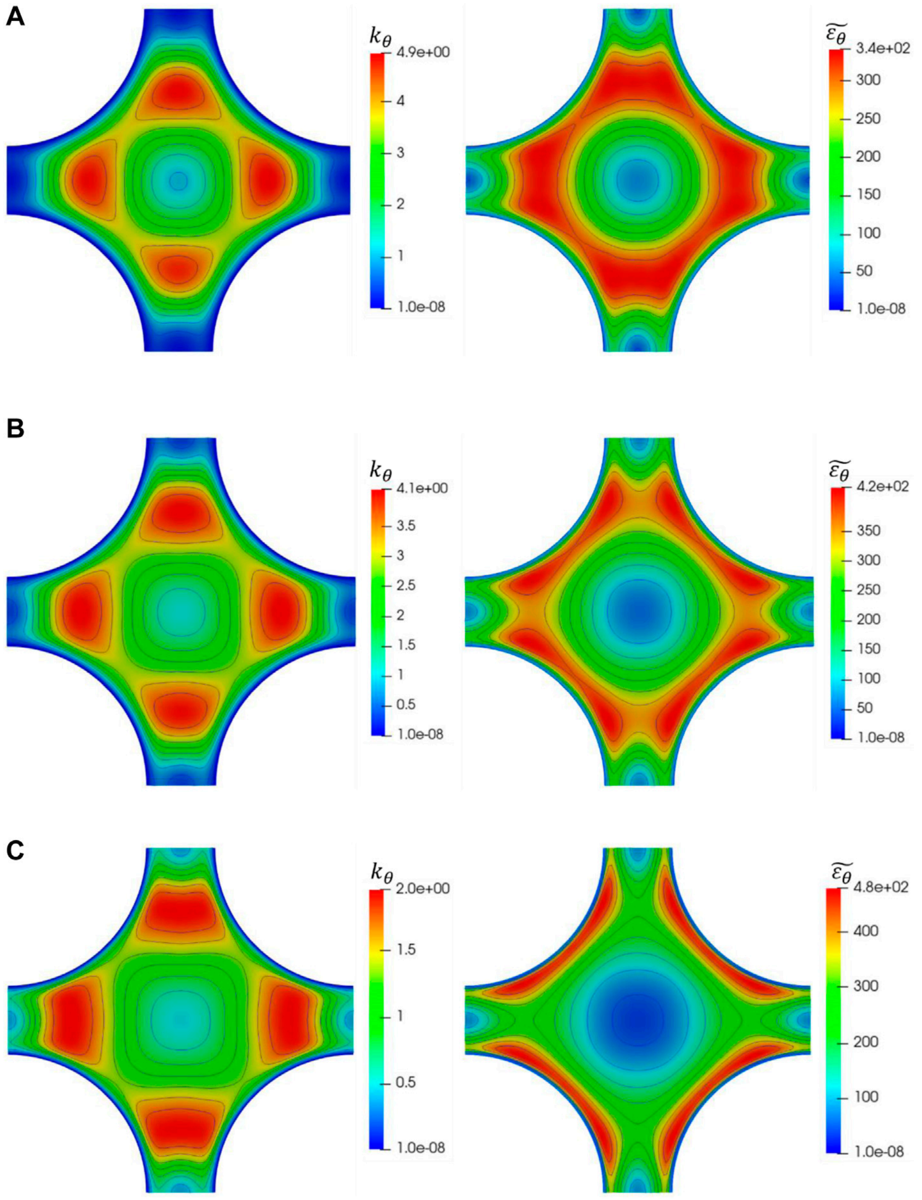

FIGURE 10 | Schematic diagram of average temperature fluctuaion (left) and its isotropic dissipation (right) on a slice for square lattice $X = 1.25$. **(A)** *Pe* = 1000; **(B)** *Pe* = 2000; **(C)** *Pe* = 4000.

influence and performance evaluation of different turbulence models on liquid metal flow can be found in the literature (You et al., 2019).

3.3.2 Turbulent Thermal Fields

1) Coolant and wall temperature

Figure 8 shows the dimensionless temperature $\theta^+ = \lambda(T - T_b)/(q_w \cdot D_h)$ on a sliced surface of square bundle $X = 1.25$. The overall dimensionless temperature in the channel decreases with the increase in *Pe*. The temperature at the rod surface is not constant. The wall temperature near the center of the channels is lower than that near the center of gaps.

Figure 6 has annotated the line ab, line bo, line oc, and arc ca, where points b and c represent the center of the gap and the channel, respectively. The dimensionless temperature field with *Pe* = 2000 is selected for analysis. In **Figure 9A**, with the decrease in *P/D*, the gap width decreases, and the overall dimensionless temperature distribution θ^+ at the gap line ab increases. In **Figures 9B,D**, the coolant dimensionless temperature distribution from gap center point b to channel center point o and the wall dimensionless temperature distribution over arc ca are smoother in pace with strengthening of *P/D*. Due to the

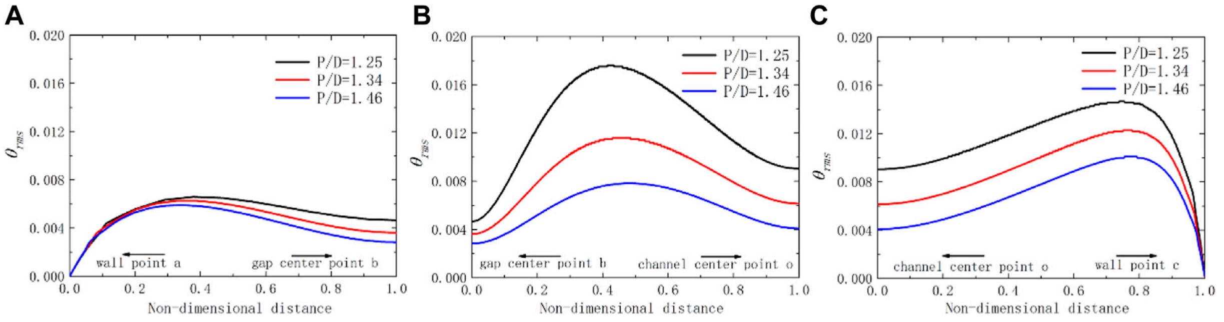

FIGURE 11 | Schematic diagram of dimensionless temperature fluctuation over lines for the square lattice at Pe = 2000 with different P/D ratios. **(A)** line ab; **(B)** line bo; **(C)** line oc.

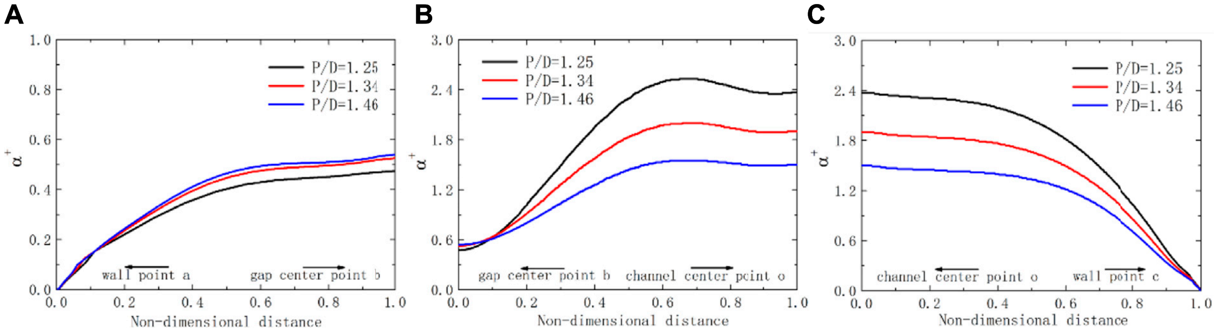

FIGURE 12 | Schematic diagram of dimensionless thermal diffusivity over lines for the square lattice at *Pe* = 2000 with different *P/D* ratios. **(A)** line ab; **(B)** line bo; **(C)** line oc.

development of velocity and sufficient cooling of the fluid near the center of the channel, the dimensionless temperature distribution over line oc decreases when the value of *P/D* decreases in **Figure 9C**.

2) Fluctuation and isotropic dissipation

The distribution and shape of k_θ and $\tilde{\varepsilon_\theta}$ for *Pe* = 100, 2000, and 4,000 are shown in **Figure 10**. k_θ has a lower local value near the center point o. The maximum value appears near the wall. The maximum value of k_θ decreases when *Pe* increases, while that of ε_θ increases. The numerical shape and distribution of k_θ and its isotropic dissipation $\tilde{\varepsilon_\theta}$ obtained from the present $k-\tilde{\varepsilon}-k_\theta-\tilde{\varepsilon_\theta}$ model is similar to that predicted by Manservisi's $k-\varepsilon-k_\theta-\varepsilon_\theta$ model (Manservisi and Menghini, 2015). Further details on over line ab, line bo, and line oc can be found in **Figure 11**. The dimensionless root square means temperature $\theta_{rms} = \lambda\sqrt{2k_\theta}/(qD_h)$ is set. From wall point a to wall point b, θ_{rms} first increases to a small peak and then begins to decrease to point b. Then along the bo line, the maximum peak value of θ_{rms} is reached near the midpoint of the bo section. Three peaks of different sizes were formed on lines ab, bo, and oc, respectively. When it goes straight toward the wall point, it will eventually approach 0. When the value is *X*, the overall value of θ_{rms} decreases.

3) Turbulence and molecular thermal diffusivity

Figure 12 shows the proportional relationship of turbulent to molecular thermal diffusivity, that is, dimensionless thermal diffusivity $a^+ = \alpha_t/\alpha$, over line ab, line bo, and line oc with the change of *P/D* for square bundle *X* = 1.25 at *Pe* = 2000. Reynolds heat flux q_t and molecular heat flux q_m can be defined as follows:

$$q_t = -\overline{v'\theta'} = \alpha_t\frac{\partial T}{\partial y}, q_m = \alpha_t\frac{\partial T}{\partial y} \tag{33}$$

Thus, the specific value of turbulent to molecular thermal diffusivity represents the ratio of Reynolds to molecular heat flux. Reynolds heat flux is mainly caused by thermal diffusion caused by turbulent flow, while molecular heat conduction generates molecular heat flux. In **Figure 12**, in the area closest to the wall point a or c, a^+ tends to 0, which means turbulent heat diffusion tends to be ignored here. With the increase in wall distance from wall point a to gap center point b, the turbulent heat diffusion gradually increases, so the value of a^+ increases. However, a^+ is still less than one over line ab, which means that the molecular heat conduction of liquid metal always affects the heat transfer at the gap area. At the gap center point b, a^+ reaches a local maximum over

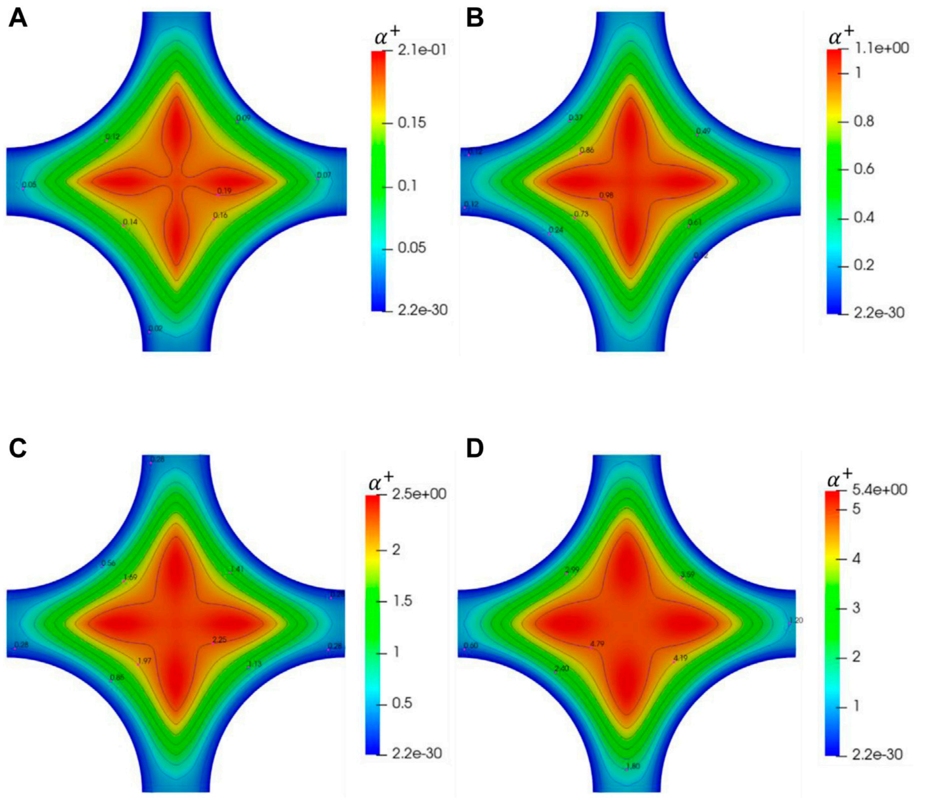

FIGURE 13 | Schematic diagram of dimensionless thermal diffusivity on a slice for square lattice *X* = 1.25. **(A)** *Pe* = 250; **(B)** *Pe* = 1000; **(C)** *Pe* = 2000; **(D)** *Pe* = 4000.

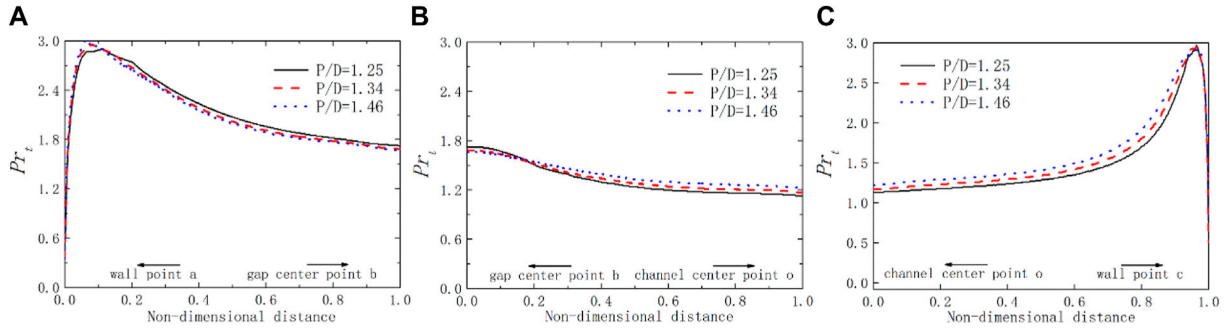

FIGURE 14 | Schematic diagram of turbulent Prandtl number over lines for the square lattice at *Pe* = 2000 with different *P/D* ratios. **(A)** line ab; **(B)** line bo; **(C)** line oc.

line ab. It increases along the bo segment and reaches its maximum near the middle of the bo segment. In most regions far from the wall over lines bo and oc, due to the development of the turbulent flow, turbulent diffusion is greater than the molecular heat conduction, so $a^+ > 1$. Interestingly, the maximum value of a^+ does not appear at the channel center point o but near point o. At the gap line ab, the smaller the gap length, the greater the influence of molecular heat conduction, so the value of a^+ increases over the line ab when the valve of *P/D* increases. But it decreases over the line bo and line oc when the valve of *P/D* increases because at the same *Pe*, the larger the *P/D*, the larger the flow area, the smaller the overall velocity, and the smaller the turbulent heat diffusion over those areas. In **Figure 13**, the dimensionless thermal diffusivity on a slice for *Pe* = 250, 1,000, 2000, and 4,000 is shown. At the same *P/D*, when the *Pe* increases, turbulent heat diffusion will be enhanced, and the grid point with $a^+ > 1$ begins to appear.

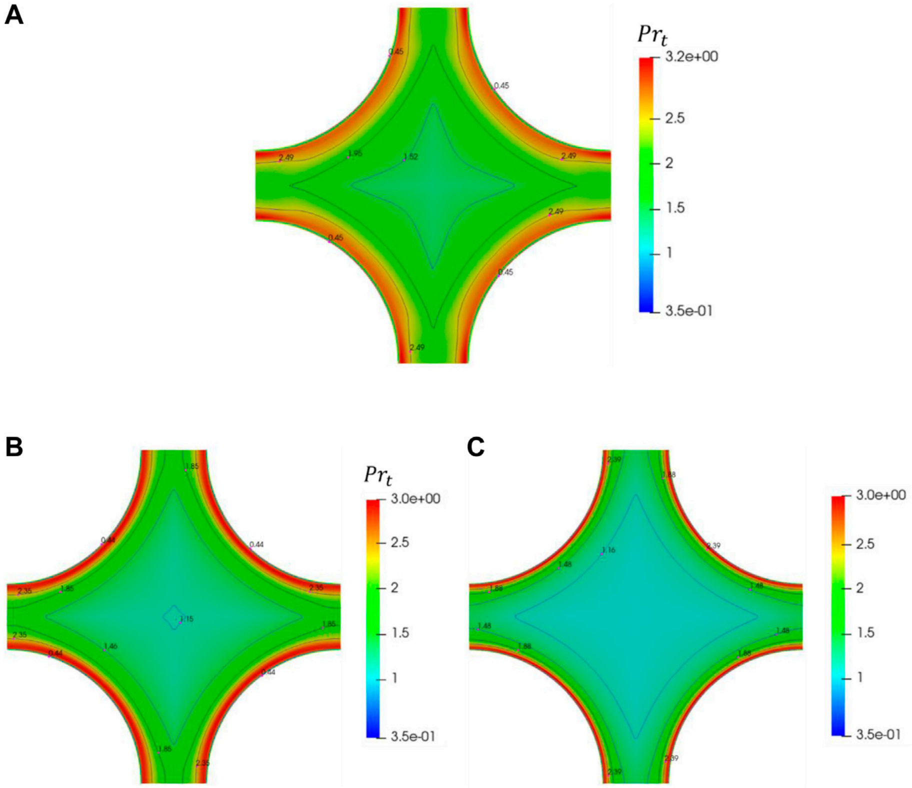

FIGURE 15 | Schematic diagram of turbulent Prandtl number on a slice for square lattice *X* = 1.25. **(A)** *Pe* = 1000; **(B)** *Pe* = 2000; **(C)** *Pe* = 4000.

TABLE 6 | Average turbulent Prandtl number under different *P/D* and *Pe*.

Pe/X	1.25	1.34	1.46
250	2.82087	2.98207	3.157
500	2.4074	2.46975	2.55527
1,000	2.05343	2.10667	2.16182
1,500	1.85231	1.89726	1.94714
2000	1.71413	1.75079	1.79239
2,500	1.60956	1.64109	1.67649
3,000	1.52892	1.55685	1.58799
3,500	1.46592	1.49062	1.51881
4,000	1.41584	1.43757	1.46309

4) Turbulent Prandtl number

In **Figure 14**, the Pr_t with the change of P/D is shown over the lines ab, bo, and oc for the square bundle with $X = 1.25$ at Pe =2000. The Pr_t is not constant and linear. It is larger than the general value of 0.85 for liquid metal. The Pr_t distribution on the line bo is to be smoother than that of lines ab and co. The value of Pr_t decreases over line ab when the value of P/D increases, while it increases over lines bo and oc. This phenomenon echoes the changing trend of dimensionless thermal diffusivity. In **Figure 15**, the turbulent Prandtl number on a slice for Pe = 1,000, 2000, and 4,000 for the square bundle is shown. When Pe increases, Pr_t near the wall and the center decreases gradually.

The average turbulent Prandtl number Pr_{tm} can be defined as follows:

$$Pr_{tm} = \frac{\int_A Pr_t dA}{\int_A dA} \tag{34}$$

Table 6 summarizes the calculation results of average turbulent Prandtl number Pr_{tm} under different P/D and Pe using the present $k-\tilde{\varepsilon}-k_\theta-\tilde{\varepsilon_\theta}$ model. One can see that at the same P/D, the average turbulent Prandtl number decreases with the increase in Pe, while at the same Pe, it increases when the value of P/D increases.

5) Performance analysis of the present four-equation model

When the same turbulence $k-\tilde{\varepsilon}$ model is kept to solve the turbulent viscosity, the present four-equation model needs to solve two more equations $k_\theta-\tilde{\varepsilon_\theta}$ than the $Pr_t = 0.85$ model. To analyze the calculation speed of the $k-\tilde{\varepsilon}-k_\theta-\tilde{\varepsilon_\theta}$ model, the single-step iterative calculation time and calculation memory of these two models are compared and listed in **Table 7**. The current test platform is HP ProDesk 680 G^4 MT with an Intel(R) Core(TM) i7-9700 CPU at 3.00 GHz and 16 GB system memory at 2,667 MHz. At present, the model solver is written based on OpenFOAM V6 version, compiled and integrated in Ubuntu 18.04 system environment. As shown in **Table 7**, the calculation time and memory required by the

TABLE 7 | Performance of the four-equation model under serial operation.

X	*Pe*	Models	Meshes/million	Single-step iteration duration/s	Memory usage/MB
1.25	1,000	$k-\tilde{\varepsilon}-k_\theta-\widetilde{\varepsilon_\theta}$	1.40	10.19	2,459
		$k-\tilde{\varepsilon}-Pr_t=0.85$		7.31	2,107
1.34	1,000	$k-\tilde{\varepsilon}-k_\theta-\widetilde{\varepsilon_\theta}$	2.46	21.83	3,766
		$k-\tilde{\varepsilon}-Pr_t=0.85$		17.42	3,458
1.46	1,000	$k-\tilde{\varepsilon}-k_\theta-\widetilde{\varepsilon_\theta}$	4.24	43.56	5,500
		$k-\tilde{\varepsilon}-Pr_t=0.85$		37.68	5,311

$k-\tilde{\varepsilon}-k_\theta-\widetilde{\varepsilon_\theta}$ model are greater than those of the $k-\tilde{\varepsilon}-Pr_t=0.85$ model.

4 CONCLUSION

The present work studied an isotropic four-equation model for low Pr number that uses simple Dirichlet wall boundaries. First, the turbulent heat transfer process of $Pr = 0.01 \sim 0.05$ fluid in the uniformly heated plane is numerically studied on the open-source program OpenFOAM. Then the flow and heat of the isotropic four-equation of the quadrilateral infinite rod bundle region are evaluated and analyzed with low Prandtl number $Pr = 0.01$. In the SGDH framework, the $Pr_t = 0.85$ model and the isotropic four-equation model are compared with available experimental correlations in the range of Pe = 250–4,000 and P/D = 1.25–1.46. The numerical results show that.

1) The full development velocity, temperature, Reynolds stress, and Reynolds heat flow of $Pr = 0.01 \sim 0.05$ fluid in-plane predicted using the isotropic four-equation model are in good agreement with the DNS results.
2) The Nu of the isotropic four-equation model lies between the experimental relationship, more conservative and similar to the Zhukov and BREST correlations for square rod bundles, while the $Pr_t = 0.85$ model gives too high a Nusselt number prediction to predict the integra heat properly. The slope of Nu predicted by the present isotropic four-equation model is similar to Manservisi's model.
3) More detailed heat exchange phenomena and local temperature distribution are obtained using the four-equation model. At the same P/D, the average turbulent Prandtl number decreases with the increase in Pe, while at the same Pe, it increases when the value of P/D increases.

The isotropic four-equation model can provide more references for calculating the thermal-hydraulic phenomena of liquid metals. But its wider applicability needs further verification.

DATA AVAILABILITY STATEMENT

The raw data supporting the conclusion of this article will be made available by the authors, without undue reservation.

AUTHOR CONTRIBUTIONS

XS: concept, research, writing, editing, code, and data processing. XL: modification, concept, research, and code. XW: research, modification, and code. YL: concept, editing, and research. QC: editing and research. QS: editing and research. XS: editing and research. GL: funding, project management, concept, and research.

FUNDING

This work was supported by the Research on key technology and safety verification of primary circuit, Grant No. 2020YFB1902104, and the Experimental study on thermal-hydraulics of fuel rod bundle, Grant No. Y828020XZ0.

REFERENCES

Abe, K., Kondoh, T., and Nagano, Y. (1995). A New Turbulence Model for Predicting Fluid Flow and Heat Transfer in Separating and Reattaching Flows-II. Thermal Field Calculations. *Int. J. Heat Mass Transfer* 38 (8), 1467–1481. doi:10.1016/0017-9310(94)00252-q

Adamov, E. O. (2001). *Naturally Safe Lead-Cooled Fast Reactor for LargeScale Nuclear Power*. Moscow: Dollezhal RDIPE.

Cerroni, D., Da Vià, R., Manservisi, S., Menghini, F., Pozzetti, G., and Scardovelli, R. (2015). Numerical Validation of Aκ-ω-Kθ-Ωθheat Transfer Turbulence Model for Heavy Liquid Metals. *J. Phys. Conf. Ser.* 655 (1), 012046. doi:10.1088/1742-6596/655/1/012046

Cheng, X., and Tak, N.-i. (2006). Investigation on Turbulent Heat Transfer to lead-bismuth Eutectic Flows in Circular Tubes for Nuclear Applications. *Nucl. Eng. Des.* 236 (4), 385–393. doi:10.1016/j.nucengdes.2005.09.006

Chierici, A., Chirco, L., Da Vià, R., and Manservisi, S. (2019). Numerical Simulation of a Turbulent Lead Bismuth Eutectic Flow inside a 19 Pin Nuclear Reactor Bundle with a Four Logarithmic Parameter Turbulence Model. *J. Phys. Conf. Ser.* 1224, 012030. doi:10.1088/1742-6596/1224/1/012030

Choi, S. K., and Kim, S. O. (2007). Treatment of Turbulent Heat Fluxes with the Elliptic-Blending Second-Moment Closure for Turbulent Natural Convection Flows. *Int. J. Heat Mass Transfer* 51 (9-10), 2377–2388. doi:10.1016/j.ijheatmasstransfer.2007.08.012

Da Vià, R., Giovacchini, V., and Manservisi, S. (2020). A Logarithmic Turbulent Heat Transfer Model in Applications with Liquid Metals for Pr = 0.01-0.025. *Appl. Sci.* 10 (12), 4337. doi:10.3390/app10124337

Da Vià, R., and Manservisi, S. (2019). Numerical Simulation of Forced and Mixed Convection Turbulent Liquid Sodium Flow over a Vertical Backward Facing Step with a Four Parameter Turbulence Model. *Int. J. Heat Mass Transfer* 135, 591–603. doi:10.1016/j.ijheatmasstransfer.2019.01.129

Da Vià, R., Manservisi, S., and Menghini, F. (2016). A K-Ω-Kθ-Ωθ Four Parameter Logarithmic Turbulence Model for Liquid Metals. *Int. J. Heat Mass Transfer* 101 (10), 1030–1041. doi:10.1016/j.ijheatmasstransfer.2016.05.084

Deng, B., Wu, W., and Xi, S. (2001). A Near-wall Two-Equation Heat Transfer Model for wall Turbulent Flows. *Int. J. Heat Mass Transfer* 44 (4), 691–698. doi:10.1016/s0017-9310(00)00131-9

Duponcheel, M., Bricteux, L., Manconi, M., Winckelmans, G., and Bartosiewicz, Y. (2014). Assessment of RANS and Improved Near-wall Modeling for Forced Convection at Low Prandtl Numbers Based on LES up to Reτ=2000. *Int. J. Heat Mass Transfer* 75, 470–482. doi:10.1016/j.ijheatmasstransfer.2014.03.080

Ejenstam, J., and Szakálos, P. (2015). Long Term Corrosion Resistance of Alumina Forming Austenitic Stainless Steels in Liquid lead. *J. Nucl. Mater.* 461, 164–170. doi:10.1016/j.jnucmat.2015.03.011

Ge, Z., Liu, J., Zhao, P., Nie, X., and Ye, M. (2017). Investigation on the Applicability of Turbulent-Prandtl-Number Models in Bare Rod Bundles for Heavy Liquid Metals. *Nucl. Eng. Des.* 314, 198–206. doi:10.1016/j.nucengdes.2017.01.032

Groetzbach, G. (2013). Challenges in Low-Prandtl Number Heat Transfer Simulation and Modelling. *Nucl. Eng. Des.* 264, 41–55. doi:10.1016/j.nucengdes.2012.09.039

Gu, L., and Su, X. (2021). Latest Research Progress for LBE Coolant Reactor of China Initiative Accelerator Driven System Project. *Front. Energ.* 15, 810–831. doi:10.1007/s11708-021-0760-1

Kawamura, H., Abe, H., and Matsuo, Y. (1999). DNS of Turbulent Heat Transfer in Channel Flow with Respect to Reynolds and Prandtl Number Effects. *Int. J. Heat Fluid Flow* 20 (3), 196–207. doi:10.1016/s0142-727x(99)00014-4

Kawamura, H., Ohsaka, K., Abe, H., and Yamamoto, K. (1998). DNS of Turbulent Heat Transfer in Channel Flow with Low to Medium-High Prandtl Number Fluid. *Int. J. Heat Fluid Flow* 19 (5), 482–491. doi:10.1016/s0142-727x(98)10026-7

Kays, W. M. (1994). Turbulent Prandtl Number-Where Are We? *Asme Trans. J. Heat Transfer* 116 (2), 284–295. doi:10.1115/1.2911398

Lai, Y. G., and So, R. M. C. (1990). Near-wall Modeling of Turbulent Heat Fluxes. *Int. J. Heat Mass Transfer* 33 (7), 1429–1440. doi:10.1016/0017-9310(90)90040-2

Manservisi, S., and Menghini, F. (2014a). A CFD Four Parameter Heat Transfer Turbulence Model for Engineering Applications in Heavy Liquid Metals. *Int. J. Heat Mass Transfer* 69 (2), 312–326. doi:10.1016/j.ijheatmasstransfer.2013.10.017

Manservisi, S., and Menghini, F. (2015). CFD Simulations in Heavy Liquid Metal Flows for Square Lattice Bare Rod Bundle Geometries with a Four Parameter Heat Transfer Turbulence Model. *Nucl. Eng. Des.* 295 (12), 251–260. doi:10.1016/j.nucengdes.2015.10.006

Manservisi, S., and Menghini, F. (2014b). Triangular Rod Bundle Simulations of a CFD κ-ϵ-κ-ϵ Heat Transfer Turbulence Model for Heavy Liquid Metals. *Nucl. Eng. Des.* 273, 251–270. doi:10.1016/j.nucengdes.2014.03.022

Mikityuk, K. (2009). Heat Transfer to Liquid Metal: Review of Data and Correlations for Tube Bundles. *Nucl. Eng. Des.* 239 (4), 680–687. doi:10.1016/j.nucengdes.2008.12.014

Moukalled, F., Mangani, L., and Darwish, M. (2016). *The Finite Volume Method in Computational Fluid Dynamics*. Berlin: Springer International Publishing.

Nagano, Y., Hattori, H., and Abe, K. (1997). Modeling the Turbulent Heat and Momentum Transfer in Flows under Different thermal Conditions. *Fluid Dyn. Res.* 20 (1-6), 127–142. doi:10.1016/s0169-5983(96)00049-4

Nagano, Y., and Kim, C. (1988). A Two-Equation Model for Heat Transport in Wall Turbulent Shear Flows. *J. Heat Transfer* 110 (3), 583–589. doi:10.1115/1.3250532

Nagano, Y., and Shimada, M. (1996). Development of a Two-equation Heat Transfer Model Based on Direct Simulations of Turbulent Flows with Different Prandtl Numbers. *Phys. Fluids* 8 (12), 3379–3402. doi:10.1063/1.869124

Reynolds, A. J. (1975). The Prediction of Turbulent Prandtl and Schmidt Numbers. *Int. J. Heat Mass Transfer* 18 (9), 1055–1069. doi:10.1016/0017-9310(75)90223-9

Schroer, C., Wedemeyer, O., Skrypnik, A., Novotny, J., and Konys, J. (2012). Corrosion Kinetics of Steel T91 in Flowing Oxygen-Containing lead–bismuth Eutectic at 450 ˚C. *J. Nucl. Mater.* 431 (1-3), 105–112. doi:10.1016/j.jnucmat.2011.11.014

Shams, A., De Santis, A., and Roelofs, F. (2019). An Overview of the AHFM-NRG Formulations for the Accurate Prediction of Turbulent Flow and Heat Transfer in Low-Prandtl Number Flows. *Nucl. Eng. Des.* 355, 110342. doi:10.1016/j.nucengdes.2019.110342

Shikazono, N., and Kasagi, N. (1996). Second-moment Closure for Turbulent Scalar Transport at Various Prandtl Numbers. *Int. J. Heat Mass Transfer* 39 (14), 2977–2987. doi:10.1016/0017-9310(95)00339-8

Su, X. K., and Gu, L. (2021). *Numerical Study on Turbulent Heat Transfer of LBE in an Annulus Based on A Four-Equation Model*. Chinese Beijing: Atomic Energy Science and technology. Avaialbe at: http://kns.cnki.net/kcms/detail/11.2044.TL.20210720.181. doi:10.13832/j.jnpe.2021.S1.0026

Su, X. K., Gu, L., Peng, T. J., Jiatai, L., Xianwen, L., and Guan, W. (2021). Research on a Four-Equation Model Based on OpenFOAM. *Nucl. Power Eng.* 42 (S1), 26–32. (in chinese).

Subbotin, V. I., Ushakov, P. A., and Kirillov, P. L. (1965). "Heat Transfer in Elements of Reactors with a Liquid Metal Coolant," in Proceedings of the 3rd International Conference on Peaceful Use of Nuclear Energy, Geneva, 192–200.

Tiselj, I., and Cizelj, L. (2012). DNS of Turbulent Channel Flow with Conjugate Heat Transfer at Prandtl Number 0.01. *Nucl. Eng. Des.* 253 (1), 153–160. doi:10.1016/j.nucengdes.2012.08.008

Wang, G., Gu, L., and Yun, D. (2021). Preliminary Multi-Physics Performance Analysis and Design Evaluation of UO2 Fuel for LBE-Cooled Subcritical Reactor of China Initiative Accelerator Driven System. *Front. Energ. Res.* doi:10.3389/FENRG.202110.3389/fenrg.2021.732801

Weller, H. G., Tabor, G., Jasak, H., and Fureby, C. (1998). A Tensorial Approach to Computational Continuum Mechanics Using Object-Oriented Techniques. *Comput. Phys.* 12 (6), 620–631. doi:10.1063/1.168744

You, B. H., Jeong, Y. H., and Addad, Y. (2019). Assessment of Advanced RANS Models Ability to Predict a Turbulent Swept Liquid Metal Flow over a Wire in a Channel. *Nucl. Eng. Des.* 353 (Nov), 1102061–11020614. doi:10.1016/j.nucengdes.2019.110206

Youssef, M. S. (2006). A Two-Equation Heat Transfer Model for wall Turbulent Shear Flows. *J. Eng. Sci.* 34 (6), 1877–1903. doi:10.21608/jesaun.2006.111184

Zhukov, A. V., Kuzina, Y. A., Sorokin, A. P., Leonov, V. N., Smirnov, V. P., and Sila-Novitskii, A. G. (2002). An Experimental Study of Heat Transfer in the Core of a BREST-OD-300 Reactor with lead Cooling on Models. *Therm. Eng.* 49 (3), 175–184.

Conflict of Interest: The authors declare that the research was conducted in the absence of any commercial or financial relationships that could be construed as a potential conflict of interest.

frontiers
in Energy Research

ORIGINAL RESEARCH
published: 25 February 2022
doi: 10.3389/fenrg.2022.835311

Study of Supercritical CO_2 Physical Property Calculation Models

Luyue Min[1], Minyun Liu[1,2], Dapeng Xi[1], Maogang He[3], Xiangyang Liu[3] and Yanping Huang[1]*

[1]CNNC Key Laboratory on Nuclear Reactor Thermal Hydraulics Technology, Nuclear Power Institute of China, Chengdu, China, [2]Department of Engineering Physics, Tsinghua University, Beijing, China, [3]MOE Key Laboratory of Thermo-Fluid Science and Engineering, Xi'an Jiaotong University, Xi'an, China

The supercritical CO_2 (SC-CO_2) thermodynamic cycle has been a promising and revolutionary technology. Related research has put higher demands on CO_2 physical property calculations in terms of computational accuracy and speed. In this study, the deviations between the experimental data and predicted data calculated by several models of CO_2 physical property calculation were obtained. According to the comparison results, the Span–Wagner equation of state, the Vesovic model, and the free-volume viscosity model are selected to construct a set of high-precision CO_2 property calculation models. For the time-consuming problem of commonly used models, new models were developed by using the polynomial fitting and interpolation method, which improved the speed of the physical property calculation by five orders of magnitude while ensuring high accuracy. On this basis, a physical property calculation program for the SC-CO_2 thermodynamic cycle could be developed, which can meet the demands of engineering applications in accuracy and calculation speed.

Keywords: supercritical CO_2, thermodynamic properties, transport properties, property models, polynomial fitting, interpolation method

Edited by:
Luteng Zhang,
Chongqing University, China

Reviewed by:
Deqi Chen,
Chongqing University, China
Gholamhossein Sodeifian,
University of Kashan, Iran

***Correspondence:**
Yanping Huang
hyanping007@163.com

Specialty section:
This article was submitted to
Nuclear Energy,
a section of the journal
Frontiers in Energy Research

Received: *14 December 2021*
Accepted: *26 January 2022*
Published: *25 February 2022*

Citation:
Min L, Liu M, Xi D, He M, Liu X and Huang Y (2022) Study of Supercritical CO_2 Physical Property Calculation Models.
Front. Energy Res. 10:835311.
doi: 10.3389/fenrg.2022.835311

INTRODUCTION

In recent years, supercritical fluid (SCF) techniques have played a catalytic role in scientific research and engineering applications. In the food, pharmaceutical, and cosmetic industries, SCF extraction technology enables soluble components to be extracted from raw materials with high speed and efficiency, taking advantage of the unique properties above the critical point (Sodeifian et al., 2016a; Sodeifian et al., 2016b). SCFs have also been introduced into the biochemical and pharmaceutical industries to improve the bioavailability of drugs by producing nano- and micro-sized drug particles (Sodeifian et al., 2017; Sodeifian and Sajadian 2018; Sodeifian et al., 2018; Sodeifian et al., 2019) and to make it simpler to control the characteristics of the ultimate product by supercritical solvent impregnation (Ameri, Sodeifian, and Sajadian,2020). Meanwhile, supercritical dyeing technology has been used to prevent environmental pollution (water) and improve the performance of the pigments during the dyeing process (Ardestani et al., 2020).

In the field of energy and power, ultra-supercritical units have drawn much attention in recent years due to their energy-saving and emission reduction advantages (Wang 2015). In related studies, supercritical carbon dioxide (SC-CO_2) has been introduced into the new energy conversions as a low-pressure alternative to supercritical water. The critical pressure of carbon dioxide is moderate. In the pseudocritical region, CO_2 has the characteristics of large specific heat, low viscosity, and high compressibility, the utilization of which makes the SC-CO_2 thermodynamic cycle system compact

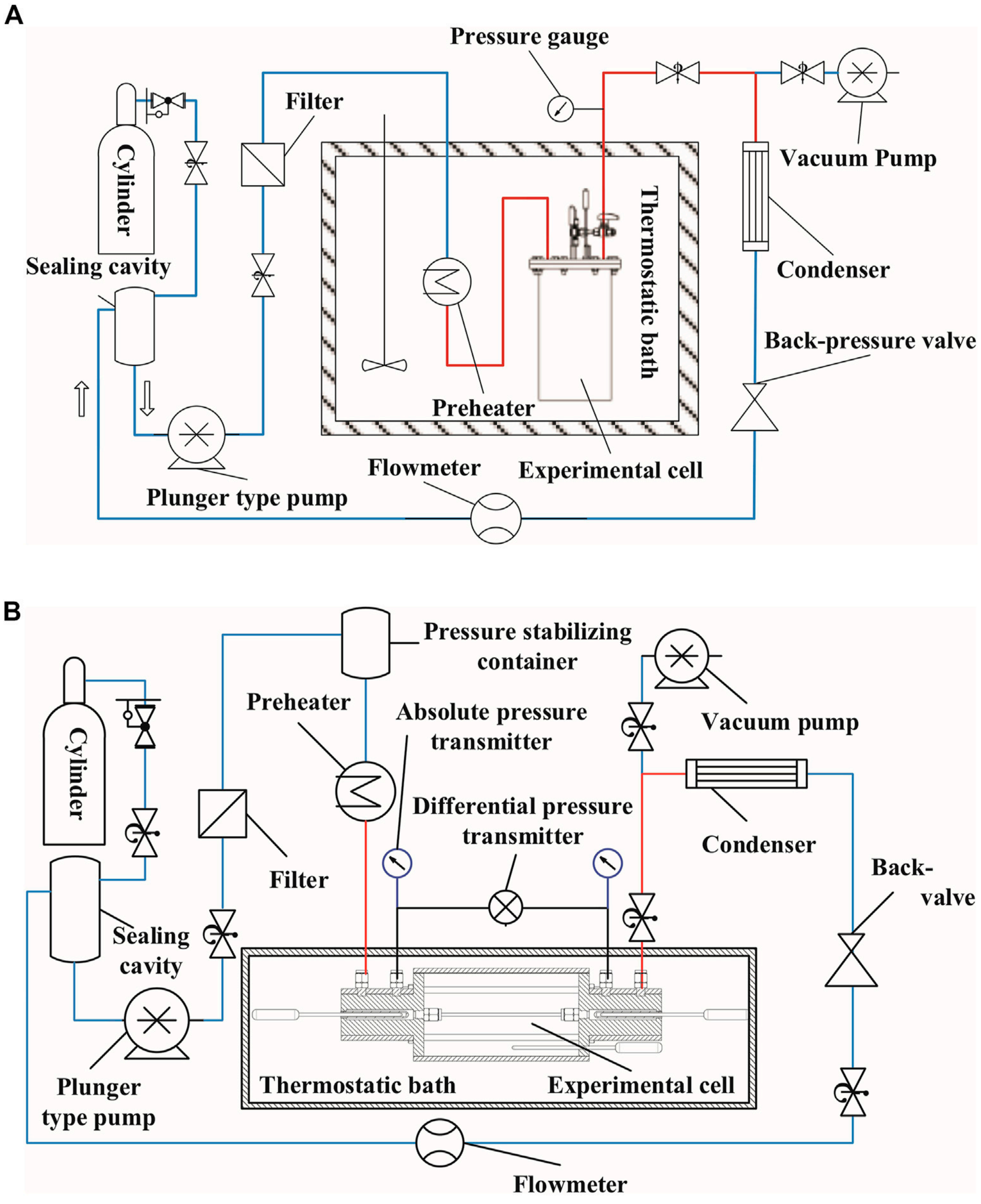

FIGURE 1 | Schematic diagram of the experimental apparatus: **(A)** c_p measurement **(B)** ρ and η measurement.

and efficient, showing a promising future in the fields of advanced nuclear power (Huang and Wang 2012) and industrial waste heat recovery (Tao and Tao 2016).

In the SC-CO_2 thermodynamic cycle, the distortions of CO_2 properties in the pseudocritical region such as the isothermal compression coefficient are beneficial to reduce the power consumption of the compressor and improve the system efficiency but also pose a greater challenge for the calculation of the properties. Moreover, cycle analysis, the design of key thermodynamic processes, and components all place high demands on the physical properties of CO_2 (Yang et al., 2020). Therefore, how to calculate the thermodynamic and transport properties of CO_2 within the cycle conditions quickly and accurately has been a research focus.

However, the existing CO_2 property calculation models and CO_2 property calculation programs are no longer well suited to the needs of the rapid development of SC-CO_2 research. For example, the Span–Wagner equation of state (Span and Wagner 1996), recognized as the equation of state with the highest accuracy, is limited by its complex form, which means that it is time-consuming. The commonly used property database NIST REFPROP, which is based on the Span–Wagner equation, is hardly available to large-scale calculations owing to the low computational speed. In previous studies, some scholars have

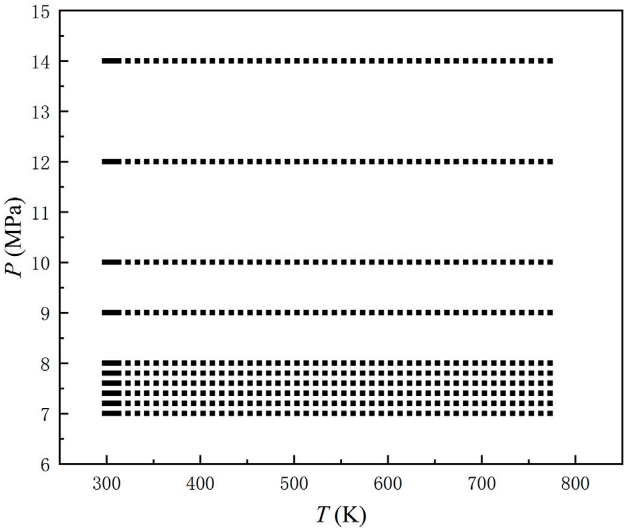

FIGURE 2 | Distribution of experimental data points.

noticed such problems and have used polynomial fitting methods (Bahadori et al., 2009; Ouyang 2011) and neural network algorithms (Zhang et al., 2019) to obtain property prediction models with higher accuracy and calculation speed. Nevertheless, these available models do not correspond to the actual needs of the SC-CO_2 thermodynamic cycle in terms of applicable working conditions and solving methods, and little research work has concentrated on the efficiency evaluation of these models to prove their superiority of computational efficiency. Thus, it is necessary to develop new models differing from the existing ones and pay attention to computational speed comparison of the commonly used prediction models with that of the new models.

This study aims to meet the demands for accuracy and efficiency of CO_2 property calculation in the thermodynamic cycle. Meanwhile, a CO_2 physical property measurement experiment was conducted to obtain precise property data. On this basis, we compared the deviations between the experimental and predicted values of various CO_2 physical property calculation models and finally selected the Span–Wagner equation of state, the Vesovic model (Vesovic et al., 1990), and the free-volume viscosity model (Liu et al., 2013) to make up a set of high-precision CO_2 property calculation models. Also, to solve the time-consuming problem of traditional high-precision models, a high-speed calculation model of CO_2 physical properties was constructed by using the polynomial fitting and interpolation method, which also satisfies the requirement for accuracy.

RESEARCH ON HIGH-PRECISION CO_2 PROPERTY MODELS

Experiment in CO_2 Physical Property Measurement

Although much research has been done on CO_2 property data, few experimental studies have been conducted in the range of supercritical conditions. Thus, to obtain precise experimental data in the supercritical region, the experiment of CO_2 physical property measurement was carried out so that the accuracy of available models could be checked.

TABLE 1 | Uncertainties of the experiment.

U(p)/MPa	U(T)/K	U(c_p)/%	U(ρ)/%	U(η)/%
0.003	0.04	0.9	0.06	1.4

In this work, the density (ρ), isobaric specific heat (c_p), and viscosity (η) of CO_2 temperatures from 298.15 to 773.15 K and pressures from 7 to 14 MPa were measured through the U-tube vibration method (Jiang 2011), flow calorimeter (Liu et al., 2014; He et al., 2015), and capillary method (Liu et al., 2011), respectively. The physical property measurement experiment apparatus is shown in **Figure 1**.

Several key technical problems have been solved in this experiment. First, a double-layer vacuum cylinder was used to ensure thermal insulation and prevent high temperature instability. Second, in order to minimize the heat loss, the fluid was heated by a microheater inside the tube assembly, and the heating tubes were fine. In addition, the horizontal placement of the experimental body proposed by Liu et al. (2014) was also used to avoid the vertical density stratification produced because of gravity.

Figure 2 presents the distribution of data points, where the horizontal and vertical coordinates indicate the temperature (in K) and pressure (in MPa), respectively. **Table 1** summarizes the total measurement uncertainties of pressure and temperature, and the extended uncertainties at confidence factor k = 2 of c_p, ρ, and η. The uncertainty of c_p comes from the measurement uncertainties of the differential temperature, the mass flow, the heating power, and the pressure. The uncertainty of ρ is mainly from the uncertainty of the density measurement itself, and the uncertainty of η is composed of the uncertainties of the inner diameter of the capillary tube, the mass flow, the differential pressure, the length of the capillary tube, the kinetic energy loss coefficient, the density, and the differential temperature. The equations for calculating synthetic uncertainty of c_p and η are as follows:

$$u_c(c_p) = \sqrt{\left(\frac{\partial c_p}{\partial \Delta T}\right)^2 u_{\Delta T}^2 + \left(\frac{\partial c_p}{\partial q_m}\right)^2 u_{q_m}^2 + \left(\frac{\partial c_p}{\partial Q}\right)^2 u_Q^2 + \left(\frac{\partial c_p}{\partial p}\right)^2 u_p^2}, \qquad (1)$$

$$u_c\ (\eta) = \sqrt{\left(\frac{\partial \eta}{\partial R}\right)^2 u_R^2 + \left(\frac{\partial \eta}{\partial q_m}\right)^2 u_{q_m}^2 + \left(\frac{\partial \eta}{\partial \Delta p}\right)^2 u_{\Delta p}^2 + \left(\frac{\partial \eta}{\partial L}\right)^2 u_L^2 + \left(\frac{\partial \eta}{\partial m}\right)^2 u_m^2 + \left(\frac{\partial \eta}{\partial \rho}\right)^2 u_\rho^2 + \left(\frac{\partial \eta}{\partial \Delta T}\right)^2 u_{\Delta T}^2}, \qquad (2)$$

where ΔT is the differential temperature, q_m is the mass flow, Q is the heating power, p is the pressure, R is the inner diameter of the capillary tube, Δp is the differential pressure, L is the length of the capillary tube, m is the kinetic energy loss coefficient, ρ is the density, and u_{factor} is the the uncertainty of some factors.

Selection and Evaluation Method

In this section, several commonly used models of CO_2 thermodynamic and transport properties were tested. c_p, ρ, and η calculated by different models were compared with

TABLE 2 | Comparison between the predicted and experimental data out of pseudocritical region.

Physical quantity	Abbreviation of models	AARE (%)	R^2
Density	FEQ (Span and Wagner 1996)	0.144	1.000
	FEK (Kunz et al., 2007)	0.145	1.000
	FES (Span and Wagner 2003)	26.771	0.782
Isobaric specific heat	FEQ (Span and Wagner 1996)	1.215	0.998
	FEK (Kunz et al., 2007)	1.244	1.000
	FES (Span and Wagner 2003)	1.244	1.000
Viscosity	VS1 (Vesovic et al., 1990)	1.819	0.998
	ECS (Klein, Mclinden, and Laesecke 1997)	3.411	0.991
	VS4 (Quinones-Cisneros and Deiters 2006)	1.713	0.998

TABLE 3 | Comparison between the predicted and experimental data in pseudocritical region.

T/K	*p*/MPa	η_{exp}/μPa·s	AE(%) VS1	VS4
8	307.2	38.17	3.665	4.716
8	309.2	25.72	1.117	2.276
9	311.2	41.47	2.409	3.388
9	313.2	33.88	2.714	3.867
10	323.2	27.95	1.495	2.110
12	323.2	43.53	0.561	1.421
12	333.2	31.57	1.562	2.049
14	333.2	41.99	0.097	0.820
14	343.2	33.76	0.930	1.276

partial experimental data. According to the comparison results, the best performing models were selected. Furthermore, the selected models were evaluated with all the experimental data to reconfirm the accuracy.

Referring to Heidaryan and Jarrahian's(2013) article, this article introduced four statistical parameters to present the comparison results, including the average relative error (ARE), average absolute relative error (AARE), absolute relative error (AE), and correlation coefficient (R^2) (see **Eq. 3–6**):

$$\mathrm{ARE}\% = \frac{100}{\mathrm{N_d}} \times \sum_{i=1}^{N_d}\left(\frac{\rho_{\mathrm{i}}^{\mathrm{exp.}} - \rho_{\mathrm{i}}^{\mathrm{calc.}}}{\rho_{\mathrm{i}}^{\mathrm{exp.}}}\right) \tag{3}$$

$$\mathrm{AARE}\% = \frac{100}{\mathrm{N_d}} \times \sum_{i=1}^{N_d}\left|\frac{\rho_{\mathrm{i}}^{\mathrm{exp.}} - \rho_{\mathrm{i}}^{\mathrm{calc.}}}{\rho_{\mathrm{i}}^{\mathrm{exp.}}}\right|, \tag{4}$$

$$\mathrm{AE}\% = 100 \times \left|\frac{\rho_{\mathrm{i}}^{\mathrm{exp.}} - \rho_{\mathrm{i}}^{\mathrm{calc.}}}{\rho_{\mathrm{i}}^{\mathrm{exp.}}}\right|, \text{ and} \tag{5}$$

$$R^2 = 1 - \frac{\sum_{i=1}^{N_d}\left(\rho_{\mathrm{i}}^{\mathrm{exp.}} - \rho_{\mathrm{i}}^{\mathrm{calc.}}\right)^2}{\sum_{i=1}^{N_d}\left(\rho^{\mathrm{mean}} - \rho_{\mathrm{i}}^{\mathrm{calc.}}\right)^2}, \tag{6}$$

where ARE indicates the bias between the evaluated data and reference data. The smaller the ARE, the smaller the systematic bias of the data. When ARE is 0, it indicates that the values of evaluated data are randomly distributed around the reference data values. The AARE characterizes the accuracy of the evaluated data compared with the reference data. The maximum value of AE is the maximum deviation of the evaluated data from the reference data. The R^2 represents the precision of the evaluated data. The closer the R^2 is to 1, the stronger the correlation between the evaluated data and the reference data.

The specific selection criteria are as follows. Comparing data out of the pseudocritical region, a smaller AARE value and R^2 value closer to 1 indicate higher accuracy and precision of the model, respectively; if the values of these two statistical parameters are close between different models, then the AE (max) values in the pseudocritical region are compared, and the model with the smaller ones is counted as the better one.

RESULTS AND DISCUSSION

Table 2 shows the comparisons between the predicted data obtained by different commonly used models and the experimental data out of the pseudocritical region. For ρ and c_p calculations, the AARE of the FEQ model (the Span–Wagner equation) is only 0.144 and 1.215%, respectively, and the R^2 are both close to 1. The values of these two parameters in contrast with those of other models indicate a high degree of accuracy and precision of the Span–Wagner equation in ρ and c_p calculations. For the calculation of η, the VS1 model and VS4 model have similar resultant values. The AAREs are 1.819 and 1.713%, and R^2 are both close to 1. Thus, to choose the better viscosity model, their predicted η values are further compared with the experimental data in the pseudocritical region. The VS1 model (also the Vesovic model) is obtained to have a smaller AE value in the pseudocritical region overall (see **Table 3**).

In addition, for η calculation, in order to make up for the shortcomings of the Vesovic model like complexity, the free-volume viscosity model with a simple form is introduced to this study. It is worth mentioning that several parameters of the model are obtained by fitting our experimental data, which means that it concentrates more on the supercritical region. Within that region (298.15 K≤ T <773.15 K and seven MP a ≤ p <14 MPa), its accuracy could be good. The equations are as follows (Liu et al., 2013):

$$\eta = \eta_0 + \Delta\eta, \tag{7}$$

where

$$\eta_0 = 4.0785 \times \frac{\sqrt{MT}}{V_c^{\frac{2}{3}}\Omega^*(T^*)} F_c \text{ and} \tag{7a}$$

TABLE 4 | Comparison of the calculated values of each model with the experimental data.

Model	Working condition	ARE (%)	AARE (%)	AE$_{max}$ (%)	R^2
Span–Wagner equation of state for ρ	General	−0.0089	0.3126	1.1744	0.9999
	Pseudocritical	0.0972	0.7606	1.2964	0.9988
Span–Wagner equation of state for c_p	General	0.1561	0.4149	4.3631	0.9991
	Pseudocritical	5.478	5.478	8.9908	0.9748
Vesovic model for η	General	0.9963	1.1117	3.8858	0.9974
	Pseudocritical	−1.5482	1.7743	4.3619	0.9928
Free-volume viscosity model for η	General	−0.0007	0.4528	1.8986	0.9996
	Pseudocritical	−0.1853	1.0962	2.4863	0.9976

TABLE 5 | Absolute error of isobaric specific heat calculation in the pseudocritical region.

No.	T/K	p/MPa	Absolute error/kJ·(kg·K)$^{-1}$	No.	T/K	p/MPa	Absolute error/kJ·(kg·K)$^{-1}$
1	304.15	7.4	5.998	8	323.15	10	0.072
2	305.15	7.6	5.040	9	323.15	12	0.064
3	305.15	7.8	1.183	10	333.15	12	0.046
4	307.15	7.8	2.088	11	333.15	14	0.040
5	307.15	8	0.918	12	343.15	14	0.013
6	311.15	9	0.277	13	353.15	14	0.026
7	313.15	9	1.229				

TABLE 6 | Specific physical properties represented by x, y, z and the n value of each model.

Model	x	y	Z	n
$T\,(h,p)$	$h/(990\,\text{kJ/kg})$	$p/(20\,\text{MPa})$	$T/(780\,\text{K})$	4
$\rho\,(h,p)$	$h/(990\,\text{kJ/kg})$	$p/(20\,\text{MPa})$	$\rho/(480\,\text{kg/m}\hat{3})$	5
$c_p\,(h,p)$	$h/(990\,\text{kJ/kg})$	$p/(20\,\text{MPa})$	$c_p/[2.4\,\text{kJ}/(\text{kg}\cdot\text{K})]$	5
$h\,(p,T)$	$T/(780\,\text{K})$	$p/(20\,\text{MPa})$	$h/(990\,\text{kJ/kg})$	4
$\lambda\,(\rho,T)$	$\rho/(480\,\text{kg/m}^3)$	$T/(780\,\text{K})$	$\lambda/[60\,\text{mW}/(\text{m}\cdot\text{K})]$	4
$\eta\,(\rho,T)$	$\rho/(480\,\text{kg/m}^3)$	$T/(780\,\text{K})$	$\eta/(40\,\mu\text{Pa}\cdot\text{s})$	3

TABLE 7 | Coefficients D$_{ij}$ of $T\,(h,p)$.

i	D$_{i0}$	D$_{i1}$	D$_{i2}$	D$_{i3}$	D$_{i4}$
0	−0.87811	3.58799	−2.79791	1.14141	−0.06412
1	4.19127	−15.32662	19.82254	−9.87656	1.20086
2	1.11324	−14.17288	41.97630	−47.01950	18.13742
3	−6.78545	41.41008	−91.03666	86.16367	−29.79073
4	3.22732	−18.53626	38.97091	−35.64303	11.99363

$$\Delta\eta = \frac{\rho l\left(\alpha\rho + \frac{pM}{\rho}\right)}{\sqrt{3RTM}}\exp\left[B\left(\frac{\alpha\rho + \frac{pM}{\rho}}{RT}\right)^{\frac{3}{2}}\right], \tag{7b}$$

where η_0 is the viscosity of dilute gas, $\Delta\eta$ is the correction term for the viscosity of dense fluid, Ω^* is the collision integral, F_c is the parameter related to dipole moment and eccentricity factor, B is the superimposed part of the free volume, M is the molar mass, $\alpha\rho$ is the energy barrier, $l = L^2/b_f$ is the L^2 is the molecular mean characteristic square length and b_f is the dissipation of potential energy.

In the aforementioned equations, α, B, and l are obtained by fitting the experimental data, and the values are as follows: α = 13.34816839, B = 8.04589798 × 10^{-11}, and l = 0.03939321.

Finally, the Span–Wagner equation of state, the Vesovic model, and the free-volume viscosity model are chosen to construct a set of high-precision CO$_2$ property calculation models. The three selected high-precision models are further evaluated to analyze their accuracy. The experimental data (298.15 K≤ T <773.15 K and seven MP a ≤ p <14 MPa) are divided into data in the general region and pseudocritical region, and the calculated data and experimental data are compared on this basis, as shown in **Table 4**.

In the general region, the ARE between experimental data and the predicted ρ calculated by the Span–Wagner equation is only -0.0089%, which is lower than the equation uncertainty (± 0.03%, ± 0.05%). In the pseudocritical region, although the average relative error is slightly larger than the equation uncertainty, it is still acceptable.

For c_p calculation by the Span–Wagner equation, the ARE is only about 0.15% in the general region, while the maximum AE is 4.3631%, and this data point is near the pseudocritical region. The error around this region is generally large, possibly due to the rough partition of the pseudocritical region, which means that this part of general region is still influenced by property distortions. If data in the controversial region are ignored, the AARE then drops to about 1%. However, in the pseudocritical region, the ARE exceeds 5%, and the maximum AE is close to 9%. The absolute error between calculated and experimental values of c_p in the pseudocritical region is presented in **Table 5**. The absolute error is large in the pseudocritical region from 7 to 8 MPa, up to 5.998 kJ/(kgK),

TABLE 8 | Coefficients D_{ij} of $\rho(h,p)$.

i	D_{i0}	D_{i1}	D_{i2}	D_{i3}	D_{i4}	D_{i5}
0	5.51141	−30.68877	66.27682	−69.14811	34.62849	−6.57949
1	−31.90696	177.99507	−367.93354	351.83442	−149.98417	20.26986
2	116.86343	−597.69806	1138.11163	−963.95423	317.08842	−10.35475
3	−84.53118	275.28642	−24.97488	−807.41087	1018.07080	−376.60235
4	−26.86934	388.49330	−1538.70210	2628.70703	−2067.58415	616.10422
5	29.46078	−254.14657	812.59139	−1232.66205	899.00831	−254.29788

TABLE 9 | Coefficients D_{ij} of $c_p\ (h,p)$.

i	D_{i0}	D_{i1}	D_{i2}	D_{i3}	D_{i4}	D_{i5}
0	78.26160	−442.48715	966.46759	−1004.94280	488.94838	−85.68895
1	−505.96403	2776.18208	−5761.21712	5524.98006	−2319.84029	285.24633
2	1283.18400	-6556.89741	12144.03687	-9327.54913	1960.78820	498.64679
3	−1047.60030	3839.11215	−2038.16407	−7565.71111	11258.16620	−4449.55008
4	−8.71962	2422.70087	−12470.44310	23962.92490	−20272.26838	6368.83762
5	209.14598	−2075.59975	7226.02384	−11644.52629	8902.51944	−2618.48425

TABLE 10 | Coefficients D_{ij} of $h(\rho,T)$.

i	D_{i0}	D_{i1}	D_{i2}	D_{i3}	D_{i4}
0	−1.42101	9.67303	−18.02611	15.97775	−5.19521
1	8.72986	−48.26339	97.33641	−85.65223	27.84470
2	−19.46200	104.01501	−206.00900	179.22737	−57.80601
3	11.08749	−59.74097	119.21196	−104.40354	33.86865
4	−0.97826	5.57283	−11.64132	10.58920	−3.54565

TABLE 11 | Coefficients D_{ij} of $\lambda(\rho,T)$.

i	D_{i0}	D_{i1}	D_{i2}	D_{i3}	D_{i4}
0	1.73319	−36.88377	202.20690	−354.37541	156.08372
1	−12.30436	241.20760	−1256.10471	2134.20547	−845.03747
2	33.86575	−565.82226	2821.67532	−4583.30612	1513.56125
3	−35.65537	562.24250	−2684.92673	4089.19850	−928.21944
4	13.23967	−199.52577	908.88515	−1255.87906	66.71366

TABLE 12 | Coefficients D_{ij} of $\eta(\rho,T)$.

i	D_{i0}	D_{i1}	D_{i2}	D_{i3}
0	−0.07622	0.23975	0.04682	0.28700
1	1.34854	−0.6812	1.31995	−1.11705
2	−0.54067	0.81125	−1.62115	1.53517
3	0.12929	−0.32631	0.69507	−0.74812

indicating the poor accuracy of the Span–Wagner equation in the pseudocritical region.

For the comparison of η, the ARE between the Vesovic model and the experimental result is below the model's minimum uncertainty of 1% in the general region. In the pseudocritical region, it is still lower than the uncertainty of 2% given by the model for this region. However, there are still several data points near the pseudocritical region with large AE up to 4%, suggesting that the η calculation of the Vesovic model in the pseudocritical region is defective.

The free-volume viscosity model has very high accuracy in η calculation throughout the region. The ARE is within 0.001% in the general region and only about 0.18% in the pseudocritical region.

These evaluation results offer some ideas for the improvement of the existing calculation programs. For example, in terms of CO$_2$ physical property calculation, the widely used program REFPROP is based partly on the Span–Wagner equation and the Vesovic model. The accuracy is relatively high as the evaluation results show. However, for the η calculation in the supercritical region, it could be more accurate than the Vesovic model used by REFPROP when using the free-volume viscosity model.

Research on Fast Calculation CO$_2$ Property Models

In engineering applications of SC-CO$_2$, such as sub-channel studies and system analysis, their computational procedures require high precision and efficiency for physical property calculations. However, the aforementioned high-precision computational models are in a relatively complicated form and have low computation speed, which greatly limits their use in engineering. Therefore, models with faster computation speeds need to be studied. In this part, two fast calculation methods are introduced: polynomial fitting and interpolation method.

Polynomial Fitted Model

In previous studies, many researchers have obtained property calculation models with high prediction accuracy in a certain

TABLE 13 | Average of relative errors between standard data and the fitted models with different maximum number of decimal digits.

Maximum number of decimal digits of coefficients		**0.1**	**0.01**	**0.001**	**0.0001**	**0.00001**
Average of relative errors from standard data (%)	$h(p,T)$	64.62139	6.924697	0.706943	0.091127	0.061878
	$T(h,p)$	57.79155	5.247569	0.663925	0.19348	0.150844
	$\rho(h,p)$	219.8697	21.96921	1.818924	0.262511	0.140797
	$c_p(h,p)$	112.5528	10.94899	1.254259	0.170878	0.130468
	$\lambda(\rho,T)$	20.49005	5.110055	2.711198	2.453105	2.447142
	$\eta(\rho,T)$	17.9272	4.332717	2.351954	2.07974	2.057038

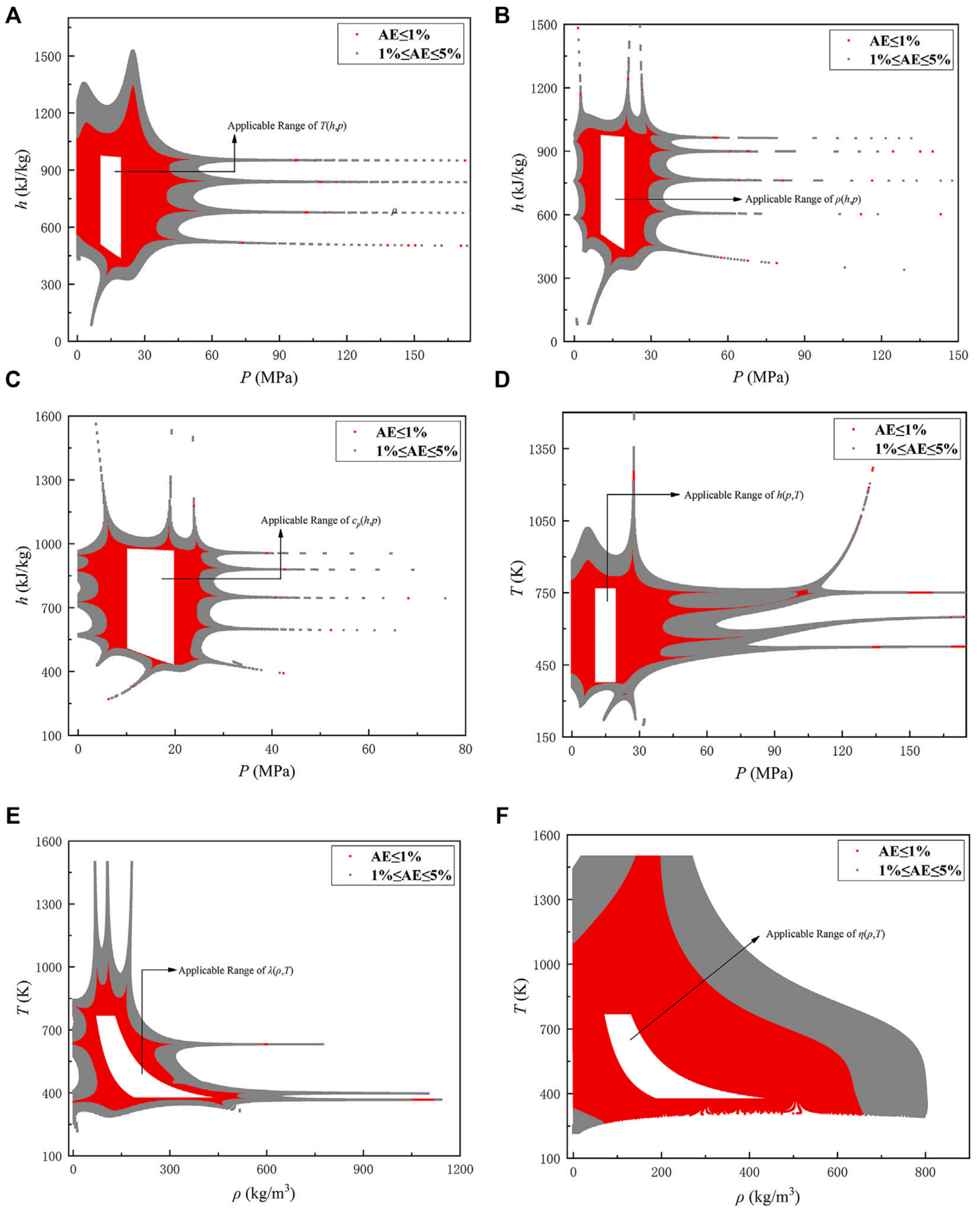

FIGURE 3 | Distribution of working points with absolute error less than 1% for each formula: **(A)** $T(h,p)$ **(B)** $\rho(h,p)$ **(C)** $c_p(h,p)$ **(D)** $h(p,T)$ **(E)** $\lambda(\rho,T)$ **(F)** $\mu(\rho,T)$.

TABLE 14 | Maximum absolute error between the two quick calculation methods and the standard data.

Physical quantity	AE$_{max}$ of the fitted model (%)	AE$_{max}$ of the interpolation method (%)
$T(h, p)$	0.1390	0.1945
$\rho(h, p)$	0.3000	1.1233
$c_p(h, p)$	1.1340	2.0117
$h(T, p)$	0.7530	0.7591
$\lambda(\rho, T)$	0.6790	1.1628
$\eta(\rho, T)$	0.0243	0.1873

temperature and pressure range, using polynomial fitting methods (Ouyang 2011) and neural network algorithms (Zhang et al., 2019). However, these existing models do not correspond to our actual needs in terms of applicable working conditions and solving methods. Thus, a new model appropriate to related research needs to be fitted.

After trying various equation forms, we found that the fitted model obtained by the polynomial form of **Eq. 8** is the best, and the prediction accuracy is extremely high in the required temperature and pressure range.

$$z(x, y) = \sum_{i=0}^{n} C_i(x) y^i, \tag{8}$$

where

$$C_i(x) = \sum_{j=0}^{n} D_{ij} x^i. \tag{8a}$$

According to the actual demand of CO$_2$ physical properties for sub-channel studies and others, the model is designed to be applicable in the range 373.15 K≤ T <773.15 K, 10 MPa≤ p <20 MPa. Since the Span–Wagner equation and the Vesovic model are highly accurate in this range, the numerical fitting will be performed based on their calculation results.

Six fitted models are finally obtained in the form of **Eq. 8**, and the specific physical properties represented by x, y, z and the value n of each model are shown in **Table 6**. The table of the fitted coefficients D_{ij} can be seen in **Tables 7–12**. According to the comparison results of relative errors between standard data and the fitted model with different maximum numbers of decimal digits (see **Table 13**), it was found that the relative errors generally decrease quickly when the number of decimal places is taken to four digits, and the reduction in relative errors is relatively small when going from 4 to 5 decimal places. Meanwhile, the accuracy of the result obtained by taking 5 decimal places is sufficient for our needs. Thus, the coefficients are retained to 5 decimal places in this article as shown in the tables.

The deviation between the data by the fitted equations and the combination of the Span–Wagner equation and the Vesovic model outside the given applicable range (373.15 K≤ T <773.15 K, 10 MPa ≤ p <20 MPa) are calculated. **Figure 3** shows that the distribution of the data points outside the given applicable range of the six equations, where the AE is less than 1 and 5%. The red and gray areas represent the range where the deviation is below 1 and 5%, respectively, and the surrounded blank area refers to the models' applicable range. Under the accuracy requirement of 1%, the six equations are still acceptable in a wide range outside the applicable region, indicating that the calculation range of fitted models is expandable.

Fast Calculation Method: Interpolation

In addition to obtaining new models by polynomial fitting, interpolation is also a commonly used method with high computational speed. The basic idea is to estimate the physical properties through linear interpolation, referring to data tables of physical properties (interpolation nodes). It is fast but strictly limited to the range given by the data table, which means that it is non-expandable.

The applicable range, the physical properties to be calculated, and the corresponding independent variables are all consistent with those in the fitted models.

The values calculated by the fitted model and the interpolation method are compared with the predicted data calculated by the Span–Wagner equation and the Vesovic model. **Table 14** presents the results: the maximum AE of them in the applicable range. The maximum AEs are all very small, within 2.02% (1% if disregarding c_p calculation and the λ interpolation calculation). The results indicate that both fitted models and the interpolation method have high accuracy. It can also be found that the fitted models generally have smaller maximum AE, which means that the accuracy of the fitted model is slightly higher than that of the interpolation method. However, considering the simplicity of the linear interpolation method compared to the fitted model calculation, the accuracy of the interpolation method is already satisfactory.

TABLE 15 | Comparison of calculation time (for 10^5 working conditions).

Physical quantity	Calculation time (ms)			CTR	
	Fitted model	Interpolation method	Span–Wagner + Vesovic model	Fitted model	Interpolation method
$T(h, p)$	28.3	3.4	806068	28483	237079
$\rho(h, p)$	32.3	2.8	786252	24342	280804
$c_p(h, p)$	31.7	2.3	808804	25514	351654
$h(T, p)$	25.4	2.9	1125590	44315	388134
$\lambda(\rho, T)$	25.4	2.8	841422	33127	300508
$\eta(\rho, T)$	13.1	2.5	776509	59275	310604

Computing Time Comparison With High-Precision Models

The fitted model, interpolation method, and the combination of the Span–Wagner equation and the Vesovic model are separately used to calculate the physical properties under 10^5 working conditions in the applicable range, and the calculation time is compared as shown in **Table 15**, where CTR is the computing time ratio:

$$CTR = \frac{\text{Calculation time of the Span} - \text{Wagner equation}}{\text{Calculation time of the fitted model (or the interpolation method)}}. \tag{9}$$

The computation time of the Span–Wagner equation + Vesovic model is four orders of magnitude more than that of the fitted models. and five orders of magnitude more than that of the interpolation method, showing the superiority of the two fast calculation models (methods) in terms of efficiency. In a cross-sectional comparison of the two fast calculation models (methods), it is found that the computation time of the interpolation method is only 1/10 of that of the fitted models. However, given that the overall accuracy of the interpolation method is slightly inferior to that of the fitted models, and the applicability is strictly limited to the given data tables, the choice of which calculation method to use should be combined with the reality in engineering applications.

CONCLUSION

Based on the experiment of CO_2 physical property measurement in the range of temperatures from 298.15 to 773.15 K and pressures from 7 to 14 MPa, some commonly used CO_2 property models are evaluated, and a set of relatively high-precision models is selected, including the Span–Wagner equation of state, the Vesovic model, and the free-volume viscosity model. Comparing ρ (the Span–Wagner equation), c_p (the Span–Wagner equation), and η (the Vesovic model, the free-volume viscosity model) calculation results with experimental data, the AARE is 0.3126, 0.4149, 0.9963, and -0.0007, respectively, out of the pseudocritical region.

Meanwhile, to achieve the goal of fast calculation of CO_2 properties, polynomial fitting and interpolation methods are introduced in the present work. The results show that both methods have high accuracy with a relative error of less than 2.02% (1% if disregarding c_p calculation and the λ interpolation calculation) and can improve the calculation speed by 4-5 two magnitudes compared with the Span–Wagner equation + Vesovic model. Additionally, the fitted model has a large expandable region under the 1% accuracy requirement, and the computation time of the interpolation method is only 1/10 of that of the fitted models.

It can be concluded that the fitted models and interpolation method can successfully and quickly predict CO_2 properties within the range of temperatures from 373.15 to 773.15 K and pressures from 10 to 20 MPa. The results are significant for research of the SC-CO_2 Brayton cycle.

DATA AVAILABILITY STATEMENT

The raw data supporting the conclusion of this article will be made available by the authors, without undue reservation.

AUTHOR CONTRIBUTIONS

LM: Software, Formal Analysis, Writing - Original Draft; ML: Methodology, Writing - Review and Editing; DX: Software, Formal Analysis; MH and XL: Investigation, Validation; YH: Conceptualization, Funding Acquisition, Supervision.

REFERENCES

Ameri, A., Sodeifian, G., and Sajadian, S. A. (2020). Lansoprazole Loading of Polymers by Supercritical Carbon Dioxide Impregnation: Impacts of Process Parameters. *J. Supercrit. Fluids* 164, 104892. doi:10.1016/j.supflu.2020.104892

Bahadori, A., Vuthaluru, H. B., and Mokhatab, S. (2009). New Correlations Predict Aqueous Solubility and Density of Carbon Dioxide. *Int. J. Greenhouse Gas Control.* 3 (4), 474–480. doi:10.1016/j.ijggc.2009.01.003

He, M., Su, C., Liu, X., Qi, X., and Lv, N. (2015). Measurement of Isobaric Heat Capacity of Pure Water up to Supercritical Conditions. *J. Supercrit. Fluids* 100, 1–6. doi:10.1016/j.supflu.2015.02.007

Heidaryan, E., and Jarrahian, A. (2013). Modified Redlich□Kwong Equation of State for Supercritical Carbon Dioxide. *J. Supercrit. Fluids* 81, 92–98. doi:10.1016/j.supflu.2013.05.009

Huang, Y., and Wang, J. (2012). Application of Supercritical Carbon Dioxide in Nuclear Reactor System. *Nucl. Power Eng.* 33 (3), 21–27. doi:10.1007/s11783-011-0280-z

Jiang, Wei. (2011). Density Measurement by U-Tube Vibration Method. *Sci. Tech. Inf.* 000 (004), 1–2. doi:10.3969/j.issn.1672-3791.2011.04.001

Klein, S. A., Mclinden, M. O., and Laesecke, A. (1997). An Improved Extended Corresponding States Method for Estimation of Viscosity of Pure Refrigerants and Mixtures. *Int. J. Refrigeration* 20 (3), 208–217. doi:10.1016/S0140-7007(96)00073-4

Kunz, O., Klimeck, R., Wagner, W., and Jaeschke, M. (2007). *The GERG-2004 Wide-Range Reference Equation of State for Natural Gases and Other Mixtures GERG TM15 2007.* Germany: Düsseldorf VDI-Verl.

Liu, X., He, M., and Zhang, Y. (2011). A Online Capillary Method for Viscosity Measurement under High Temperature and Pressure. *J. Eng. Thermophys.* 32 (8), 1283–1285.

Liu, X., He, M. G., and Zhang, Y. (2013). Viscosity Model Based on the Free Volume Theory and the Crossover Function. *J. Eng. Thermophys.* V34 (001), 22–25.

Liu, X., Su, C., He, K., and He, M. (2014). Measurement of Isobaric Heat Capacity of Pure Water at High Temperature and High Pressure. *J. Eng. Thermophys.* 35 (5), 844–847.

Ouyang, L. B. (2011). New Correlations for Predicting the Density and Viscosity of Supercritical Carbon Dioxide under Conditions Expected in Carbon Capture and Sequestration Operations. *Open Pet. Eng. J.* 5 (1), 13–21. doi:10.2174/1874834101104010013

Quiñones-Cisneros, S. E., and Deiters, U. K. (2006). Generalization of the Friction Theory for Viscosity Modeling. *J. Phys. Chem. B* 110 (25), 12820–12834. doi:10.1021/jp0618577

Saadati Ardestani, N., Sodeifian, G., and Sajadian, S. A. (2020). Preparation of Phthalocyanine green Nano Pigment Using Supercritical CO2 Gas Antisolvent (GAS): Experimental and Modeling. *Heliyon* 6 (9), e04947. doi:10.1016/j.heliyon.2020.e04947

Sodeifian, G., Razmimanesh, F., and Sajadian, S. A.. 2019. Solubility Measurement of a Chemotherapeutic Agent (Imatinib Mesylate) in Supercritical Carbon

Dioxide: Assessment of New Empirical Model. *J. Supercrit. Fluids* 146 89–99. doi:10.1016/j.supflu.2019.01.006

Sodeifian, G., Saadati Ardestani, N., Sajadian, S. A., and Ghorbandoost, S. (2016a). Application of Supercritical Carbon Dioxide to Extract Essential Oil from Cleome Coluteoides Boiss: Experimental, Response Surface and Grey Wolf Optimization Methodology. *J. Supercrit. Fluids* 114, 55–63. doi:10.1016/j.supflu.2016.04.006

Sodeifian, G., Sajadian, S. A., and Saadati Ardestani, N. (2017). Determination of Solubility of Aprepitant (An Antiemetic Drug for Chemotherapy) in Supercritical Carbon Dioxide: Empirical and Thermodynamic Models. *J. Supercrit. Fluids* 128, 102–111. doi:10.1016/j.supflu.2017.05.019

Sodeifian, G., Sajadian, S. A., and Saadati Ardestani, N. (2016b). Optimization of Essential Oil Extraction from Launaea Acanthodes Boiss: Utilization of Supercritical Carbon Dioxide and Cosolvent. *J. Supercrit. Fluids* 116, 46–56. doi:10.1016/j.supflu.2016.05.015

Sodeifian, G., and Sajadian, S. A. (2019). Utilization of Ultrasonic-Assisted RESOLV (US-RESOLV) with Polymeric Stabilizers for Production of Amiodarone Hydrochloride Nanoparticles: Optimization of the Process Parameters. *Chem. Eng. Res. Des.* 142, 268–284. doi:10.1016/j.cherd.2018.12.020

Sodeifian, G., Sajadian, S. A., and Daneshyan, S.. 2018. Preparation of Aprepitant Nanoparticles (Efficient Drug for Coping with the Effects of Cancer Treatment) by Rapid Expansion of Supercritical Solution with Solid Cosolvent (RESS-SC). *J. Supercrit. Fluids* 140: 72–84. doi:10.1016/j.supflu.2018.06.009

Span, R., and Wagner, W. (1996). A New Equation of State for Carbon Dioxide Covering the Fluid Region from the Triple-Point Temperature to 1100 K at Pressures up to 800 MPa. *J. Phys. Chem. Reference Data* 25 (6), 1509–1596. doi:10.1063/1.555991

Span, R., and Wagner, W. (2003). Equations of State for Technical Applications. III. Results for Polar Fluids. *Int. J. Thermophys.* 24 (1), 111–162. doi:10.1023/A:1022362231796

Tao, X., and Tao, W. (2016). S-CO2 Waste Heat Recovery System. *Construction Mater. Decoration*, 226–227. doi:10.3969/j.issn.1673-0038.2016.51.149

Vesovic, V., Wakeham, W. A., Olchowy, G. A., Sengers, J. V., Watson, J. T. R., and Millat, J. (1990). The Transport Properties of Carbon Dioxide. *J. Phys. Chem. Reference Data* 19 (3), 763–808. doi:10.1063/1.555875

Wang, C. (2015). *The Design of Brayton Circle for S-CO2 PBR and Reactor Core Thermodynamic Analysis*. Harbin, China: Harbin Engineering University.

Yang, F., Liu, H., Yang, Z., and Duan, Y. (2020). Working Fluid Thermophysical Properties of the Supercritical Carbon Dioxide Cycle. *Therm. Power Generation* 49 (No.40710), 27–35. doi:10.19666/j.rlfd.202006163

Zhang, C., Jiang, J. B., and Peng, X. D. (2019). Comparison and Correction of CO2 Properties Model in Critical Region. *CIESC J.* 70 (8), 3058–3070. doi:10.11949/0438-1157.20190184

Conflict of Interest: The authors declare that the research was conducted in the absence of any commercial or financial relationships that could be construed as a potential conflict of interest.

frontiers
in Energy Research

TECHNOLOGY AND CODE
published: 02 March 2022
doi: 10.3389/fenrg.2022.823872

Research of Thermal Hydraulic Conditions Effect on PWR CIPS Risk

Shuqi Meng, Yalun Yan, Yousen Hu*, Yisong Hu and Tianming Ruan

China Nuclear Power Technology Research Institute Co., Ltd., Shenzhen, China

In order to reveal the effect of thermal hydraulic conditions on the PWR CIPS risk, the evaluation of a PWR CIPS risk in the first cycle under different core flow rates, average primary temperatures, power levels, and primary pressures was conducted by combining thermal hydraulic codes LINDEN and CRUD (Chalk River unidentified deposit) analysis software CAMPSIS. The research result illustrating the essential effect of thermal hydraulic conditions on CIPS is changing the SNB (subcooled nucleate boiling) level of the fuel assembly's surface; thus, boron precipitation and local power distribution will be affected. Theoretical evidence and statistical support of the effect of thermal hydraulic conditions on the PWR CIPS risk could be obtained *via* this research.

Keywords: PWR (pressurized water reactor), thermal hydraulic, CIPS (crud-induced power shift), boron precipitation, SNB (subcooled nucleate boiling)

Edited by:
Luteng Zhang,
Chongqing University, China

Reviewed by:
Shanshan Bu,
Chongqing University of Technology, China
Yan Xiang,
Royal Institute of Technology, Sweden

****Correspondence:***
Yousen Hu
huyousen@cgnpc.com.cn

Specialty section:
This article was submitted to
Nuclear Energy,
a section of the journal
Frontiers in Energy Research

Received: *28 November 2021*
Accepted: *17 January 2022*
Published: *02 March 2022*

Citation:
Meng S, Yan Y, Hu Y, Hu Y and Ruan T (2022) Research of Thermal Hydraulic Conditions Effect on PWR CIPS Risk. Front. Energy Res. 10:823872. doi: 10.3389/fenrg.2022.823872

INTRODUCTION

During power operation, the corrosion products in the primary circuit of the PWR (pressurized water reactor) will deposit on the fuel surface and form a CRUD (Yoo et al., 2020) (Chalk River unidentified deposit). As an additive to control reactivity, the precipitation of boric acid inside the CRUD might induce local power abnormality, which will cause a CIPS (crud-induced power shift) risk in severe circumstances (Frattini et al., 2001; Yang and Tang, 2012; Yang et al., 2020). Jiao et al. (2021) developed a deposition model which could calculate the axial CRUD thickness and solid phase distribution of fuel; Li and Lyu developed an analysis code for calculating the CRUD deposition and radioactivity level in the PWR primary loop based on the concentration difference driving principle (Li, 2017; Li et al., 2018; Lyu et al., 2020); Zou et al. (2013) developed a thermal-physical-chemical coupling CIPS analysis model; Yang and other researchers used American commercial software to evaluate CIPS risks of AP1000 and CAP1400 units during power operation (Yang and Tang, 2012; Yang et al., 2020). Zhou and Jones (2002) developed a model to simulate boron precipitation inside the CRUD and verified the model based on Callaway plant measurement data. Doncel et al. (2007) carried out a series of experiments to simulate boron precipitation inside the CRUD and revealed the influence of the effect of thermal-hydraulic and hydrochemical conditions on boron precipitation. The Global PWR operation experience shows that SNB (subcooled nucleate boiling) on the fuel surface is an important factor affecting the CIPS (Sabol et al., 1997; Deshon, 2004; Lange, 2017). Differences in PWR design parameters and operating conditions will cause different thermal hydraulic conditions, changing the overall and local SNB level of fuel assemblies, and finally impact the risk of the CIPS. Using the thermal-hydraulic analysis program LINDEN (Bai et al., 2013) and CRUD analysis software CAMPSIS (China Nuclear Power Technology Research Institute Co. and Ltd., 2021), which have been validated based on 12 operating reactors' measurement data, the first cycle's CIPS risk of a PWR unit is analyzed under different core flow rates, average temperature of the primary loop, power levels, and primary loop pressure, which provides theoretical basis and data support for systematic evaluation of the influence of thermal hydraulic conditions on the CIPS risk of PWR units.

CHEMICAL KINETIC MODEL

Deposition of Corrosion Products

PWR measurement data show that the main components of fuel CRUD are nickel (Ni), iron (Fe), and chromium (Cr) mixing spinel (Deshon, 2004; Riess, 2017). Along the axial direction of the fuel assembly, nickel oxide (NiO) usually precipitates in the SNB region, while nickel ferrite ($NiFe_2O_4$) and magnetite (Fe_3O_4) are more likely to deposit in the region where SNB does not occur (Deshon, 2005; Riess, 2017). In addition, ^{58}Co, ^{60}Co, ^{54}Mn, and other radioisotopes can be detected in the primary coolant during PWR power operation, which indicates that Co and Mn also exist in the CRUD, but their contents are relatively small compared with Ni, Fe, and Cr, which can be ignored in CIPS analysis. For Ni, Fe, and Cr, combined with the corrosion potential–pH diagrams at high temperature-high pressure and the experimental results (Tremaine and Leblanc, 1980; Frattini and Fruzzetti, 2002; Liu et al., 2011; Riess, 2017), the following chemical reactions were established to simulate the CRUD formation process on the fuel surface:

$$Fe_3O_4 + 6H^+ + H_2 \leftrightarrow 3Fe^{2+} + 4H_2O; \tag{1}$$

$$Fe_3O_4 + 3H^+ + H_2 \leftrightarrow 3FeOH^+ + H_2O; \tag{2}$$

$$Fe_3O_4 + H_2 + 2H_2O \leftrightarrow 3Fe(OH)_{2,aq}; \tag{3}$$

$$NiFe_2O_4 + 6H^+ + H_2 \leftrightarrow Ni^{2+} + 2Fe^{2+} + 4H_2O; \tag{4}$$

$$3NiFe_2O_4 + 6H^+ + H_2 \leftrightarrow 3Ni^{2+} + 2Fe_3O_4 + 4H_2O; \tag{5}$$

$$NiFe_2O_4 + 2H^+ \leftrightarrow Ni^{2+} + Fe_2O_3 + H_2O; \tag{6}$$

$$NiO + 2H^+ \leftrightarrow Ni^{2+} + H_2O; \tag{7}$$

$$NiO + H^+ \leftrightarrow NiOH^+; \tag{8}$$

$$NiO + H_2O \leftrightarrow Ni(OH)_{2,aq}; \tag{9}$$

$$Ni + 2H^+ \leftrightarrow Ni^{2+} + H_2; \tag{10}$$

$$Ni + H^+ + H_2O \leftrightarrow NiOH^+ + H_2; \tag{11}$$

$$Ni + 2H_2O \leftrightarrow Ni(OH)_{2,aq} + H_2; \tag{12}$$

$$FeCr_2O_4 + 2H^+ \leftrightarrow Fe^{2+} + Cr_2O_3 + H_2O; \tag{13}$$

$$FeCr_2O_4 + 2H_2O \leftrightarrow Fe(OH)_3^- + Cr_2O_3 + H^+; \tag{14}$$

$$FeCr_2O_4 + 6H^+ + H_2 \leftrightarrow Fe^{2+} + 2Cr^{2+} + 4H_2O. \tag{15}$$

Diffusion caused by turbulent mixing and intense precipitations caused by SNB are the main reasons for the formation of the CRUD (Kang and Sejvar, 1985). Assuming that there is a diffusion layer between the bulk coolant and fuel surface, the formation process of the CRUD could be divided into the mass transfer from the bulk coolant to diffusion layer and the diffusion layer to fuel surface (Kang and Sejvar, 1985; Lee, 1990). For fuel per unit area, assuming the mass transfer process reaches a steady state in the diffusion layer, based on the mass balance principle, following formulas could be derived:

$$w_{se,i} + w_{ms,i} - w_{s,i} = 0; \tag{16}$$

$$w_{se,i} = \dot{m}_e \cdot C_i; \tag{17}$$

$$w_{ms,i} = k_{ms,i} \cdot (C_i - C_{w,i}); \tag{18}$$

$$w_{s,i} = k_{s,i} \cdot (C_{w,i} - C_{0,i}), \tag{19}$$

where $w_{se,i}$ represents the deposition rate caused by SNB, in g/(cm^2·s); $w_{ms,i}$ and $w_{s,i}$ represents the deposition rate of the bulk coolant to diffusion layer and the diffusion layer to fuel surface, respectively, in g/(cm^2·s); $\dot{m}_e$ represents the SNB rate, calculated by LINDEN, in g/(cm^2·s); $k_{ms,i}$ and $k_{s,i}$ represent the deposition coefficients from the bulk coolant to diffusion layer and from the diffusion layer to fuel surface, respectively, which can be calculated by the Chilton–Colburn formula (Meng et al., 2021),in g/(cm^2·s); C_i and $C_{0,i}$ represent the solubility of corrosion products in the bulk coolant and fuel surface, respectively, which are fitted according to Gibbs' law and experimental data of the simulated PWR primary loop water environment (Rummery and Macdonald, 1975; Chen et al., 1983; Beverskog and Puigdomenech, 1997a; Beverskog and Puigdomenech, 1997b; Beverskog, 1997; Huang et al., 2009; Henshaw et al., 2016), in g/g; $C_{w,i}$ represents the solubility of corrosion products in the diffusion layer, in g/g; *i* corresponds to Ni, Fe, and Cr.

Combining **Eqs 16–19** and eliminating $C_{w,i}$, the deposition rate of corrosion products can be calculated by the following formula:

$$w_{s,i} = \frac{k_{s,i}\dot{m}_e}{k_{s,i} + k_{ms,i}} C_i + \frac{k_{s,i}k_{ms,i}}{k_{s,i} + k_{ms,i}} (C_i - C_{0,i}). \tag{20}$$

Boron Precipitation

A serious CIPS event occurred in the Callaway plant (Deshon, 2004), and the measurement data showed that boron precipitated in the SNB region in the form of bonaccordite (Ni_2FeBO_5) (Sawicki, 2007); Henshaw et al. (2008) developed a model for calculating the boron precipitation based on wick boiling, assuming that boron mainly precipitated in the form of lithium metaborate ($LiBO_2$); in the boron precipitation model developed by Zhou and Jones (2002), it is assumed that all boron precipitates in the form of crystal boric acid (H_3BO_3) under the action of SNB; Doncel et al. (2007) not only detected $LiBO_2$ and H_3BO_3 but also found lithium tetraborate ($Li_2B_4O_7$) in artificial CRUD. Based on the aforementioned operation experience and experimental results, the boron precipitation model in this study has been hypothesized and simplified as follows:

1) At present, only the Callaway plant detected boron precipitation in the form of Ni_2FeBO_5, and the maximum thickness of the Callaway plant CRUD exceeds 100 microns, which belongs to the PWR with a very high scale level. In addition, Ni_2FeBO_5 has stable thermodynamic properties and can only be formed under extreme conditions, so the precipitation of boron in the form of Ni_2FeBO_5 is not considered;
2) Referring to the experiment on the influence of the artificial CRUD on boric acid adsorption behavior carried out by the Electric Power Research Institute (Deshon and Frattini, 2002), it is assumed that boron precipitated in the form of H_3BO_3 depends on the physical adsorption of boric acid by the CRUD, and SNB of the coolant will significantly accelerate the physical adsorption rate. Physical adsorption is mainly driven by the concentration difference and does not involve borate-related chemical reactions;

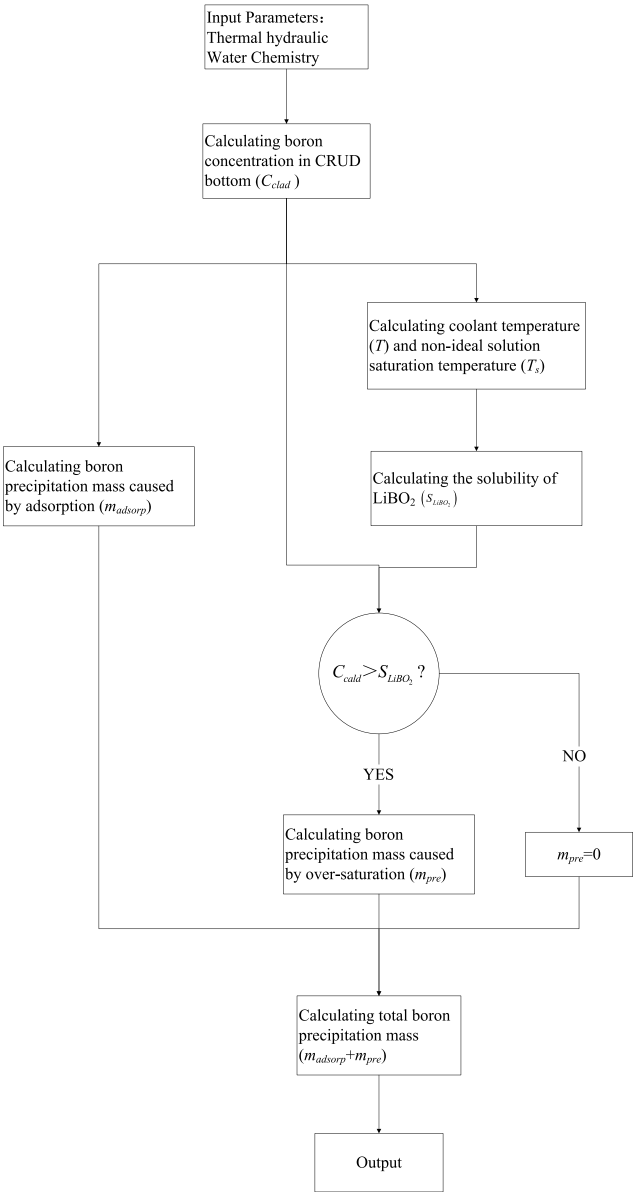

FIGURE 1 | Calculation flow of the boron precipitation model.

TABLE 1 | Criteria for CIPS risk.

Number of fuel assemblies/box	Low risk/g	Medium risk/g	High risk/g
121	90	290	570
157	110	370	740
177	130	420	830
193	140	450	910
217	150	500	1000
241	170	540	1130

Note: The level of the CIPS to low risk, medium risk, and high risk is −3%, −5%, and −10%, respectively.

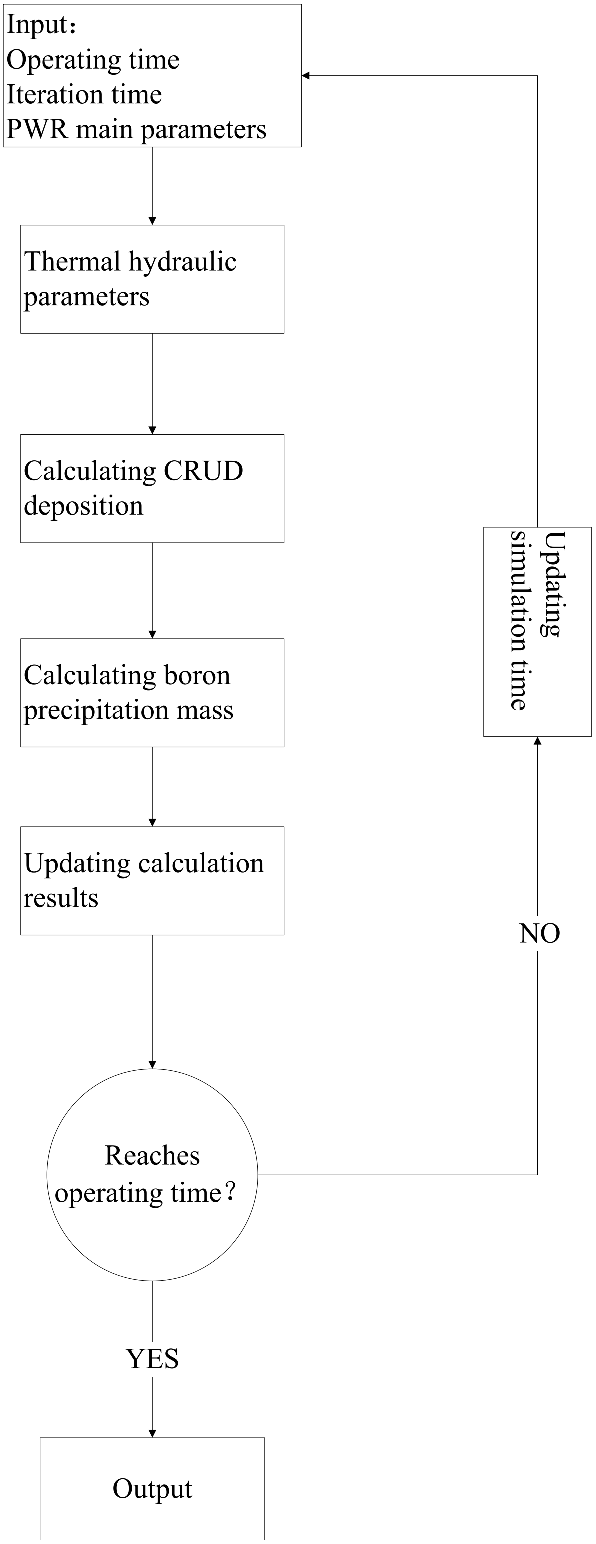

FIGURE 2 | Analysis flow of the influence of thermal hydraulic conditions on the CIPS.

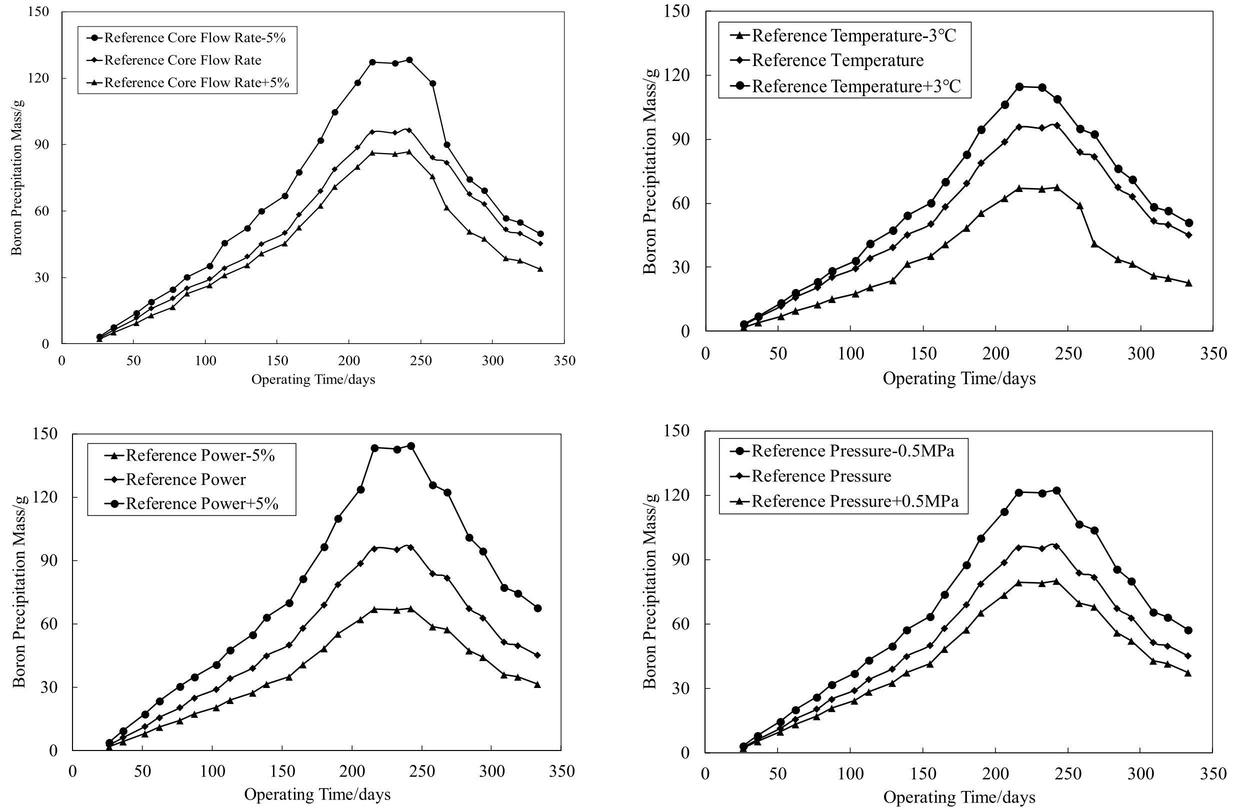

FIGURE 3 | Boron precipitation under different thermal hydraulic conditions.

3) The bottom temperature of the CRUD increases due to wick boiling, while the solubility of $LiBO_2$ decreases with the increase in temperature (Sabol et al., 1997) and precipitates after reaching the threshold. The precipitation process of $Li_2B_4O_7$ is the same as that of $LiBO_2$. According to the molar ratio of boron to lithium of these two borates, the amount of boron precipitated in $LiBO_2$ is multiplied by two, which can be used as the estimated value of boron precipitated in $Li_2B_4O_7$.

To sum up, the boron precipitation model involves two major effects: physical adsorption and borate precipitation. For the region where SNB occurs, physical adsorption always exists, while borate precipitation occurs only when the CRUD increases to a certain thickness. The calculation flow of boron precipitation is shown in **Figure 1**, and the formulas involved are as follows:

$$C_{clad} = C_{bulk} \cdot \exp\left(\frac{\dot{m}_e \delta_c}{\rho_s D \varepsilon}\right); \tag{21}$$

$$m_{adsorp} = aC_{clad}^2 + b; \tag{22}$$

$$S_{LiBO_2} = 5 \times 10^{-6} + T^2 - 6.02 \times 10^{-2} \times T + 1.5889; \tag{23}$$

$$T \approx T_s + \frac{0.4qk_c^{1.5}\varepsilon^{1.5}}{\sqrt{r_c N_c h_e}}; \tag{24}$$

$$m_{pre} = \frac{3M_B \varepsilon}{M_{LiBO_2}} \rho_{LiBO_2} \left(\delta_c - \delta_p\right), \tag{25}$$

where C_{clad} and C_{bulk} represent the boron concentration in the CRUD bottom and bulk coolant, respectively, in mol/kg; δ_c and δ_p represent CRUD thickness and the CRUD thickness threshold which can reach boron precipitation, respectively, in cm; ρ_s represents the coolant saturation density, in g/cm^3; D represents the diffusion rate of boron in the CRUD, which can be calculated according to the Stokes–Einstein equation, in cm^2/s; ε represents porosity, dimensionless number; m_{adsorp} represents the adsorption amount of boron per unit mass of the CRUD, in g/g; a and b are physical adsorption curve coefficients, which are fitted according to experimental points (Deshon and Frattini, 2002); S_{LiBO_2} represents the solubility of $LiBO_2$ (Sabol et al., 1997; Frattini et al., 2001), in mol/kg; T and T_s represent the coolant temperature and non-ideal solution saturation temperature (Henshaw et al., 2008), respectively, in °C; q represents power density which could be calculated by LINDEN, in W/m^2; h_e represents the boiling heat transfer coefficient, in W/(m^2·k); k_c represents the coefficient of thermal conductivity, in W/(m·k); r_c represents the radius of the steam channel, in cm; N_c represents the steam channel density, in 1/cm^2; m_{pre} represents the amount of boron precipitated in per unit area of the fuel surface, in g/cm^2; M_B and M_{LiBO_2} represent the molar mass of boron and $LiBO_2$, respectively, in g/mol; ρ_{LiBO2} represents the density of $LiBO_2$, in g/cm^3.

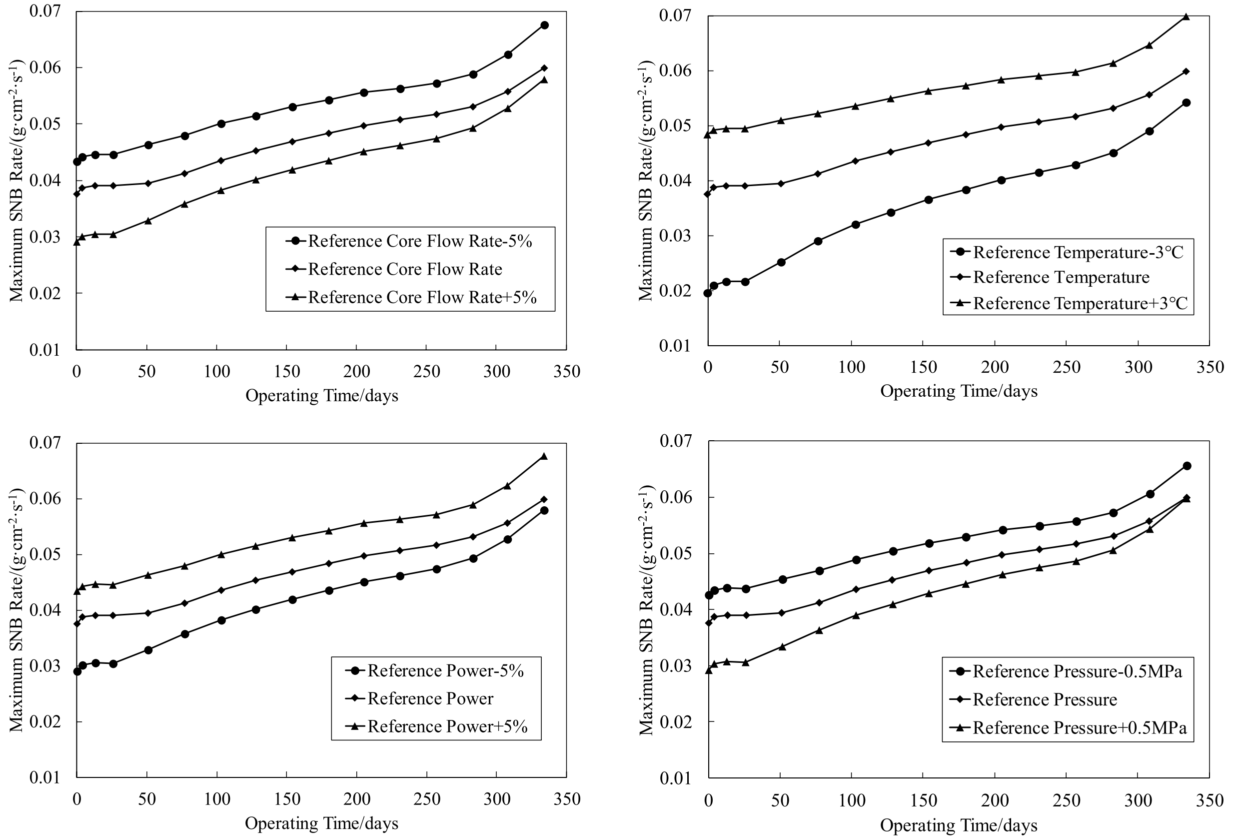

FIGURE 4 | Maximum SNB rate under different thermal hydraulic conditions.

EFFECT OF THERMAL HYDRAULIC CONDITIONS ON THE CIPS

CIPS Risk Criteria

According to the PWR operation data of the CIPS and the software developed by American research institutions, the total amount of boron precipitation is selected as the CIPS risk judgment standard (Yang and Tang, 2012; Yang et al., 2020; Lange, 2017), as shown in **Table 1**. Some researchers believe that the CIPS is a phenomenon caused by the local increase of boron precipitation mass of fuel assemblies. It is necessary to simulate the local CRUD behavior of fuel assemblies in more detail (Haq et al., 2011; Hu et al., 2019) and calculate the power offset degree of fuel assemblies by coupling nuclear physics calculation codes to accurately predict the CIPS risk of the PWR. However, **Table 1** is still the most widely accepted CIPS risk criteria.

Thermal Hydraulic Sensitivity Analysis Results

The CRUD analysis software CAMPSIS realizes the function of the chemical kinetic model (China Nuclear Power Technology Research Institute Co. and Ltd., 2021). Based on the whole core flow field and temperature field distribution input by the thermal hydraulic analysis code LINDEN, the CIPS risk assessment is carried out for the first cycle of a PWR (the core assembly number is 157 boxes) under different core flow rates, average temperature of the primary circuit, power levels, and primary circuit pressure. The process is shown in **Figure 2**. The total amount of boron deposition in the first cycle of a PWR under different thermal and hydraulic conditions is obtained by reasonably disturbing the upper and lower intervals of the benchmark thermal hydraulic parameters, as shown in **Figure 3**. The variation trend of SNB corresponding to each condition is shown in **Figures 4**, **5**, in which the maximum SNB rate indicates the SNB situation of the hottest fuel assembly, while the total mass evaporation rate reflects the intensity of SNB in the whole core. The analysis results show that

1) By reducing the reference core flow rate (Deshon, 2004) (82800 m^3/h) by 5%, the maximum boron precipitation increases from 96 to 128 g, and the CIPS risk level elevates from a low risk to medium risk. Accordingly, the maximum SNB rate and total mass evaporation rate increase by 12.97 and 74.61%, respectively. On the contrary, with the increase of 5% reference core flow rate, the maximum boron precipitation decreases from 96 to 87 g, and the maximum SNB rate and total mass evaporation rate decrease by 3.32 and 43.79%, respectively;

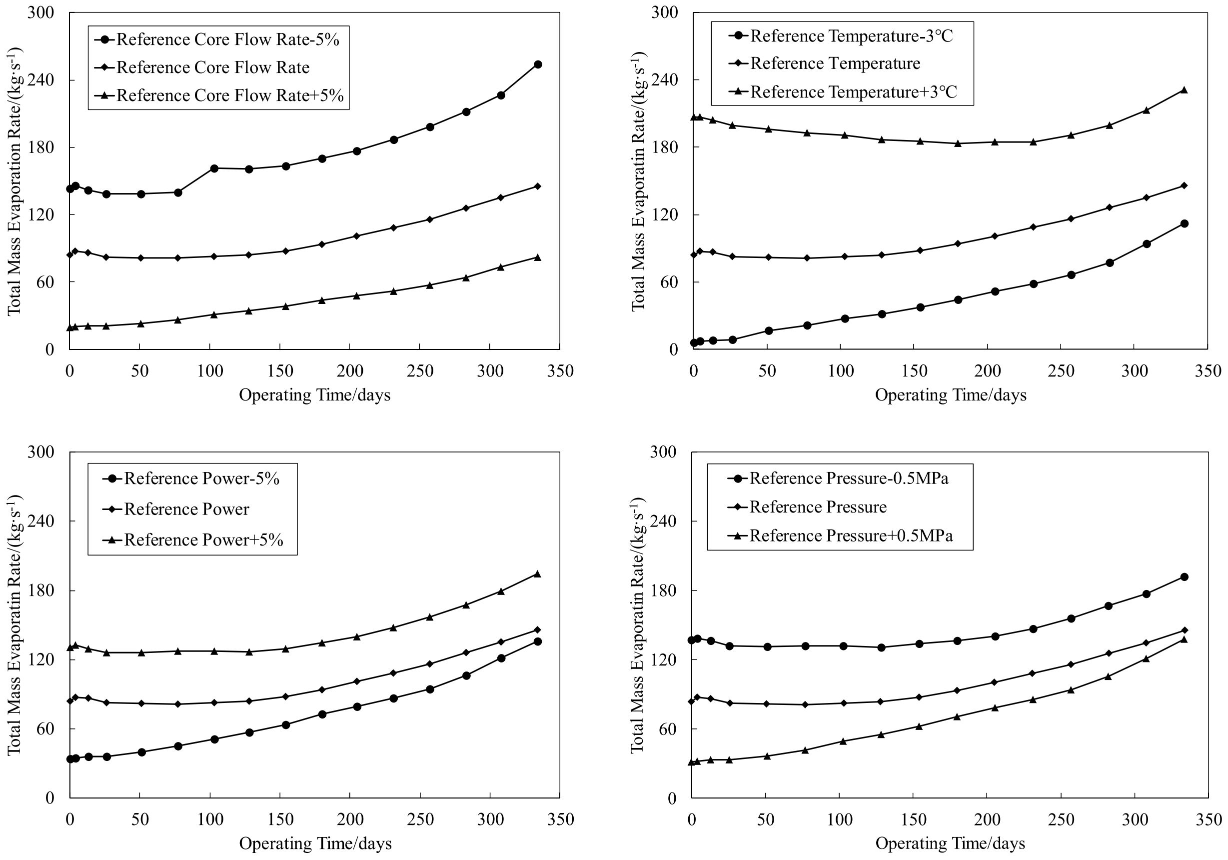

FIGURE 5 | Total steam production rate of core under different thermal hydraulic conditions.

2) By increasing the reference temperature (Deshon, 2004) (293.06°C) by 3°C, the maximum boron precipitation increases from 96 to 115 g, and the CIPS risk level elevates from a low risk to medium risk. Accordingly, the maximum SNB rate and total mass evaporation rate increase by 16.60 and 58.72%, respectively. On the contrary, with the decrease of 3°C reference temperature, the maximum boron precipitation decreases from 96 to 68 g, and the maximum SNB rate and total mass evaporation rate decrease by 9.27 and 23.24%, respectively;
3) By increasing the reference power (Deshon, 2004) (3411 MW) by 2%, the maximum boron precipitation increases from 96 to 145 g, and the CIPS risk level elevates from a low risk to medium risk. Accordingly, the maximum SNB rate and total mass evaporation rate increase by 12.97 and 33.39%, respectively. On the contrary, with the decrease of 2% reference power, the maximum boron precipitation decreases from 96 to 68 g, and the maximum SNB rate and total mass evaporation rate decrease by 3.32 and 33.39%, respectively;
4) By reducing the reference pressure (Deshon, 2004) (15.50 MPa) by 0.5 MPa, the maximum boron precipitation increases from 96 to 122 g, and the CIPS risk level elevates from a low risk to medium risk. Accordingly, the maximum SNB rate and total mass evaporation rate increase by 9.63 and 31.85%, respectively. On the contrary, with the increase of 0.5 MPa reference pressure, the maximum boron precipitation decreases from 96 to 80 g, and the maximum SNB rate and total mass evaporation rate decrease by 0.28 and 5.06%, respectively.

To sum up, the intensity of SNB changes with different thermal hydraulic conditions, which affects the axial CRUD distribution of fuel assemblies and finally leads to the difference of boron precipitation; thus, the risk of the CIPS changes accordingly. Thermal hydraulic conditions are developing in the direction of intensifying SNB, and the risk of the CIPS is increasing, which is consistent with the international PWR operation experience (Sabol et al., 1997; Deshon, 2004; Lange, 2017), further proving the importance of SNB's influence on the CIPS.

CONCLUSION

The CIPS risk of a PWR first cycle under different thermal hydraulic conditions is analyzed by using LINDEN and CAMPSIS, based on the international common CIPS risk criteria. The conclusions are as follows:

1) CIPS is a special phenomenon which combines thermodynamic hydraulics and chemical kinetics;
2) The change in thermal hydraulic conditions finally reflects the influence on the intensity of SNB of fuel assemblies;
3) The degree of SNB is an important factor affecting the CIPS. The more severe SNB is, the more boron precipitates in the fuel assembly, and the risk of the CIPS increases accordingly.
4) The risk of the CIPS in the PWR can be reduced by controlling material corrosion (reducing the total amount of the CRUD), adjusting the chemical parameters of the primary circuit (changing the solubility of corrosion products), and updating fuel management strategies (inhibiting the severity of SNB).

The research methods and analysis results in this study can be used in many PWR reactor types, but the wider applicability, the difference between predicted values and actual PWR operating conditions, and how to accurately carry out the CIPS risk assessment of a continuous cycle still need further demonstration.

DATA AVAILABILITY STATEMENT

The original contributions presented in the study are included in the article/Supplementary Material; further inquiries can be directed to the corresponding author.

AUTHOR CONTRIBUTIONS

MS developed the thermal-hydraulic and chemistry model. YY developed the boron precipitation model. HYo tested the thermal-hydraulic model. HYi performed coding and testing models. RT performed coding and testing models.

FUNDING

The study was supported by National Natural Science Foundation of China(U20B2011). A part of this study was also supported by the China Nuclear Power Technology Research Institute Co.,Ltd.

REFERENCES

Bai, N., Zhu, Y., and Ren, Z. (2013). Development and Verification of Subchannel Analysis Code LINDEN[J]. *At. Energ. Sci. Technology.* 47 (ZL), 299–301. doi:10.7538/yzk.2013.47.S0.0299 (in Chinese).

Beverskog, B. (1997). Puigdomenech, Revised Pourbaix Diagrams for Iron at 25-300°C[J]. *Corrosion Sci.* 38 (12), 2121–2135. doi:10.1016/s0010-938x(9600067-4)

Beverskog, B., and Puigdomenech, I. (1997a). Revised Pourbaix Diagrams for Chromium at 25-300 °C. *Corrosion Sci.* 39 (1), 43–57. doi:10.1016/s0010-938x(97)89244-x

Beverskog, B., and Puigdomenech, I. (1997b). Revised Pourbaix Diagrams for Nickel at 25-300 °C. *Corrosion Sci.* 39 (5), 969–980. doi:10.1016/s0010-938x(97)00002-4

Chen, C. M., Aral, K., and Theus, G. J. (1983). Computer-calculated Potential pH Diagrams to 300°C[R]. EPRI Technical Report. California. EPRI-NP-3137-Vol.3.

China Nuclear Power Technology Research Institute Co., Ltd. (2021). *China General Nuclear Power Group Co., Ltd., China General Nuclear Power Co.* China: Ltd. CRUD behavior analysis software [CAMPSIS] V1.0 [CP]. 2021SR0623899(in Chinese).

Deshon, J., and Frattini, P. (2002). *Adsorption of Boric Acid on Synthetic Fuel Crud oxides[R]*. California: EPRI Technical Report. 1003384.

Deshon, J. (2004). *PWR Axial Offset Anomaly (AOA) guidelines[R]*. California: EPRI Technical Report. 1008102.

Deshon, J. (2005). *Modeling PWR Fuel Corrosion Product Deposition and Growth process[R]*. California: EPRI Technical Report. 1011743.

Doncel, N., Chen, J. X., and Deshon, J. (2007). Water Chemistry Influence on AOA, Phase 3 of the Spanish experiment at STUDSVIK[C]. in Proceedings of the 2007 International LWR Fuel Performance Meeting. San Francisco, USA

Frattini, P., and Fruzzetti, K. (2002). *Impact of Nickel Oxide Solubility on Pressurized Water Reactor Fuel deposit chemistry[R]*. California: EPRI Technical Report. 1003155.

Frattini, P. L., Blok, J., Chauffriat, S., Sawicki, J., and Riddle, J. (2001). Axial Offset Anomaly: Coupling PWR Primary Chemistry with Core Design. *Nucl. Energ.* 40 (2), 123–135. doi:10.1680/nuen.40.2.123.39952

Haq, I. u., Cinosi, N., Bluck, M., Hewitt, G., and Walker, S. (2011). Modelling Heat Transfer and Dissolved Species Concentrations within PWR Crud. *Nucl. Eng. Des.* 241, 155–162. doi:10.1016/j.nucengdes.2010.10.018

Henshaw, J., Gibson, C., and McGURK, J. C. (2016). *Zinc Chemistry in PWR Fuel crud[C]*. Brighton, United Kingdom: Nuclear Plant Chemistry Conference.

Henshaw, J., Mcgurk, J. C., and Sims, H. E. (2008). A Model of Chemistry and thermal Hydraulics in PWR Fuel Crud Deposits[J]. *J. Nucl. Mater.* 353 (1-2), 1–11. doi:10.1016/j.jnucmat.2005.01.028

Hu, H., Weibel, J. A., and Garimella, S. V. (2019). A Coupled Wicking and Evaporation Model for Prediction of Pool Boiling Critical Heat Flux on Structured Surfaces. *Int. J. Heat Mass Transfer.* 136, 373–382. doi:10.1016/j.ijheatmasstransfer.2019.03.005

Huang, J., Wu, X., and Han, E.-H. (2009). Influence of pH on Electrochemical Properties of Passive Films Formed on Alloy 690 in High Temperature Aqueous Environments. *Corrosion Sci.* 51 (12), 2976–2982. doi:10.1016/j.corsci.2009.08.002

Jiao, C., Han, X., and Hou, H. (2021). Model Development of the Deposition Process of Chalk Rivers Unidentified deposit on the Fuel Cladding Surface of PWR[J]. *J. Harbin Eng. Univ.* 42 (6), 915–920. doi:10.11990/jheu.202008053 (in Chinese).

Kang, S., and Sejvar, J. (1985). *The CORA-II Model of PWR Corrosion-Product transport[R]*. California: EPRI Technical Report. EPRI-NP-4246.

Lange, T. L. (2017). *Methodology for an Advanced Risk Assessment of Crud Induced Power Shift Using Coupled Multi-Physics Simulations and a Monte Carlo Scenario Analysis of the Potential Financial benefits[D]*. USA: The University of Tennessee.

Lee, C. B. (1990). *Modeling of Corrosion Product Transport in PWR Primary coolant[D]*. USA: Massachusetts Institute of Technology.

Liu, X., Wu, X., and Han, E.-H. (2011). Influence of Zn Injection on Characteristics of Oxide Film on 304 Stainless Steel in Borated and Lithiated High Temperature Water. *Corrosion Sci.* 53 (10), 3337–3345. doi:10.1016/j.corsci.2011.06.011

Li, L. (2017). *Study on Activation and Migration Model of Corrosion Products in the Main Loop of Water-Cooled Reactor [D]*. Beijing: North China Electric Power University. (in Chinese).

Li, L., Zhang, J., and Zhang, J. (2018). Analysis of the Activated Corrosion Products and Dose Rate in a Typical PWR under Operation Condition[J]. *Nucl. Sci. Eng.* 38 (4), 540–545. (in Chinese).

Lyu, W., Chen, M., and Huang, Q. (2020). Development of Calculation Code CPAP for Radioactive Activation Product of Pressurized Water Reactor Nuclear Power Plant[J]. *Nucl. Tech.* 43 (4), 25–32. doi:10.11889/j.0253-3219.2020.hjs.43.040005 (in Chinese).

Meng, S., Hu, Y., and Li, C. (2021). A CIPS Risk Evaluation Methodology Applicable for PWR[J]. *Nucl. Tech.* 44 (09), 86–91. doi:10.11889/j.0253-3219.2021.hjs.44.090601 (in Chinese).

Riess, R. (2017). Chemistry Experience in the Primary Heat Transport Circuits of Kraftwerk Union Pressurized Water Reactors. *Nucl. Technology.* 29 (2), 153–159. doi:10.13182/nt76-a31574

Rummery, T. E., and Macdonald, D. D. (1975). Prediction of Corrosion Product Stability in High-Temperature Aqueous Systems. *J. Nucl. Mater.* 55 (1), 23–32. doi:10.1016/0022-3115(75)90134-8

Sabol, G. P., Secker, J. R., and Kormuth, J. (1997). *Root Cause Investigation of Axial Power Offset anomaly[R]*. California: EPRI Technical Report. TR-108320.

Sawicki, J. A. (2007). Evidence of Ni2FeBO5 and M-ZrO2 Precipitation in Fuel Rod Deposits in AOA-Affected High Boiling Duty PWR Core[J]. *J. Nucl. Mater.* 374, 248–269. doi:10.1016/j.jnucmat.2007.08.04

Tremaine, P. R., and Leblanc, J. C. (1980). The Solubility of Magnetite and the Hydrolysis and Oxidation of Fe2+ in Water to 300°C. *J. Solution Chem.* 9 (6), 415–442. doi:10.1007/bf00645517

Yang, J., Qin, H., and Liu, C. (2020). Research on the CIPS Effection of Using Enriched 10 B boron Acid in PWR Primary Coolant System[J]. *Nucl. Sci. Eng.* 40 (6), 932–936. (in Chinese).

Yang, P., and Tang, C. (2012). CIPS Risk Analysis for AP1000 PWR First Cycle. *Nucl. Sci. Eng.* 32 (3), 284–288. doi:10.3969/j.issn.0258-0918.2012.03.017 (in Chinese).

Yoo, J., Lee, S. W., and Park, Y. J. (2020). *Implementation of the Crud Layer Model into the Space code[C]*. South Korea: Transactions of the Korean Nuclear Society Virtual Spring Meeting.

Zhou, D., and Jones, B. G. J. (2002). Boron Concentration Model and Effects of boron Holdup on Axial Offset Anomaly (AOA) in PWRs[C]. in Proceedings of ICONE10 10th International Conference on Nuclear Engineering. Arlington, USA

Zou, L., Zhang, H., Gehin, J., and Kochunas, B. (2013). Coupled Thermal-Hydraulic/Neutronics/Crud Framework in Prediction of Crud-Induced Power Shift Phenomenon. *Nucl. Technology.* 183 (3), 535–542. doi:10.13182/nt13-a19440

Conflict of Interest: Authors MS, YY, HYo, HYi, and RT were employed by the company China Nuclear Power Technology Research Institute Co., Ltd.

frontiers
in Energy Research

ORIGINAL RESEARCH
published: 14 March 2022
doi: 10.3389/fenrg.2022.843237

Dynamic Characteristic Study of Supercritical CO_2 Recompression Brayton Cycle System

Qinghui Zhu[1], Ruiyan Han[1], Siyuan Yang[2], Bo Zhang[1] and Zhuqiang Yang[1]*

[1]Key Laboratory of Complex Energy Conversion and Utilization, School of Energy and Power Engineering, Dalian University of Technology, Dalian, China, [2]Key Laboratory of Thermo-Fluid Science and Engineering of Ministry of Education, School of Energy and Power Engineering, Xi'an Jiaotong University, Xi'an, China

The supercritical carbon dioxide (SCO_2) Brayton cycle has been regarded as the main development direction of future nuclear power generation by more and more scholars, due to its high environmental efficiency and high thermoelectric conversion rate. However, due to fluctuations in the operation of the primary loop of the system with nuclear energy, parameters such as the power of the heat source and the mass flow of the working medium in the system will change, which will affect the dynamic performance and operation of the SCO_2 Brayton cycle system. Therefore, it is necessary to study the dynamic response of the system performance under disturbance conditions, analyze the operating characteristics of the SCO_2 Brayton cycle system. In this paper, a comprehensive dynamic model of SCO_2 recompression Brayton cycle, which analyzes the response curves of critical parameters under the disturbance of heat source heating power and system mass flow rate, is accurately developed based on Simulink software. In order to verify the validity of the proposed model, the simulation results are compared with the experimental results conducted by Sandia Laboratory under the same conditions. The results show that the model has high accuracy, and can reflect the dynamic response of system performance under parameter perturbation. In this paper, the closed-loop simulation is innovatively performed to show the dynamic response to step-change in the heat source power and mass flow rate. And the thermal efficiency is about 31.85%, when the system operates stably at the design point of working condition. If a disturbance is applied to the system, the temperature change will be mainly concentrated near the heat source of the cycle, and the change near the precooler will be relatively small. The change of the heat source power will lead to a large monotonic variation of cycle efficiency. By contrast, an inflection point in cycle efficiency will be resulted in by changing the system mass flow rate. The results of this paper would provide good approaches for the design, control, and improvement of the SCO_2 Brayton cycle.

Keywords: supercritical carbon dioxide, recompression brayton cycle, dynamic model, system simulation, matlab/simulink

Edited by:
Jun Wang,
University of Wisconsin-Madison,
United States

Reviewed by:
Fubin Yang,
Beijing University of Technology,
China
Chenglong Wang,
Xi'an Jiaotong University, China

Correspondence:
Bo Zhang
zhangbo@dlut.edu.cn

Specialty section:
This article was submitted to
Nuclear Energy,
a section of the journal
Frontiers in Energy Research

Received: *25 December 2021*
Accepted: *31 January 2022*
Published: *14 March 2022*

Citation:
Zhu Q, Han R, Yang S, Zhang B and Yang Z (2022) Dynamic Characteristic Study of Supercritical CO_2 Recompression Brayton Cycle System.
Front. Energy Res. 10:843237.
doi: 10.3389/fenrg.2022.843237

INTRODUCTION

Nowadays, energy shortage and environmental degradation have recently attracted more and more concern. Improving the energy utilization efficiency of thermal power generation systems has become an inevitable choice to achieve sustainable development of energy (Sarkar, 2015). As a promising alternative power block, the SCO_2 Brayton cycle has been regarded as the main development direction of future power generation by more and more scholars due to its high environmental efficiency and high thermoelectric conversion rate (Dostal et al., 2002; Dostal et al., 2017; Ma et al., 2017; MonjurulEhsan et al., 2018). During the whole cycle, CO_2 remains in a supercritical state. This recyclable heat source has a wide temperature range and high efficiency, and is suitable for solar energy, nuclear energy, distributed energy, Marine power, fuel cell, and other fields, and is considered to be one of the most promising energy conversion systems at present (Viswanathan et al., 2006; Moisseytsev and Sienicki, 2009; Jokar et al., 2017; Milani et al., 2017; Cao et al., 2018).

Among the six recommended reactor types of the fourth-generation nuclear energy system, except for supercritical water reactor, the energy conversion of the other reactor types can use the Brayton cycle, among which sodium-cooled fast reactor and lead cooled fast reactor are recommended to use CO_2 as the working medium (Ahn and Lee, 2014; Crespi et al., 2017; Park et al., 2018). CO_2 has good stability and nuclear physical properties, and behaves as an inert gas in the temperature range of reactor core coolant. It is easy to reach the supercritical state due to its moderate critical pressure (7.38 MPa) and low critical temperature (30.98°C) (Span and Wagner, 1996). Besides, it is abundant, cheap, and easy to obtain. The compressor operation point is set in the high-density area near the pseudo-critical area, and the reactor operation point is set in the low-density area after the pseudo-critical temperature, so as to greatly reduce the consumption of small compression work, thus improving the circulation efficiency (Neises and Turchi, 2014; Ahn et al., 2015). SCO_2 has a high density, no phase change, good heat transfer performance, and low viscosity within the range of nuclear reactor operating parameters. The advantages of SCO_2 can reduce the volume of compressor, turbine and other components (Lv et al., 2018), make the equipment structure compact, reduce the occupied space, and reduce the construction cost and time of nuclear power plant.

Many studies have been conducted on the performance of SCO_2 power generation Brayton cycles. Sandia National Laboratory (Pasch et al., 2012) and the U.S. Department of Energy Office of Nuclear Energy have jointly developed the 780 kW SCO_2 Brayton cycle power system, which is one of the earliest S-CO_2 power generation Brayton cycle systems in operation in the world. The main components include two turbo-generator compressors and associated motors and controllers, three printed circuit heat exchangers, six shell, and tube heaters and associated controllers. Under the conditions of turbine inlet temperature of 811 K, compressor exhaust pressure of 13.8 MPa and rotational speed of 75,000 rpm, the expected circulating efficiency is 32%. Argonne National Key Laboratory of the United States (Chang and Grandy, 2008; Moisseytsev and Sienicki, 2009; Anderson et al., 2015) chose the pool layout as the basis of the design to study the layout form of the SCO_2 Brayton cycle in the 250 MW sodium-cooled fast reactor. Massachusetts Institute of Technology (MIT) (Sinicki et al., 2007) systematically investigated four different CO_2 cycle configurations, including intercooling, reheating, recompression, and precompression cycles. And the recompression cycle was found to yield the highest efficiency while still maintaining simplicity. The Korea Atomic Energy Laboratory (Seong and Kim, 2012; Seong, 2014) designed the Kalimer-600 Sodium Cooled Fast Reactor and established a simplified model to analyze the thermodynamic performance of Kalimer-600 coupled with the SCO_2 Brayton cycle. The maximum thermal efficiency of the optimized sodium cooling SCO_2 cycle arrangement is 42.8%. Xi'an Thermal Power Research Institute Co., Ltd(Huang et al., 2020; Su et al., 2020) has completed and put into operation the first 5 MW SCO_2 cycle power generation test unit in the world. The unit is currently the largest one in the world, which is of great significance for further improving the efficiency and flexibility of energy utilization and accelerating the construction of the power system with new energy as the main body.

Some layouts have been investigated in the literature for the dynamic characteristic study of supercritical/*trans*-critical CO_2 power cycle. Minh (Luu et al., 2017) proposed and analyzed a start-up scheme of the solar-assisted recompression SCO_2 Brayton cycle from cold start to full load operation, and established a comprehensive dynamic model of the whole solar energy integration process. Carleton University (Richard Dupuis and Henry, 2018) built a 250 kW SCO_2 simple regeneration Brayton cycle power plant and developed a dynamic model of the power plant in a Matlab/Simulink environment. The purpose of the dynamic model is to simulate the operating point under high-pressure conditions as well as the potential equipment failure mode and its control strategy. Rui Wang (Wang et al., 2020) proposed a dynamic model of a CO_2 mixture *trans*-critical power cycle (CMTPC) system and verified it with experimental data. Olumayegun (Olumayegun and Wang, 2019) established a dynamic model in Matlab/Simulink to evaluate the dynamic performance and control of the waste heat recovery SCO_2 power cycle in the cement industry.

Based on the analysis of the above literature, most studies on SCO_2 Brayton cycle systems focus on evaluating performance through energy analysis, design parameter optimization, system configuration, and economic analysis under constant heat source conditions. The existing research lacks the dynamic characteristics of SCO_2 recompression Brayton cycle with nuclear energy as heat source. However, due to fluctuations in the operation of the primary loop of the system, parameters such as the power of the heat source and the mass flow of the working medium in the system will change, which will affect the dynamic performance and operation of the SCO_2 Brayton cycle system. Therefore, it is necessary to study the dynamic response of the system performance under disturbance conditions and analyze the operating characteristics of the SCO_2 Brayton cycle system.

Meanwhile, the open-loop simulation is used in most of the papers, but the system input of open-loop simulation is fixed. There is a lack of feedback in the system so that the dynamic

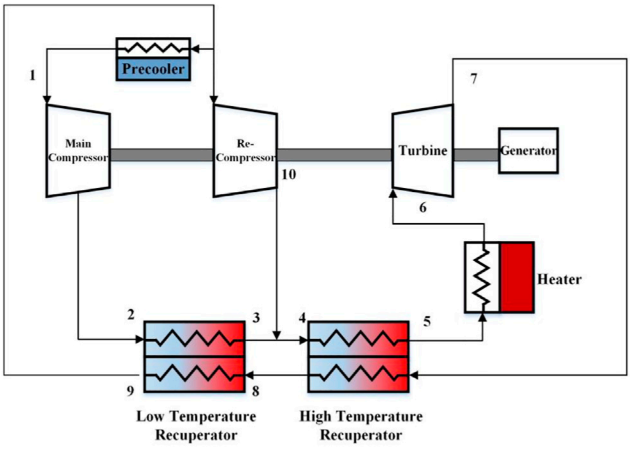

FIGURE 1 | SCO$_2$ recompression Brayton cycle system.

calculation results are distorted in a long time range. In this paper, the dynamic numerical model of the SCO$_2$ recompression Brayton cycle is established on Matlab/Simulink platform. The thermophysical properties of SCO$_2$ fluid come from the REFPROP physical property library established by the National Institute of Standards and Technology (NIST). The system will be performed closed-loop simulations and applied perturbations at specific locations such as heater and mass flow rate. Then the effects on major SCO$_2$ Brayton cycle parameters and individual system components will be examined. Due to the lack of public experimental data experimental data of the SCO$_2$ Brayton cycle, the simulation calculation research will lay the foundation for the corresponding unit control strategy and the engineering application of the SCO$_2$ cycle system.

NUMERICAL MODEL

General Description

SCO$_2$ Brayton cycle power generation system is a closed Brayton cycle. Due to the physical characteristics of SCO$_2$, the exhaust temperature of the turbine is very high in the closed Brayton cycle. In order to improve the cycle efficiency, the hyperthermal turbine exhaust is often used to preheat the new working medium. In the recuperator, the pressure of working medium on the cold side is high, and its inlet temperature is close to the quasi-critical temperature point, so its isobaric specific heat is high and its heat absorption capacity is strong. The working medium pressure in the hot-side is low, and its temperature is far from the pseudo-critical temperature point, and its isobaric specific heat is low. Therefore, in the simple SCO$_2$ Brayton cycle, the temperature of the fluid on the cold-side of the recuperator is significantly lower than the temperature of the fluid on the hot side, which means that the regenerative heat does not preheat the new working medium at the heat source to a high temperature as possible. As a result, the heat absorption at the heat source is still large. Compared with the simple SCO$_2$ Brayton cycle, the SCO$_2$ recompression Brayton cycle system subtly reduces heat loss and improves efficiency. When the turbine inlet temperature is 500 °C, a comparative study is conducted on the different configurations of the SCO$_2$ cycle system, and the conclusion is drawn that the SCO$_2$ recompression Brayton cycle has the highest efficiency applicable to the new generation of nuclear energy (Liu et al., 2019).

Figure 1 shows the recompression SCO$_2$ dynamic circulation system. It is mainly composed of a main compressor, recompressor, low temperature recuperator, high temperature recuperator, heater, turbine, precooler, and so on. The low-temperature and low-pressure fluid are compressed by the main compressor (point1), then enters the low-temperature side of the low-temperature recuperator (point2) to be gradually heated, and merges with the fluid which comes from the recompressor (point3). After that, the fluid flows through the low-temperature side of the high-temperature recuperator (ponit4,point5), is heated by the heat source, and directly enters the turbine (point6) to perform work. The exhaust gas after the work is cooled by the high-temperature recuperator (point7) and low-temperature recuperator (point8), then split (point9). Part of the working medium enters the precooler for cooling, and then enters the main compressor (point1), while the other part enters the recompressor for compression and boost (point10). The two parts converge at the cold-side inlet of the high temperature recuperator to form a closed loop.

Turbomachinery Model

The turbomachinery models for the turbine, main compressor, and recompressor were designed by using the thermodynamic equations of turbomachinery. But the rapid change of CO$_2$ near the critical point makes the simulation of compressors challenging. Therefore, turbine performance curves are used in the model to accurately predict turbomachinery performance. This paper refers to compressor and turbine performance curves from Sandia Laboratories (Pasch et al., 2012).

The input parameters of the compressor include inlet pressure, inlet temperature, flow rate and rotational speed. If the isentropic efficiency of the compressor is constant, the entropy value and enthalpy value of the inlet and outlet fluid of the compressor can be calculated as follows:

$$S_{\text{out,comp}} = S_{\text{in,comp}} = S\left(P_{\text{in,comp}}, T_{\text{in,comp}}\right) \tag{1}$$

$$h_{\text{in,comp}} = h\left(P_{\text{in,comp}}, T_{\text{in,comp}}\right) \tag{2}$$

According to the performance curve of the compressor, the enthalpy rise of the flow through the compressor and the isentropic efficiency of the compressor are calculated as follows:

$$\Delta h_{comp} = f_{chart}\left(N, m\right) \tag{3}$$

$$\eta_{comp} = f_{chart}\left(N, m\right) \tag{4}$$

The actual enthalpy value at the compressor outlet is calculated according to the isentropic efficiency as follows:

$$h_{\text{out,comp}} = h_{\text{in,comp}} + \frac{h_{\text{out,is,comp}} - h_{\text{in,comp}}}{\eta_{\text{comp}}} \tag{5}$$

Then the pressure and temperature of the compressor outlet fluid are calculated as follows:

$$P_{\mathrm{out,comp}} = P\left(h_{\mathrm{out,is,comp}}, S_{\mathrm{out,c}}\right) \tag{6}$$

$$T_{\mathrm{out,c}} = T\left(h_{\mathrm{out,is,c}}, S_{\mathrm{out,c}}\right) \tag{7}$$

Compressor power consumption is:

$$W_{\mathrm{comp}} = m \cdot \left(h_{\mathrm{out,comp}} - h_{\mathrm{in,comp}}\right) \tag{8}$$

Similarly, if the isentropic efficiency is constant, the entropy value and enthalpy value of the inlet and outlet fluid of the turbine are calculated as follows:

$$S_{\mathrm{out,turb}} = S_{\mathrm{in,turb}} = S\left(P_{\mathrm{in,turb}}, T_{\mathrm{in,turb}}\right) \tag{9}$$

$$h_{\mathrm{in,turb}} = h\left(P_{\mathrm{in,turb}}, T_{\mathrm{in,turb}}\right) \tag{10}$$

According to the turbine performance curve, the enthalpy drop and isentropic efficiency of the fluid flowing through the turbine are calculated as follows:

$$\Delta h_{\mathrm{turb}} = f_{\mathrm{char}t}\left(N, m\right) \tag{11}$$

$$\eta_{\mathrm{t}} = f_{\mathrm{chart}}\left(N, m\right) \tag{12}$$

The actual enthalpy value of turbine outlet is calculated according to isentropic efficiency as follows:

$$h_{\mathrm{out,turb}} = h_{\mathrm{in,turb}} - \eta_{\mathrm{turb}} \cdot \left(h_{\mathrm{in,turb}} - h_{\mathrm{out,is,turb}}\right) \tag{13}$$

Then the pressure and temperature of the fluid at the turbine outlet are calculated as follows:

$$P_{\mathrm{out,turb}} = P\left(h_{\mathrm{out,is,turb}}, S_{\mathrm{out,turb}}\right) \tag{14}$$

$$T_{\mathrm{out,turb}} = T\left(h_{\mathrm{out,is,turb}}, S_{\mathrm{out,turb}}\right) \tag{15}$$

The work done by the turbine:

$$W_{\mathrm{turb}} = m \cdot \left(h_{\mathrm{out,turb}} - h_{\mathrm{in,turb}}\right) \tag{16}$$

Recuperators and Precooler Model

Performance of printed circuit heat exchanger (PCHE) is a key research area in SCO_2 recompression cycles. PCHE owns the advantages of small volume, strong pressure bearing capacity, and wide application range, which can meet the heat transfer requirements of the SCO_2 Brayton cycle. There are three heat exchangers in the recompressed SCO_2 Brayton cycle, including a LTR, a HTR, and a precooler. The working medium of HTR and LTR on the hot and cold sides is SCO_2, the hot-side working medium of the precooler is SCO_2, and the cold-side working medium is water.

Heat exchangers are usually designed in terms of temperature and pressure, but it is more convenient and accurate to calculate enthalpy and pressure, especially in the SCO_2 cycle. Because temperature is highly nonlinear, while enthalpy is usually linear. In the system, the enthalpy and pressure in the heat exchanger are assumed to change linearly with the length of the heat exchanger to design the heat exchanger.

In order to simplify the model, the assumptions are made as follows:

(1) Since the diameter of the PCHE microchannel is very small, it is assumed that the temperature and pressure of the fluid change only in the axial direction (flow direction);
(2) In a finite region, all calculations of fluid properties can be performed based on the assumed linear change in enthalpy and pressure;
(3) When the fluid passes through the heat exchanger, the heat exchanger absorbs heat uniformly in the direction of the pipe. The change of specific heat and density of the medium is uniform and linear;
(4) The heat exchanger model was created as a countercurrent configuration with constant conductivity (UA).

In order to accurately capture the effects of changes in CO_2 properties, each heat exchanger is divided into a series of sub-heat exchangers. Then, the total heat transfer rate of the entire heat exchanger is distributed equally among the discrete sub-heat exchangers (Dyreby, 2014). In this paper, the precooler modeled uses 10 sub-heat exchangers, HTR uses six sub-heat exchangers, and LTR uses six sub-heat exchangers. It is assumed that the enthalpy in the heat exchanger varies linearly with the length of heating or cooling. Therefore, the cold-side inlet enthalpy and hot-side outlet enthalpy of each sub-heat exchanger are calculated:

$$h_{\mathrm{c,in,i}} = h_{\mathrm{c,out,i}} + \frac{i * \left(h_{\mathrm{c,in}} - h_{\mathrm{c,out}}\right)}{N} \tag{17}$$

$$h_{\mathrm{h,out,i}} = h_{\mathrm{h,in,i}} + \frac{i * \left(h_{\mathrm{h,in}} - h_{\mathrm{h,out}}\right)}{N} \tag{18}$$

where N is the number of sub-heat exchangers.

The inlet and outlet temperatures of each sub-heat exchanger can be calculated using pressure and enthalpy. The heat capacity of the hot-side and cold-side of the sub-heat exchanger can be determined:

$$C_{\mathrm{h,i}} = m_{\mathrm{h}} * \frac{h_{\mathrm{h,in,i}} - h_{\mathrm{h,out,i}}}{T_{\mathrm{h.in.i}} - T_{\mathrm{h,out,i}}} \tag{19}$$

$$C_{\mathrm{c,i}} = m_{\mathrm{c}} * \frac{h_{\mathrm{c,in,i}} - h_{\mathrm{c,out,i}}}{T_{\mathrm{c.in.i}} - T_{\mathrm{c,out,i}}} \tag{20}$$

$$C_{\mathrm{min}} = \min\left(C_{\mathrm{h,i}}, C_{\mathrm{c,i}}\right) \tag{21}$$

$$C_{\mathrm{max}} = \max\left(C_{\mathrm{h,i}}, C_{\mathrm{c,i}}\right) \tag{22}$$

The efficiency of the sub-heat exchanger can be calculated by the following equation:

$$\varepsilon_{\mathrm{i}} = \frac{h_{\mathrm{hot,in}} - h_{\mathrm{hot,out}}}{N * C_{\mathrm{min\,,i}} * \left(T_{\mathrm{h,in,i}} - T_{\mathrm{c,in,i}}\right)} \tag{23}$$

The number of dimensionless heat transfer units (NTU) of the sub-heat exchanger is calculated as follows:

$$NTU_{\mathrm{i}} = \log\left(\frac{1 - \varepsilon_i C_{r,i}}{1 - \varepsilon_i}\right) \tag{24}$$

where C_r is the heat capacity ratio between two streams, defined as the ratio between the minimum heat capacity and the maximum heat capacity.

$$C_{\mathrm{r}} = C_{\mathrm{min}} / C_{\mathrm{max}} \tag{25}$$

The total thermal conductivity of the heat exchanger is the sum of the thermal conductivity values of the sub-heat exchanger:

$$UA = \sum_{i=1}^{N} \left(NTU_i * C_{\min,i}\right) \tag{26}$$

About the cold and hot flow, the general mass conservation equation of the control volume is as follow:

$$V\frac{d\rho}{dt} = m_{\text{in}} - m_{\text{out}} \tag{27}$$

The energy conservation equation of heat flow can be expressed as:

$$m_{\text{h}}c_{\text{p,h}}\left(T_{\text{c1}} - T_{\text{c2}}\right) + Q = \rho_h V_h c_{p,h}\frac{d\overline{T_h}}{d\tau} \tag{28}$$

The energy conservation equation of cold flow can be expressed as:

$$m_c c_{p,c}\left(T_{c1} - T_{c2}\right) + Q = \rho_c V_c c_{p,c}\frac{d\overline{T_c}}{d\tau} \tag{29}$$

The average temperature of CO$_2$ on each side of the heat exchanger can be obtained by:

$$\bar{T}_h = \frac{1}{2}\left(T_{h1} + T_{h2}\right) \tag{30}$$

$$\bar{T}_c = \frac{1}{2}\left(T_{c1} + T_{c2}\right) \tag{31}$$

The heat transfer rate in the heat exchanger is:

$$Q = UA\Delta T_m \tag{32}$$

$$\Delta T_m = \frac{\left(T_{h1} - T_{c2}\right) - \left(T_{h2} - T_{c1}\right)}{\ln\left(\frac{T_{h1}-T_{c2}}{T_{h2}-T_{c1}}\right)} \tag{33}$$

where, m_{h} and m_{c} are the mass flows of SCO$_2$ on the hot-side and the cold-side, respectively. T_{h1}, T_{h2}, T_{c1} and T_{c2} are the hot-side inlet temperature, hot-side outlet temperature, cold-side inlet temperature and cold-side outlet temperature of SCO$_2$, respectively; $c_{\text{p,h}}$ and $c_{\text{p,c}}$ are the specific heat capacities of SCO$_2$ on the hot-side and the cold-side, respectively; ρ_{h} and ρ_{c} are the mean densities of SCO$_2$ on the hot-side and the cold-side respectively; V_{h} and V_{c} are the volumes of SCO$_2$ on the hot-side and the cold-side respectively; t is time.

The pressure drop for the hot and cold-sides of heat exchanger (Meshram et al., 2016) is as follows:

$$\Delta p = f\frac{L}{d}\rho\frac{v^2}{2} \tag{34}$$

$$f = 0.8386Re^{-0.5985} + 0.00295 \tag{35}$$

where f is the friction coefficient, L is the length of PCHE channel, d is the equivalent hydraulic diameter of the PCHE semicircular channel, ρ is the density of SCO$_2$, and v is the flow rate of SCO$_2$. The design parameters of HTR and LTR refer to the data of Sandia Laboratory (Pasch et al., 2012).

Split-Flow/Mix-Flow Model

In the cycle, SCO$_2$ from the hot-side outlet of the LTR enters the main compressor and the recompressor at a certain split ratio of 3:2. The input parameter of split-flow model is total mass flow rate. And the outputs are mass flow rates of main compressor and recompressor.

The SCO$_2$ from the main compressor flows through the cold-side of the LTR and the SCO$_2$ from the recompressor converges at the inlet of the cold-side of the HTR. The input parameters of mix-flow model are cold-side outlet temperature of LTR, cold-side outlet pressure of low temperature recuperator, cold-side outlet mass flow rate of low temperature recuperator, outlet temperature of recompressor, outlet pressure of recompressor, outlet mass flow rate of recompressor. The outputs are cold-side inlet temperature of HTR, the cold-side inlet pressure of HTR, and cold-side inlet mass flow rate of HTR.

Heater Model

Unlike recuperators, the heater model does not include heat transfer calculations. Its working process complies with the conservation equation of mass and energy. According to the given design conditions, the heat transfer power of the heater can be determined, so the thermophysical properties of outlet SCO$_2$ can be calculated from the thermophysical properties of inlet SCO$_2$. The heat transfer rate is calculated as follow:

$$Q = m\left(h_{out} - h_{in}\right) \tag{36}$$

where m is the mass flow rate, h_{out} is outlet enthalpy of SCO2, and h_{in} is inlet enthalpy of SCO$_2$.

System Model

On the Simulink platform, the input and output of each component are connected according to the layout of the SCO$_2$ circulation system and the working medium process. The open-loop simulation system of the SCO$_2$ Brayton circulation system is built, as shown in **Figure 2**.

The model includes the main compressor, recompressor, turbine, HTR, LTR, precooler, heater, split-flow, and mix-flow module. The thermophysical properties of SCO2 fluid come from the REFPROP physical property library established by the National Institute of Standards and Technology (NIST). The simulation model directly accesses REFPROP.DLL in MATLAB/Simulink through the M file, and dynamically connects to the database, so as to realize the simple and convenient call and calculation of CO2 physical parameters.

VALIDATION

In order to verify the accuracy of the algorithm established in the simulation process and the feasibility of the SCO$_2$ cycle simulation system, this section will compare the simulation results with the experimental results conducted by Sandia Laboratory (Pasch et al., 2012) under the same conditions.

The static operation results of the simulation and the experimental results of Sandia Laboratory (Pasch et al., 2012) are shown in **Table 1**. It represents inlet and outlet temperature, inlet and outlet pressure, and other parameters of the main components of the system. By comparing the static simulation

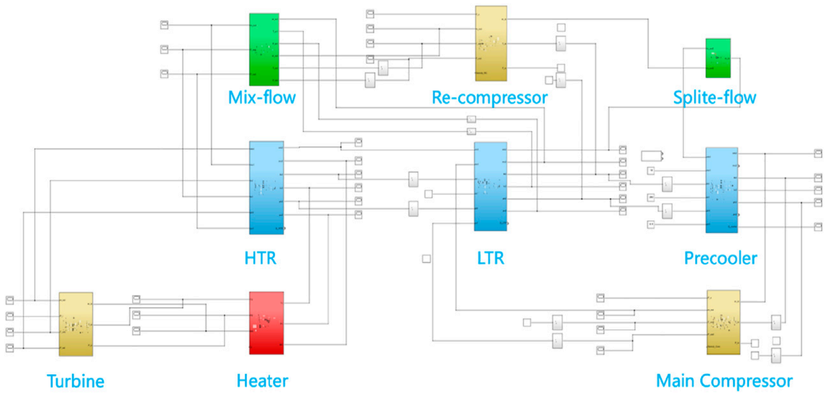

FIGURE 2 | Simulation model of SCO_2 recompression Brayton cycle system.

TABLE 1 | The steady-state simulation results of the temperature compared with Sandia values.

Number	Sandia temperature (°C)	Calculative temperature (°C)	Relative difference (%)	Sandia Pressure (MPa)	Calculative pressure (MPa)	Relative difference (%)
1	305.0	305.3	0.10	7.76	7.70	−0.77
2	324.0	323.6	−0.12	13.84	13.81	0.22
3	389.0	391.9	0.75	13.73	13.71	−0.15
4	389.0	391.2	0.56	13.61	13.71	0.74
5	698.0	696.6	−0.20	13.60	13.57	−0.22
6	810.0	808.7	−0.16	13.50	13.50	0.00
7	750.0	748.9	−0.17	7.89	7.89	−0.01
8	418.0	416.9	−0.26	7.82	7.83	0.13
9	335.0	335.2	−0.06	7.76	7.77	0.13
10	391.0	389.8	−0.31	13.73	13.74	0.07

TABLE 2 | Detailed condition of the steady state.

Parameter	Value
Heat source power	780.0 kW
Turbine power	381.7 kW
Main compressor power requirement	47.1 kW
Recompressor power requirement	86.2 kW
HTR heat transfer power	2,197.4 kW
LTR heat transfer power	696.5 kW
Precooler heat transfer power	543.4 kW
Split ratio	0.6
CO_2 mass flow ratio	5.77 kg/s
Cooling water mass flow ratio	10.00 kg/s
Cycle net-work	248.5 kW
Cycle thermal efficiency	31.85%

results with the laboratory data, it can be seen that both the temperature and the pressure relative difference of each device in the system is within 1%. In general, it can be seen that the thermodynamic characteristics of the SCO_2 recompression Brayton cycle system reflected in the simulation results agree well with the experimental results of Sandia, which can prove that the simulation model built in this paper has high static accuracy. The results of the steady-state operating parameters of the system are shown in **Table 2**. The isentropic efficiency of the turbine, main compressor, and recompressor is set at 86, 67, and 70%, respectively. Heat and pressure losses in connection lines are negligible, and the calculated cycle efficiency excludes auxiliary power losses, mechanical drive losses, and generator losses. Finally, the cycle thermal efficiency of the system is 31.85%.

RESULTS AND DISCUSSION

Analysis of the System When Reducing the Heating Power

When the simulation runs stably under the parameters of the design point, a disturbance is added to the heat of the heater during 60–65 s, at the same time remain the revolving speed of the turbine constant. The heating power decreases from 780 to 663 kW, which is a decrease of 15%. The thermodynamic parameters of the heat source, turbine machinery, recuperator, and precooler are obtained on the simulation platform.

Figure 3 shows the dynamic response of cycle temperature while reducing heat source power. The heat source power decreases sharply, so it can be approximately regarded as a step change. The heater outlet temperature drops sharply from a stable value of 808.7–744.8 K in about 5 s, while the turbine outlet temperature (HTR hot-side input temperature) drops from

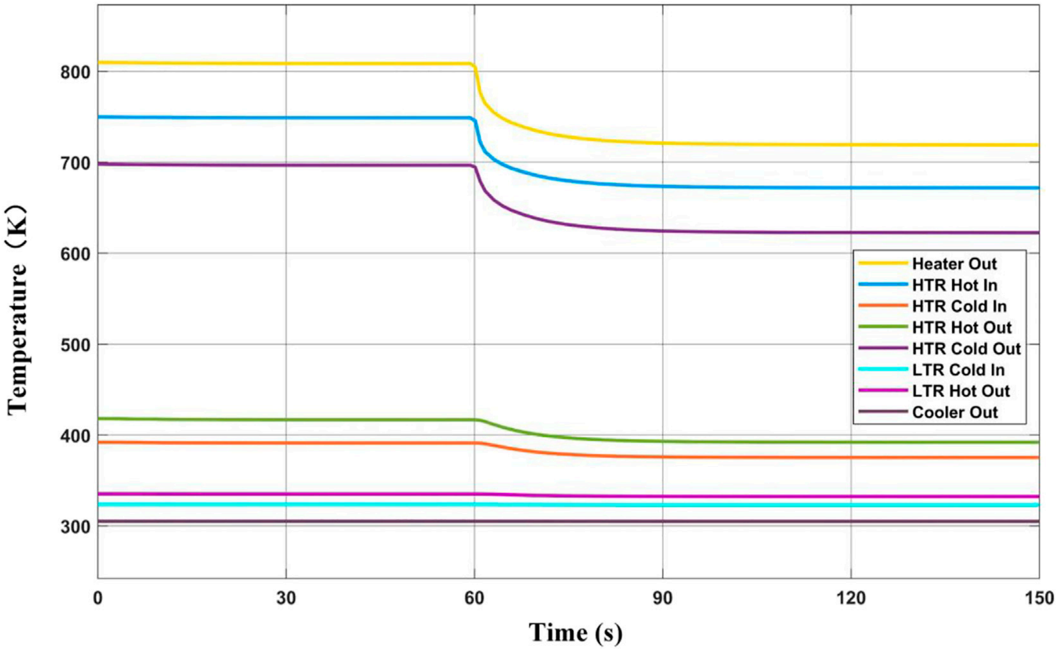

FIGURE 3 | Dynamic response of cycle temperature while reducing heat source power.

748.9 to 694.5 K. The HTR cold-side outlet temperature decreases from 696.7 to 648.5 K, which has the same changing trend as the HTR hot-side inlet temperature because the regenerator is counter-current. After that, the temperature decline slows down because the power of the heat source has not changed, and the heat return from HTR affects the inlet temperature of the heater. The thermal inertia of heat exchangers is large, so the thermal response speed will be reduced. Compared with the above three places, the temperature change rate of the HTR hot-side outlet and cold-side inlet is significantly smaller. Similarly, the temperature change range of LTR cold-side outlet temperature and the hot-side inlet is smaller, and the hot-side outlet temperature of the precooler is almost unchanged. At about 120 s, the system reaches a new steady state. The outlet temperature of the heat source is 719.2 K; the outlet temperature of the turbine is 671.6 K; the inlet temperature of the recompressor drops from 335.2 to 332.5 K; and the inlet temperature of the main compressor drops from 305.3 to 305.2 K.

The heat transfer of the heat exchangers in the cycle system is shown in **Figure 4**. It can be seen from the figure that the decrease of heat source power leads to the decrease of heat transfer of HTR, LTR, and precooler. Meanwhile, due to the thermal inertia of the heat exchangers, the response of the above three heat exchangers to the heat source power fluctuation gradually slows down. HTR heat transfer power reduces from 2,197.4 kW to 1850.5 kW, decreasing by 15.8%; LTR heat transfer power reduces from 696.5 to 566.2 kW, decreasing by 18.7%; precooler heat transfer power reduces from 543.4 to 531.1 kW, decreasing by 2.3%. The power variation of the turbine machinery of the cycle system is shown in **Figure 5**, and the dynamic response of the cycle thermal efficiency is shown in **Figure 6**. The output power of the turbine is greatly reduced because the inlet working condition of the turbine changes so that the turbine works under the off-design condition. The inlet working conditions of the main compressor and the recompressor change slightly, so the power consumption changes slightly. The net power output of the cycle decreased significantly from 248.5 to 145.4 kW. This results in a dramatic drop in the cycle thermal efficiency from 31.9 to 22.0%.

Analysis of the System When Increasing the Heating Power

When the simulation system is in the stable stage, a disturbance is added to the heat of the heater during 60–65 s, and the control turbine speed unchanged. The heating capacity increases from 780 to 900 kW, which is an increase of 15%. Monitor the change of various thermodynamic parameters of system components on the platform, collect the data and draw the corresponding change curves.

Figure 7 shows the effect of increasing heat source power on the cycle temperature. The outlet temperature of the heat source rises from the stable value of 808.7–865.1 K in about 5 s, while the turbine outlet temperature rises to 794.6 K. The HTR cold-side outlet temperature decreases from 696.7 to 648.5 K, which has the same changing trend as the HTR hot-side inlet temperature. After that, the temperature of all components slows down. The temperature change rate of HTR hot-side outlet and cold-side inlet is obviously less than that of the above three places. The temperature change range of LTR cold-side outlet temperature and hot-side inlet is smaller, and the hot-side outlet temperature

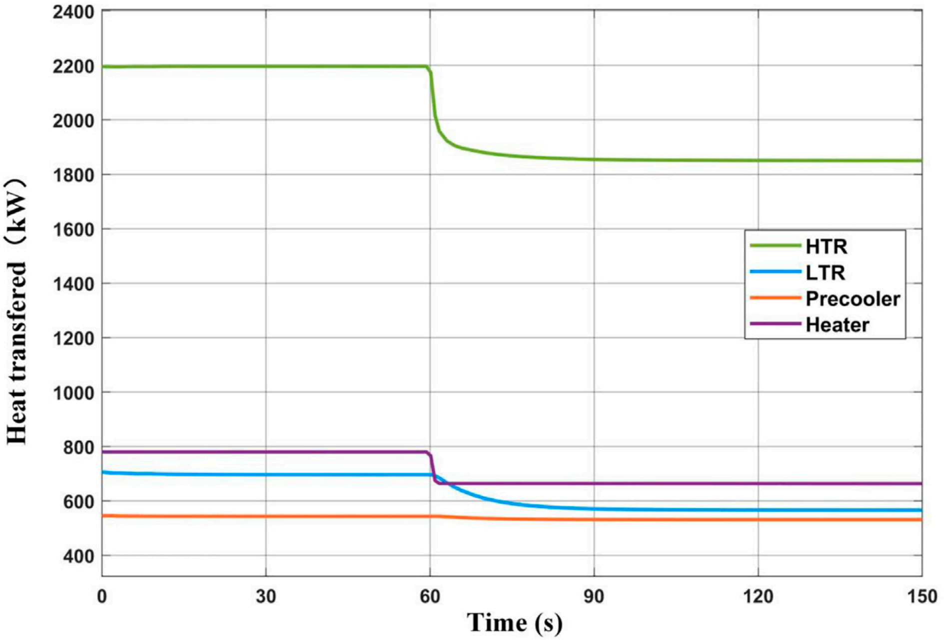

FIGURE 4 | Dynamic response of heat transfer in heat exchangers while reducing heat source power.

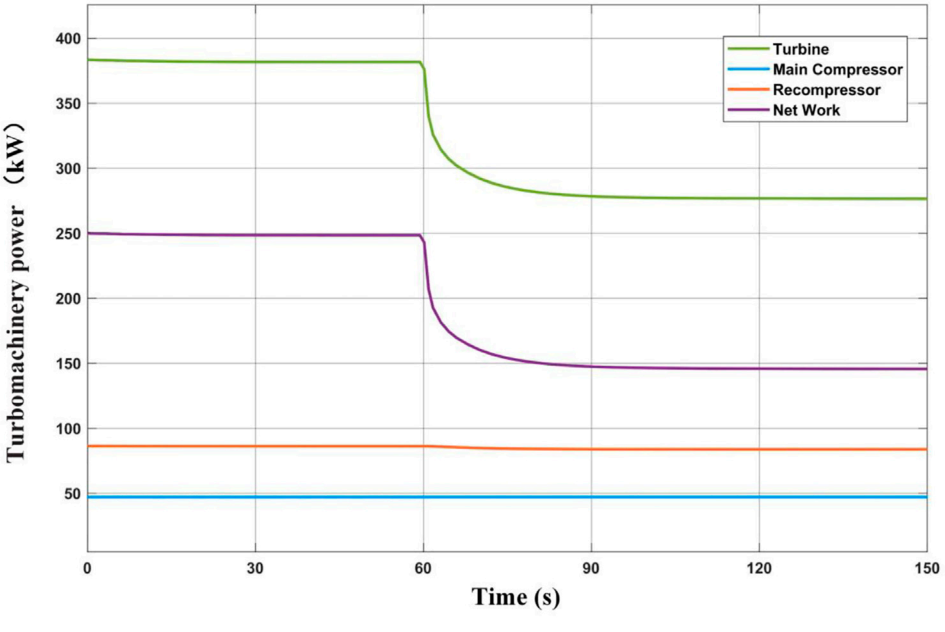

FIGURE 5 | Dynamic response of turbine machinery power while reducing heat source power.

of the precooler is almost unchanged. At about 120 s, the system reaches a new steady state. The outlet temperature of the heat source is 877.1 K; the outlet temperature of the turbine is 804.1 K; the inlet temperature of the recompressor rises from 335.2 to 338.2 K; the inlet temperature of the main compressor is almost unchanged.

The increase of heat source power leads to the increase of heat transfer of HTR, LTR, and precooler. At the same time, the response of the above three heat exchangers to the heat source power fluctuation gradually slows down. HTR heat transfer power rises from 2,197.4 kW to 2,424.6 kW, increasing by 10.3%; LTR heat transfer power rises from

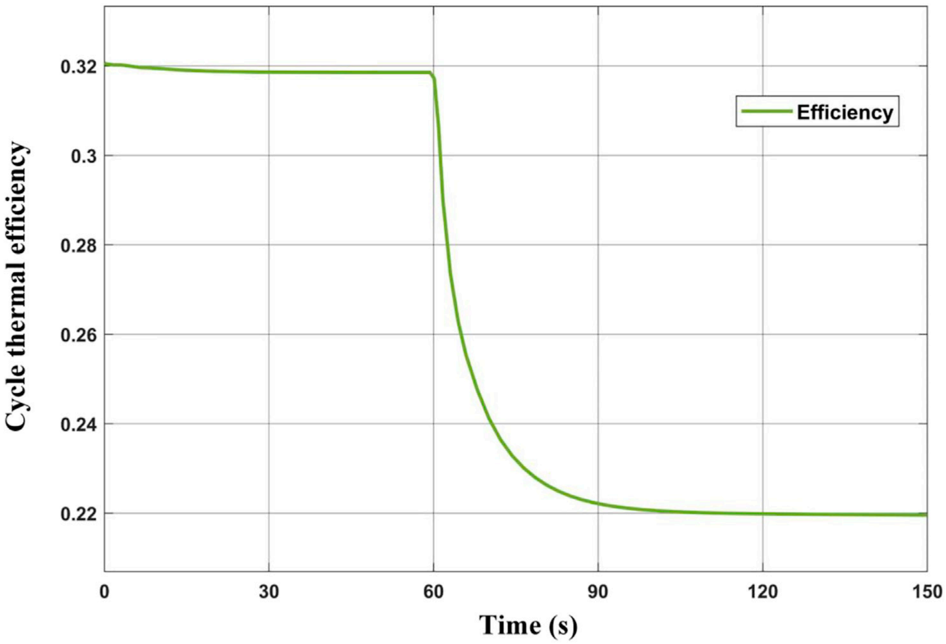

FIGURE 6 | Dynamic response of system thermal efficiency while reducing heat source power.

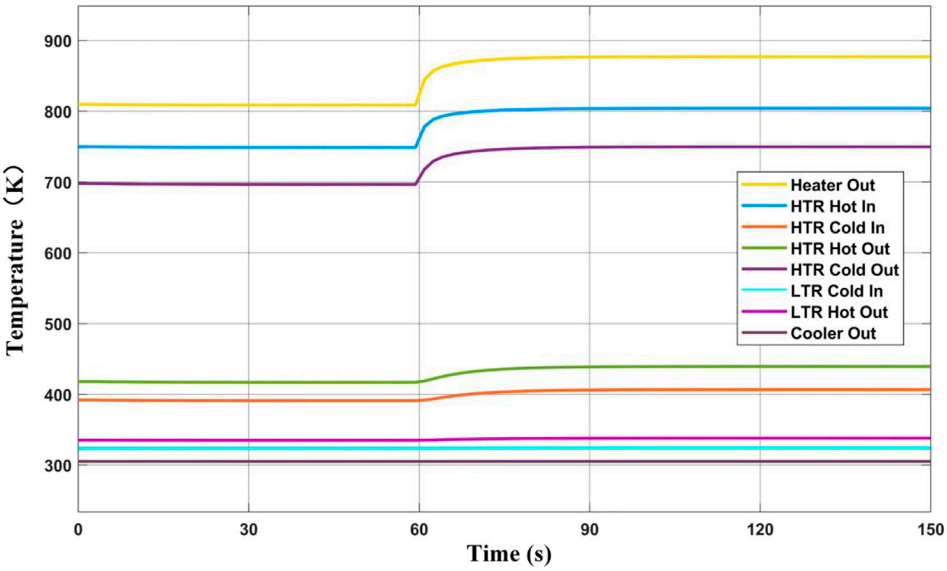

FIGURE 7 | Dynamic response of cycle temperature while increasing heat source power.

696.5 to 809.6 kW, increasing by 16.2%; Precooler heat transfer power rises from 543.4 to 555.9 kW, increasing by 2.3%. The power output of the turbine increases considerably. The power consumption of the main compressor and the recompressor changes slightly, and the net-work output of the cycle system increases significantly from 248.5 to 351.1 kW. The dynamic response of the cycle thermal efficiency is shown in **Figure 8**. It can be seen from the figure that the thermal efficiency of the cycle system increases from 31.9 to 39.1%.

Analysis of the System When Reducing the Cycle Mass Flow Rate

When the simulation system is in the stable phase, a disturbance is applied to the flow rate of the heater inlet.

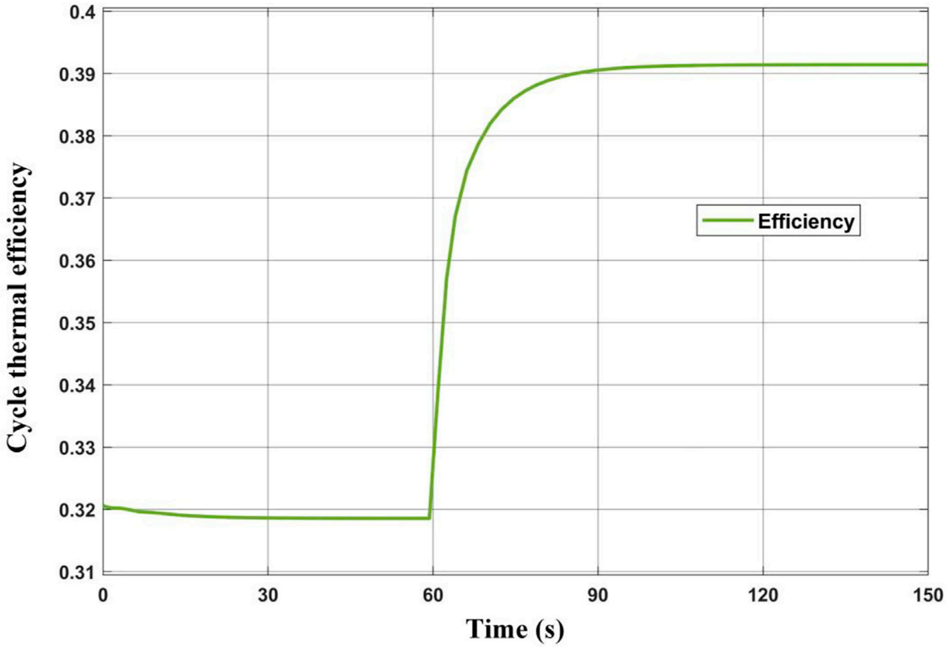

FIGURE 8 | Dynamic response of system thermal efficiency while increasing heat source power.

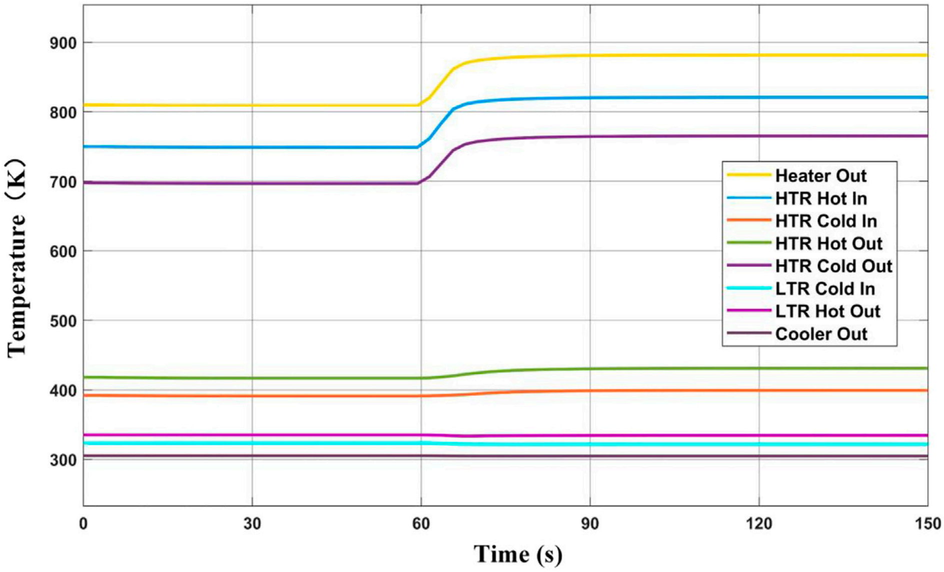

FIGURE 9 | Dynamic response of cycle temperature while reducing the cycle mass flow rate.

During 60–65 s, the system flow rate decreased from 5.77 kg/s to 5.48 kg/s, which is a decrease of 5%. Monitor the change of various thermodynamic parameters of system components on the platform, collect the data and draw the corresponding change curves.

Figure 9 shows the effect of reducing the system mass flow rate on the cycle temperature. If the heat source power is kept constant and the system mass flow rate is reduced, the outlet temperature of the heater will rise from a stable value of 808.7–861.1 K within 5 s, and the outlet temperature of the turbine increases to 803.5K. Because the regenerator is counter-current, the HTR cold-side outlet temperature which has the same variation trend as the HTR hot-side inlet temperature rises to 741.0 K. After that, the temperature rise rate slows down, because the mass flow rate of the system has not changed, and the heat which

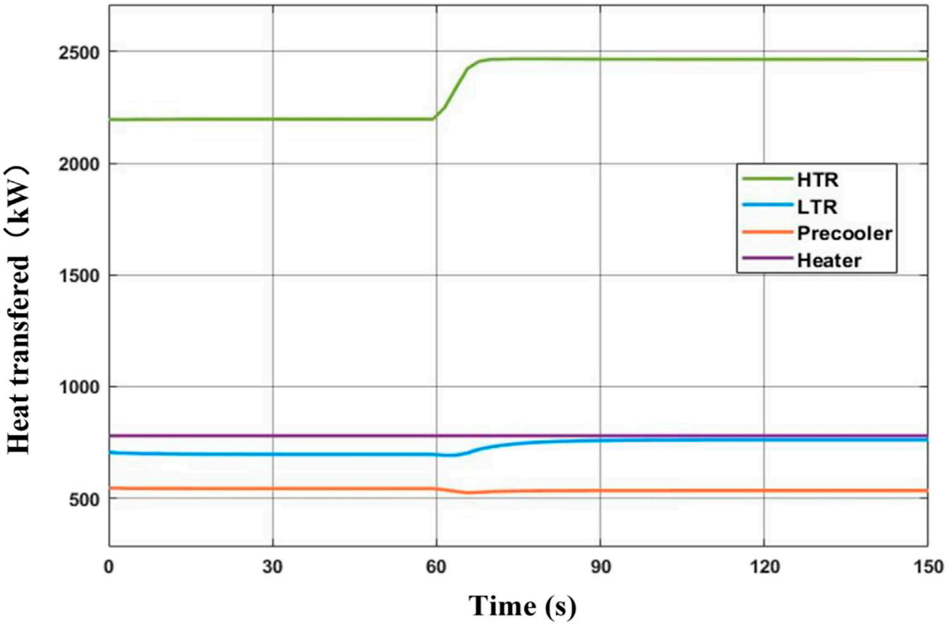

FIGURE 10 | Dynamic response of heat transfer in heat exchangers while reducing the cycle mass flow rate.

returns from the HTR will affect the inlet temperature of the heater. Due to the influence of thermal inertia, the temperature change rate of the HTR cold-side inlet and the HTR hot-side outlet is less than that of the above three places. As the mass flow rate of working medium on the hot-side of the precooler decreases and the inlet temperature and mass flow rate of the cold-side water remain unchanged, the outlet temperature of the working medium on the hot-side decreases from 305.3 to 304.8 K. The compressor outlet temperature (LTR cold-side inlet temperature) decreases from 323.6 to 321.6 K. The LTR hot-side outlet temperature decreases from 335.2 to 334.0 K, which has the same changing trend as the LTR cold-side inlet temperature. After 5 s, the LTR hot-side outlet temperature increases to 334.5 K and remains stable because the cycle system mass flow rate has not changed and the inlet temperature still rises slowly.

The heat transfer power of the heat exchangers in the cycle system is shown in **Figure 10**. The power of the heat source remains the same. The heat transfer power of HTR and LTR increases due to the rising temperature of the hot-side inlet. The heat transfer of the HTR increases to 2,465.4 kW, increasing by 12%; The heat transfer power of the LTR increases to 760.4 kW, increasing by 9.17%. The heat transfer power of the precooler decreases to 524.3 kW within 5 s and then increases to 534.6 kW because the inlet temperature decreases firstly and then increases. The power variation of the turbine machinery of the circulating system is shown in **Figure 11**, and the dynamic response of the cycle thermal efficiency is shown in **Figure 12**. Within 5 s of the change of cycle mass flow, the work done by the turbine decreases. After the flow is stable, the work done by the turbine increases due to the increase in inlet temperature. The power consumption of the main compressor and the recompressor is reduced, but the reduction range is relatively small. The cycle net-work decreases to 231.8 kW in 5 s and then increases to 256.4 kW in about 120 s, which results in the cycle efficiency decreasing from 31.9 to 29.7% within 5 s, then increasing to 32.9% and finally stabilizing.

Analysis of the System When Increasing the Cycle Mass Flow Rate

When the simulation system is in the stable phase, a disturbance is applied to the flow rate of the heater inlet. In 60–65 s, the system flow rate increases from 5.77 kg/s to 6.06 kg/s, which is an increase of 5%. Monitor the change of various thermodynamic parameters of system components on the platform, collect the data, and draw the corresponding change curves.

Figure 13 shows the effect of increasing the system mass flow rate on the cycle temperature. The temperature variation trend of each part is opposite to that of decreasing system flow rate. The outlet temperature of the heat source is reduced to 762.1 K within 5 s, the outlet temperature of the turbine is reduced to 700.3 K, and the HTR cold-side outlet temperature is reduced to 654.4 K. After that, the temperature drop slows down. The temperature change rate of the HTR cold-side inlet and the hot-side outlet is less than that of the above three places. The outlet temperature of the precooler increases from 305.3 to 305.5 K due to the decrease of the mass flow rate of SCO_2 on the hot side of the precooler. The main compressor outlet temperature (LTR cold-side inlet temperature) then increased from 323.6 to 325.7 K. The LTR hot-side inlet temperature increases from 335.2 to 337.2 K. After 5 s, the

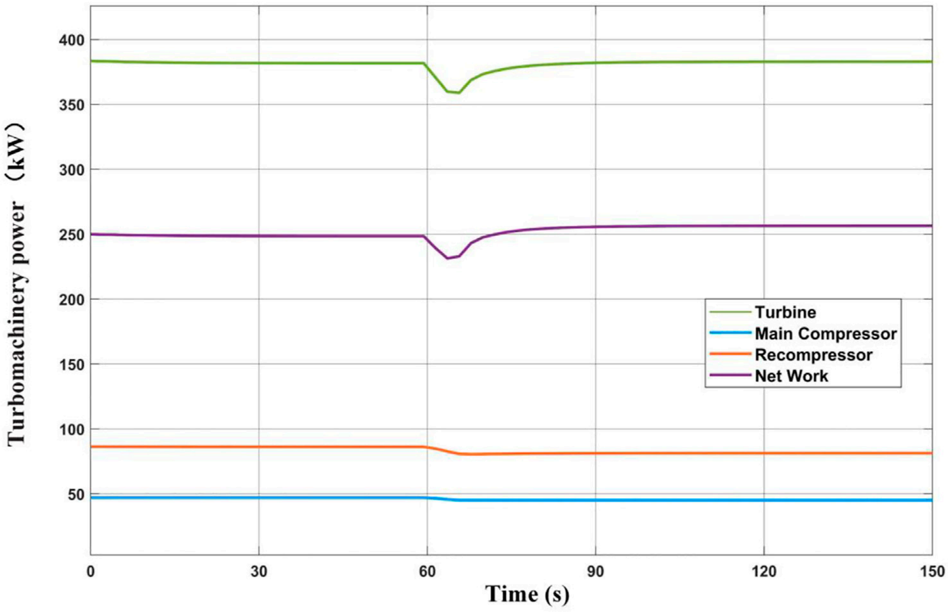

FIGURE 11 | Dynamic response of turbine machinery power while reducing the cycle mass flow rate.

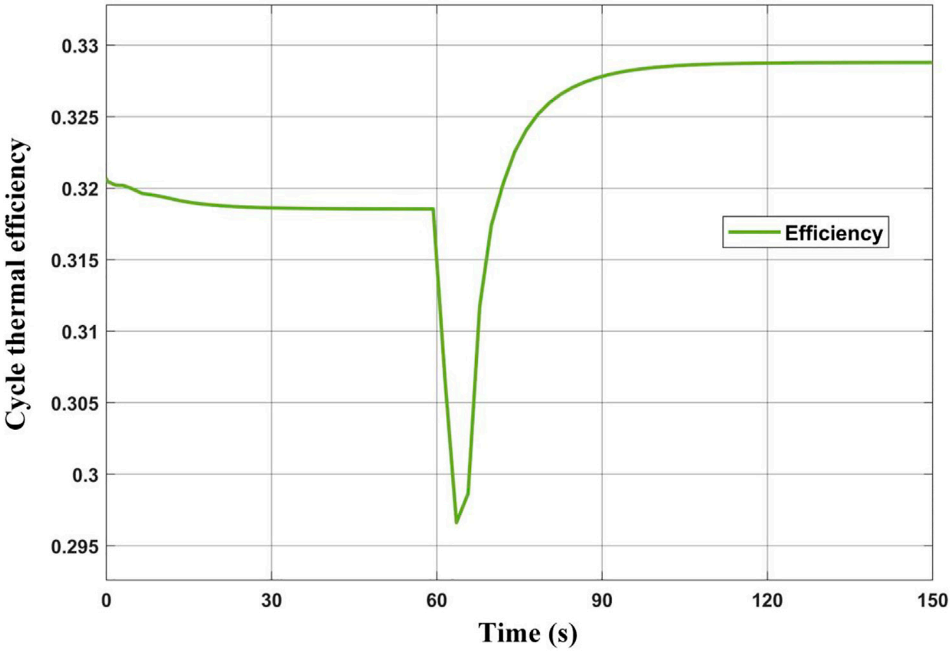

FIGURE 12 | Dynamic response of system thermal efficiency while reducing the cycle mass flow rate.

LTR hot-side outlet temperature decreases to 336.4 K and then remains stable because the cycle system flow rate has not changed and the LTR hot-side inlet temperature still decreases slowly.

The power of the heat source remains the same. The heat transfer power of HTR and LTR decreases due to the falling temperature of the hot-side inlet. The heat transfer of the HTR decreases to 1931.5 kW, increasing by 12.1%; The heat transfer power of the LTR decreases to 645.1 kW, decreasing by 7.4%. Within 5 s of the change of cycle mass flow rate, the work done by the turbine increases. After the flow is stable, the work done by the turbine decreases due to the decrease in inlet temperature. The

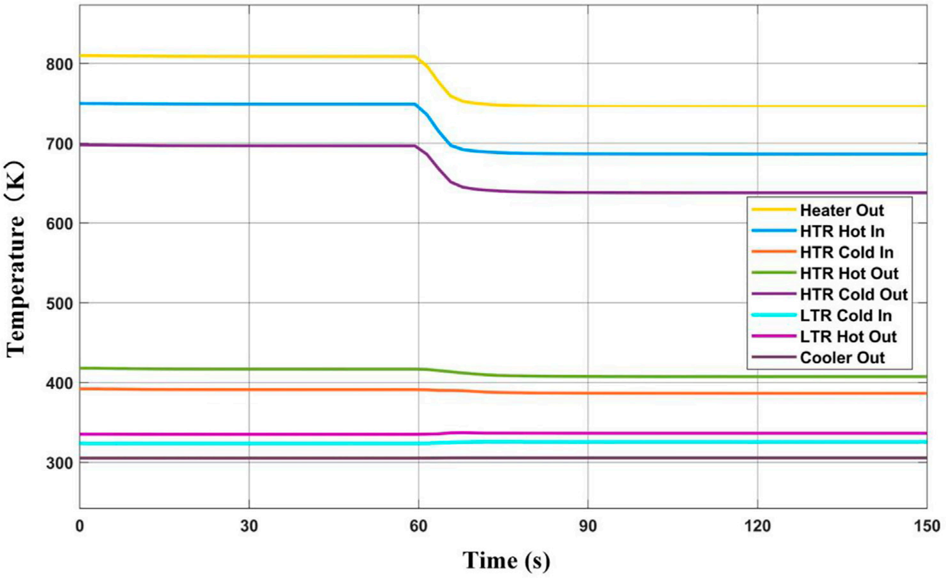

FIGURE 13 | Dynamic response of cycle temperature while increasing the cycle mass flow rate.

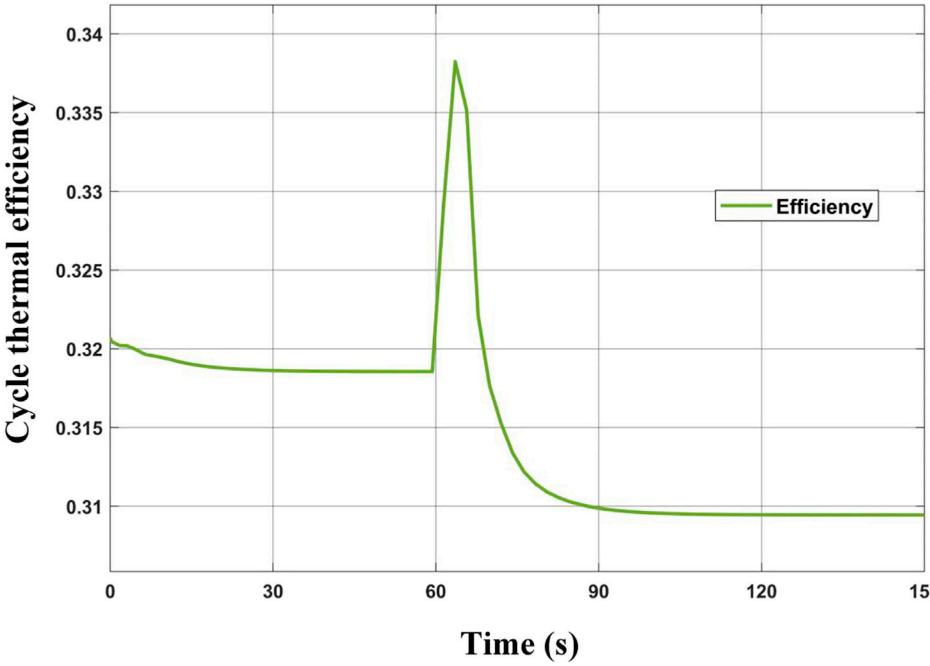

FIGURE 14 | Dynamic response of system thermal efficiency while increasing the cycle mass flow rate.

power consumption of the main compressor and the recompressor increases slightly. the dynamic response of the cycle thermal efficiency is shown in **Figure 14**. The cycle net-work increases to 262.9 kW in 5 s and then increases to 241.4 kW in about 120 s, which results in the cycle efficiency increasing from 31.9 to 33.7% within 5 s, then decreasing to 30.9% and finally stabilizing.

CONCLUSION

In this paper, the component model of the SCO_2 recompression Brayton cycle system, including compressor, turbine, HTR, LTR, precooler, and heater model, is established based on the idea of modularization and the conservation of mass equation, energy conservation equation, and heat transfer equation. A closed-loop simulation system is established in Matlab/Simulink software through the arrangement of the cycle system and the connection relationship of the components. The response characteristics of components inlet and outlet temperature, heat transfer of heat exchangers, turbine machinery power, and other parameters in the system were studied by applying heat source heating power and cycle system mass flow rate disturbance experiments. The main conclusions can be summarized as follows:

(1) The model has high accuracy, and can reflect the dynamic response of system performance under parameter perturbation. Due to the lack of public experimental data experimental data of the SCO2 Brayton cycle, the simulation calculation research will lay the foundation for the corresponding unit control strategy and the engineering application of the SCO2 cycle system. The steady-state thermodynamic analysis at design point conditions of the SCO2 recompression Brayton cycle system predicted a thermal efficiency of 31.85%.
(2) The model calculation results show: When a disturbance is applied to the system, the response time of the components behind the disturbance is the shortest, and the response time of each component gradually increases along the path of the cycle, and the time to reach the steady state becomes longer successively.
(3) The parameters of the cycle system are sensitive to the change of heat source power. The temperature change is mainly concentrated near the heat source of the cycle, while the change near the precooler is relatively small. The effect on cycle efficiency decreases from 31.9 to 22.0%. The effect of increasing heat source power on the cycle system is just the opposite.
(4) Reducing the system flow will increase the temperature near the heat source of the cycle, and decrease the temperature near the precooler. The cycle efficiency decreasing from 31.9 to 29.7% within 5 s, then increasing to 32.9%, and finally stabilizing. Increasing system mass flow rate has the opposite effect on the system.
(5) Under various perturbations, the outlet temperature of the precooler changes very slightly. Due to the high degree of non-ideality of thermophysical properties such as viscosity, density, heat capacity, and conductivity, small changes in the inlet working condition of the main compressor can have a significant impact on the total system performance. Therefore, it is necessary to control the inlet situation of the compressor to ensure its reasonable operating range.
(6) According to the results of the dynamic characteristics after applying the disturbance, a control strategy for the S-CO2 recompression Brayton cycle system is proposed. During the disturbance, the inlet temperature of the main compressor is controlled by cooling water to maintain the design point; the inlet temperature of the turbine is controlled by the bypass control valve and additional heat accumulator. Based on the above control strategy, the stable operation of the system is realized.

DATA AVAILABILITY STATEMENT

The original contributions presented in the study are included in the article/supplementary material, further inquiries can be directed to the corresponding author.

AUTHOR CONTRIBUTIONS

BZ, QZ, and RH contributed to conception and design of the study. QZ organized the calculation model. RH performed the analysis. QZ wrote the first draft of the manuscript. BZ, RH, SY, and ZY wrote sections of the manuscript. All authors contributed to manuscript revision, read, and approved the submitted version.

FUNDING

This project was supported by the National Natural Science Foundation of China (51876020), Innovation Center of Nuclear Power Technology for National Defense Industry, and the Fundamental Research Funds for the Central Universities.

REFERENCES

Ahn, Y., Bae, S. J., Kim, M., Cho, S. K., Baik, S., Lee, J. I., et al. (2015). Review of Supercritical CO2 Power Cycle Technology and Current Status of Research and Development. *Nucl. Eng. Techn.* 47 (6), 647–661. doi:10.1016/j.net.2015.06.009

Ahn, Y., and Lee, J. I. (2014). Study of Various Brayton Cycle Designs for Small Modular Sodium-Cooled Fast Reactor. *Nucl. Eng. Des.* 276, 128–141. doi:10.1016/j.nucengdes.2014.05.032

Anderson, M., Sienicki, J., Moisseytsev, A., Nellis, G., and Klein, S. (2015). *Advanced Supercritical Carbon Dioxide Brayton Cycle Development*. Madison, WI: University of Wisconsin.

Cao, Y., Rattner, A. S., and Dai, Y. (2018). Thermoeconomic Analysis of a Gas Turbine and Cascaded CO2 Combined Cycle Using thermal Oil as an Intermediate Heat-Transfer Fluid. *Energy* 162, 1253–1268. doi:10.1016/j.energy.2018.08.110

Chang, F., and Grandy, C. (2008). *Advanced Burner Test Reactor Preconceptual Design report*. United States: Argonne National Laboratories.

Crespi, F., Gavagnin, G., Sánchez, D., and Martínez, G. S. (2017). Supercritical Carbon Dioxide Cycles for Power Generation: A Review. *Appl. Energ.* 195, 152–183. doi:10.1016/j.apenergy.2017.02.048

Dostal, V., Driscoll, M. J., Hejzlar, P., and Todreas, N. E. (2002). "A Supercritical CO$_2$ Gas Turbine Power Cycle for Next-Generation Nuclear Reactors[C]," in International Conference on Nuclear Engineering, Arlington, Virginia, USA, April 14–18, 2002.

Dostal, V., Hejzlar, P., and Driscoll, M. J. (2017). High-Performance Supercritical Carbon Dioxide Cycle for Next-Generation Nuclear Reactors. *Nucl. Techn.* 154 (3), 265–282. doi:10.13182/nt154-265

Dyreby, J. J. (2014). Modeling the Supercritical Carbon Dioxide Brayton Cycle with Recompression [PhD thesis]. Madison: The University of Wisconsin.

Huang, Y., Su, H., Zheng, Q., Yin, Y., and Wang, T. (2020). Research on Aerodynamic Characteristics of 5 MW Supercritical Carbon Dioxide Test Boiler[J]. *Therm. Power Generation* 49 (12), 36–40. doi:10.19666/j.rlfd.202006162

Jokar, M. A., Ahmadi, M. H., Sharifpur, M., Meyer, J. P., Pourfayaz, F., and Ming, T. (2017). Thermodynamic Evaluation and Multi-Objective Optimization of Molten Carbonate Fuel Cell-Supercritical CO 2 Brayton Cycle Hybrid

System. *Energ. Convers. Manag.* 153, 538–556. doi:10.1016/j.enconman.2017.10.027

Liu, Y., Wang, Y., and Huang, D. (2019). Supercritical CO2 Brayton Cycle: A State-Of-The-Art review[J]. *Energy* 189 (12), 115900. doi:10.1016/j.energy.2019.115900

Luu, M. T., Milani, D., Mcnaughton, R., and Abbas, A. (2017). Dynamic Modelling and Start-Up Operation of a Solar-Assisted Recompression Supercritical CO 2 Brayton Power Cycle. *Appl. Energ.* 199, 247–263. doi:10.1016/j.apenergy.2017.04.073

Lv, G., Yang, J., Shao, W., and Wang, X. (2018). Aerodynamic Design Optimization of Radial-Inflow Turbine in Supercritical CO2 Cycles Using a One-Dimensional Model. *Energ. Convers. Manag.* 165, 827–839. doi:10.1016/j.enconman.2018.03.005

Ma, Y., Liu, M., Yan, J., and Liu, J. (2017). Thermodynamic Study of Main Compression Intercooling Effects on Supercritical CO2 Recompression Brayton Cycle. *Energy* 140, 746–756. doi:10.1016/j.energy.2017.08.027

Meshram, A., Clifford, D., Pradip, K., Sagar, D., Ortega, J. D., and Jaiswal, A. K. (2016). Modeling and Analysis of a Printed Circuit Heat Exchanger for Supercritical CO2 Power Cycle Applications[J]. *Appl. Therm. Eng.* 109, 861. doi:10.1016/j.applthermaleng.2016.05.033

Milani, D., Luu, M. T., Mcnaughton, R., and Abbas, A. (2017). A Comparative Study of Solar Heliostat Assisted Supercritical CO2 Recompression Brayton Cycles: Dynamic Modelling and Control Strategies. *J. Supercrit. Fluids* 120, 113–124. doi:10.1016/j.supflu.2016.09.009

Moisseytsev, A., and Sienicki, J. J. (2009). Investigation of Alternative Layouts for the Supercritical Carbon Dioxide Brayton Cycle for a Sodium-Cooled Fast Reactor. *Nucl. Eng. Des.* 239 (7), 1362–1371. doi:10.1016/j.nucengdes.2009.03.017

Monjurul Ehsan, M., Guan, Z., Klimenko, A. Y., and Wang, X. (2018). Design and Comparison of Direct and Indirect Cooling System for 25 MW Solar Power Plant Operated with Supercritical CO2 Cycle. *Energ. Convers. Manag.* 168, 611–628. doi:10.1016/j.enconman.2018.04.072

Neises, T., and Turchi, C. (2014). A Comparison of Supercritical Carbon Dioxide Power Cycle Configurations with an Emphasis on CSP Applications. *Energ. Proced.* 49, 1187–1196. doi:10.1016/j.egypro.2014.03.128

Olumayegun, O., and Wang, M. (2019). Dynamic Modelling and Control of Supercritical CO2 Power Cycle Using Waste Heat from Industrial Processes. *Fuel* 249, 89–102. doi:10.1016/j.fuel.2019.03.078

Park, J. H., Park, H. S., Kwon, J. G., Kim, T. H., and Kim, M. H. (2018). Optimization and Thermodynamic Analysis of Supercritical CO2 Brayton Recompression Cycle for Various Small Modular Reactors. *Energy* 160 (OCT.1), 520–535. doi:10.1016/j.energy.2018.06.155

Pasch, J. J., Thomas, M.C, and Darryn, D. (2012). *Supercritical CO2 Recompression Brayton Cycle:completed Assembly Description*. United States: Sandia National Laboratories.

Richard, D., Andrew, G., and Henry, S. (2018). "Development of A Dynamic Model for A 250 Kw Supercritical Co2 Simple Regenerative Brayton Cycle Plant[C]," in Proceedings of Montreal 2018 Global Power and Propulsion Forum, Montreal, Canada, May 7–9, 2018.

Sarkar, J. (2015). Review and Future Trends of Supercritical CO2 Rankine Cycle for Low-Grade Heat Conversion. *Renew. Sust. Energ. Rev.* 48, 434–451. doi:10.1016/j.rser.2015.04.039

Seong, S.-H. (2014). Simulation of Some Performance-Related Events of KALIMER-600. *Ann. Nucl. Energ.* 63, 176–187. doi:10.1016/j.anucene.2013.07.047

Seong, S.-H., and Kim, S.-O. (2012). Performance Evaluation of Control Strategies for Power Maneuvering Event of the KALIMER-600. *Ann. Nucl. Energ.* 42, 50–62. doi:10.1016/j.anucene.2011.12.003

Sinicki, J., Moisseytsev, A., Cho, D., Momozaki, Y., Kilsdonk, D., Haglund, R., et al. (2007). "Supercritical Carbon Dioxide Brayton Cycle Energy Conversion for Sodium-Cooled Fast Reactors/Advanced Burner Reactors[R]," in GLOBAL 2007: Advanced Nuclear Fuel Cycles and Systems, Boise, United State, September 9–13, 2007.

Span, R., and Wagner, W. (1996). A New Equation of State for Carbon Dioxide Covering the Fluid Region from the Triple-Point Temperature to 1100 K at Pressures up to 800 MPa. *J. Phys. Chem. Reference Data* 25 (6), 1509–1596. doi:10.1063/1.555991

Su, H., Huang, Y., Yin, Y., Wang, T., Guo, X., and Wang, Y. (2020). Coupling Calculation Model of Thermal Characteristics and Wall Temperature of 5 MW Supercritical Carbon Dioxide Experimental Boiler[J]. *Therm. Power Generation* 49 (10), 151–156. doi:10.19666/j.rlfd.202001031

Viswanathan, R., Coleman, K., and Rao, U. (2006). Materials for Ultra-supercritical Coal-Fired Power Plant Boilers[J]. *Int. J. Press. Vessels Piping* 83 (11-12), 778–783. doi:10.1016/j.ijpvp.2006.08.006

Wang, R., Shu, G., Wang, X., Tian, H., Li, X., Wang, M., et al. (2020). Dynamic Performance and Control Strategy of CO2-mixture Transcritical Power Cycle for Heavy-Duty Diesel Engine Waste-Heat Recovery. *Energ. Convers. Manag.* 205, 112389. doi:10.1016/j.enconman.2019.112389

Conflict of Interest: The authors declare that the research was conducted in the absence of any commercial or financial relationships that could be construed as a potential conflict of interest.

The reviewer CW declared a shared affiliation with one of the authors, SY, to the handling editor at time of review.

NOMENCLATURE

Symbol

A heat transfer area, m^2
C heat capacity, kW/K
c_p isobaric specific heat, J/(kg·K)
d equivalent hydraulic diameter, mm
f friction coefficient
h enthalpy, kJ/kghot-side flow
L channel length, m
m mass flow rate, kg/s
N revolving speed, rpm
NTU dimensionless number of transfer units
n number of sub-heat exchangers
Q heat transfer rate, kW
P pressure, MPa
Q heat transfer rate, kW
Re Reynolds number
$\mathbf{S}$ entropy,
T temperature, K
$\bar{T}$ average temperature, K
U overall heat transfer coefficient, kW/(m^2·K)
v flow velocity, m/s
$\boldsymbol{W}$ power of turbomachinery, kW

Greek

Δh enthalpy variation, kJ/kg
Δp pressure drop, kPa
ΔT_m logarithmic mean temperature difference, K
ε sub-heat exchanger efficiency
η efficiency
ρ density, kg/m^3
τ time, s

Subscripts

c cold-side flow
$chart$ performance chart
$comp$ compressor
h enthalpy, kJ/kghot-side flow
i serial number
in inlet
is isentropic
$\min$ minimum
out outlet
r ratio
$turb$ turbine

Abbreviations

HTR high temperature recuperator
LTR low temperature recuperator
PCHE printed circuit heat exchanger

frontiers
in Energy Research

ORIGINAL RESEARCH
published: 17 March 2022
doi: 10.3389/fenrg.2022.835224

Experimental Study on Prototype of Printed Circuit Heat Exchanger

Dongxu Zhang*, **Minfu Zhao**, **Peng Liang** and **Weiqing Li**

Reactor Engineering Technology Research Institute, China Institute of Atomic Energy, Beijing, China

The printed circuit heat exchanger (PCHE) is the key equipment of the supercritical carbon dioxide Brayton cycle applied to sodium cooled fast reactor. It is required that the equipment not only can operate in high temperature and high pressure environment but also has high efficiency and compact structure. The China Institute of Atomic Energy has carried out the research on a sodium-supercritical carbon dioxide PCHE and has designed and manufactured a heat exchanger prototype with the heat transfer power of 50 kW. In addition, the supercritical carbon dioxide test loop and sodium test loop have been built to test the performance of the heat exchanger prototype. The conclusions are as follows: 1) The heat exchange power of the heat exchanger under rated working condition is 54.2 kW, and the deviation is around 8%, which meets the design requirements; 2) With the increase of the flow ratio of sodium to carbon dioxide, the temperature difference at the high temperature end decreases, and the temperature difference at the low temperature end increases; 3) The change of flow rate of the carbon dioxide has a great influence on heat transfer power; 4) The total heat transfer coefficient of the heat exchanger increases with the increase of the pressure of carbon dioxide; when the pressure increases from 15.5 to 20 MPa, the total heat transfer coefficient increases by 12.8%.

Keywords: printed circuit heat exchanger, supercritical carbon dioxide, Brayton cycle, test verification, nuclear reactor

OPEN ACCESS

Edited by:
Wei Ding,
Helmholtz Center Dresden-Rossendorf, Germany

Reviewed by:
Guopeng Yu,
Sun Yat-sen University, China
Luteng Zhang,
Chongqing University, China

***Correspondence:**
Dongxu Zhang
dongxu221@163.com

Specialty section:
This article was submitted to Nuclear Energy, a section of the journal Frontiers in Energy Research

Received: *14 December 2021*
Accepted: *28 January 2022*
Published: *17 March 2022*

Citation:
Zhang D, Zhao M, Liang P and Li W (2022) Experimental Study on Prototype of Printed Circuit Heat Exchanger. Front. Energy Res. 10:835224. doi: 10.3389/fenrg.2022.835224

INTRODUCTION

The supercritical carbon dioxide Brayton cycle system is one of the most promising power conversion systems, which has the advantages of clean working fluid, good fluidity, high efficiency, high energy density, and small size of the equipment. It could eliminate the safety problems caused by sodium–water reaction, so it extremely has the engineering application prospects in sodium-cooled fast reactor (Wang et al., 2019).

As a cycle working fluid, the supercritical carbon dioxide has the characteristics of good fluidity and high density, which can reduce the size of key equipment, such as heat exchanger and compressor (Dostal, 2004; Yang, 2014). The heat exchanger is the key equipment of the supercritical carbon dioxide Brayton cycle, and its heat transfer performance has a direct influence on the efficiency of the reactor cycle system. The printed circuit heat exchanger (PCHE) is used in the supercritical carbon dioxide Brayton cycle system, which is a compact heat exchanger with the characteristics of less leakage and high efficiency, and it can be used in high-temperature and high-pressure conditions (Yu et al., 2017).

Ngo et al. (2006) had analyzed the thermal hydraulic performance of PCHE with the S-type fin structure with water and supercritical carbon dioxide as working fluid. They found that, compared with the heat exchanger in the heat pump system, the volume of the PCHE with S-type fin structure was reduced by 3.3 times, the pressure drop of the carbon dioxide side was reduced by 37%, and the water side was reduced by 10 times.

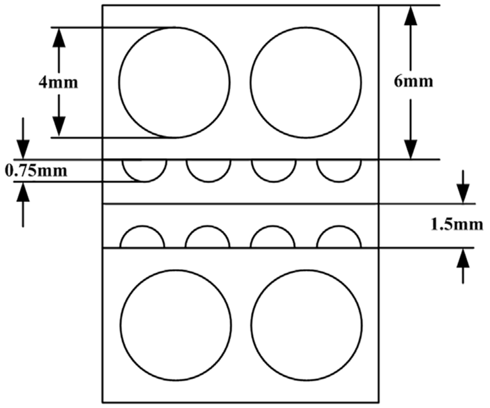

FIGURE 1 | Internal structure of the PCHE.

FIGURE 2 | Picture of PCHE prototype with heat transfer power of 50 kW.

Kim et al. (2012) had studied the thermal–hydraulic performance of helium in PCHE in the range of 350˂Re˂1,200. The hot side temperature was 25–550°C, the cold side temperature was 20–100°C, the test pressure was 1.5–1.9 MPa, and the mass flow rate was 40–100 kg/h. According to the inlet and outlet parameters of the heat exchanger, a correlation equation between Fanning's friction factor and Nusselt number was proposed. The numerical results with FLUENT were consistent with the experimental results. According to the CFD calculation, the Nusselt number correlation equation on the basis of the local average pitch was proposed, which was better than the correlation equation obtained by the experimental method. In addition, Kim and No. (2011) had studied the thermal–hydraulic performance of PCHE in high temperature gas cooled reactor with helium–water working fluid in the laminar flow range. Then, the numerical results had been compared with the experimental results, and a unified correlation between Fanning's friction factor and Nusselt number suitable for different working fluids was proposed.

Baik et al. (2017) developed the PCHE design code on the basis of MATLAB to accurately reflect the real gas effect near the critical point and carried out performance tests under various CO_2 conditions, including gas phase, liquid phase, and supercritical phase. The test temperature and pressure were 26–43°C and 7.3–8.6 MPa, respectively, with Reynolds number range of 15,000–100,000 and Prandtl number range of 2–33. They found that the designed PCHE showed satisfying heat transfer performance under both on-design and off-design conditions, which had more than 90% effectiveness within 200-mm small core. The correlations of friction factor and heat transfer were proposed.

Liu et al. (2020) designed and built the PCHE prototype of the straight channels and carried out experimental research on local thermal and hydraulic performance under wide operating conditions. The hot side system pressure was 7.53–11.97 MPa and the cold side was 0.14–0.18 MPa; the fluid temperature on the hot side was 26.40–121.27°C and that on the cold side was 23.10–60.96°C; the mass flow on the hot side was 50.03–780.11 kg/(m^2 s) and that on the cold side was 94.64–282.27 kg/(m^2 s). New correlations between convective heat transfer coefficient and Fanning friction coefficient were proposed, which had been applied in an analytical code for designing PCHE. The results showed good agreements between predictions and experimental bulk-fluid temperature along the axis, and the predicted and observed locations of the pinch point also showed good uniformity.

Cheng et al. (2020) experimentally studied the performance of a 100-kW PCHE for a module of a full-scale MW pre-cooler with water and SCO_2 as working medium and mainly studied the effects of inlet Reynolds number and temperature on both sides of the heat exchanger on heat transfer, pressure drop, and efficiency of the heat exchanger. They found that the total heat transfer coefficient and heat transfer rate increased with the increase of inlet Reynolds number. With the increase of Re_i on the hot side and cold side of PCHE by 69.48% and 79.61%, the overall heat transfer coefficient increased by 17.91% and 19.02%, respectively. Because the higher inlet Reynolds number increased the disturbance of fluid in the channel, the pressure drop increased with the increase of inlet Reynolds number. Higher efficiency could be obtained by increasing the inlet Reynolds number of water or decreasing the inlet Reynolds number of SCO_2.

Recently, a relevant research on the supercritical carbon dioxide power cycle systems has been conducted in the China Institute of Atomic Energy, including the development of a prototype with sodium-supercritical carbon dioxide of PCHE and a facility has been set up to test the performance of the PCHE.

INTRODUCTION OF THE PROTOTYPE OF HEAT EXCHANGER

The heat exchanger is the key equipment of the supercritical carbon dioxide Brayton cycle. The designed power of the heat exchanger is 50 kW. The core of the heat exchanger is formed by carbon dioxide plates and sodium plates, which is arranged alternately with one layer of sodium plate and two layers of carbon dioxide plates. The configuration is shown in **Figure 1**. The sodium plate is composed of circular channels with the

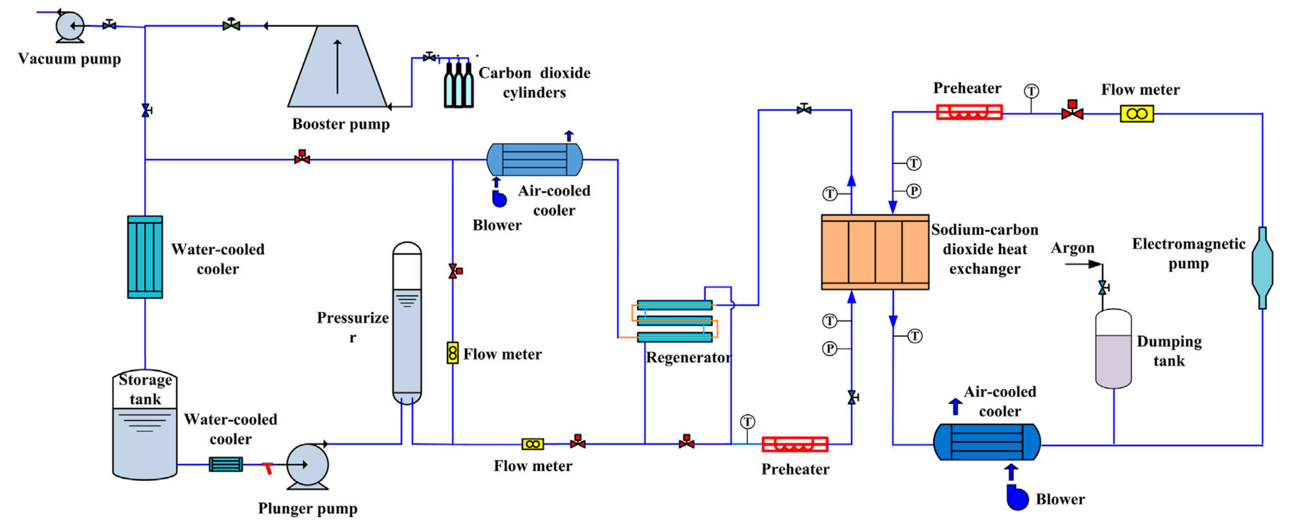

FIGURE 3 | Test system of the performance of the prototype.

diameter of 4 mm and the channel spacing of 6 mm. The circular channels are formed by two semi-circular channels. Each sodium plate has 40 channels with the thickness of 3 mm. The carbon dioxide plate is composed of semicircular channels with the diameter of 1.5 mm and the channel spacing of 2.5 mm. Each carbon dioxide plate has 26 channels with the thickness of 1.5 mm. The core size is 110°mm × 273°mm × 224°mm, and the final structure of the heat exchanger is shown in **Figure 2**.

INTRODUCTION OF THE TEST LOOP

The performance verification test system of the heat exchanger consists of two test loops, namely, the supercritical carbon dioxide test loop and the sodium test loop, which provides test condition for each side. The test system is shown in **Figure 3**.

The carbon dioxide is supplied by a plunger pump with a maximum pressure of 25 MPa and a flow rate of 2 m^3/h. The carbon dioxide flows through the pressurizer and regenerator, is heated by a preheater with a capacity of 120-kW DC, and then enters the heat exchanger. The carbon dioxide exchanges heat with the sodium in the heat exchanger. After the high-temperature carbon dioxide flows out of the heat exchanger, it is cooled by the air-cooled cooler with the capacity of 70 kW, is reduced the pressure by the pressure regulating valve and then further cooled by the water-cooled cooler with the capacity of 65 kW, and finally enters the storage tank. The pressure fluctuation generated during the operations is maintained and absorbed by the pressurizer in the test loop.

The sodium test loop is driven by an electromagnetic pump with a maximum flow rate of 1 m^3/h, and the mass flow rate is measured by the electromagnetic flow meter. The sodium is heated by the preheater with a capacity of 100-kW AC and flows through the heat exchanger. The sodium exchanges heat with the carbon dioxide in the heat exchanger. The sodium is finally cooled by the air-cooled cooler with the capacity of 50 kW and returns to the inlet of the electromagnetic pump. The pressure fluctuation and the thermal expansion of the working fluid are maintained and absorbed by the dumping tank in the test loop.

The flow rate of the carbon dioxide is measured by a mass flow meter with the measuring range of 0–0.5 kg/s and the accuracy of ±0.2%, and the sodium is measured by an electromagnetic flow meter with the measuring range of 0–0.33 kg/s and the accuracy of ±0.5%. The pressures are measured by pressure sensors with the measuring range of 0–25 MPa and the accuracy of ±0.1% at the inlet and outlet of the heat exchanger. In addition, the inlet and outlet temperatures of the heat exchanger are measured by the thermocouples with the measuring range of 0–600°C and the accuracy of ±0.5°C. All the parameters are recorded by a data acquisition system.

EXPERIMENTAL RESULTS AND ANALYSIS

In the test, the sodium side pressure was 0.1–0.2 MPa, the flow rate was 0.17–0.30 kg/s, and the inlet temperature was 490–520°C; the carbon dioxide side pressure was 15, 18, and 20 MPa, the flow rate was 0.21–0.24 kg/s, and the inlet temperature was 310–340°C. A total of 18 groups of steady-state experimental data were obtained.

During the test operation, the inlet pressure, mass flow rate, inlet and outlet temperature of the two sides, and the wall temperature of the heat exchanger were recorded. The experimental data were recorded every 1 s in the test system. Take the rated condition for an example, 1,800 continuous data points in the stable period are selected, and the average value of these data points is taken as the test data. The reduced test results are shown in **Table 1**.

TABLE 1 | Test results under rated condition.

Number	Item	Unit	Hot side	Cold side
1	Working fluid		Sodium	CO_2
2	Mass flow rate	kg/s	0.245	0.244
3	Pressure	MPa	0.13	19.98
4	Inlet temperature	°C	501.5	317.8
5	Outlet temperature	°C	326.7	498.5
6	Heat power	kW	54.8	54.2

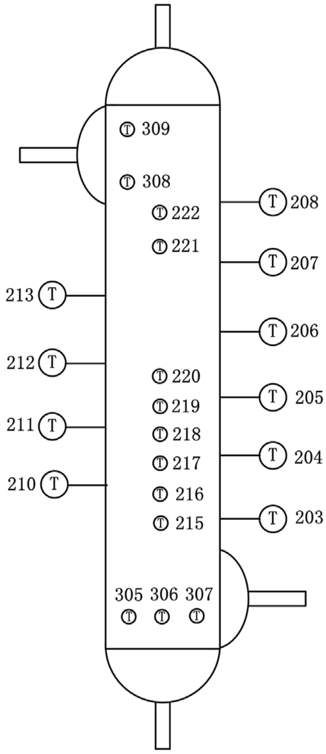

FIGURE 4 | Wall temperature layout of the heat exchanger.

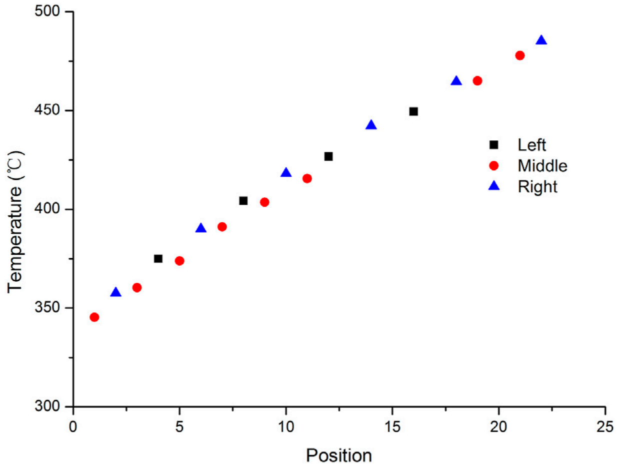

FIGURE 5 | Wall temperature under rated working condition.

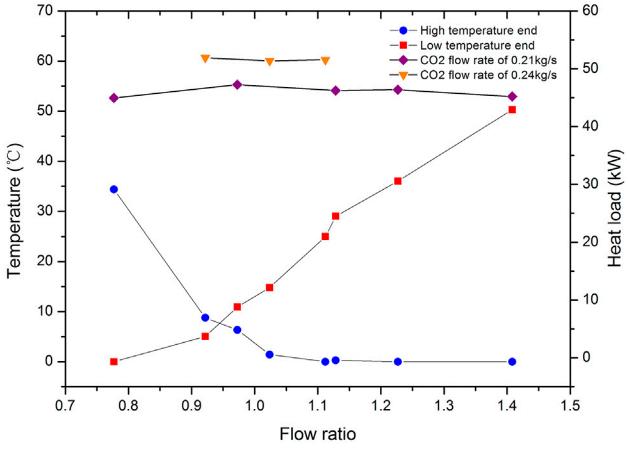

FIGURE 6 | Variation of temperature difference and heat transfer power with the flow ratio.

The calculation equations of the heat transfer power on sodium side and carbon dioxide side are as follows,

$$Q_H = m_H \overline{C_P} \left(T_{Hi} - T_{Ho}\right)$$
$$Q_C = m_C \left(h_{Co} - h_{Ci}\right)$$

where Q_H is the heat transfer power on the sodium side, m_H is the mass flow rate of sodium, T_{Hi} and T_{Ho} are the inlet and outlet temperature, and $\overline{C_P}$ is the average specific heat at constant pressure; Q_C is the heat transfer power on the carbon dioxide side, m_C is the mass flow rate of carbon dioxide, and h_{Ci} and h_{Co} are the inlet and outlet enthalpy.

The uncertainty in the test mainly comes from the systematic error and instrument accuracy, and the accuracy of instrument has been introduced above. The systematic error mainly includes the following aspects: 1) The temperature measuring points are arranged on the inlet and outlet pipes of the heat exchanger, and there is a certain deviation between the actual temperature and the measured value; 2) Because of heat dissipation, the heat transfer power on the sodium side will be greater than that on the carbon dioxide side, but the heat insulation is good, so that there is little difference between them; 3) The data acquisition system may produce errors in the process of signal conversion. By analyzing the test results under rated working condition, it can be seen that the accuracy of the pressure sensor is high; within the range of pressure error, the enthalpy of carbon dioxide changes little; and the main error is caused by temperature. Within the deviation of 0.5°C, the enthalpy difference is 0.62 kJ; according to the error transmission, the maximum error on the carbon dioxide side is 0.53 kW at 20 MPa. The specific heat of sodium is 1.33 kJ/(kg °C) at 501.5°C and 1.40 kJ/(kg°C) at 326.7°C; there is little difference between them, and the average value of the specific heat within the test temperature range is reasonable. In addition, considering the flow measurement error and temperature error,

TABLE 2 | Pressure effect on the heat transfer performance.

Pressure (MPa)	CO_2 mass flow rate (kg/s)	Na mass flow rate (kg/s)	Heat transfer power (kW)	Heat transfer coefficient (Wm^{-1}°C^{-1})
15.5	0.240	0.264	51.4	1,230
18.0	0.240	0.243	54.7	1,273
20.0	0.244	0.245	54.2	1,388

the maximum error on the sodium side is 0.54 kW. Considering the system error and heat dissipation, the heat transfer power on sodium side is 54.8 kW and that on carbon dioxide side is 54.2 kW, the relative error on both sides is within 1%. The difference of heat transfer power on both sides is 0.6 kW, the deviation of the heat balance is 1.09%, and the heat balance is good.

The heat transfer power of the heat exchanger under rated condition is 54.2 kW. According to the inlet and outlet temperature measured in the test, the total heat transfer coefficient of the heat exchanger under rated condition can be calculated. The calculation equations are as follows:

$$\boldsymbol{Q} = \boldsymbol{K} \cdot \boldsymbol{A} \cdot \Delta \boldsymbol{t}_{m}$$

$$\Delta \boldsymbol{t}_{m} = \frac{\Delta \boldsymbol{t}_{max} - \Delta \boldsymbol{t}_{min}}{\boldsymbol{ln}\left(\Delta \boldsymbol{t}_{max} / \Delta \boldsymbol{t}_{min}\right)}$$

where K is the total heat transfer coefficient of the heat exchanger, A is the heat transfer area, and Δt_m is the logarithmic mean temperature difference between two fluids. The expression of heat transfer coefficient is derived from the above two equations, as follows.

$$\boldsymbol{K}_{exp} = \frac{\boldsymbol{Q}_{exp}}{\boldsymbol{A} \cdot \Delta \boldsymbol{t}_{m}} = \frac{\boldsymbol{Q}_{exp}}{\boldsymbol{A} \cdot \frac{\Delta \boldsymbol{t}_{max} - \Delta \boldsymbol{t}_{min}}{\boldsymbol{ln}\left(\Delta \boldsymbol{t}_{max} / \Delta \boldsymbol{t}_{min}\right)}}$$

The heat transfer area is 7.3 m^2, and taking the inlet and outlet temperatures measured in the test into the equation, the total heat transfer coefficient of the heat exchanger under rated condition is 1,264 W/(m^2°C), and the designed total heat transfer coefficient is 1,301 W/(m^2°C); the difference between the two values is small.

In order to study the temperature change of the fluid along the flow channel, 18 temperature measuring points were arranged on the three walls of the heat exchanger along the flow direction. In addition, temperature measuring points were arranged at the outlet of the heat exchanger to measure the temperature non-uniformity. All the temperature measuring points were arranged on the surface of the heat exchanger. The arrangement of the wall temperature measuring points is shown in **Figure 4**. **Figure 5** shows the variation of the wall temperatures of the heat exchanger with the axial position.

As can be seen from **Figure 5**, the wall temperature of the heat exchanger increases linearly in the axial direction and along the flow direction of carbon dioxide. The inlet wall temperatures T305 ~ 307 of carbon dioxide side are 332.5, 330.4, and 328.7°C, respectively, and the outlet wall temperatures T308 and T309 of carbon dioxide side are 486.7 and 496.6°C, respectively. Because of the influence of cross flow, the temperature is non-uniform.

The test was conducted not only under rated condition but also under some other different experimental conditions. As shown in **Figure 6**, it shows the effect of different flow rates of sodium and carbon dioxide on the performance of the heat exchanger when the pressure of carbon dioxide is 15 MPa. The x-axis is the ratio of mass flow of sodium to carbon dioxide. As the flow ratio increases, the temperature difference at the inlet end on the sodium side (high temperature end) gradually decreases, and the temperature difference at the outlet end on the sodium side (low temperature end) gradually increases. This is because when the mass flow rate of sodium is small, the sodium side is cooled sufficiently, so the sodium outlet temperature is close to the carbon dioxide inlet temperature. When the mass flow rate of sodium is large, the carbon dioxide is heated sufficiently so that the carbon dioxide outlet temperature is close to the sodium inlet temperature. As can be seen from **Figure 6**, when the mass flow rate of carbon dioxide is constant, the heat transfer power of the heat exchanger changes little with the flow rate of sodium. However, the flow rate of sodium is constant, and the heat transfer power changes significantly with the flow rate of carbon dioxide.

The pressure influence of the carbon dioxide side on the heat transfer performance is also studied at same conditions. The results show that the heat transfer coefficient of the heat exchanger increases with the pressure increase of the carbon dioxide; when the pressure increases from 15.5 to 20 MPa, the heat transfer coefficient increases by 12.8%, as shown in **Table 2**. This is caused by the different physical properties of carbon dioxide at different pressures. **Figure 7** shows the variation law of thermal conductivity of carbon dioxide under different pressures. It can be seen that the higher the pressure, the greater the thermal conductivity, so the greater the heat transfer coefficient under the same conditions.

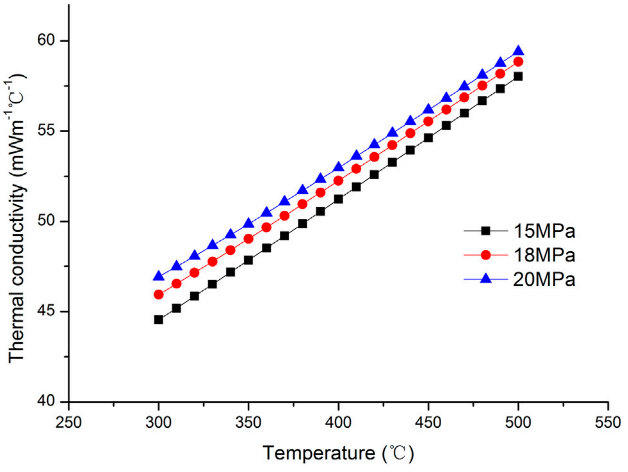

FIGURE 7 | The thermal conductivity of CO_2 varies with pressure and temperature.

CONCLUSION

In this paper, the experimental research on the prototype of sodium-supercritical carbon dioxide PCHE has been carried out under the rated condition and other different conditions. The influence of different parameters on the heat exchanger is studied, and the conclusions are as follows:

1) Under the rated condition, the heat transfer power is 54.2 kW, and the deviation is around 8%. The test results show that the prototype of the heat exchanger meets the design requirements;
2) The temperature difference of the high temperature end decreases with the increase of the flow ratio of sodium to carbon dioxide, and the temperature difference of the low temperature end increases with the increase of the flow ratio;
3) When the flow rate of sodium was constant, the heat transfer power changes significantly with the flow rate of carbon dioxide, the flow rate of carbon dioxide has a great effect on the heat transfer power; when the flow rate of carbon dioxide is constant, the effect of flow rate of sodium on heat transfer power is relatively small;
4) Under the same working conditions, the heat transfer coefficient of the heat exchanger increases with the increase of pressure of the carbon dioxide; when the pressure increases from 15.5 to 20 MPa, the total heat transfer coefficient increases by 12.8%.

DATA AVAILABILITY STATEMENT

The original contributions presented in the study are included in the article/Supplementary Material, further inquiries can be directed to the corresponding author.

AUTHOR CONTRIBUTIONS

DZ was mainly responsible for the test operation, data analysis, and paper drafting. MZ was mainly contributed to the data analysis. PL was mainly responsible for the numerical calculation. WL was mainly responsible for paper review and modification.

FUNDING

The present investigation is supported by the National Key R and D Program of China (2018YFE0116100).

ACKNOWLEDGMENTS

The authors wish to thank the CIAE team who performed the test verification under rated condition and different other conditions and provided the test data for analysis.

REFERENCES

Baik, S., Kim, S. G., Lee, J., and Lee, J. I. (2017). Study on CO2 - Water Printed Circuit Heat Exchanger Performance Operating under Various CO_2 Phases for S-CO_2 Power Cycle Application. *Appl. Therm. Eng.* 113, 1536–1546. doi:10.1016/j.applthermaleng.2016.11.132

Cheng, K., Zhou, J., Zhang, H., Huai, X., and Guo, J. (2020). Experimental Investigation of thermal-hydraulic Characteristics of a Printed Circuit Heat Exchanger Used as a Pre-cooler for the Supercritical CO2 Brayton Cycle. *Appl. Therm. Eng.* 171, 115116. doi:10.1016/j.applthermaleng.2020.115116

Dostal, V. (2004). "A Supercritical Carbon Dioxide Cycle for Next Generation Nuclear Reactors. Doctoral Dissertation. Cambridge, MA(USA): MIT.

Kim, I., No, H., Lee, J., and Jeon, B. (2012). Thermal Hydraulic Performance Analysis of the Printed Circuit Heat Exchanger Using a Helium Test Facility and CFD Simulations. *Nucl. Eng. Des.* 239 (11), 2399–2408. doi:10.1016/j.nucengdes.2009.07.005

Kim, I., and No, H. (2011). Thermal Hydraulic Performance Analysis of a Printed Circuit Heat Exchanger Using a Helium–Water Test Loop and Numerical Simulations. *Appl. Therm. Eng.* 31 (17-18), 4064–4073. doi:10.1016/j.applthermaleng.2011.08.012

Liu, S.-h., Huang, Y.-p., Wang, J.-f., Liu, R.-l., and Zang, J.-g. (2020). Experimental Study of thermal-hydraulic Performance of a Printed Circuit Heat Exchanger with Straight Channels. *Int. J. Heat Mass Transfer* 160, 120109. doi:10.1016/j.ijheatmasstransfer.2020.120109

Ngo, T. L., Kato, Y., Nikitin, K., and Tsuzuki, N. (2006). New Printed Circuit Heat Exchanger with S-Shaped Fins for Hot Water Supplier. *Exp. Therm. Fluid Sci.* 30, 811–819. doi:10.1016/j.expthermflusci.2006.03.010

Wang, J., Feng, Y., and Han, D. (2019). Review on Supercritical Carbon Dioxide Power Cycle Application in Sodium Cooled Fast Reactor. *Nucl. Sci. Eng.* 39 (2), 289–297. doi:10.3969/j.issn.0258-0918.2019.02.017

Yang, W. (2014). Gen IV Energy Conversion Systems——Research on Modeling of Supercritical Carbon Dioxide Brayton Cycle and Technology Readiness Assessment. Doctoral Dissertation. Xiamen(China): Xiamen University.

Yu, G., Chen, Y., Li, X., and Wu, X. (2017). Research Progress in Heat Transfer and Fluid Flow of Printed Circuit Heat Exchanger. *Fluid Machinery* 45 (12), 73–79. doi:10.3969/j.issn.1005-0329.2017.12.015

Conflict of Interest: The authors declare that the research was conducted in the absence of any commercial or financial relationships that could be construed as a potential conflict of interest.

frontiers | Frontiers in Energy Research

ORIGINAL RESEARCH
published: 01 April 2022
doi: 10.3389/fenrg.2022.885564

Numerical Study on Heat Transfer and Enhancement Mechanism in PCM-Filled Shell-and-Tube Heat Exchangers

Jiabin Fang*, Tao Han, Yixin Bi, Haobing Yan and Jinjia Wei

School of Chemical Engineering and Technology, Xi'an Jiaotong University, Xi'an, China

A numerical model was established using the enthalpy-porosity approach to study the heat transfer characteristics of a shell-and-tube phase change heat exchanger filled with paraffin wax RT50. The influence of exchanger placement forms, tube diameters and fin structures on the phase change process of RT50 was analyzed. The results depicted that the vertical heat exchanger has a faster melting rate than the horizontal one as the tube diameter is large. However, the opposite results were obtained in case the tube diameter is small. For the horizontal exchanger, the heat conduction is dominant at the beginning and end of the melting process, while the natural convection plays a more important role at the intermediate stage of melting. Besides, the duration of the melting is mainly determined by the natural convection. In addition, adopting fins on the outer of the tube can significantly improve the heat transfer and therefore shorten the melting time. Compared with finless tube, the use of annular-fin tube can reduce the melting time by 31.6% mainly because of the intensifying of heat conduction, while the use of straight-fin tube can shorten the melting time by 42.1% attributed to the enhancement of both natural convection and heat conduction during the melting process.

Keywords: phase change material, melting, fins, natural convection, heat storage

Edited by:
Luteng Zhang,
Chongqing University, China

Reviewed by:
Naveed Ahmed,
National University of Sciences and Technology (NUST), Pakistan
Wei Wu,
Northwest University, China
Hossain Nemati,
Islamic Azad University, Iran

****Correspondence:***
Jiabin Fang
jiabinfang@mail.xjtu.edu.cn

Specialty section:
This article was submitted to Nuclear Energy, a section of the journal Frontiers in Energy Research

Received: *28 February 2022*
Accepted: *10 March 2022*
Published: *01 April 2022*

Citation:
Fang J, Han T, Bi Y, Yan H and Wei J (2022) Numerical Study on Heat Transfer and Enhancement Mechanism in PCM-Filled Shell-and-Tube Heat Exchangers. Front. Energy Res. 10:885564. doi: 10.3389/fenrg.2022.885564

INTRODUCTION

The intensifying of global warming and worldwide energy crisis have forced the world to optimize the current energy structure. Nuclear power as an eco-friendly technology has already plays a significant role in promoting this energy transition and greatly alleviates the fossil fuel dependence. One of the novel options is to integrate the nuclear reactor with thermal energy storage (TES), and this coupled system can greatly improve the stability and reliability of nuclear power plants in case of accidents (Alkaabi et al., 2019; Norouzi et al., 2021). The existing TES technologies can be mainly classified into three types: sensible heat thermal energy storage (SHTES), latent heat thermal energy storage (LHTES) and thermochemical energy storage (TCES). In LHTES system, phase change materials (PCMs) are used to store or release heat within a narrow temperature change (Dutil et al., 2011) and regarded as one of the most promising energy storage technologies (Agyenim et al., 2010) due to the advantages of large energy storage density and good chemical stability (Sharma et al., 2002).

The shell-and-tube heat exchanger is widely used in the LHTES system. So far, a lot of analytical, experimental and numerical investigations have been conducted on the heat transfer performance of the phase change shell-and-tube heat exchanger. Lacroix (Lacroix, 1993) established a theoretical

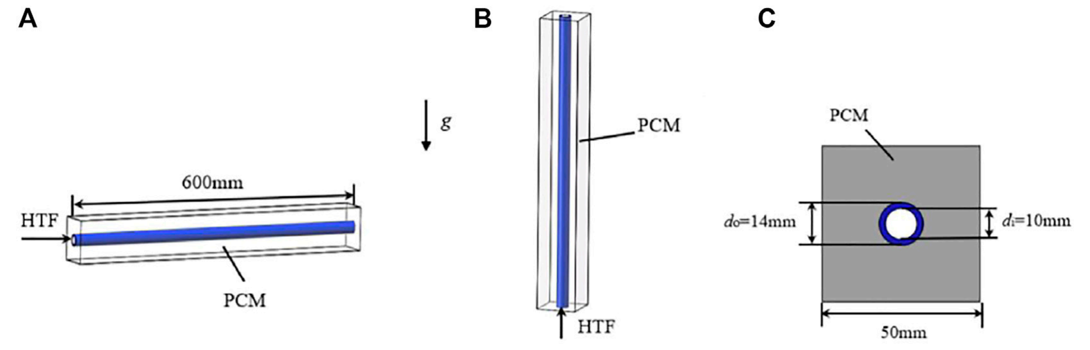

FIGURE 1 | Shell-and-tube phase-change heat storage unit: **(A)** horizontal placement, **(B)** vertical placement and **(C)** cross-section of the unit.

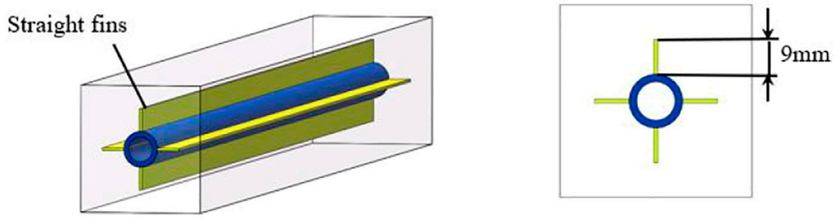

FIGURE 2 | The shape and dimensions of the straight-fin-tube heat storage unit.

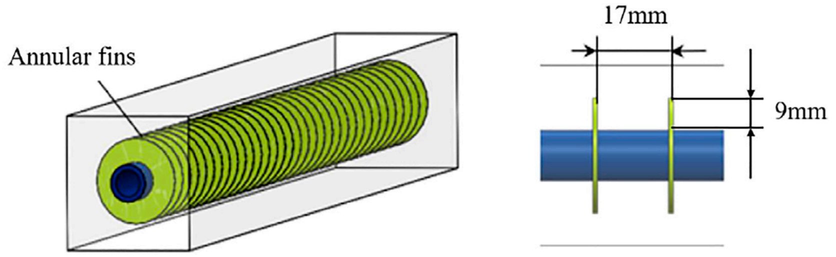

FIGURE 3 | The shape and dimensions of the annular-fin-tube heat storage unit.

model to predict the transient behavior of a shell-and-tube LHTES system filled with PCM. The result showed that the common problem of PCM is owing to its low thermal conductivity, which causes the low heat transfer rate and delayed response. Blen et al. (2008) experimentally studied the melting and solidification characteristics of $CaCl_2.6H_2O$ as the PCM in a vertical double concentric tube energy storage system. They investigated the influence of different designs and operating parameters, such as the number of fins in the PCM, the mass flow rate and the inlet temperature of heat transfer fluid (HTF) on the melting and solidification process. It was found that the design parameters have a more significant impact on the melting process than the operating parameters.

With the rapid development of computational fluid dynamics, the numerical investigations on LHTES have become a research hotspot. By establishing the numerical model, it is convenient to optimize the shape and size of exchangers, obtain the instantaneous solidification/melting rate of PCM and evaluate the thermal performance of LHTES system without spending a large amount of research funding (Viskanta, 2018). Lamberg et al. (2004) used the enthalpy-porosity method and an effective heat capacity method to numerically study the solidification/melting process of paraffin at low temperatures. They proved that when the natural convection is ignored, the simulation results have obvious errors. Nemati and Habibi (2021) developed an analytical and numerical analysis of RT27 solidification in partially filled spherical capsules. After validating the results, RT27 solidification in spheres with different diameters and wall temperature was simulated. In their study, the convection in the free space over the RT27 surfaces was also considered since the capsule was allowed to breathe freely. Hosseini et al. (2012) adopted a combination of experimental and numerical methods to study the buoyancy-

TABLE 1 | Thermophysical properties of RT50 (Hosseini et al., 2012).

Properties	**RT50**
T_s [K]	318
T_{liq} [K]	324
ρ [kg/m^3]	780
c_p [J/(kg·K)]	2000
k [W/(m·K)]	0.2
L [J/kg]	168,000
β [1/K]	0.0006

driven convection during the melting process of paraffin wax RT50 in a shell-and-tube thermal energy exchanger. They found that an appropriate increase of inlet water temperature can effectively reduce the heat transfer time. Pahamli et al. (2016) studied the influence of parameters such as eccentricity, flow rate, and inlet water temperature on the PCM melting process through numerical simulation.

A challenge of the application of LHTES is that most PCMs have the low thermal conductivity, resulting in great obstacles to the charging and discharging processes (Guo and Goumba, 2018; Zheng et al., 2018). Therefore, various methods have been proposed including PCM encapsulation (Yu et al., 2018; Shin et al., 2019), adding fins (Gharebaghi and Sezai, 2007; Rathod and Banerjee, 2015), using metal foam (Allen et al., 2015; Ghahremannezhad et al., 2020) and high thermal conductivity nanoparticles (Ibrahem et al., 2017; Ghalambaz et al., 2021) to solve this problem. Among them, adding fins to the shell-and-tube thermal energy storage system for enhancing the heat transfer is regarded as the most common measure which has been widely used. Guo and Zhang (2008) numerically established a two-dimensional transient model to study the effects of aluminum fins, tube radius, boundary conditions and thermal conductivity of the PCM on the charge and discharge time in the LHTES. Meghari et al. (2021) carried out the CFD numerical simulations to evaluate the melting process of a PCM embedded in a spherical capsule. They adopted a thin straight circumferential fin along the capsule equator to increase the heat exchange area. The results depicted that the melting time is reduced 14 times in the case of PCM with fins compared to the configuration without fins. Zhang et al. (2020) applied the fractal-tree-shaped structure to the metal fin design of the shell-and-tube LHTES, and they found that the heat release performance was significantly improved. Sciacovelli et al. (2015) used the different tree-shaped fins to enhance the performance of the shell-and-tube LHTES. They also proposed a shape optimization strategy to improve the transient operating system.

By literature survey, the heat transfer characteristics in different phase change stages of PCM have not been deeply analyzed in LHTES system. Besides, the mechanism of heat transfer enhancement during the phase change process is also rarely mentioned. In the present work, a heat storage unit belonging to a shell-and-tube phase-change exchanger was numerically researched. By adopting the enthalpy-porosity approach, a numerical model was established to investigate the effects of heat storage unit placement forms (vertical and horizontal), tube diameters and fin structures on the heat transfer and flow behavior of PCM during its phase change process. Furthermore, the mechanism of heat transfer enhancement by natural convection was also explained for finned tube heat storage units.

MODEL DESCRIPTION

Physical Model

In previous studies, most of researchers mainly focused on the design and operating parameters of the shell-and-tube heat exchanger in LHTES, but the placement of the exchanger has received rare attention. In the present work, a heat storage unit of a shell-and-tube phase-change exchanger was investigated as the research object depicted in **Figure 1**, and the effects of two different placement forms on the heat storage process were compared. As shown in **Figures 1A,B**, the researched unit with the length of 600 mm was placed horizontally and vertically. The force of gravity is

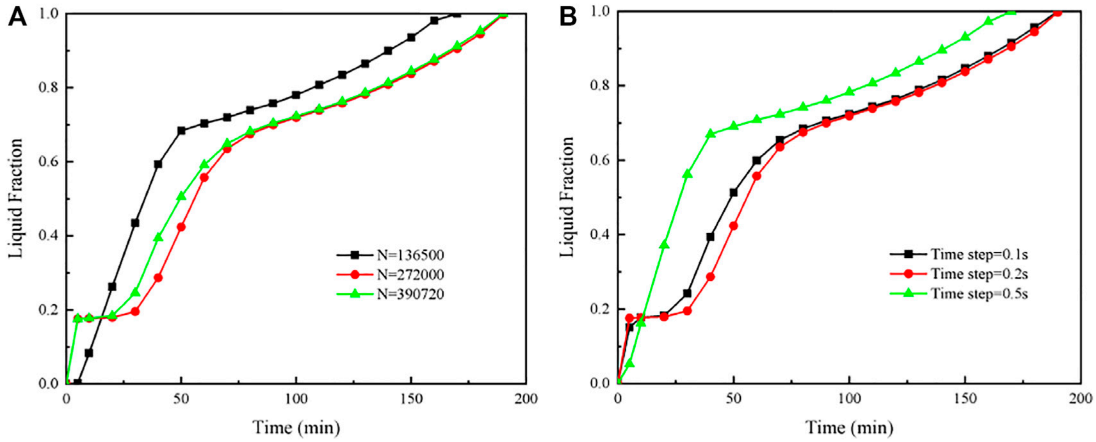

FIGURE 4 | Independence validations on **(A)** grid number and **(B)** time step.

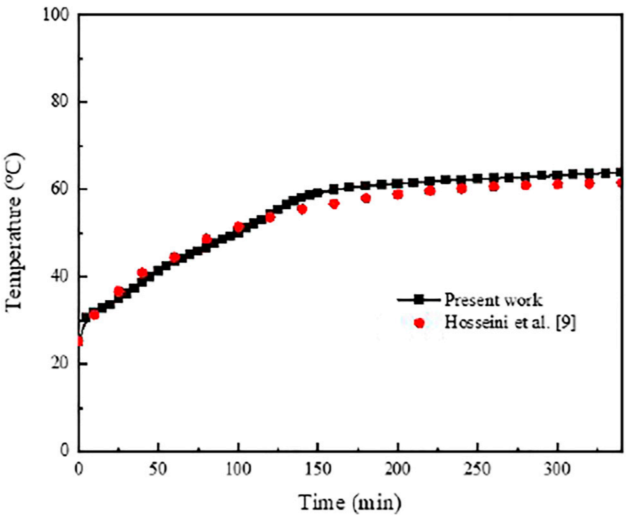

FIGURE 5 | Comparison of the average temperature profile in the PCM obtained from the present numerical model against the experimental results from Hosseini et al. (Hosseini et al., 2012).

vertical downwards as indicated in the figure. The PCM fills the shell side, and the tube side was arranged in the middle of the PCM, which can be clearly observed from the cross-sectional view in **Figure 1C**. Paraffin wax RT50 was chosen as the PCM, and water as the HTF goes through the tube side. **Table 1** list the thermophysical properties of RT50.

Besides, the dynamic viscosity of RT50 was considered temperature-dependent, and the relationship between dynamic viscosity and temperature can be expressed as:

$$\mu = Ae^{BT} \tag{1}$$

where A and B are both constant, and were respectively set to 0.819 and -0.01546 (Hosseini et al., 2012).

For organic phase change materials, the thermal conductivity is usually small, which is also one of the shortcomings in LHTES applications. A common solution is to use finned tubes to enhance the heat transfer. Some studies investigated the effects of fin height as well as its spacing on heat transfer enhancement, and some researchers have already designed various fin structures to improve the heat transfer efficiency. However, most of the new fin structures are complicated and difficult to widely used. The present study adopted the two common fin structures, straight fins and annular fins, and investigated their influence on the PCM melting process. For better comparison, the same surface area and the volume were designed for both types of fins. **Figure 2** and **Figure 3** depict the straight-fin-tube and annular-fin-tube heat storage unit, in which the fins were installed on the horizontal heat storage tube as shown in **Figure 1A**. It can be seen from the cross-sectional view in **Figures 2**, **3**, the height is 9 mm and the thickness is 2 mm for both types of fins. There are 33 annular fins with the spacing of 17 mm installed on the outer of the tube. The material for both tubes and fins is 304 stainless steel, and its thermal conductivity and density were set to be 16.2 W $m^{-1}{\cdot}K^{-1}$ and 7,930 kg m^{-3}, respectively.

Numerical Model

In order to simplify the numerical model, the following hypotheses were proposed: 1) The shell side of the heat storage unit was regarded as adiabatic due to the good thermal insulation. 2) The natural convection was considered during the melting of PCM. As mentioned by some studies (Sarı and Kaygusuz, 2002; Dhaidan et al., 2013; Yazici et al., 2014), the convective heat transfer cannot be neglected during the phase-change heat storage process. 3) Both the water and PCM have uniform and isotropic thermophysical properties. 4) The thickness of the tube and the fin was also considered in this paper.

For the solution of the phase-change process, the enthalpy-porosity method (Brent et al., 1988; Gong et al., 1999) has been widely used, and the phase interface can be determined by solving the enthalpy distribution. The governing equations include continuity equation, momentum equation and energy equation as below.

Continuity equation:

$$\nabla \cdot \vec{V} = 0 \tag{2}$$

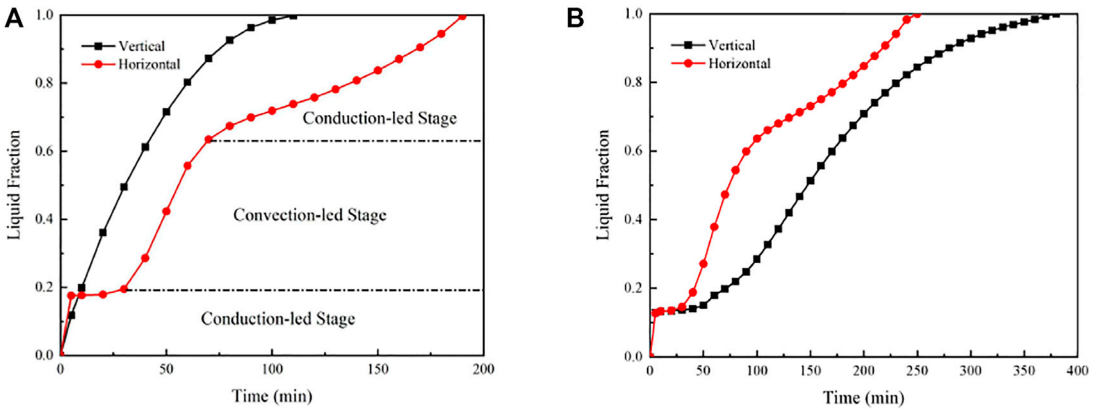

FIGURE 6 | Variations of liquid fraction versus time for the vertical and horizontal heat storage units. **(A)** d_o = 14 mm, d_i = 10 mm. **(B)** d_o = 10 mm, d_i = 6 mm.

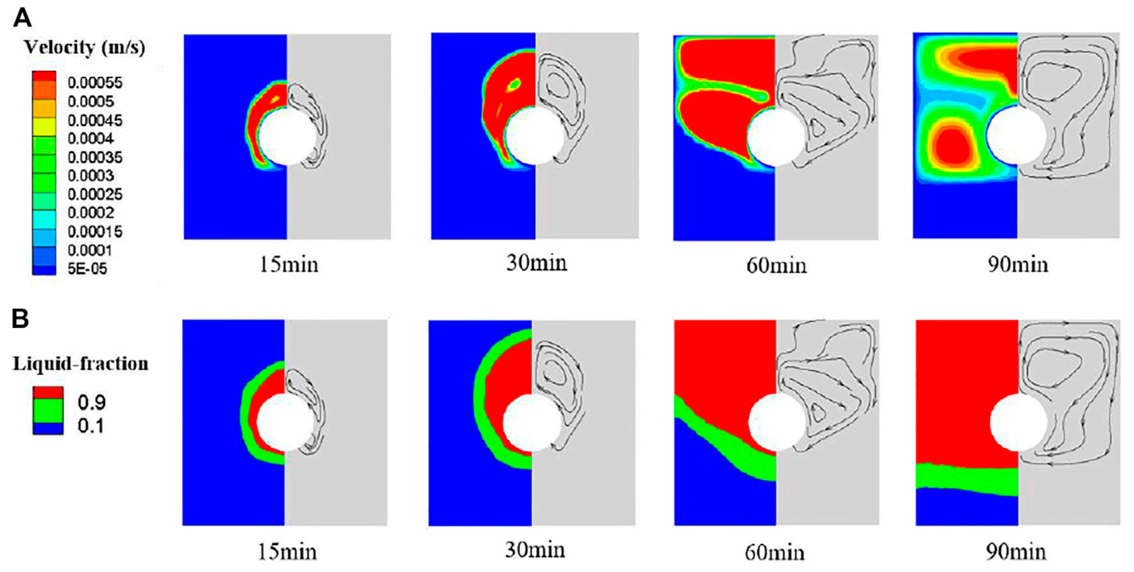

FIGURE 7 | Profiles of the velocity and liquid fraction on the middle cross-section along the length of the horizontal heat storage unit during the PCM melting process. **(A)** Velocity profiles. **(B)** Liquid fraction profiles. The black arrows indicate the flow direction of the liquid PCM. The outer/inner diameter (d_o/d_i) of the tube is 14/10 mm.

Momentum equation:

$$\frac{\partial \vec{V}}{\partial t} + \vec{V} \cdot \nabla \vec{V} = \frac{1}{\rho}\left(-\nabla P + \mu \nabla^2 \vec{V} + \rho \beta \vec{g}\left(T - T_{\mathrm{ref}}\right)\right) + \vec{S} \tag{3}$$

Energy equation:

$$\frac{\partial h_{\mathrm{sens}}}{\partial t} + \frac{\partial h_{\mathrm{lat}}}{\partial t} + \nabla \cdot \left(\vec{V} h_{\mathrm{sens}}\right) = \nabla \cdot \left(\frac{k}{\rho c_p} \nabla h_{\mathrm{sens}}\right) \tag{4}$$

where h_{sens} is the sensible enthalpy, which can be expressed as:

$$h_{\mathrm{sens}} = h_{\mathrm{ref}} + \int_{T_{\mathrm{ref}}}^{T} c_p \mathrm{d}T = h_{\mathrm{ref}} + c_p \int_{T_{\mathrm{ref}}}^{T} \mathrm{d}T \tag{5}$$

And the latent enthalpy h_{lat} can be written as follows:

$$h_{\mathrm{lat}} = \lambda L \tag{6}$$

where L is the latent heat of the material, and λ can be definned as:

$$\lambda = \begin{cases} \dfrac{h_{lat}}{L} = 0 & if\ T < T_s \\ \dfrac{h_{lat}}{L} = 1 & if\ T > T_{\mathrm{liq}} \\ \dfrac{h_{lat}}{L} = \dfrac{T - T_s}{T_{liq} - T_s} & if\ T_s < T < T_{\mathrm{liq}} \end{cases} \tag{7}$$

In **Eq. 3**, the source term $\vec{S}$ is the Darcy's law damping terms which are added to the momentum equation due to phase change effect on convection, and can be calculated as the following equation:

$$\vec{S} = \frac{(1 - \lambda)}{\lambda^2 + \chi} A_{mush} \vec{V} \tag{8}$$

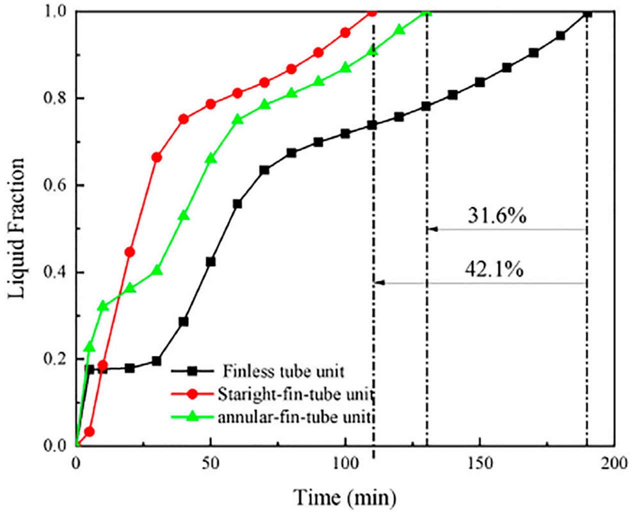

FIGURE 8 | Variations of liquid fraction versus time for the horizontal heat storage units with the finless tube, straight-fin tube and annular-fin tube. The outer/inner diameter (d_o/d_i) of the tube is 14/10 mm.

A_{mush} is mushy zone constant, which is usually taken between 10^4–10^7. In the present study, it was set to 10^6. Besides, the constant χ is a small number to prevent division by zero.

Boundary and Initial Conditions

The initial temperature of the PCM T_0 was set to 25°C, and the inlet temperature $T_{\mathrm{f,i}}$ and velocity v of the HTF are respectively 70°C and 0.044 m/s. In addition, the outer surface of the shell side was assumed to be insulated.

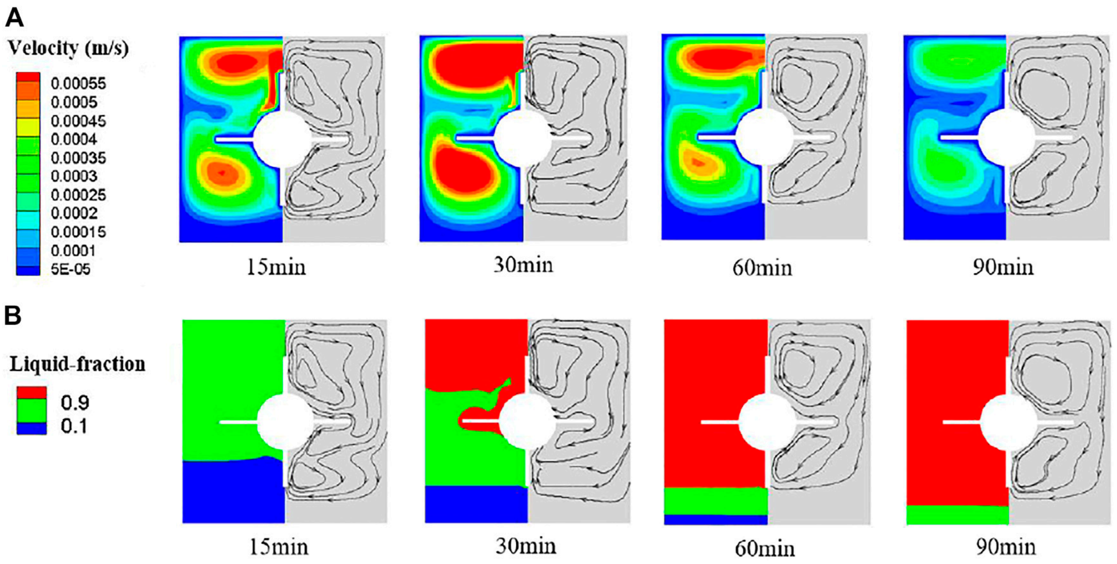

FIGURE 9 | Profiles of the velocity and liquid fraction on the middle cross-section along the length of the horizontal heat storage unit with the straight-fin tube during the PCM melting process. **(A)** Velocity profiles. **(B)** Liquid fraction profiles.

Computational Methodology and Validation

The governing equations were solved by the commercial CFD code ANSYS Fluent 19.2. The Semi-Implicit Pressure-Linked Equation (SIMPLE) algorithm (Patankar, 2018) was employed to solve the pressure-velocity coupling equations, and the PRESTO scheme was adopted for the pressure correction equation. Besides, the number of mesh grids and time step independence validations were also performed. As illustrated in **Figure 4**, the numerical results have an acceptable accuracy as the number of mesh grids exceeds 272,000 and the time step is lower than 0.2 s. Therefore, the grid number of 272,000 and the time step of 0.2 s were used in the present simulation in order to reduce the computational cost. In addition, the residual errors were set to 10^{-6} for the energy equation and 10^{-5} for other variables.

In order to validate the numerical model established in the present study, the average temperature profile in the PCM was compared with the experimental results obtained from Hosseini et al. (Hosseini et al., 2012). As shown in **Figure 5**, good agreement can be observed, and the temperature deviation is within 5%.

RESULTS AND DISCUSSION

Effects of the Heat Storage Unit Placement Forms on the Phase-Change Process

The effects of the unit placement forms on the phase-change process were investigated. **Figure 6** depicts the variation trends of liquid fraction versus time for the vertical and horizontal heat storage units at different tube diameters. It can be found that the vertical heat storage unit has a higher melting rate than the horizontal one when the tube diameter is larger. However, the opposite results were obtained at the smaller tube diameter as shown in **Figure 6B**. In terms of melting time, the phase change process in the vertical heat storage unit was greatly affected by the tube diameter (i.e. the thickness of the PCM). Besides, compared with the vertical heat storage unit, the PCM melting process is more complicated in the horizontal one, which can be divided into three stages according to the dominant heat transfer: the conduction-led stage in the initial period, the convection-led stage in the intermediate period and the conduction-led stage in the final period. **Figure 7** shows the profiles of velocity and liquid fraction on the middle cross-section of the horizontal heat storage unit. Combined with **Figure 6A**, the three stages during the PCM melting process can be further analyzed.

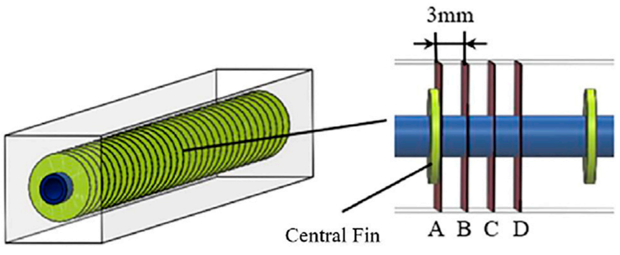

FIGURE 10 | Schematic of four selected typical cross-section positions of the annular-fin-tube heat storage unit.

In the initial stage, the thin layer of PCM which directly contacts with the tube wall is heated and rapidly melts due to the heat conduction. And then, the heat conduction is worsened because of the increased thermal resistance as the thickness of the liquid PCM increases. At this moment, the variation of liquid fraction tends to be flattened as depicted in **Figure 6A**. As the liquid region gradually

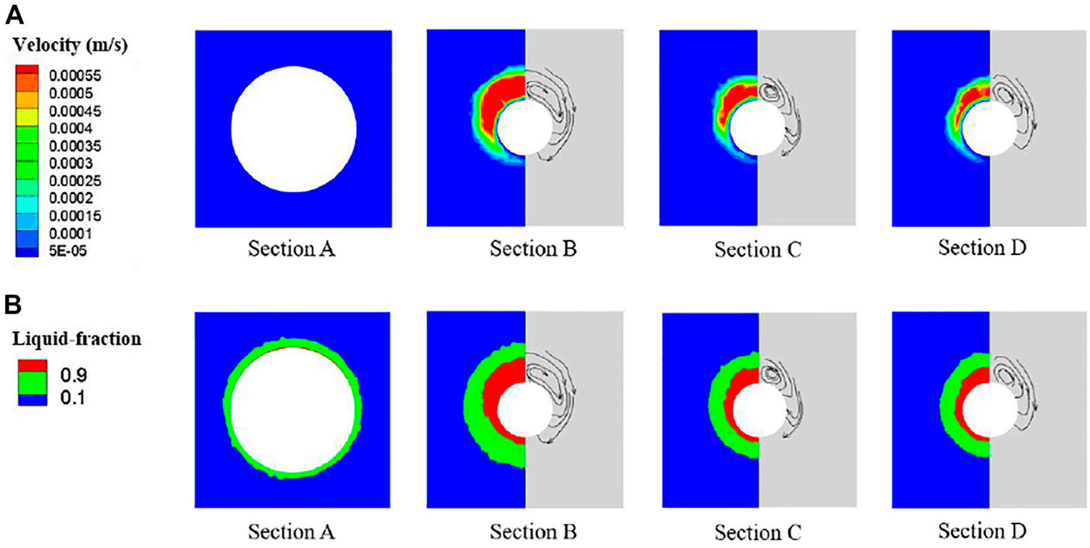

FIGURE 11 | Profiles of the velocity and liquid fraction on the four selected cross-sections of the annular-fin-tube horizontal heat storage unit at the moment of 15 min. **(A)** Velocity profiles. **(B)** Liquid fraction profiles.

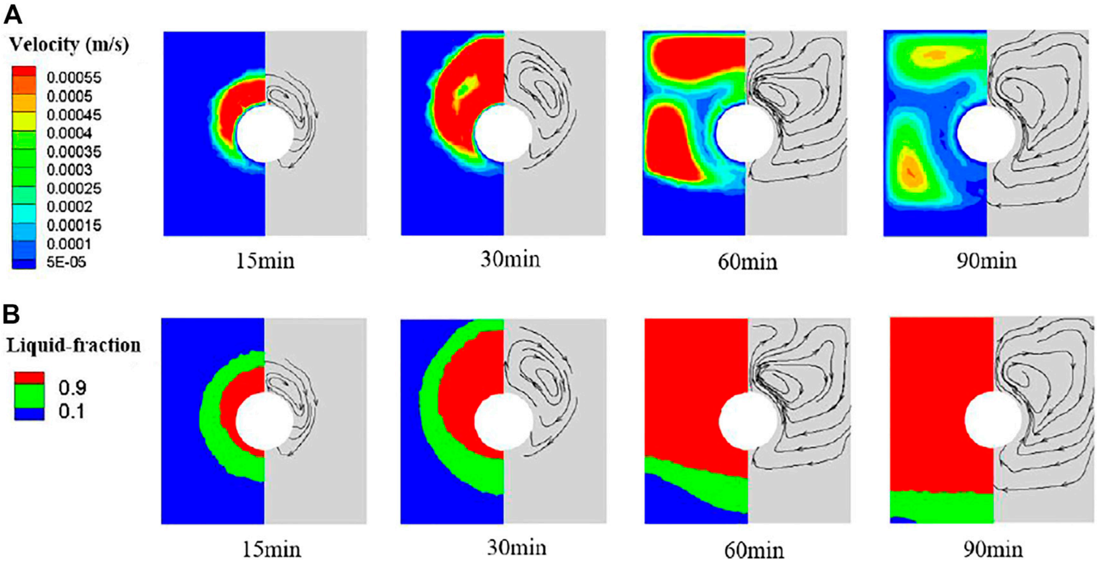

FIGURE 12 | Profiles of the velocity and liquid fraction on cross-section B of the annular-fin-tube horizontal heat storage unit during the PCM melting process. **(A)** Velocity profiles. **(B)** Liquid fraction profiles.

expands, the natural convection occurs driven by the density differences. It can be observed from **Figure 7**, the liquid PCM climbs up along the hot tube wall and descends along the cold solid-liquid interface, forming a natural convection cycle. Thus, the melting rate of RT50 significantly increases in this intermediate stage. After 60 min, the solid-liquid interface drops to the lower part of the shell side, and the PCM in the upper part completely melts. As the solid-liquid interface shrinks, the natural convection is weakened, leading to the reduction of melting rate. In the final stage, the heat conduction dominants again due to the thinning of the solid PCM.

Effects of Finned Tubes on the Phase-Change Process of PCM

To investigate the enhancement of PCM melting process by adopting finned tubes, the straight-fin tube and the annular-fin

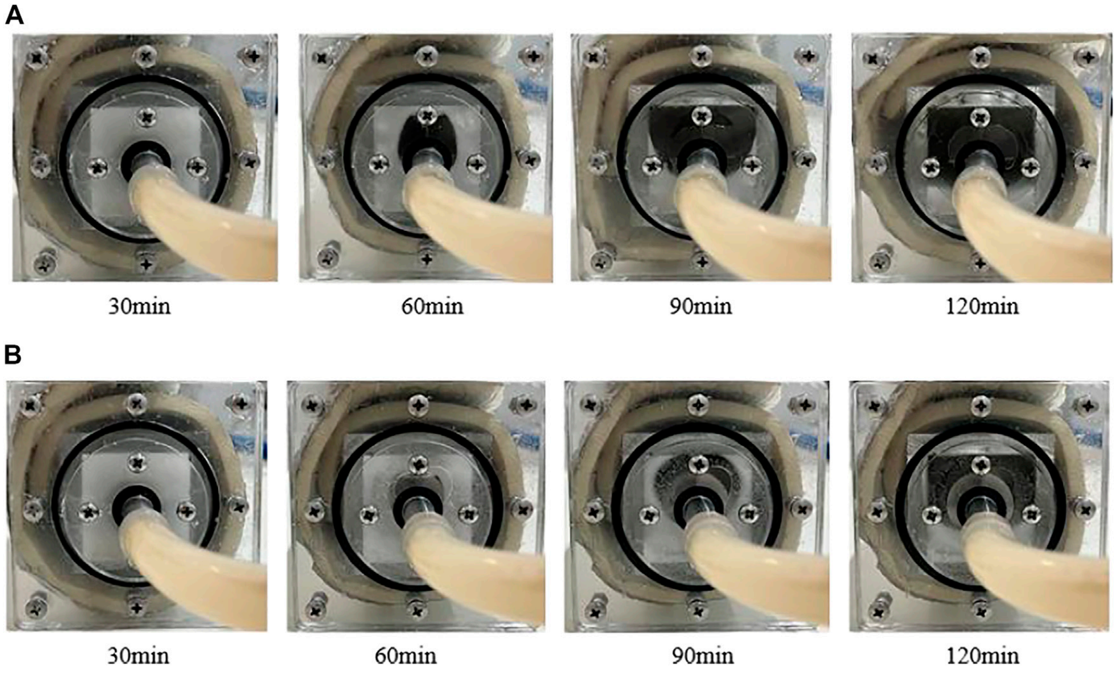

FIGURE 13 | Melting process of Paraffin wax RT50 in the finned tube heat storage units. **(A)** Straight-fin-tube heat storage unit. **(B)** Annular-fin-tube heat storage unit.

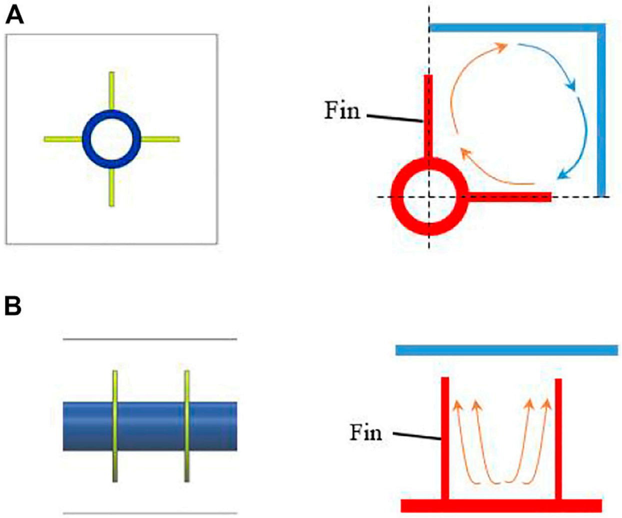

FIGURE 14 | Schematic of natural convective heat transfer in the finned tube heat storage units. **(A)** Straight-fin-tube heat storage unit. **(B)** Annular-fin-tube heat storage unit.

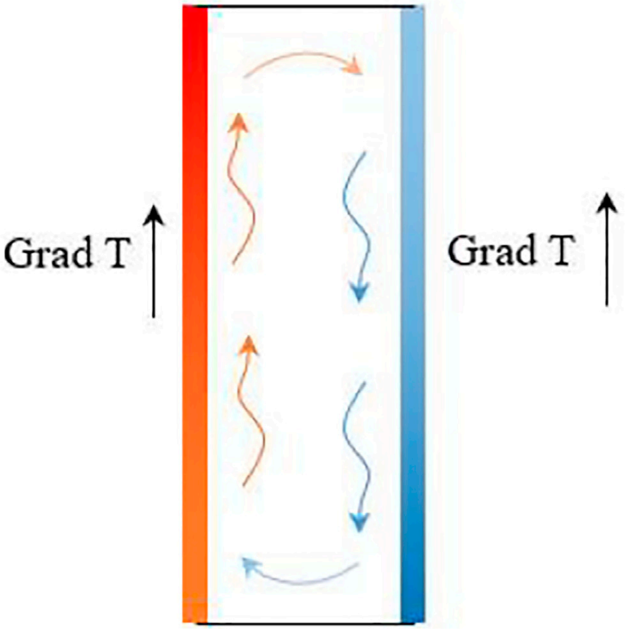

FIGURE 15 | Schematic of natural convective cycle and wall temperature gradients.

tube were compared in the horizontal heat storage units. It can be seen from **Figure 8**, compared with the finless tube, the melting time of PCM is shortened by 31.6% with the annular-fin tube and 42.1% by using the straight-fin tube. Obviously, the reinforced heat transfer by the straight-fin tube is much better. By analyzing the velocity and liquid fraction profiles as illustrated in **Figure 9**, it can be found that the PCM flow region is significantly enlarged for a very short time by adopting the straight-fin tube at the beginning of the melting process, basically covering the entire unit. Therefore, the total melting time of PCM is reduced, which is mainly determined by the convection-led stage, since the natural convection is greatly enhanced.

In order to better observe the phase change process in the annular-fin-tube heat storage unit, four typical cross-sections at 0 mm, 3 mm, 6 mm and 9 mm away from the middle fin were selected as indicated in **Figure 10** based on the left-right symmetry of the heat storage unit. Cross-section D is almost located at the middle of the two adjacent annular fins, and cross-section A is located on the surface of the middle fin. At the moment of 15 min, the velocity and liquid fraction profiles on the selected cross-sections were displayed in **Figure 11**. As can be found that there are no streamlines on the cross section A. The liquid region on cross section B is the largest, and gradually shrinks as the distance from the middle fin increases due to the weaken of heat conduction. During the melting process, the profiles of velocity and liquid fraction on cross section B were also drawn in **Figure 12**. Both the flow fields and liquid fraction are quite similar to those in the finless tube heat storage unit as shown in **Figure 7**. Since the convective region is not significantly expanded by the annular fins, the enhancement of convective heat transfer is limited. Therefore, the reduction of PCM melting time due to the annular fins is mainly attributed to the heat conduction intensifying in the initial period as can be clearly seen from **Figure 8**.

In order to verify the numerical simulation results obtained from the present numerical model, the experimental studies on the melting process of Paraffin wax RT50 in the straight-fin-tube and annular-fin-tube heat storage units were respectively performed. Note that Paraffin wax RT50 is white in the solid state and colorless in the liquid state. Compare **Figures 13A,B**, it can be found that the melting rate of RT50 by using the straight-fin tube is higher than that with the annular-fin tube, which is consistent with the numerical results as mentioned above. Since the melting process has obviously stepped into the conduction-led stage in the final period after 120 min, the melting rate of RT50 becomes slowly in this stage due to its low thermal conductivity. Thus, the melting process on the cross-section was not involved in **Figure 13** after 120 min. Besides, the complete melting time of RT50 in the experiments is a little longer than that in the numerical simulations owing to the poor insulation measures. In addition, more experimental studies will be carried out in the future work.

Mechanism of Natural Convective Heat Transfer in the Finned Tube Heat Storage Units

The natural convection can be simplified in the finned tube heat storage units as shown in **Figure 14**. As for the straight-fin-tube heat storage unit depicted in **Figures 14A**, a relatively closed space is formed by the hot tube and straight fins as well as the cold shell. In this space, the liquid PCM climbs up along the hot wall and descends down along the cold wall, forming a natural convective cycle. In the case of the annular-fin-tube heat storage unit drawn in **Figure 14B**, the natural convective cycle cannot be formed by the temperature difference, since the annular fins are parallel to each other. In this situation, the flow rises along the hot wall, and is forced to change its direction when it encounters the upper cold shell, which is similar to the flow in the finless tube unit. Thus, the annular-fin tube cannot effectively enhance the convective heat transfer in the PCM melting process.

As is well-known, the thermal conductivity of paraffin wax often used as PCM in LHTES is very small, and the application of fins has a limited effect on heat conduction enhancement. Therefore, the enhancement of natural convection heat transfer by fins should be carefully considered. Two suggestions on the design of the finned tube applied in the phase change heat storage unit were finally proposed in this paper. 1) The hot finned tube wall and the cold shell should be arranged vertically facing each other in the closed space to form a natural convective cycle. 2) The temperature gradient in the hot wall and the cold wall should be designed vertically upwards, as indicated in **Figure 15**, in order to enhance the natural convection.

CONCLUSION

In this paper, a numerical model was established by using the enthalpy-porosity approach to study the melting behavior of Paraffin wax RT50 in a heat storage unit belonging to a shell-and-tube heat exchanger. The effects of heat storage unit placement forms, tube diameters and fin structures on the phase change process of RT50 were investigated, and the heat transfer characteristics during different melting periods were deeply analyzed. Besides, the mechanism of heat transfer enhancement due to fins and the fin design suggestions in the heat storage unit were also proposed. The main conclusions are drawn as follows:

1) The phase-change process in the vertical heat storage unit was greatly affected by the tube diameter (i.e. the thickness of PCM). For the heat storage unit in horizontal arrangement, the melting process of RT50 can be divided into three stages in terms of dominant heat transfer: the conduction-led stage in the initial period, the convection-led stage in the intermediate period and the conduction-led stage in the final period. In addition, the melting time (or melting rate) of RT50 was mainly determined by the convection-led stage.
2) For heat transfer enhancement, the straight and annular fins were installed on the outer of the tube in the horizontal heat storage unit. Compared with the finless tube, the complete melting time of RT50 was shortened by 42.1% and 31.6% respectively for the straight-fin tube and the annular-fin tube. Thus, adopting the straight fins is a better option to improve the phase change process for the present heat storage unit.
3) The mechanism of heat transfer enhancement by fins was also analyzed. For the straight-fin-tube heat storage unit, the natural convective heat transfer was significantly intensified during the melting process of RT50. By using the annular fins, the conduction in the initial melting period was improved, but the annular fins have limited effect on enhancing the natural convection.
4) The suggestions on the fin design applied to the present heat storage unit were given. To improve the natural convection, the hot fin tube wall and the cold shell should be arranged vertically facing each other to form a relatively closed space, where the natural convective cycle is more likely to occur.

Besides, the temperature gradients both in the hot wall and cold wall should be vertical upwards.

DATA AVAILABILITY STATEMENT

The raw data supporting the conclusion of this article will be made available by the authors, without undue reservation.

AUTHOR CONTRIBUTIONS

JF is responsible for guiding experimental and numerical simulation work, guiding the revision of papers, and providing funds for research; TH is responsible for planning and completing numerical simulation and experimental work, processing data, writing the first draft and revision of articles, etc.; YB is responsible for guiding article revision, HY is responsible for assisting experiments, and JW is responsible for providing research process guidance and financial support.

FUNDING

The present work is supported by Funds of International Cooperation and Exchange of the National Natural Science Foundation of China (Research collaboration NSFC-VR) (No. 51961135102).

REFERENCES

Agyenim, F., Hewitt, N., Eames, P., and Smyth, M. (2010). A Review of Materials, Heat Transfer and Phase Change Problem Formulation for Latent Heat thermal Energy Storage Systems (LHTESS). *Renew. Sust. Energ. Rev.* 14, 615–628. doi:10.1016/j.rser.2009.10.015

Alkaabi, A. K., Addad, Y., and Alameri, S. A. (2019). "Hydro-thermal Assessment Around Triangularly Positioned PCM Containers in a Hybrid TES-Nuclear Power Plant System," in Proceedings of 2019 International Congress on Advances in Nuclear Power Plants (ICAPP'19), Juan-les-pins, France, May 2019.

Allen, M. J., Sharifi, N., Faghri, A., and Bergman, T. L. (2015). Effect of Inclination Angle during Melting and Solidification of a Phase Change Material Using a Combined Heat Pipe-Metal Foam or Foil Configuration. *Int. J. Heat Mass Transfer* 80, 767–780. doi:10.1016/j.ijheatmasstransfer.2014.09.071

Blen, K., Takgil, F., and Kaygusuz, K. (2008). Thermal Energy Storage Behavior of CaCl2.6H2O during Melting and Solidification. *Energy Sourc. A: Recovery, Utilization, Environ. Effects* 30, 775–787. doi:10.1080/15567030601082175

Brent, A. D., Voller, V. R., and Reid, K. J. (1988). Enthalpy-Porosity Technique for Modeling Convection-Diffusion Phase Change: Application to the Melting of a Pure Metal. *Numer. Heat Transfer* 13, 297–318. doi:10.1080/10407788808913615

Dhaidan, N. S., Khodadadi, J. M., Al-Hattab, T. A., and Al-Mashat, S. M. (2013). Experimental and Numerical Investigation of Melting of Phase Change Material/nanoparticle Suspensions in a Square Container Subjected to a Constant Heat Flux. *Int. J. Heat Mass Transfer* 66, 672–683. doi:10.1016/j.ijheatmasstransfer.2013.06.057

Dutil, Y., Rousse, D. R., Salah, N. B., Lassue, S., and Zalewski, L. (2011). A Review on Phase-Change Materials: Mathematical Modeling and Simulations. *Renew. Sust. Energ. Rev.* 15, 112–130. doi:10.1016/j.rser.2010.06.011

Ghahremannezhad, A., Xu, H., Salimpour, M. R., Wang, P., and Vafai, K. (2020). Thermal Performance Analysis of Phase Change Materials (PCMs) Embedded in Gradient Porous Metal Foams. *Appl. Therm. Eng.* 179. doi:10.1016/j.applthermaleng.2020.115731

Ghalambaz, M., Mehryan, S. A. M., Veismoradi, A., Mahdavi, M., Zahmatkesh, I., Kazemi, Z., et al. (2021). Melting Process of the Nano-Enhanced Phase Change Material (NePCM) in an Optimized Design of Shell and Tube thermal Energy Storage (TES): Taguchi Optimization Approach. *Appl. Therm. Eng.* 193, 116945. doi:10.1016/j.applthermaleng.2021.116945

Gharebaghi, M., and Sezai, I. (2007). Enhancement of Heat Transfer in Latent Heat Storage Modules with Internal Fins. *Numer. Heat Transfer, A: Appl.* 53, 749–765. doi:10.1080/10407780701715786

Gong, Z.-X., Devahastin, S., and Mujumdar, A. S. (1999). Enhanced Heat Transfer in Free Convection-Dominated Melting in a Rectangular Cavity with an Isothermal Vertical wall. *Appl. Therm. Eng.* 19, 1237–1251. doi:10.1016/s1359-4311(99)00003-4

Guo, C., and Zhang, W. (2008). Numerical Simulation and Parametric Study on New Type of High Temperature Latent Heat thermal Energy Storage System. *Energ. Convers. Manag.* 49, 919–927. doi:10.1016/j.enconman.2007.10.025

Guo, X., and Goumba, A. P. (2018). Process Intensification Principles Applied to Thermal Energy Storage Systems—A Brief Review. *Front. Energ. Res.* 6, 17. doi:10.3389/fenrg.2018.00017

Hosseini, M. J., Ranjbar, A. A., Sedighi, K., and Rahimi, M. (2012). A Combined Experimental and Computational Study on the Melting Behavior of a Medium Temperature Phase Change Storage Material inside Shell and Tube Heat Exchanger. *Int. Commun. Heat Mass Transfer* 39, 1416–1424. doi:10.1016/j.icheatmasstransfer.2012.07.028

Ibrahem, A. M., El-Amin, M. F., and Sun, S. (2017). Effects of Nanoparticles on Melting Process with Phase-Change Using the Lattice Boltzmann Method. *Results Phys.* 7, 1676–1682. doi:10.1016/j.rinp.2017.04.032

Lacroix, M. (1993). Numerical Simulation of a Shell-And-Tube Latent Heat thermal Energy Storage Unit. *Solar energy* 50, 357–367. doi:10.1016/0038-092x(93)90029-n

Lamberg, P., Lehtiniemi, R., and Henell, A.-M. (2004). Numerical and Experimental Investigation of Melting and Freezing Processes in Phase Change Material Storage. *Int. J. Therm. Sci.* 43, 277–287. doi:10.1016/j.ijthermalsci.2003.07.001

Meghari, Z., Bouhal, T., Benghoulam, M., Rhafiki, T. E., Khattabi, E. M. E., doghmi, H., et al. (2021). Numerical Simulation of a Phase Change Material in a Spherical Capsule with a Hollow Fin. *J. Energ. Storage* 43, 103024. doi:10.1016/j.est.2021.103024

Nemati, H., and Habibi, M. (2021). Analytical and Numerical Analysis of Phase Change Material Solidification in Partially Filled Capsules Considering Breathing Vent. *J. Energ. Storage* 40, 102725. doi:10.1016/j.est.2021.102725

Norouzi, N., Fani, M., and Talebi, S. (2021). Exergetic Design and Analysis of a Nuclear SMR Reactor Tetrageneration (Combined Water, Heat, Power, and Chemicals) with Designed PCM Energy Storage and a CO2 Gas Turbine Inner Cycle. *Nucl. Eng. Tech.* 53, 677–687. doi:10.1016/j.net.2020.07.007

Pahamli, Y., Hosseini, M. J., Ranjbar, A. A., and Bahrampoury, R. (2016). Analysis of the Effect of Eccentricity and Operational Parameters in PCM-Filled Single-Pass Shell and Tube Heat Exchangers. *Renew. Energ.* 97, 344–357. doi:10.1016/j.renene.2016.05.090

Patankar, S. V. (2018). *Numerical Heat Transfer and Fluid Flow*. Boca Raton: CRC Press.

Rathod, M. K., and Banerjee, J. (2015). Thermal Performance Enhancement of Shell and Tube Latent Heat Storage Unit Using Longitudinal Fins. *Appl. Therm. Eng.* 75, 1084–1092. doi:10.1016/j.applthermaleng.2014.10.074

Sarı, A., and Kaygusuz, K. (2002). Thermal and Heat Transfer Characteristics in a Latent Heat Storage System Using Lauric Acid. *Energ. Convers. Manag.* 43, 2493–2507. doi:10.1016/s0196-8904(01)00187-x

Sciacovelli, A., Gagliardi, F., and Verda, V. (2015). Maximization of Performance of a PCM Latent Heat Storage System with Innovative Fins. *Appl. Energ.* 137, 707–715. doi:10.1016/j.apenergy.2014.07.015

Sharma, A., Sharma, S. D., and Buddhi, D. (2002). Accelerated thermal Cycle Test of Acetamide, Stearic Acid and Paraffin Wax for Solar thermal Latent Heat

Storage Applications. *Energ. Convers. Manag.* 43, 1923–1930. doi:10.1016/s0196-8904(01)00131-5

Shin, D. H., Park, J., Choi, S. H., Ko, H. S., Karng, S. W., and Shin, Y. (2019). A New Type of Heat Storage System Using the Motion of Phase Change Materials in an Elliptical-Shaped Capsule. *Energ. Convers. Manag.* 182, 508–519. doi:10.1016/j.enconman.2018.12.091

Viskanta, R. (2018). *Phase-change Heat Transfer, Solar Heat Storage: Latent Heat Materials*. Boca Raton: CRC Press, 153–222.

Yazici, M. Y., Avci, M., Aydin, O., and Akgun, M. (2014). On the Effect of Eccentricity of a Horizontal Tube-In-Shell Storage Unit on Solidification of a PCM. *Appl. Therm. Eng.* 64, 1–9. doi:10.1016/j.applthermaleng.2013.12.005

Yu, Q., Romagnoli, A., Al-Duri, B., Xie, D., Ding, Y., and Li, Y. (2018). Heat Storage Performance Analysis and Parameter Design for Encapsulated Phase Change Materials. *Energ. Convers. Manag.* 157, 619–630. doi:10.1016/j.enconman.2017.12.040

Zhang, C., Li, J., and Chen, Y. (2020). Improving the Energy Discharging Performance of a Latent Heat Storage (LHS) Unit Using Fractal-Tree-Shaped Fins. *Appl. Energ.* 259, 114102. doi:10.1016/j.apenergy.2019.114102

Zheng, Z.-J., Xu, Y., and Li, M.-J. (2018). Eccentricity Optimization of a Horizontal Shell-And-Tube Latent-Heat thermal Energy Storage Unit Based on Melting and Melting-Solidifying Performance. *Appl. Energ.* 220, 447–454. doi:10.1016/j.apenergy.2018.03.126

Conflict of Interest: The authors declare that the research was conducted in the absence of any commercial or financial relationships that could be construed as a potential conflict of interest.

NOMENCLATURE

$\boldsymbol{c_p}$ specific heat capacity (J·kg^{-1}·K^{-1})

$\boldsymbol{d}$ tube diameter (m)

$\boldsymbol{g}$ gravity (m·s^{-2})

$\boldsymbol{h}$ enthalpy (J·kg^{-1})

$\boldsymbol{k}$ thermal conductivity (W·m^{-1}·K^{-1})

$\boldsymbol{L}$ latent heat (J·kg^{-1})

$\boldsymbol{P}$ pressure (Pa)

$\vec{\mathrm{S}}$ source term

$\boldsymbol{T}$ temperature (K)

$\vec{\mathrm{V}}$ velocity vector (m·s^{-1})

$\boldsymbol{v}$ velocity (m·s^{-1})

Greek symbol

$\boldsymbol{\beta}$ expansion coefficient (K^{-1})

$\boldsymbol{\lambda}$ liquid fraction

$\boldsymbol{\mu}$ dynamic viscosity (Pa·s)

$\boldsymbol{\rho}$ density (kg·m^{-3})

Subscripts

i inner

lat latent

liq liquid

o outer

ref reference

s solidus

sens sensible

f,i fluid inlet

frontiers | Frontiers in Energy Research

ORIGINAL RESEARCH
published: 13 April 2022
doi: 10.3389/fenrg.2022.890795

Comparison of Intergroup Mass Transfer Coefficient Correlations in Two-Group IATE for Subcooled Boiling Flow

Longxiang Zhu[1,2]*, Joseph L. Bottini[3], Caleb S. Brooks[3] and Luteng Zhang[1]

[1]Key Laboratory of Low-Grade Energy Utilization Technologies and Systems (Chongqing University), Ministry of Education, Chongqing, China, [2]Postdoctoral Station of Power Engineering and Engineering Thermophysics, Chongqing University, Chongqing, China, [3]Department of Nuclear, Plasma, and Radiological Engineering, University of Illinois at Urbana-Champaign, Urbana, IL, United States

The interfacial area concentration (IAC) is of vital importance in determining the interfacial transfer terms of mass, momentum, and energy between phases in the two-fluid model. The two-group (2-G) interfacial area transport equation (IATE) dynamically models the IAC evolution of large and small bubbles, and the intergroup transfer bookkeeps the mass transferring between two groups. Different intergroup mass transfer coefficient correlations are employed in the 2-G IATE model, which include one old correlation and three new correlations previously developed by the authors. The two-group IATE is benchmarked with subcooled boiling experimental dataset. The group-1 interfacial area concentration results show that the three modified correlations improve the physically incorrect prediction by the old correlation. With the modified correlations, the 2-G IATE is foundationally capable of predicting the group-1 interfacial area concentration in subcooled boiling flow.

Keywords: two-phase flow, boiling flow, IATE, two-group, intergroup transfer

Edited by:
Mingjun Wang,
Xi'an Jiaotong University, China

Reviewed by:
Zhaoming Meng,
Harbin Engineering University, China
Yacine Addad,
Khalifa University, United Arab Emirates

Correspondence:
Longxiang Zhu
lxzhu@cqu.edu.cn

Specialty section:
This article was submitted to Nuclear Energy, a section of the journal Frontiers in Energy Research

Received: *06 March 2022*
Accepted: *28 March 2022*
Published: *13 April 2022*

Citation:
Zhu L, Bottini JL, Brooks CS and Zhang L (2022) Comparison of Intergroup Mass Transfer Coefficient Correlations in Two-Group IATE for Subcooled Boiling Flow. Front. Energy Res. 10:890795. doi: 10.3389/fenrg.2022.890795

INTRODUCTION

The two-fluid model is now widely used to simulate two-phase flow systems like in RELAP5 (Thermal Hydraulics Group, 1998) and (TRACE (2010)). The model is formulated with two sets of conservation equations to separately consider the vapor phase and the liquid phase (Ishii and Hibiki, 2011) and the interface exists between the two phases. The interfacial area concentration, a_i, plays a key role in the interfacial drag closure and the interfacial heat transfer closures in the two-fluid model, as it determines the interfacial transfer terms of mass, momentum, and energy between phases (Khan et al., 2020) (Liu et al., 2021). **Figure 1** shows the diagram of the interface between the liquid and the vapor phase. The interfacial transfer terms can be written in the following form,

$$Interfacial\ \ transfer = a_i \times \text{driving flux} \tag{1}$$

Many researchers (Hibiki and Ishii, 2002) developed empirical interfacial area concentration correlations, including Ishii and Mishima (1980), Zeitoun et al. 1994, Zeitoun and Shoukri (1996), and Hibiki et al. (2006). The correlations can be divided into two kinds, namely geometry-based semi-empirical correlations and empirical correlations (Zhu et al., 2021). Different correlations are used in bubbly, slug, and the following regimes because they are

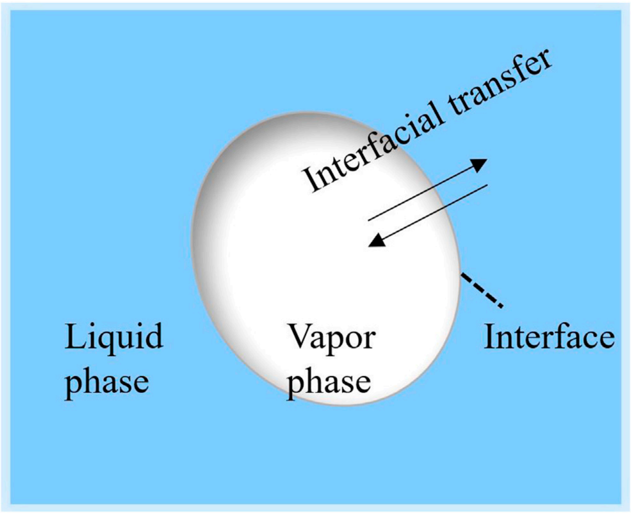

FIGURE 1 | The interfacial mass, momentum, and energy transfer through the interface between liquid and vapor phase.

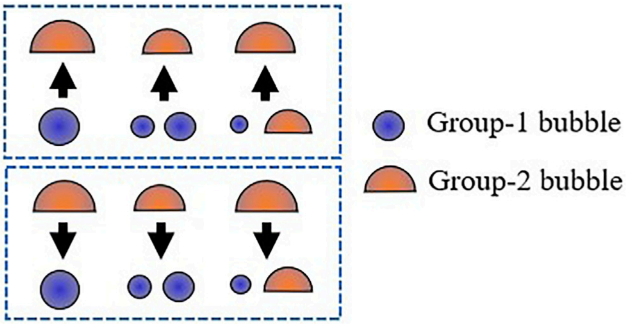

FIGURE 2 | Illustration of the intergroup transfer between group-1 and group-2 bubbles.

dependent on the flow regime. As a result, numerical instabilities can occur at the transitions between the flow regimes. However, the interfacial area transport equation (IATE) is developed to dynamically model the interfacial area concentration across the flow regimes. The successful closure of interfacial area concentration in the two-fluid model relies on the interfacial area transport equation.

Kocamustafaogullari and Ishii (1995) developed the one-group IATE based on the fluid particle number density transport equations analogous to Boltzmann's transport equation. The one-group IATE disregards the type of bubbles and treats them equally as spherical bubbles. Hibiki et al. (2003) provided the formulation of one-group IATE for subcooled boiling flow with the bubble layer thickness model. Brooks and Hibiki (2016) proposed a complete framework of the one-dimensional one-group (1-G) IATE model for phase change flow, then Zhu et al. (2021) further validate the 1-G IATE using extensive boiling flow datasets and improved the condensation closure in the model. At low void fractions, the one-group two-fluid model is sufficient for describing cases with uniform bubble size (Hibiki and Ishii, 2000a). However, for high void fraction cases, large bubbles in cap shape or slug shape come into existence as the consequence of bubble coalescence, bubble expansion, or heating from the wall. Under the high-void-fraction circumstance, the one-group IATE does not accurately predict a_i due to the spherical-shape and uniform-size assumption being applied to large bubbles (Zhu et al., 2019).

As the void fraction increases, the differences in shape, size, and number density between larger bubbles and small bubbles necessitate the separate consideration of bubbles in the two-fluid model (Hibiki and Ishii, 2000b). In order to account for the different mechanisms for heat and mass transfer of bubbles with different shapes and sizes, the two-group (2-G) IATE model is introduced in the work of Ishii and Kim (2004). Spherical and distorted bubbles are categorized as group-1 bubbles while cap and slug bubbles are categorized as group-2 bubbles in the two-group model (Hibiki and Ishii, 2000b). The separation of bubble groups thereby requires an additional set of conservation equations for the gas phase. Brooks et al. (2014) proposed the one-dimensional two-group IATE for subcooled boiling flow considering the uniform phase distribution pattern across the channel. Group-1 bubbles are averaged within a bubble layer while the group-2 bubbles span all the way across the channel.

Intergroup transfer happens between group-1 bubbles and group-2 bubbles: small bubbles can grow into large ones contributed from the coalescence, expansion, and nucleation, while the large bubbles can shrink into small ones as a result of the disintegration, condensation, and pressurization. **Figure 2** shows the transfer between small and big bubbles. Intergroup transfer of the interfacial area concentration between groups is important for two-group IATE as it tracks and partitions of the gas phase into the bubble groups. This bookkeeping of bubble groups is facilitated by the intergroup mass transfer coefficient. The intergroup mass transfer correlation was first developed by Sun (2001). Zhu et al. (2020) provided a thorough review of the intergroup mass transfer coefficient and proposed three modified correlations for the term. Two analytical intergroup mass transfer coefficient correlations are also developed based on the bubble size distribution functions, including the Nukiyama-Tanasawa distribution Nukiyama and Tanasawa (1939) and the Rosin-Rammler distribution Rosin and Rammler (1933). Also, one empirical intergroup mass transfer coefficient correlation is obtained from the experimental data.

This paper focuses on the benchmark of the 2-G IATE with subcooled boiling experimental data using different intergroup mass transfer coefficient correlations. The modeling of two-group IATE and the various correlations of intergroup mass transfer coefficient are presented in **section 2**. The prediction results of interfacial area concentration and the sink/source terms are presented in **section 3**, accompanied by the discussion about the performance of the old and three modified correlations.

TABLE 1 | Correlations for the group-1 intergroup mass transfer coefficient.

Model	Correlation
Sun et al. (2004)	$\chi_1 = 4.44 \times 10^{-3} (\frac{D_{sm,1}}{D_c})^{0.36} \alpha_1^{-1.35}$
Analytical correlation with Nukiyama-Tanasawa distribution (Zhu et al., 2020)	$\chi_{1,NT} = \frac{\frac{4}{3} D_c^{*3} \exp(-2D_c^*)}{1-(2D_c^{*2}+2D_c^*+1)\exp(-2D_c^*)}$
Analytical correlation with Rosin-Rammler distribution (Zhu et al., 2020)	$\chi_{1,RR} = \frac{\frac{8}{27} D_c^{*2} \exp\{-(\frac{D_c^*}{1.5})^2\}}{1-\exp(-(\frac{D_c^*}{1.5})^2)}$
Empirical Correlation (Zhu et al., 2020)	$\chi_1 = \frac{b}{3} \frac{D_c^{*p+1} \exp[-bD_c^*]}{D_c^{*p} (bD_c^*)^{-p} (G(p+1)-G(p+1,bD_c^*))}$ where, $q = 1$, $p = 0.25$, $b = 0.780$, $a = 0.808$

TABLE 2 | Summary of conditions considered in the benchmark.from the database of Bottini et al. (2020).

Run#	Inlet pressure (kPa)	Heat flux (kW/m^2)	Inlet liquid velocity (m/s)	Inlet subcooling (°C)	Max void fraction
1	232.6	68	0.95	5.35	0.61
2	273.0	90	1.25	5.95	0.52
3	248.7	56	0.68	6.47	0.55
4	489.9	90	1.32	5.12	0.31
5	900.8	90	1.33	4.04	0.24

MODELING

Brooks et al. (2014) proposed the one-dimensional two-group IATE for subcooled boiling flow with the consideration of bubble layer thickness model; however, only intergroup mass transfer from group-1 bubbles to group-2 bubbles was modeled. Kumar and Brooks (2018) developed the model to include the intergroup mass transfer from group-2 to group-1. Therefore, incorporating the intergroup mass transfer from both group-1 and group-2 bubble sides, the change in group a_i in the one-dimensional, steady-state two-group IATE model for subcooled boiling flow is,

$$\Delta\langle a_{i,1}\rangle_B = \frac{\Delta z}{\langle\langle v_{g,1}\rangle\rangle}\Big\{\langle\phi_{WN,1}\rangle + \langle\phi_{Exp,1}\rangle_B + \sum_j \langle\phi_{j,1}\rangle_B - \langle\phi_{\Delta\dot{m}_{12}}\rangle + \langle\phi_{CO,1}\rangle_B + \langle\phi_{Conv,1}\rangle_B\Big\} \tag{2}$$

and

$$\Delta\langle a_{i,2}\rangle = \frac{\Delta z}{\langle\langle v_{g,2}\rangle\rangle}\Big\{\langle\phi_{Exp,2}\rangle + \sum_j \langle\phi_{j,2}\rangle + \langle\phi_{\Delta\dot{m}_{12}}\rangle + \langle\phi_{Conv,2}\rangle\Big\} \tag{3}$$

where subscripts g, 1, 2, and B denote vapor, group-1, group-2, and averaging over the bubble layer, respectively. The brackets <> and <<>> represent cross-sectional area average and void-weighted area average. The bracket $<>_B$ represent the bubble-layer average, which is calculated by the improved flat bubble layer thickness model in Zhu et al. (2022). The terms a_i, z, v, and ϕ are interfacial area concentration, axial coordinate, velocity, and interfacial area concentration source/sink rate, respectively. There are nine source/sink terms in **Eqs 2**, **3**: the wall nucleation term, the two expansion terms, the two bubble interaction terms, the two convection terms, the condensation term, and the intergroup mass transfer term. The wall nucleation term, $<\phi_{WN,1}>$, and the expansion terms, $<\phi_{EXP}>$, are modeled and described in Brooks et al. (2014). The bubble interaction terms, $<\phi_j>$, and convection term, $<\phi_{Conv}>$, are described in Kumar and Brooks (2018). The condensation term for subcooled boiling flow, $<\phi_{CO,1}>$, is modified by Zhu et al. (2019). The intergroup transfer term, $<\phi_{\Delta\dot{m}12}>$, is modeled by Kumar and Brooks (2018) and is written as,

$$\langle\phi_{\Delta\dot{m}_{12}}\rangle = \sum_j \langle\phi_{j,12}\rangle + \max\big(0, \langle\phi_{V,12}\rangle\big) + \min\big(0, \langle\phi_{V,21}\rangle\big) \tag{4}$$

where,

$$\langle\phi_{V,12}\rangle = \langle\phi_{\Gamma,12}\rangle + \langle\phi_{DP,12}\rangle, \qquad \langle\phi_{V,21}\rangle = \langle\phi_{\Gamma,21}\rangle + \langle\phi_{DP,21}\rangle \tag{5}$$

where,

$$\langle\phi_{\Gamma,12}\rangle = \chi_1\left(\frac{D_c}{\langle D_{sm,1}\rangle}\right)^2\left(\frac{\langle a_{i,1}\rangle}{\langle\alpha_{g,1}\rangle}\right) \times \left(\frac{\langle\Gamma_{g,1}\rangle - \big(\langle\eta_{CO,1}\rangle + \langle\eta_{WN}\rangle\big)\langle\rho_g\rangle}{\langle\rho_g\rangle}\right) \tag{6}$$

$$\langle\phi_{DP,12}\rangle = -\chi_1\left(\frac{D_c}{\langle D_{sm,1}\rangle}\right)^2\left(\frac{\langle a_{i,1}\rangle}{\langle\alpha_{g,1}\rangle}\right)\left(\frac{\langle\alpha_{g,1}\rangle}{\langle\rho_g\rangle}\right)\langle\langle v_{g,1}\rangle\rangle\frac{d\langle\rho_g\rangle}{dz}, \tag{7}$$

$$\langle\phi_{\Gamma,21}\rangle = \chi_2\left(\frac{D_c}{\langle D_{sm,2}\rangle}\right)^2\left(\frac{\langle a_{i,2}\rangle}{\langle\alpha_{g,2}\rangle}\right)\left(\frac{\langle\Gamma_{g,2}\rangle}{\langle\rho_g\rangle}\right), \tag{8}$$

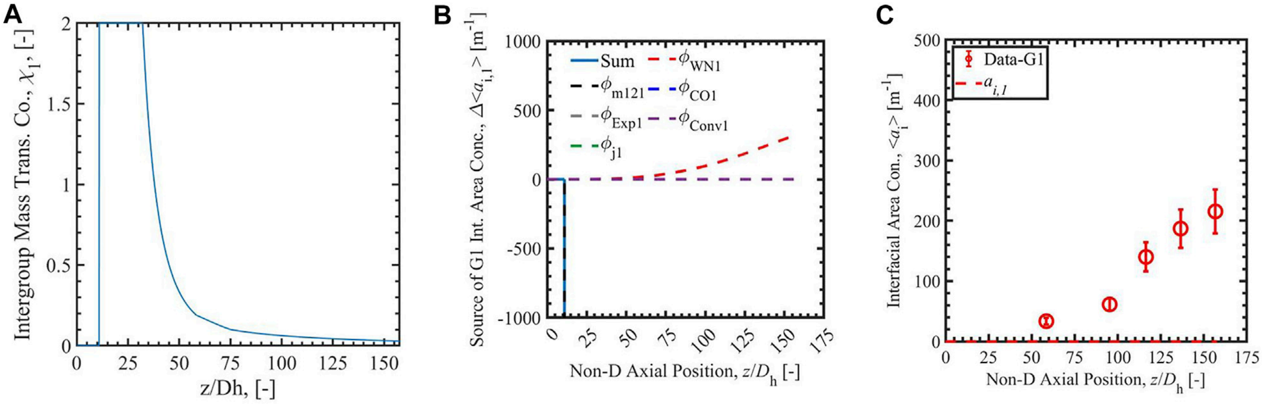

FIGURE 3 | The Run 1 results of group-1 intergroup mass transfer coefficient **(A)**, the source of group-1 interfacial area concentration **(B)**, and the interfacial area concentration **(C)** calculated by correlation Sun et al. (2004).

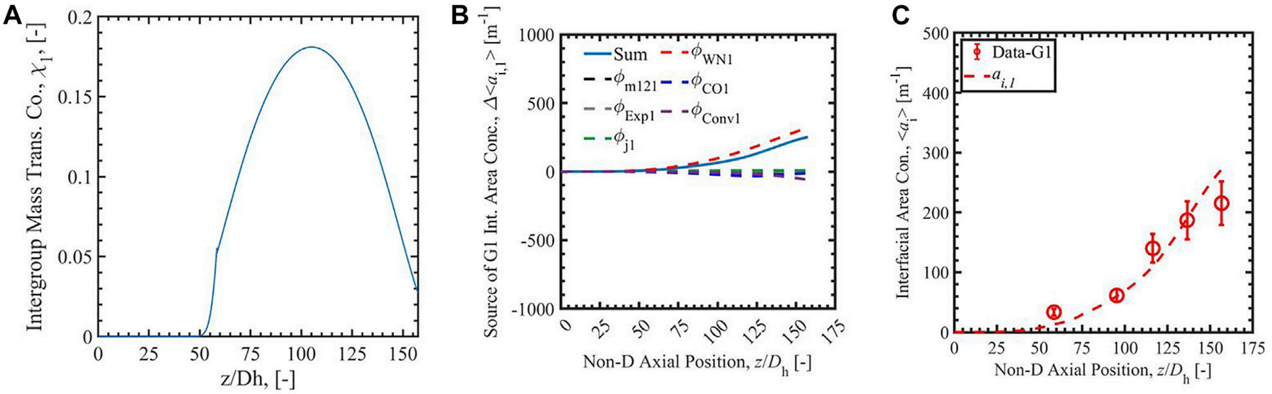

FIGURE 4 | The Run 1 results of group-1 intergroup mass transfer coefficient **(A)**, the source of group-1 interfacial area concentration **(B)**, and the interfacial area concentration **(C)** calculated with analytical-NT correlation (Zhu et al., 2020).

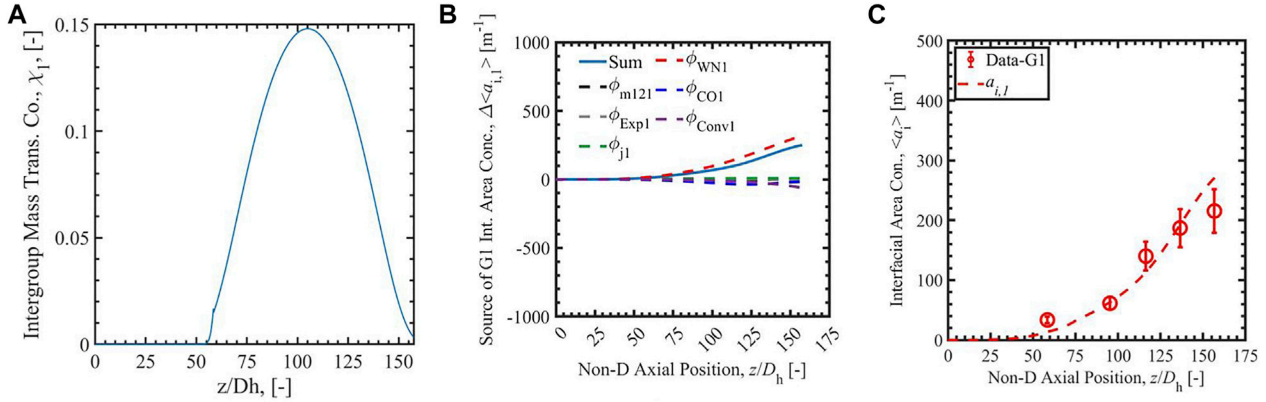

FIGURE 5 | The Run 1 results of group-1 intergroup mass transfer coefficient **(A)**, the source of group-1 interfacial area concentration **(B)**, and the interfacial area concentration **(C)** calculated with analytical-RR correlation (Zhu et al., 2020).

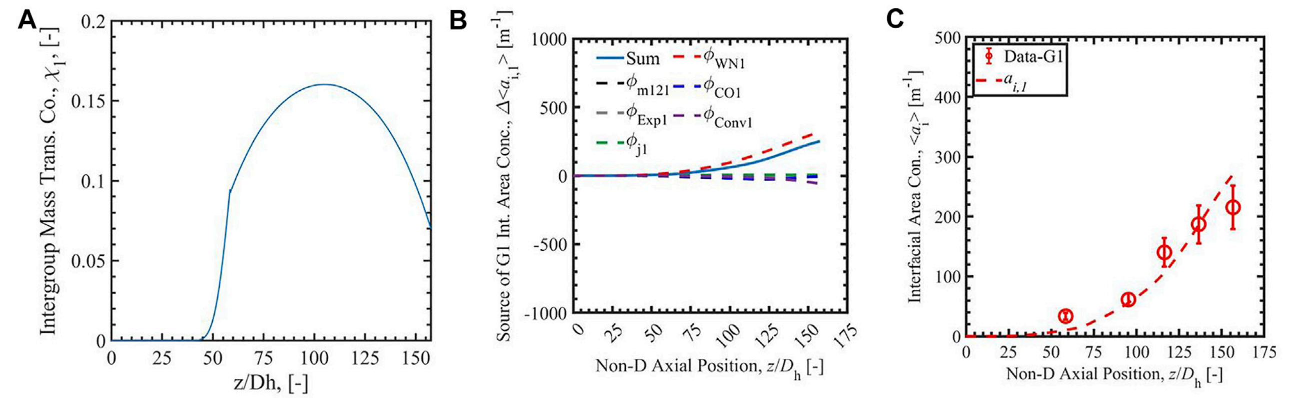

FIGURE 6 | The Run 1 results of group-1 intergroup mass transfer coefficient **(A)**, the source of group-1 interfacial area concentration **(B)**, and the interfacial area concentration **(C)** calculated with empirical correlation (Zhu et al., 2020) (fourth row).

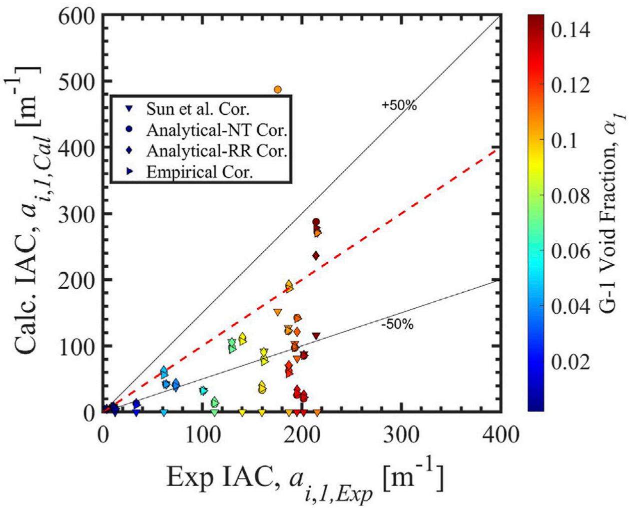

FIGURE 7 | The $a_{i,1}$ benchmark of 2-G IATE using four group-1 intergroup mass transfer coefficient correlations.

$$\langle\phi_{DP,21}\rangle = -\chi_2\left(\frac{D_c}{\langle D_{sm,2}\rangle}\right)^2\left(\frac{\langle a_{i,2}\rangle}{\langle\alpha_{g,2}\rangle}\right)\left(\frac{\langle\alpha_{g,2}\rangle}{\langle\rho_g\rangle}\right)\langle\langle v_{g,2}\rangle\rangle\frac{d\langle\rho_g\rangle}{dz} \tag{9}$$

where the terms α, ρ, η, χ, D_{sm}, D_c are void fraction, density, volume change rate per unit mixture volume, intergroup mass transfer coefficient, Sauter mean diameter, and critical bubble diameter at the group boundary, respectively. The subscripts V, Γ, DP, 12, and 21 denote volume change, interphase mass transfer, pressure change, group-1 to group-2, and group-2 to group-1, respectively.

In **Eqs 6**, **8**, the interphase mass transfer rate per unit volume for group-n vapor, $\Gamma_{g,n}$, is a key term which cannot be measured directly and is hard to estimate in subcooled boiling flow with the theoretical models. However, this term can be determined based on the one-dimensional two-group mass balance equations (Ishii and Hibiki, 2011),

$$\frac{\partial\rho_g\langle\alpha_{g,1}\rangle_B\langle\langle v_{g,1}\rangle\rangle}{\partial z} = \Gamma_{g,1} - \Delta\dot{m}_{12} \tag{10}$$

$$\frac{\partial\rho_g\langle\alpha_{g,2}\rangle\langle\langle v_{g,2}\rangle\rangle}{\partial z} = \Gamma_{g,2} + \Delta\dot{m}_{12} \tag{11}$$

The intergroup mass transfer term, $\Delta\dot{m}_{12}$, is difficult to model in subcooled boiling flow, so it is assumed to be small relative to $\Gamma_{g,1}$ in **Eq. 9**. The relative magnitude of $\Delta\dot{m}_{12}$ to $\Gamma_{g,2}$ in **Eq. 10** is inconsequential to the calculation of $<\phi_{\Delta\dot{m}12}>$ due to the suppression using the min function in **Eq. 4**. Therefore, $\Delta\dot{m}_{12}$ is assumed to be negligible in **Eqs 9**, **10**. Even though in some instances (e.g., when χ_1 is nonzero) $\Delta\dot{m}_{12}$ will not be negligible relative to $\Gamma_{g,1}$, the analysis uses the same $\Gamma_{g,1}$ to isolate the effect of χ_1 on $<\phi_{\Delta\dot{m}12}>$. More rigorous analysis to the two-group IATE can be applied once $\Gamma_{g,n}$ is modeled correctly.

In **Eqs. 6**, **8**, the intergroup mass transfer coefficient for group-n vapor, χ_n, is another important parameter in the multigroup formulation and needs to be modeled accurately. The group-1 intergroup mass transfer coefficient, χ_1, and the group-2 intergroup mass transfer coefficient, χ_2, can be related analytically (Kumar and Brooks, 2018) as $\chi_2 = (\chi_1 \cdot n_{b,1})/n_{b,2}$ where $n_{b,n}$ is the number density of group-n bubbles. The group-1 intergroup mass transfer coefficient was first developed by Sun et al. (2004), then Zhu et al. (2020) proposed three new correlations: an analytical correlation with Nukiyama-Tanasawa distribution, an analytical correlation with Rosin-Rammler distribution, and an empirical correlation. The correlations for the group-1 intergroup mass transfer coefficient are summarized in **Table 1**. In the equations, $D_c{}^*$ is the dimensionless critical bubble diameter which is calculated $D_c{}^* = 1.5D_c/D_{sm,1}$. G (z,x) and G(z) are the upper incomplete Gamma function and the complete Gamma function. In addition, a constant value of 0, 1, or 0.01 has been assigned to χ_1 in some works (Zhu et al., 2020).

The two analytical correlations are based on the distributions proposed by Nukiyama and Tanasawa (1939), and by Rosin and Rammler (1933). Both are single-peaked, right-skewed distributions; but the height and the location of the peak are different with the same characteristic parameter, i.e., the bubble nondimensional diameter. The factors in the power-law and exponential function of the nondimensional diameter are different in the two analytical correlations. Consequentially, in the range of $D_{\mathrm{sm},1}/D_{\mathrm{c}}\in[0.2,0.8]$, the intergroup mass transfer coefficient calculated by the analytical correlation with Nukiyama-Tanasawa distribution is larger than the correlation with Rosin-Rammler distribution. The empirical correlation is developed using an annulus condensing dataset (Kumar et al., 2019), an annulus flashing dataset (Kumar et al., 2019), an annulus boiling dataset (Bottini et al., 2020), and a pipe flashing dataset (Ooi et al., 2020). The empirical correlation predicts larger intergroup mass transfer coefficient values in the range of $D_{\mathrm{sm},1}/D_{\mathrm{c}}\in[0.2,0.5]$; thus it better captures the data-points trend of the four datasets compared with the analytical correlations.

RESULTS AND DISCUSSION

The subcooled boiling database by Bottini et al. (2020) is used to validate the two-group IATE model with four different group-1 intergroup mass transfer coefficient correlations: correlation Sun et al. (2004), analytical-NT correlation, analytical-RR correlation, and empirical correlation (Zhu et al., 2020). The experiment was conducted in an internally heated annulus channel with inner and outer diameters of 19.1 and 38.1 mm, respectively. The test section has a heated length of 2.85 m and an unheated length of 1.63 m. Four-sensor conductivity probes at three ports are used to measure interfacial area concentration and other two-phase parameters for group-1 and group-2 bubbles in the heated section. The conditions by Bottini et al. (2020) considered for the benchmark of two-group IATE model are listed in **Table 2**.

Figures 3–6 present the calculation results of Run 1 in the database of Bottini et al. (2020) with two-group IATE model using the correlation Sun et al. (2004), the analytical-NT correlation, the analytical-RR correlation, and the empirical correlation (Zhu et al., 2020). The subfigure A) in each figure is the calculated group-1 intergroup mass transfer coefficients. The χ_1 calculated by the correlation Sun et al. (2004) is observed to exceed the physical limit, 2, stated by Ishii and Hibiki (2011), in the lower region of the heated section where void fraction is small; thus, it is manually set to be two in the calculation. The cause of the nonphysical value is the power-law relation between χ_1 and α_1 in the correlation Sun et al. (2004), shown in the equation in **Table 1**. The χ_1 calculated by the correlationSun et al. (2004) is also observed to decrease when the void fraction increases along the heated length. On the contrary, χ_1 calculated by analytical-NT correlation, analytical-RR correlation, and empirical correlation (Zhu et al., 2020) increases along the heated length in the lower test section. This trend is more physically appropriate: the group-1 intergroup mass transfer coefficient should increase when more group-1 bubbles are present as χ_1 evaluates the amount of group-1 bubbles transferring to group-2 bubbles. Compared to the χ_1 calculated by the correlation Sun et al. (2004), χ_1 calculated by the other three correlations also has a smaller range, the maximum of which is ~0.18 for the three cases.

In the figures, the subfigure B) shows the source terms of group-1 interfacial area concentration: the intergroup mass transfer, wall nucleation, condensation, expansion, convection, and bubble interaction. The sum of the terms is shown with a solid blue line in the subfigures, and the intergroup mass transfer term is shown as a dashed black line. The subfigure C) is the comparison of simulated interfacial area concentration with experimental data for group-1 bubbles presented as red dots and red line. In the source term subfigures with the correlation Sun et al. (2004), the sum of the terms is negative or even infinite, dominated by a strong intergroup mass transfer term caused by the large χ_1 mentioned above. The intergroup term is so large on account of the unphysically large χ_1 term that any $a_{i,1}$ generated by other means is immediately transferred to group-2, resulting in unphysical growth in group-2 a_i while keeping $a_{i,1}$ near-zero. This highlights the necessity of a new group-1 intergroup mass transfer coefficient correlation. With the new analytical-NT correlation, and analytical-RR correlation, the sums of terms calculated by 2-G IATE are positive values in the whole heated section. The calculated $a_{i,1}$ is positive and increases along the heated length. The results show an improvement of the new analytical and empirical group-1 intergroup mass transfer coefficient correlations compared to the correlation Sun et al. (2004). In addition, compared with the χ_1 scale by analytical correlations, the constant value of 0 or 1 should not be assumed to χ_1, which give under- and over-prediction of intergroup transfer term. The constant value of 0.01 should not be assigned to the whole heated section. It overpredicts in the low void fraction section and affects the section later. Thus, the correlations which can dynamically predict χ_1 are needed.

Figure 7 shows the group-1 interfacial area concentration benchmark of 2-G IATE with four group-1 intergroup mass transfer coefficient correlations, i.e., the correlation Sun et al. (2004), the analytical-NT correlation, the analytical-RR correlation, and the empirical correlation (Zhu et al., 2020). The results calculated by the correlation Sun et al. (2004) are not physically correct: the group-1 values of a_i are zero as explained above, while the group-2 part is the contributor to the a_i values here. However, when using the analytical-NT correlation, the analytical-RR correlation, and the empirical correlation, the 2-G IATE is foundationally capable to handle the transition to group-2 bubbles in subcooled boiling flow. A lot more works are still required to improve the two-group IATE in subcooled boiling flow, such as an accurate two-group interphase mass transfer model for $\Gamma_{g,n}$.

CONCLUSION

At high void fractions, the two-group (2-G) IATE model is developed to account for the different mechanisms for heat and mass transfer of bubbles with different shapes and sizes. Spherical and distorted bubbles are categorized as group-1 bubbles while cap and slug bubbles are categorized as group-2 bubbles. Intergroup transfer of the IAC between groups tracks and partitions the gas phase into the bubble groups, and the accurate modeling of the intergroup mass transfer coefficient is important for the two-group IATE.

In this paper, the 2-G IATE is benchmarked with subcooled boiling experimental data from Bottini et al. (2020). Different intergroup mass transfer coefficient correlations are employed in the 2-G IATE model, which include the correlation Sun et al. (2004), the analytical correlation with Nukiyama-Tanasawa distribution (Zhu et al., 2020), the analytical correlation with Rosin-Rammler distribution (Zhu et al., 2020), and the empirical correlation by Zhu et al. (2020). The group-1 interfacial area concentration results show that the three modified correlations improve the physically incorrect prediction by the correlation Sun et al. (2004). With the modified correlations, the 2-G IATE is foundationally capable of predicting the group-1 interfacial area concentration in subcooled boiling flow. More rigorous analysis to the two-group IATE can be applied once two-group Γg is modeled correctly. The IATE model will be coupled with system codes in the next phase to present the numerical improvement across flow regimes.

DATA AVAILABILITY STATEMENT

The original contributions presented in the study are included in the article/Supplementary Material, further inquiries can be directed to the corresponding author.

AUTHOR CONTRIBUTIONS

LoZ: conceptualization, investigation, methodology, validation, formal analysis, visualization, writing—original draft, project administration; JB: writing—review and editing; CB: methodology, writing—review and editing, supervision; LuZ: writing—review and editing.

REFERENCES

Bottini, J. L., Zhu, L., Ooi, Z. J., Zhang, T., and Brooks, C. S. (2020). Experimental Study of Boiling Flow in a Vertical Heated Annulus with Local Two-phase Measurements and Visualization. *Int. J. Heat Mass Transfer* 155, 119712. doi:10.1016/j.ijheatmasstransfer.2020.119712

Brooks, C. S., and Hibiki, T. (2016). Modeling and Validation of Interfacial Area Transport Equation in Subcooled Boiling Flow. *J. Nucl. Sci. Techn.* 53 (8), 1192–1204. doi:10.1080/00223131.2015.1096852

Brooks, C. S., Ozar, B., Hibiki, T., and Ishii, M. (2014). Interfacial Area Transport of Subcooled Boiling Flow in a Vertical Annulus. *Nucl. Eng. Des.* 268, 152–163. doi:10.1016/j.nucengdes.2013.04.041

Hibiki, T., Ho Lee, T., Young Lee, J., and Ishii, M. (2006). Interfacial Area Concentration in Boiling Bubbly Flow Systems. *Chem. Eng. Sci.* 61, 7979–7990. doi:10.1016/j.ces.2006.09.009

Hibiki, T., and Ishii, M. (2002). Interfacial Area Concentration of Bubbly Flow Systems. *Chem. Eng. Sci.* 57, 3967–3977. doi:10.1016/s0009-2509(02)00263-4

Hibiki, T., and Ishii, M. (2000). One-group Interfacial Area Transport of Bubbly Flows in Vertical Round Tubes. *Int. J. Heat Mass Transfer* 43 (15), 2711–2726. doi:10.1016/s0017-9310(99)00325-7

Hibiki, T., and Ishii, M. (2000). Two-group Interfacial Area Transport Equations at Bubbly-To-Slug Flow Transition. *Nucl. Eng. Des.* 202 (1), 39–76. doi:10.1016/s0029-5493(00)00286-7

Hibiki, T., Situ, R., Mi, Y., and Ishii, M. (2003). Modeling of Bubble-Layer Thickness for Formulation of One-Dimensional Interfacial Area Transport Equation in Subcooled Boiling Two-phase Flow. *Int. J. Heat mass transfer* 46, 1409–1423. doi:10.1016/s0017-9310(02)00418-0

Ishii, M., and Hibiki, T. (2011). *Thermo-fluid Dynamics of Two-phase Flow*. 2nd Edition. Springer.

Ishii, M., and Kim, S. (2004). Development of One-Group and Two-Group Interfacial Area Transport Equation. *Nucl. Sci. Eng.* 146, 257–273. doi:10.13182/nse01-69

Ishii, M., and Mishima, K. (1980). *Study of Two-Fluid Model and Interfacial Area. No. NUREG/CR-1873*. IL (USA): Argonne National Lab. ANL-80-111.

Khan, I., Wang, M., Zhang, Y., Tian, W., Su, G., and Qiu, S. (2020). Two-phase Bubbly Flow Simulation Using CFD Method: A Review of Models for Interfacial Forces. *Prog. Nucl. Energ.* 125, 103360. doi:10.1016/j.pnucene.2020.103360

Kocamustafaogullari, G., and Ishii, M. (1995). Foundation of the Interfacial Area Transport Equation and its Closure Relations. *Int. J. Heat Mass Transfer* 38 (3), 481–493. doi:10.1016/0017-9310(94)00183-v

Kumar, V., and Brooks, C. S. (2018). Inter-group Mass Transfer Modeling in the Two-Group Two-Fluid Model with Interfacial Area Transport Equation in Condensing Flow. *Int. J. Heat Mass Transfer* 119, 688–703. doi:10.1016/j.ijheatmasstransfer.2017.11.087

Kumar, V., Ooi, Z. J., and Brooks, C. S. (2019). Forced Convection Steam-Water Experimental Database in a Vertical Annulus with Local Measurements. *Int. J. Heat Mass Transfer* 137, 216–228. doi:10.1016/j.ijheatmasstransfer.2019.03.099

Liu, K., Wang, M., Gan, F., Tian, W., Qiu, S., and Su, G. H. (2021). Numerical Investigation of Flow and Heat Transfer Characteristics in Plate-type Fuel Channels of IAEA MTR Based on OpenFOAM. *Prog. Nucl. Energ.* 141, 103963. doi:10.1016/j.pnucene.2021.103963

Nukiyama, S., and Tanasawa, Y. (1939). An Experiment on the Atomization of Liquid : 3rd Report, on the Distribution of the Size of Droplets. *Trans. Soc. Mech. Eng. Jpn.* 5 (18), 131–135. doi:10.1299/kikai1938.5.131

Ooi, Z. J., Zhang, T., and Brooks, C. S. (2020). Experimental Dataset with High-Speed Visualization for Vertical Upward Steam-Water Flow with Transition from Annulus to Circular Channel. *Int. J. Heat Mass Transfer* 161, 120281. doi:10.1016/j.ijheatmasstransfer.2020.120281

Rosin, P., and Rammler, E. (1933). Laws Governing the Fineness of Powdered Coal. *J. Inst. Fuel* 7, 29–36.

Sun, X., Kim, S., Ishii, M., and Beus, S. G. (2004). Model Evaluation of Two-Group Interfacial Area Transport Equation for Confined Upward Flow. *Nucl. Eng. Des.* 230 (1-3), 27–47. doi:10.1016/j.nucengdes.2003.10.014

Sun, X. (2001). *Two-group Interfacial Area Transport Equation for a Confined Test Section*. West Lafayette: Purdue University.

Thermal Hydraulics Group (1998). *RELAP5/MOD3 CODE MANUAL. Vol. I: Code Structure, System Models and Solution Methods*. USA: RELAP5/MOD3.2.2 Beta.

TRACE (2010). *Theory Manual Field Equations, Solution Methods, and Physical Models*. U. S. Nuclear Regulatory Commission.

Zeitoun, O., and Shoukri, M. (1996). Bubble Behavior and Mean Diameter in Subcooled Flow Boiling. *J. Heat Transfer* 118, 110–116. doi:10.1115/1.2824023

Zeitoun, O., Shoukri, M., and Chatoorgoon, V. (1994). Measurement of Interfacial Area Concentration in Subcooled Liquid-Vapour Flow. *Nucl. Eng. Des.* 152, 243–255. doi:10.1016/0029-5493(94)90089-2

Zhu, L., Ooi, Z. J., Bottini, J. L., Brooks, C. S., and Shan, J. (2020). Bubble Diameter Distribution and Intergroup Mass Transfer Coefficient in Flows with Phase Change. *Int. J. Heat Mass Transfer* 163, 120456. doi:10.1016/j.ijheatmasstransfer.2020.120456

Zhu, L., Ooi, Z. J., and Brooks, C. S. (2019). "Current Capability of Interfacial Area Transport Approaches in Subcooled Boiling," in *18th International Topical Meeting on Nuclear Reactor Thermal Hydraulics*. NURETH.

Zhu, L., Ooi, Z. J., Brooks, C. S., and Shan, J. (2021). Modeling Sensitivity in Prediction of Interfacial Area Concentration in Boiling Flow. *Prog. Nucl. Energ.* 133, 103638. doi:10.1016/j.pnucene.2021.103638

Zhu, L., Zhang, T., Bottini, J. L., and Brooks, C. S. (2022). Two-dimensional Quantitative Study of Boiling Flow Evolution in Vertical Inner-Heated Annulus Channel. *Int. J. Heat Mass Transfer* 183, 122190. doi:10.1016/j.ijheatmasstransfer.2021.122190

Conflict of Interest: The authors declare that the research was conducted in the absence of any commercial or financial relationships that could be construed as a potential conflict of interest.

NOMENCLATURE

a_i interfacial area concentration [m^{-1}]

D diameter [m]

G gap width [m]

$\Delta\dot{m}_{12}$ intergroup mass transfer rate per unit mixture volume [kg/m^3/s]

n_b bubble number density [m^{-3}]

z axial position [m]

Greek

α void fraction [-]

Γ vapor generation rate to the k-phase per unit volume [kg/m^3/s]

Δ difference

η volume source rate [s^{-1}]

ρ density [kg/m^3]

ϕ Interfacial area concentration source or sink term [1/m/s]

χ intergroup mass transfer coefficient

Superscripts

$*$ nondimensional

' boundary value between cap bubble and slug bubble

Subscripts

1 group-1

12 from group-1 to group-2

2 group-2

21 from group2 to group-1

c critical value at the boundary of group-1 and group-2 bubbles

CO condensation

Conv convection

DP pressure change

Exp expansion

g vapor phase

j interaction

sm Sauter mean

V volume change

WN wall nucleation

Brackets

$\langle\rangle$ area-averaged

$\langle\rangle_B$ bubble layer averaged

$\langle\langle\rangle\rangle$ void-weighted area-averaged

frontiers | Frontiers in Energy Research

ORIGINAL RESEARCH
published: 04 May 2022
doi: 10.3389/fenrg.2022.877366

Neutronics and Thermohydraulics Coupling Analysis on Novel Organic Cooled Reactor Based on Single-Channel Model

Feng Wang[1,2]*, *Xinyue Gu*[1,2], *Delun Guan*[1,2] *and Wang Dou*[1,2]

[1]*Key Laboratory of Low-Grade Energy Utilization Technologies and Systems, Chongqing University, Chongqing, China,* [2]*School of Energy and Power Engineering, Chongqing University, Chongqing, China*

A conceptual design for a 100 MW(th) organic cooled reactor is proposed with the application of organic fluid HB-40 as a coolant. In order to obtain the axial and radial power distribution, a physical model for the proposed core is developed using the Monte Carlo particle transport code MCNP. Moreover, a single-channel model is developed using multi-physics simulation software COMSOL to calculate the temperature distribution of the fuel elements and corresponding coolant channels. A neutronics-thermohydraulics coupling calculation method is established to couple the MCNP code and COMSOL software by means of mesh mapping and data transfer. Through coupling calculation, the high fidelity power and temperature distribution can be obtained. The key thermohydraulics parameters of the hottest channel in the core are investigated, and the changes after coupling calculation are analyzed. The proposed core design and coupling method can be used as a reference for further optimization of organic cooled reactors.

Keywords: organic cooled reactor, single-channel model, coupling calculation, MCNP, COMSOL multi-physics

Edited by:
Wei Ding,
Helmholtz Association of German Research Centres (HZ), Germany

Reviewed by:
Minghui Chen,
University of New Mexico, United States
Kui Zhang,
Xi'an Jiaotong University, China

****Correspondence:***
Feng Wang
wangfeng@cqu.edu.cn

Specialty section:
This article was submitted to Nuclear Energy, a section of the journal Frontiers in Energy Research

Received: *16 February 2022*
Accepted: *23 March 2022*
Published: *04 May 2022*

Citation:
Wang F, Gu X, Guan D and Dou W (2022) Neutronics and Thermohydraulics Coupling Analysis on Novel Organic Cooled Reactor Based on Single-Channel Model. Front. Energy Res. 10:877366. doi: 10.3389/fenrg.2022.877366

INTRODUCTION

Small modular reactors have become a research hotspot in the field of nuclear energy, characterized by low power (less than 300 MWe), modular design and construction, outstanding safety, and economic performance. Among all worldwide designs of small modular reactors, an organic cooled reactor (OCR) is considered one of the most promising concepts (Shirvan et al., 2016).

OCR is a reactor concept that uses an organic fluid as a coolant, allowing high temperature and low-pressure operation, along with negligible corrosion on loop structure materials (Elberg and Fritz, 1963; International Atomic Energy Agency, 1967). OCR is compact, safe, and reliable, which can be used in many fields such as desalination, district heating, and hydrogen production. Since the 1950s, the United States, the Soviet Union, Canada, and other countries have built a number of test OCRs for different purposes (Binstock, 1960; Mccurnin, 1963; Hewson, 1965; Tegart, 1970; Tsykanov et al., 1981). In recent years, the advent of high-temperature fluids, together with advances in hydrocracking and reforming technologies driven by the oil and gas industries, make the OCR concept even more viable. In 2014, the Massachusetts Institute of Technology proposed a core design to be deployed offshore underwater for powering coastal areas, which was moderated by graphite and cooled by an organic fluid (Shirvan and Forrest, 2016). In 2019, the Royal Military College of Canada undertook a conceptual design of an organic cooled and moderated reactor for heating and powering remote areas of northern Canada (Shannon et al., 2020).

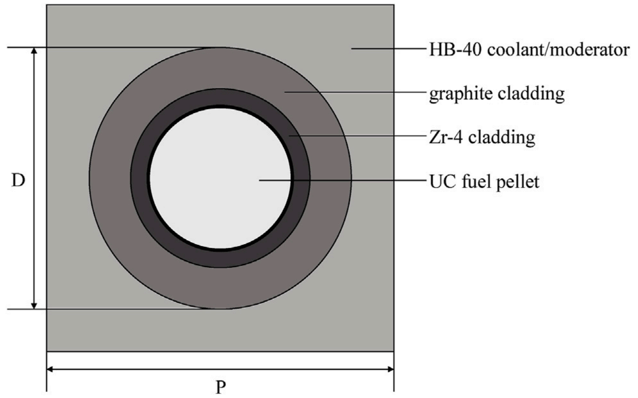

FIGURE 1 | Schematic diagram of the optimized fuel element.

The current research on OCR is mostly limited to neutronics analysis (li et al., 2021; Wang et al., 2021). Little research has been carried out on thermohydraulics. In this study, a conceptual design of an OCR core with thermal power of 100 MW(th) is proposed, and the organic fluid HB-40 is used as a coolant. The Monte Carlo particle transport code MCNP is used to develop the physical model of the core for neutronics calculations, and the multi-physics simulation software COMSOL is used to develop the single-channel model for thermohydraulics calculations. By coupling the MCNP code and COMSOL software through mesh mapping and data transfer, a neutronics-thermohydraulics coupling method is established, and the upcoming research on thermohydraulics characteristics is carried out on this basis.

CORE DESIGN

Organic Coolant Properties

The OCR core designed in this study uses HB-40 (18wt% o-terphenyl, 82wt% hydrogenated terphenyl) as a coolant, an organic mixture that remains liquid at room temperature. HB-40 was used in the WR-1 Reactor in Canada between 1965 and 1985, where it would undergo a cracking reaction when exposed to high temperature along with radiation and would generate volatile gases as well as high boiling substances (Tegart, 1970). It is important to emphasize that HB-40 is assumed to remain stable in this research. Its physical properties only change with temperature, ignoring the cracking reaction or the effect of cracking products on the flow and heat transfer performance. The main properties of HB-40 are summarized as follows (Smee et al., 1975).

The density ρ (kg·m^{-3}) as a function of temperature T (K) is

$$\rho = 1.0181 \times 10^{3} - 7.3891 \times 10^{-1} (T - 273.15). \quad (1)$$

The viscosity μ (Pa s) over the temperature range 423–673 K is calculated as

$$\mu = EXP\left(- 11.6260 + 2.1856 \times 10^{3} T^{-1} \right). \quad (2)$$

The formula for calculating the specific heat c_p (J·kg^{-1}·K^{-1}):

$$c_p = 1.5049 \times 10^{3} + 3.5476 (T - 273.15). \quad (3)$$

The formula of the thermal conductivity k (W·m^{-1}·K^{-1}) for temperatures from 398 to 673 K:

$$k = 1.2677 \times 10^{-1} - 1.0864 \times 10^{-4} (T - 273.15). \quad (4)$$

Optimal Design of Fuel Element

Because HB-40 triggers cracking when exposed to radiation, in order to decrease the fluid damage caused by fast neutrons and photons, the structure of the fuel element is optimized by adding a graphite layer to the original Zr-4 cladding as moderator, as shown in **Figure 1**. It should be emphasized here that the optimized fuel element is designed to be held in the under-moderated region, although the calculation details are not presented to avoid a lengthy article.

Considering that the thermal conductivity of graphite will be reduced by lattice defects due to neutron irradiation, an average effective thermal conductivity of 10 W/(m K) is assumed (Snead et al., 2002). In addition, because of the fine material compatibility of HB-40, which eliminates the possibility of fuel-coolant interaction in case of cladding rupture, UC is chosen as the fuel material for its greater thermal conductivity compared to UO$_2$. The former has a thermal conductivity of 23 W/(m K) at 1,000°C, while the latter is only about 2.6 W/(m K) (Yu, 2002). The use of UC can improve the heat transfer characteristics of fuel pellets to compensate for the bad thermal conductivity of HB-40.

TABLE 1 | Parameters of the core structure.

Parameters	Value
UC fuel pellet diameter	5.14 mm
Gas gap	He
Gap width	0.080 mm
Zr-4 cladding thickness	0.60 mm
Overall fuel diameter (fuel pellet + gap + Zr-4 cladding + graphite cladding)	9.5 mm
Fuel rod pitch	12.59 mm
Fuel assembly pitch	21.503 cm
Barrel inner diameter	188 cm
Barrel outer diameter	198 cm
Reactor vessel inner diameter	260 cm
Reactor vessel outer diameter	310 cm

TABLE 2 | Parameters at steady-state operation.

Parameters	Value
Reactor core power	100 MW (th)
Operating pressure	1.15 MPa
Coolant inlet temperature	553 K
Coolant outlet temperature	593 K
Coolant mass flow rate	973 kg/s
Average flow rate	1.43 m/s

Parameters of the Core Design

The OCR core is rated at 100 MW(th) and consists of 37 fuel assemblies (FAs). Each assembly includes 264 fuel rods, 24 guide tubes for control rod movement, and 1 measuring tube, arranged in square arrays of 17 × 17. The active height of FAs is 200 cm, and the equivalent diameter of the core is 147.5 cm. The detailed dimensions of the core are shown in **Table 1**, and the steady-state operation parameters are shown in **Table 2**.

In order to flatten the power distribution, the FAs are loaded in three zones according to ^{235}U enrichment. 13 FAs with enrichment of 1.95 w/o are arranged in the inner core, 16 FAs with enrichment of 4.25 w/o are arranged in the outer core, the remaining 8 FAs with enrichment of 2.75 wo/o are arranged in mid-place of the core.

To meet the demand of reactivity control, 21 of the 37 FAs contain control rod bundles with Ag-In-Cd as absorber material and 8 FAs contain burnable toxic rod bundles with borosilicate glass as absorber material. The arrangement of FAs is centrosymmetric, as shown in **Figure 2**. It must be emphasized here that all calculations in this study are performed at hot full-power operation, and all control rods are assumed to be withdrawn, also with a boric acid concentration of 0 ppm.

METHODOLOGY OF COUPLING

Physical Model

The Monte Carlo code MCNP5 is developed by Los Alamos National Laboratory, United States, which can treat an arbitrary three-dimensional configuration of materials in geometric cells. In this research, MCNP5 is used to build the physical model for the proposed core. **Figure 3** shows the cross-sectional view of the core model. Besides the FAs, the baffle, barrel, and pressure vessel are also considered for the accuracy of neutronics calculations. F4 tally card is applied for neutron flux calculations, and F7 tally card is applied to obtain the radial and axial power distribution. In order to obtain axial power distribution, all FAs in the model are divided into 20 segments along the axial direction, and the power density of each segment in different FAs is calculated. For each

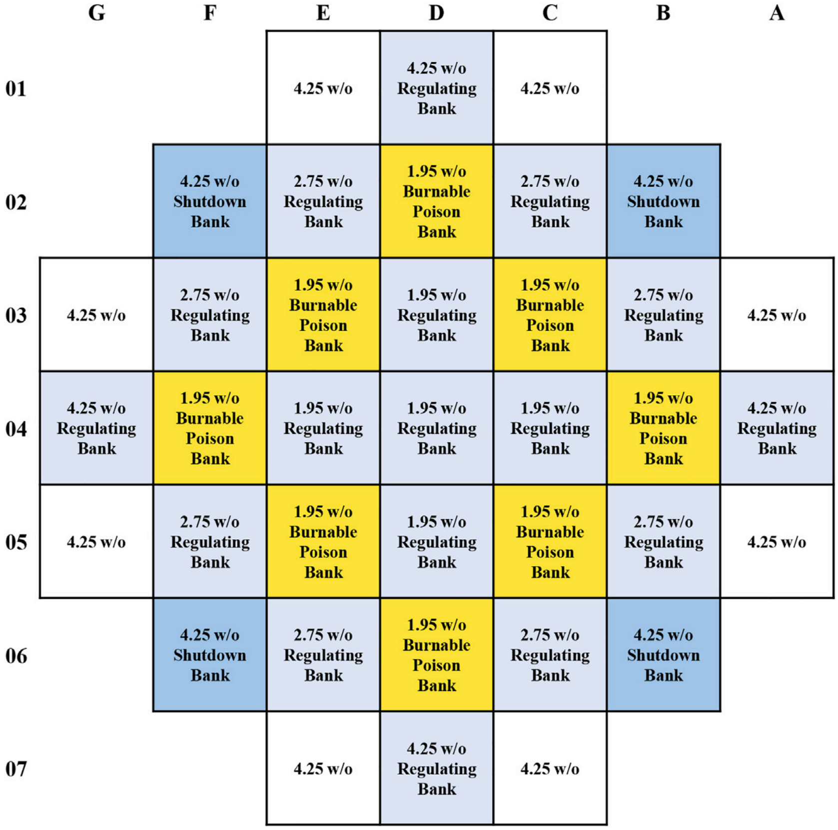

	G	F	E	D	C	B	A
01			4.25 w/o	4.25 w/o Regulating Bank	4.25 w/o		
02		4.25 w/o Shutdown Bank	2.75 w/o Regulating Bank	1.95 w/o Burnable Poison Bank	2.75 w/o Regulating Bank	4.25 w/o Shutdown Bank	
03	4.25 w/o	2.75 w/o Regulating Bank	1.95 w/o Burnable Poison Bank	1.95 w/o Regulating Bank	1.95 w/o Burnable Poison Bank	2.75 w/o Regulating Bank	4.25 w/o
04	4.25 w/o Regulating Bank	1.95 w/o Burnable Poison Bank	1.95 w/o Regulating Bank	1.95 w/o Regulating Bank	1.95 w/o Regulating Bank	1.95 w/o Burnable Poison Bank	4.25 w/o Regulating Bank
05	4.25 w/o	2.75 w/o Regulating Bank	1.95 w/o Burnable Poison Bank	1.95 w/o Regulating Bank	1.95 w/o Burnable Poison Bank	2.75 w/o Regulating Bank	4.25 w/o
06		4.25 w/o Shutdown Bank	2.75 w/o Regulating Bank	1.95 w/o Burnable Poison Bank	2.75 w/o Regulating Bank	4.25 w/o Shutdown Bank	
07			4.25 w/o	4.25 w/o Regulating Bank	4.25 w/o		

FIGURE 2 | Schematic diagram of the arrangement of 37 FAs. Different types are shown with different colors (dark blue, shutdown control rod assembly bank; blue, regulating control rod assembly bank; yellow, burnable toxic rod assembly bank; white, assemblies that contain neither control rods nor burnable toxic rods).

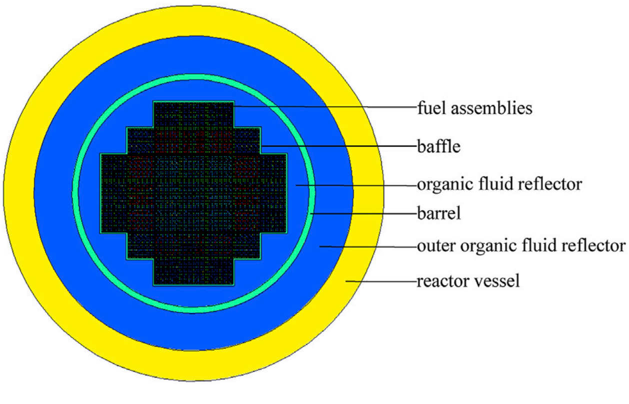

FIGURE 3 | Cross-sectional view of the physical model.

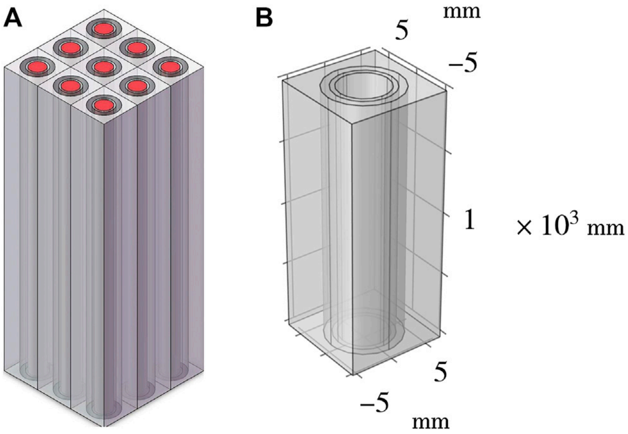

FIGURE 4 | Schematic diagram of **(A)** 3 × 3 channels model **(B)** single-channel model.

calculation in MCNP, there are 330 generations, including 30 inactive generations, with an initial neutron number of 100,000 per generation, and a total of 30 million particle behaviors are recorded in every calculation.

Single-Channel Model

The single-channel model is commonly applied for the steady-state thermohydraulics analysis of the core, which assumes that each coolant channel is isolated and closed, and there is no exchange of energy and momentum between the channels (Zhang and Huang, 2009). **Figure 4** shows the schematic diagram of the 3 × 3 channels model and the single-channel model. Compared with the 3 × 3 channels model, only one channel needs to be taken for calculation in the single-channel model, which reduces the calculation cost. Based on the single-channel model, the temperature distributions of fuel elements and corresponding coolant channels in each assembly are calculated in turn.

Thermohydraulics boundary conditions are defined for the solid and fluid domains separately in COMSOL (Weng et al., 2021). The temperature boundary of 553 K and "outflow boundary" are applied to the coolant inlet and outlet, respectively. The four surrounding faces are "symmetric boundaries" and the upper and lower surfaces for the solid part are set as adiabatic. The volumetric heat source is added to the fuel pellet, which is the calculated axial power density distribution. The heat transfer field of both solid and fluid domains is coupled with the turbulent field of the fluid domain, and the contact boundary between the fluid and the solid is set as a "wall" by default. The inlet boundary condition of the turbulent field is set as the inlet flow rate, and the outlet boundary condition is set as a constant pressure of $P_0 = 1.15$ MPa with backflow suppression.

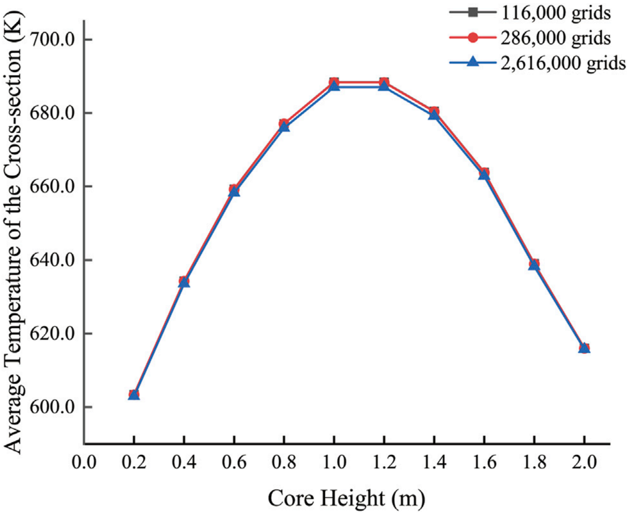

FIGURE 5 | Axial temperature distribution of the single-channel model with different numbers of grids.

Due to the irradiated swelling problem of UC, which will force the fuel pellet to come into contact with the inner wall of the cladding during reactor operation, a contact heat conduction model is used for the gap heat conduction between the fuel pellet and the Zr-4 cladding. The equivalent heat transfer coefficient at the interface of irradiated UO_2 fuel pellet and Zr-4 cladding is generally taken to be 5678 W/(m^2·K) in the current fuel element design for pressurized water reactor power plants (Yu, 2002). Because the fuel element structures are similar and both UC and UO_2 suffer from irradiated swelling, the empirical gap equivalent heat transfer coefficient h_g = 5678 W/(m^2·K) is adopted in this research to deal with the heat conduction of the gap.

The neutronics properties of each fuel rod in the same assembly are similar, so the coolant temperature and density distribution of each channel in the same assembly are considered to be approximately equal in the thermohydraulics calculations. The assembly power obtained by neutronics calculation can be converted into single-channel power in thermohydraulics calculation. And when the results of thermohydraulics calculation are fed back to neutronics calculation, the temperature and density parameters of single-channel will correspond to the parameters of assemblies in neutronics calculation. In addition, the coolant inlet flow rate in the

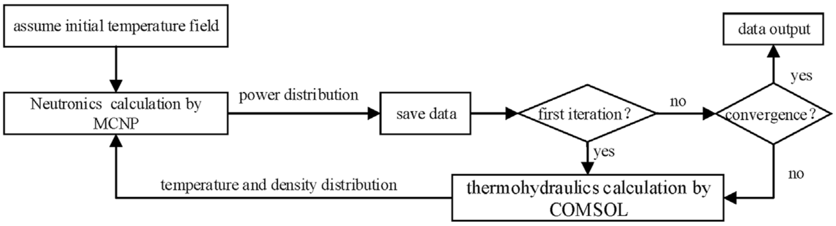

FIGURE 6 | Flowchart of the coupling procedure.

single-channel model is determined by the coolant flow rate of the corresponding assembly, which is assigned according to the assembly power non-uniformity factor.

Grid Irrelevance Verification

Three grid quantities are provided for the grid irrelevance analysis of the single-channel model. The average temperatures of the cross sections at different axial positions are calculated under different grid quantities, as shown in **Figure 5**. It is found that the simulated temperature values are basically the same under the same calculation conditions, which meet the requirements of grid irrelevance. In this study, the calculation is completed using the model with a grid number of 116,000.

Neutronics-Thermohydraulics Coupling Calculation Method

In the coupled neutronics-thermohydraulics calculation, an initial temperature field is first assumed. We regard the average temperature of the coolant inlet and outlet as the initial coolant temperature, which is 573 K. The axial power density distributions of each assembly are obtained from the neutronics calculation, and the temperature fields of fuel elements and coolant channels in different assemblies are solved in turn by the thermohydraulics calculation. As the coolant density is determined by its temperature, the coolant density parameters of each assembly in MCNP input file can be updated after thermohydraulics calculation and the neutron transport process can be simulated again to obtain the new axial power density distribution of each assembly. The iterative calculation converges when the difference in the calculated power distribution is less than 5% compared with the previous step. Otherwise, the updated power density distribution will be imported into COMSOL for further calculation. The neutronics-thermohydraulics coupling calculation process is shown in **Figure 6**.

The coupling strategy between MCNP and COMSOL included mesh mapping and data transfer. In the core model built by MCNP, the fuel pellets and coolant channels in each assembly are divided into 20 segments along the axial direction. Each segment of the fuel pellet and coolant channel is considered a cell. Meanwhile, in the single-channel model built by COMSOL, the solid and fluid domains are divided into 20 corresponding segments along the axial direction to produce 20 fuel pellet cells and coolant channel cells, as shown in **Figure 7**. Make sure that the fuel pellet cells and coolant channel cells of different axial heights in the MCNP model can find overlapping cells in the COMSOL model. In the subsequent coupling calculation, the data of temperature, density, and power distribution would be transferred manually based on these overlapping cells.

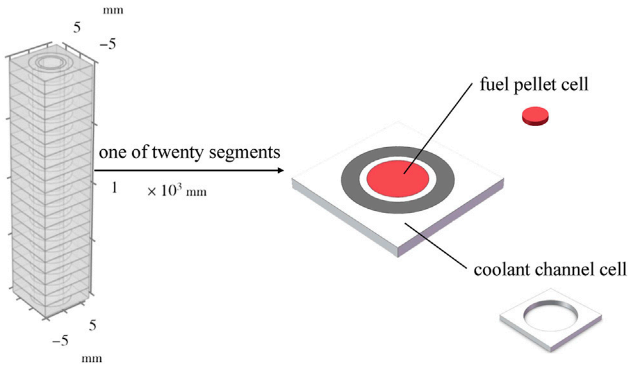

FIGURE 7 | Schematic diagram of the meshes used for data transfer.

Regarding the data transfer process, firstly, the power density of fuel pellet cells at different axial heights of each assembly is calculated by MCNP. Secondly, the data are imported to COMSOL manually as the heat source. Then, the temperature fields of fuel elements and coolant channels of each assembly are obtained by calculating COMSOL, and the average temperature and density of the coolant cells at different axial heights are derived. Finally, the obtained coolant density values at different axial heights of each assembly are used to update the original coolant density values of the corresponding assembly's cells in the MCNP input file so that the axial power density distribution of each assembly can be calculated again.

RESULTS AND DISCUSSIONS

Power Density Distribution

The neutron flux for each assembly after the coupling calculation is shown in **Figure 8** (only 1/4 of the core is shown due to symmetry). We can see that the closer to the core center, the higher the neutron flux. It is also worth noting that the fast neutron flux of each assembly is always higher than resonant neutrons and thermal neutrons. The total

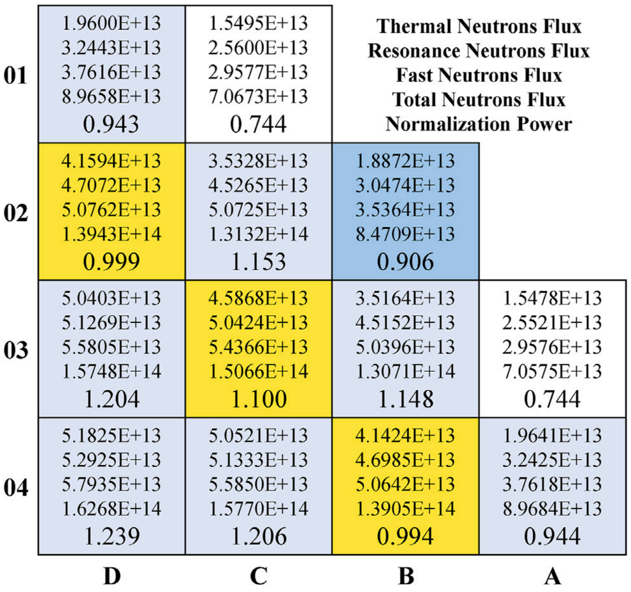

Thermal Neutrons Flux
Resonance Neutrons Flux
Fast Neutrons Flux
Total Neutrons Flux
Normalization Power

	D	C	B	A
01	1.9600E+13 3.2443E+13 3.7616E+13 8.9658E+13 0.943	1.5495E+13 2.5600E+13 2.9577E+13 7.0673E+13 0.744		
02	4.1594E+13 4.7072E+13 5.0762E+13 1.3943E+14 0.999	3.5328E+13 4.5265E+13 5.0725E+13 1.3132E+14 1.153	1.8872E+13 3.0474E+13 3.5364E+13 8.4709E+13 0.906	
03	5.0403E+13 5.1269E+13 5.5805E+13 1.5748E+14 1.204	4.5868E+13 5.0424E+13 5.4366E+13 1.5066E+14 1.100	3.5164E+13 4.5152E+13 5.0396E+13 1.3071E+14 1.148	1.5478E+13 2.5521E+13 2.9576E+13 7.0575E+13 0.744
04	5.1825E+13 5.2925E+13 5.7935E+13 1.6268E+14 1.239	5.0521E+13 5.1333E+13 5.5850E+13 1.5770E+14 1.206	4.1424E+13 4.6985E+13 5.0642E+13 1.3905E+14 0.994	1.9641E+13 3.2425E+13 3.7618E+13 8.9684E+13 0.944

FIGURE 8 | Distributions of neutron fluxes and normalization power in each FA.

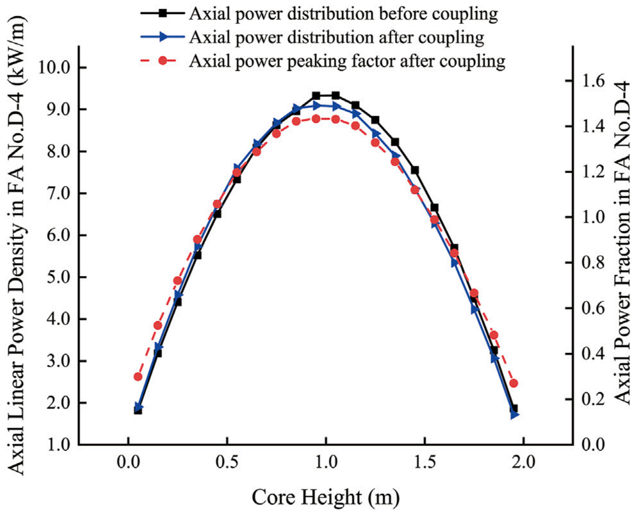

FIGURE 9 | Distribution of axial line power density and normalized power density of D-4 assembly.

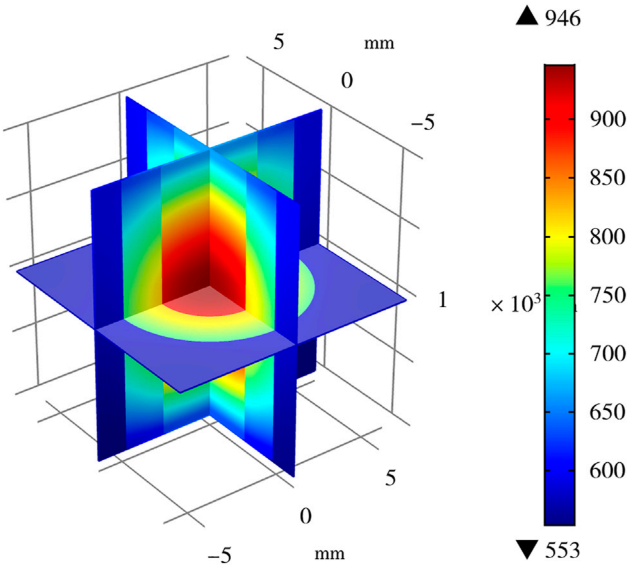

FIGURE 10 | Three-dimensional temperature distribution for the single-channel model of D-4 assembly.

neutron flux of the core is calculated as 1.15 × 10^{14}/cm^2·s, of which the thermal neutron flux is 3.14 × 10^{13}/cm^2·s, accounting for 27.3%; the resonant neutron flux is 3.96 × 10^{13}/cm^2·s, accounting for 34.4%; and the fast neutron flux is 4.42 × 10^{13}/cm^2·s, accounting for 38.3%.

Finally, the normalized power distribution of the assemblies is given in the fifth row. As presented in **Figure 8**, the radial power peaking factor of the core is 1.239, and the assembly with the highest power density is D-4, located in the center of the core. Coolant channel with the highest power output is called the hottest channel, so the hottest channel is considered to exist in assembly D-4. The axial line power density distribution of D-4 before and after the coupling calculation is shown in **Figure 9**. After the coupling calculation, the axial power distribution of D-4 tends to be more like a cosine shape with less fluctuation, and the maximum line power density decreases to 9.10 kW/m. The axial power peaking factor of D-4 is 1.434. Therefore, the total power peaking factor of the core is 1.78.

Temperature Distribution

Figure 10 shows the three-dimensional temperature for the single-channel model of D-4 assembly after the coupling calculation. Due to the uneven axial power distribution, the temperature in the center is significantly higher, with a maximum temperature of 946.8 K.

Regarding the steady-state thermohydraulics parameters of D-4, a comparison of the results before and after coupling is shown in **Table 3**. After the coupling calculation, the line power density of D-4 is reduced. Because the coolant flow rate of assemblies is distributed according to the power non-uniformity factor, the coolant flow rate of D-4 is consequently lower. Therefore, the calculated temperature distribution after coupling is basically the same. For example, the maximum temperature of the fuel pellet is only 7.6 K lower than that before coupling.

Figure 11 shows the temperature variation along the radial direction for the single-channel model of D-4 at axial height z = 1 m after coupling calculation. The curve shows three stages, whose structure in the order of temperature from the highest to the lowest are the fuel pellet, cladding (Zr-4 cladding and graphite cladding), and the coolant. There is a large temperature gradient between every two stages, and their

TABLE 3 | Steady-state thermohydraulics parameters of D-4 assembly.

Parameters	Before coupling	After coupling
Maximum line power density (kW·m^{-1})	9.34	9.09
Maximum temperature of fuel pellet (K)	954.4	946.8
Maximum surface temperature of Zr-4 cladding (K)	822.2	818.2
Maximum surface temperature of graphite cladding (K)	806.3	802.6
Coolant flow rate (m·s^{-1})	1.795	1.770
Coolant outlet temperature (K)	593.15	593.15

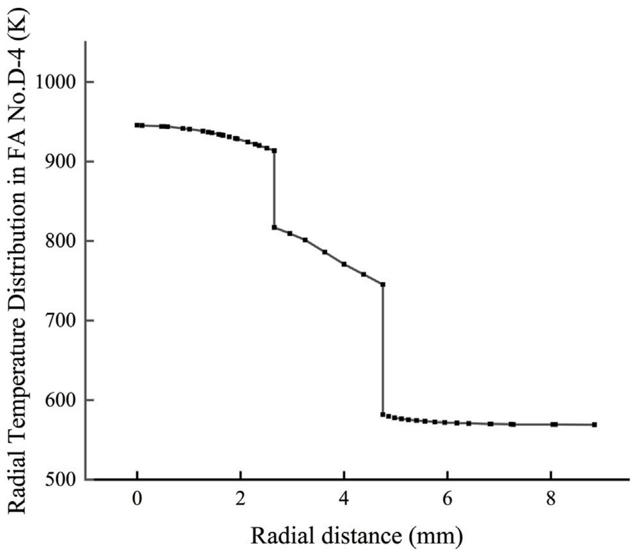

FIGURE 11 | Radial temperature distribution of D-4 assembly (z = 1 m).

formation is due to the existence of a gas gap and flow boundary layer, respectively.

Minimum Departure From Nucleate Boiling Ratio

For reactor design, the maximum heat flux at the surface of the fuel element is required to be less than the critical heat flux. Furthermore, the Departure from Nucleate Boiling Ratio (DNBR) concept is introduced to express the ratio of the critical heat flux q_{DNB} (W/m^2) to the actual heat flux q (W/m^2). The Atomic Energy of Canada Limited recommends the following correlation to calculate the critical heat flux of fresh HB-40 (Smee et al., 1975):

$$q_{DNB} = 1000\left(5.1\Delta T_{sub} V^{\frac{2}{3}} - 409\right). \tag{5}$$

In **Equation (5)**, $\Delta T_{sub} = T_{SAT} - T_{BULK}$ is the sub-cooling degree of coolant, where T_{SAT} and T_{BULK} are the coolant saturation temperature and the body temperature, respectively. $T_{SAT} = 0.88 \times \sqrt{\frac{\ln P - 0.9454}{5.568 \times 10^{-6}}} + 273.15$, where P is the coolant channel pressure in terms of bar and V is the coolant flow rate in terms of m/s.

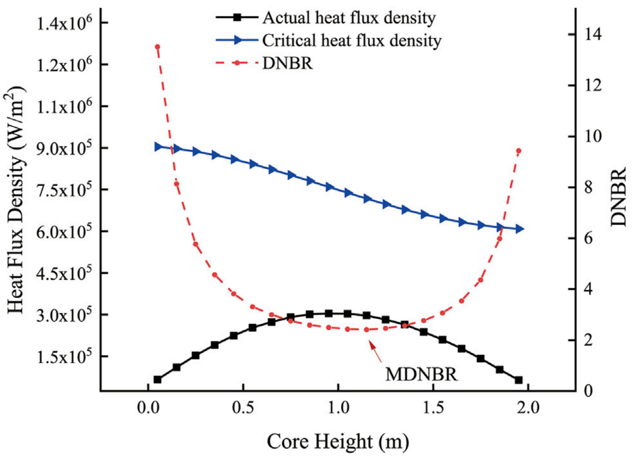

FIGURE 12 | Axial variation of heat flux on the fuel surface.

The power distribution analysis indicates that the hottest channel is located in the D-4 assembly. The variation of the critical heat flux along the axial height of the fuel element in D-4 is calculated with the correlation. The variation of actual heat flux is exported from the single-channel model in COMSOL. The results are compared as shown in **Figure 12**. Influenced by the power distribution, the actual heat flux is high in the middle and low at both ends. Because the body temperature of coolant keeps increasing from inlet to outlet, the critical heat flux decreases along the axial height. Based on the ratio of the critical heat flux and actual heat flux, the variation of DNBR at rated power and steady state is obtained. The minimum departure from the nucleate boiling ratio is calculated as 2.41 at axial height z = 1.15 m, behind the maximum heat flux point, which is at axial height z = 0.95 m.

CONCLUSION

In order to obtain accurate neutronics and thermohydraulics parameters of the OCR core, a coupled neutronics-thermohydraulics calculation method is established based on the single-channel model, applying the Monte Carlo code MCNP and the multi-physics software COMSOL. By analyzing the results of coupled calculations, the conclusions are as follows.

1) For the proposed conceptual OCR design, the neutronics-thermohydraulics calculations yielded a total power peaking factor of 1.78, a total neutron flux of $1.15 \times 10^{14}/\text{cm}^2\cdot\text{s}$, a maximum channel temperature of 947 K, and a MDNBR value of 2.4, which are within the specification of the neutronics-thermohydraulics design basis limits.

2) After the coupling calculation, the line power density of the assembly, where the hottest channel is located, is reduced. However, the temperature distribution is basically the same because the coolant flow rate of assemblies is distributed according to the non-uniformity power factor.

This research provides a reference for future design and optimization of OCR, but further analyses should consider the effects of cracking products on organic fluid properties to predict the neutronics-thermohydraulics characteristic more accurately.

DATA AVAILABILITY STATEMENT

The raw data supporting the conclusion of this article will be made available by the authors without undue reservation.

AUTHOR CONTRIBUTIONS

XG is responsible for code programming, data processing, and editing. FW is responsible for concept and project management. DG is responsible for editing. WD is responsible for editing.

ACKNOWLEDGMENTS

The authors acknowledge the support of Science and Technology on Reactor System Design Technology Laboratory (JG2018119). They also gratefully acknowledge the financial support provided by the National Key R&D Program of the People's Republic of China (2018YFB0104502).

REFERENCES

Binstock, M. H. (1960). *Fuel Element Development for piqua OMR*. Canoga Park, CA: Atomics International.

Elberg, S., and Fritz, G. (1963). "Physical properties of organic nuclear reactor coolants: EUR 400.e," in *144th National ACS Meeting Division of Industrial and Engineering Chemistry. Symposium on Organic Nuclear Reactor Coolant Technology*. (Los Angeles, CA: European Atomic Energy Community).

Hewson, R. A. (1965). *Compilation of piqua Nuclear Power Facility Operating Limits and Controls and post-critical Operational Tests*. Canoga Park, CA: Atomics International.

International Atomic Energy Agency (1967). *Organic Liquids as Reactor Coolants and Moderators*. Vienna: IAEA.

li, Q., Xia, B., Li, S., and Lu, D. (2021). Study on the Concept of Organic-Cooled Microreactor. *Nucl. Power Eng.* 42 (5), 266–270. doi:10.13832/j.jnpe.2021.05.0266

Mccurnin, W. R. (1963). *Evaluate the Performance of Two OMRE Fourth Core Fuel Elements: NAA-SR-9008*. Canoga Park, CA: Atomics International.

Shannon, C., Chan, P., and Bonin, H. W. (2020). Conceptual Design of an Organic-Cooled Small Nuclear Reactor to Support Energy Demands in Remote Locations in Northern Canada. *CNL Nucl. Rev.* 9, 39–44. doi:10.12943/CNR.2019.00002

Shirvan, K., Ballinger, R., Buongiorno, J., Forsberg, C., Kazimi, M., and Todreas, N. (2016). Technology Selection for Offshore Underwater Small Modular Reactors. *Nucl. Eng. Techn.* 48 (6), 1303–1314. doi:10.1016/j.net.2016.06.002

Shirvan, K., and Forrest, E. (2016). Design of an Organic Simplified Nuclear Reactor. *Nucl. Eng. Techn*. 48 (4), 893–905. doi:10.1016/j.net.2016.02.019

Smee, J. L., Puttagunta, V. R., Robertson, R. F. S., and Hatcher, S. R. (1975). *Organic Coolant Summary Report*. Pinawa, Manitoba: Atomic Energy of Canada Ltd.

Snead, L. L., Balden, M., Causey, R. A., and Atsumi, H. (2002). High thermal Conductivity of Graphite Fiber Silicon Carbide Composites for Fusion Reactor Application. *J. Nucl. Mater.* 307-311, 1200–1204. doi:10.1016/S0022-3115(02)01115-7

Tegart, D. R. (1970). "Operation of the WR-1 Organic Cooled Research Reactor," in *American Nuclear Society Conference on Reactor Operating Experience* (Pinawa, Manitoba: Atomic Energy of Canada Ltd.).

Tsykanov, V. A., Chechetkin, Y. V., Kormushkin, Y. P., Polivanov, I. F., Pochechura, V. P., Yakshin, E. K., et al. (1981). Experimental Nuclear Heat Supply Station Based on the Arbus Reactor. *At Energy* 50 (6), 333–338. doi:10.1007/BF01126338

Wang, F., Sun, Y., and Su, X. (2021). Novel Organic Nuclear Reactor Fuel Assembly Physical Calculation and Reactor Core. *Mater. Rev.* 35 (18), 18195–18199. doi:10.11896/cldb.20070337

Weng, M., Liu, S., Liu, Z., Qi, F., Zhou, Y., and Chen, Y. (2021). Development and Application of Monte Carlo and COMSOL Coupling Code for Neutronics/thermohydraulics Coupled Analysis. *Ann. Nucl. Energ.* 161, 108459. doi:10.1016/j.anucene.2021.108459

Yu, P. (2002). *Thermal Analysis of Nuclear Reactor*. Beijing: Atomic Energy Press.

Zhang, X., and Huang, Y. (2009). "Single-Channel Model for Steady Thermal-hydraulic Analysis in Nuclear Reactor," in *2009 Annual Symposium, Chinese Nuclear Society* (Beijing: Atomic Energy Press), 254–259.

Conflict of Interest: The authors declare that the research was conducted in the absence of any commercial or financial relationships that could be construed as a potential conflict of interest.

frontiers | Frontiers in Energy Research

ORIGINAL RESEARCH
published: 18 May 2022
doi: 10.3389/fenrg.2022.891105

Research on Countercurrent Flow Limitation in Reactor Hot Leg at the Loss of Coolant Accident-Thermohydraulic Calculation With System Code RELAP5

Xiang Li[1], Lingyuan Gao[2], Caihong Xu[2], Ting Wang[2], Wan Sun[1]*, Wen Zhu[3], Luteng Zhang[1], Zaiyong Ma[1], Longxiang Zhu[1] and Liangming Pan[1]

[1]Key Laboratory of Low-Grade Energy Utilization Technologies and Systems (Chongqing University), Ministry of Education, Chongqing, China, [2]China Nuclear Power Technology Research Institute Co., Ltd., Shenzhen, China, [3]Nuclear Power Institute of China (NPIC), Chengdu, China

OPEN ACCESS

Edited by:
Mingjun Wang,
Xi'an Jiaotong University, China

Reviewed by:
Hui He,
Shanghai Jiao Tong University, China
Yago Rivera,
Polytechnic University of Valencia, Spain
Zhaoming Meng,
Harbin Engineering University, China

***Correspondence:**
Wan Sun
sunwan@cqu.edu.cn

Specialty section:
This article was submitted to Nuclear Energy, a section of the journal Frontiers in Energy Research

Received: *07 March 2022*
Accepted: *21 April 2022*
Published: *18 May 2022*

Citation:
Li X, Gao L, Xu C, Wang T, Sun W, Zhu W, Zhang L, Ma Z, Zhu L and Pan L (2022) Research on Countercurrent Flow Limitation in Reactor Hot Leg at the Loss of Coolant Accident-Thermohydraulic Calculation With System Code RELAP5. Front. Energy Res. 10:891105. doi: 10.3389/fenrg.2022.891105

Since the counter current flow limitation (CCFL) of the two-phase flow has an important influence on the safety analysis of the reactor, it is also of great significance to study some characteristics and flow pattern transitions of the two-phase flow. In order to explore the characteristics and influencing factors of two-phase counter current flow in the hot leg under the condition of the Loss of Coolant Accident, this research, using RELAP5 simulation calculation, analyzed the effect of the lengths of the flow path of the hot leg, the shapes of the upper outlet of the inclined pipe, and the shapes of the elbow connecting the horizontal pipe and the inclined pipe on the characteristics of the CCFL. This research also evaluated the limitation of the model. The simulation founded that under the same liquid flow rate, the longer the horizontal pipe, the lower the gas flow rate at the beginning of the counter current flow; the effect of the elbow on the CCFL was not great; compared with the sharp outlet shape, the J_f of the gentle circle was slightly larger. The method established in this study is suitable for the prediction of CCFL in the hot leg during Loss of Coolant Accident.

Keywords: two-phase flow, RELAP5, counter current flow limitation, hot leg, LOCA

INTRODUCTION

The Loss of Coolant Accident, a break in the loop boundary or a stuck safety valve, etc., causes the coolant from the loop to flow out of the loop area. Flow erosion in piping systems is a concern for many industrial practices. The driving pressure head of natural circulation depends on the density difference between the up and down sections of the loop. In this process, if the main pump of the first loop of the nuclear power station stops idling, the natural circulation begins to change into a single phase, and the system pressure gradually drops. At this time, a lot of gas phase may be generated by flashing at the top of the core due to the high pressure, and thus the density difference increases in the pipeline, and ultimately the ability of natural circulation increases. But the resulting steam flow into the heat transfer pipe may be condensed, and soon the pressure in the primary loop is reduced to the pressure in the secondary loop. If the natural circulation is interrupted, CCFL will occur, and the

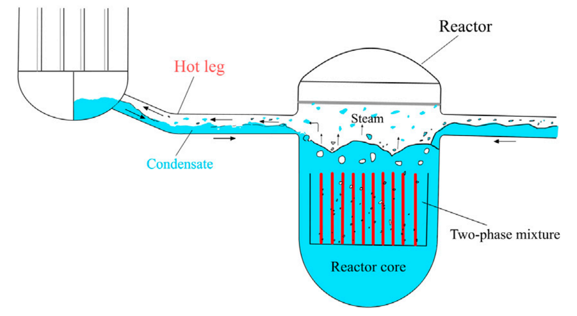

FIGURE 1 | Counter current flow in the hot leg during the condensate flow back.

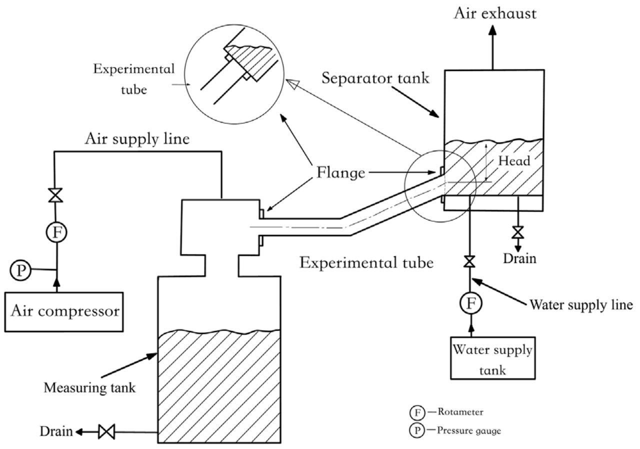

FIGURE 2 | Schematic of experimental setup (Ohnuki, 1986).

TABLE 1 | Experiment section dimensions description.

No	θ/°	D/m	l/m	H/m	h/m	Type
I	40	0.026	0.10	-	0.10	A
II	40	0.026	0.30	-	0.10	A
III	40	0.026	0.10	0.01	0.10	B
IV	40	0.026	0.19	0.02	0.10	B
V	40	0.026	0.19	0.05	0.10	B
VI	40	0.026	0.19	0.08	0.10	B
VII	40	0.026	0.19	0.08	0.10	B
VIII	40	0.026	0.10	0.01	0.10	C
IX	40	0.026	0.19	0.08	0.10	D

steam generated in the core will rise to the steam generator in the hot leg, be cooled by the secondary circuit, and then flow back down the pipe. Such counter current flow may take away some of the heat, as shown in **Figure 1**. In recent years, international scholars have carried out research on the characteristics of two-phase countercurrent flow in different pipeline systems. Among them, the two-phase countercurrent flow in the hot leg was studied by Siddiqul et al. (1986), Ardron and Banerjee (1986). Wongwises (1998) conducted a study of two-phase counter current flow in the hot leg of a PWR. Kang et al. (Hewitt et al., 1965) and Yu et al. (Chun et al., 2000), specifically studied the effect of liquid level in the hot leg on its CCFL characteristics. Murase et al. (2012) used the Fluent software to numerically simulate the CCFL in the hot leg, and to model the full-scale hot leg model and the 1/15 reduced-scale hot leg test piece respectively. For the full-scale hot leg model, the numerical calculation results were dimensionless. And they were in good agreement with the experimental data. But for the reduced size hot leg test piece model, the numerical calculation model underestimated the discharge fluid flow. Researchers have devoted great efforts to provide credible thermal-hydraulic system codes for the analyses of transients and accidents scenarios in nuclear power plants (Wang et al., 2021). And this paper mainly used RELAP5 for simulation calculation, and evaluated the CCFL model. Simultaneously, this paper studied the effect of the lengths of horizontal pipe, the shapes of the upper exit of inclined pipe, and the shapes of elbow connecting horizontal pipe with inclined on the characteristics of the CCFL.

EXPERIMENT INTRODUCTION

When LOCA occurs in a PWR, during the reflooding phase, the water collected at the steam generator inlet may flow back through the hot leg against the steam from the upper plenum, which creates a steam blockage in the primary loop. Among them, the counter current flow of water from the steam generator affects the accumulation of water and its horizontal distribution in the

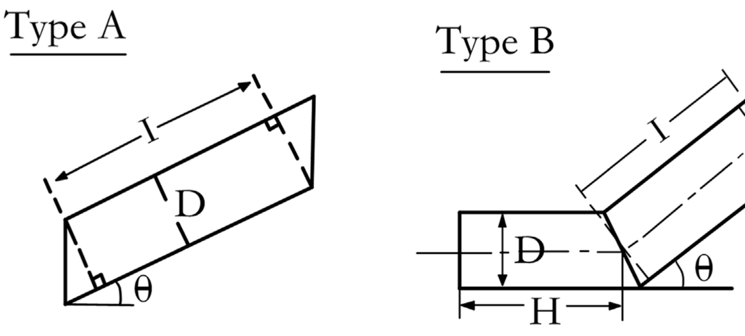

FIGURE 3 | Schematic diagram of experimental Types A and B.

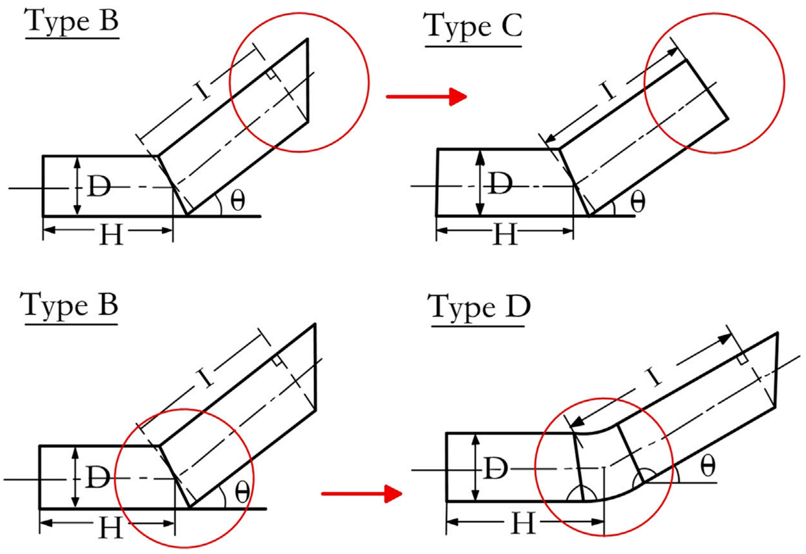

FIGURE 4 | Schematic diagram of experimental Types C and D.

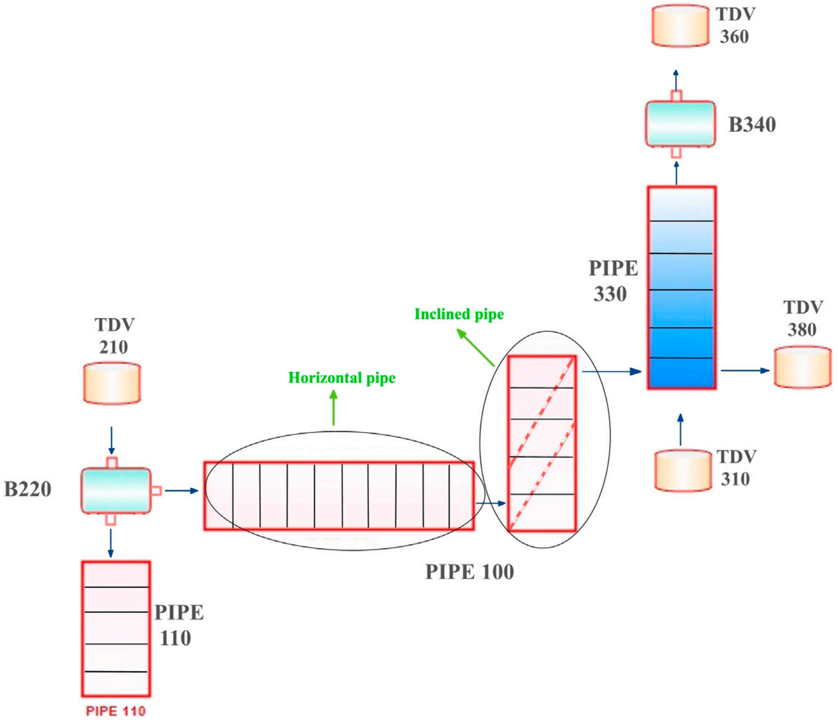

FIGURE 5 | Nodes division diagram.

upper plenum, thereby affects the cooling of the multi-dimensional core, and the flow rate of water depends on the CCFL characteristics in the hot leg. In 1986, Akira (Ohnuki, 1986) conducted an experiment research in order to study the characteristics of CCFL in the model flow channel. This paper conducted a simulation study based on this experiment. The experimental system as shown in **Figure 2**. The cross section of the separator tank was a square of 0.21 m × 0.21 m and the height

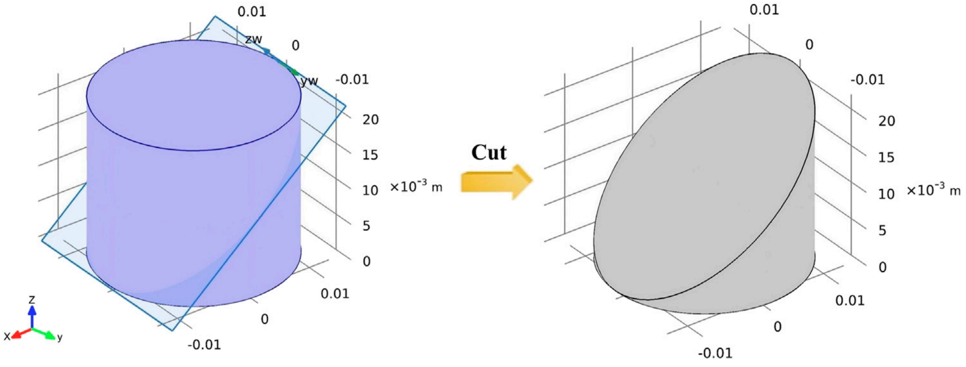

FIGURE 6 | Schematic diagram of sharp incision in inclined pipe.

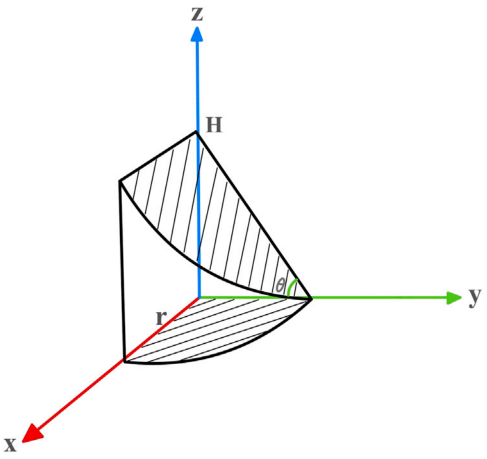

FIGURE 7 | Coordinate chart for area calculation of sharp inclined pipe.

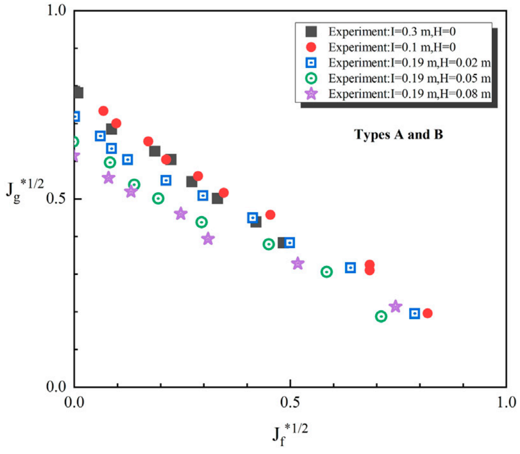

FIGURE 8 | Influence of the horizontal pipe length (Ohnuki, 1986).

is 0.38 m. And the 0.03 m inner diameter water supply pipe located at the bottom of the measuring tank. The experimental section was visualized, and the separator tank was opened to the atmosphere. During the experimental procedure, to obtain an initial holdup of water in the separator tank, a continuous high flow rate of air was first supplied into the measuring tank. The water level *h* in the separator tank was kept constant during the experiment. When the air quality was constant Q_g , the volume flow Q_f of falling water was calculated from the rising velocity of the water level in the measuring tank. After measured the Q_f for the specified Q_g , the water in the measuring tank was drained. And the procedure mentioned above was repeated.

Four pipe configurations were used in this study (Type A, Type B, Type C and Type D). **Figure 3** to **Figure 4** were schematic diagrams of the experimental pipes. In fact, the shape of upper exit of the PWR hot leg is a circular section. The shapes of elbow connecting the horizontal pipe and the inclined are smooth, and this section diameter is constant.

Type A was composed of inclined pipes only; Type B was composed of horizontal pipes connected to inclined pipes. Therefore, an improved pipe type was used instead of the Type B to study the effects of the shapes of upper exit and elbow. The shape of upper exit of Type C was a circular section, which was an improvement on Type B; Type D had a double-edged connection with the inclined pipe, which was an improvement to Type B, as shown in **Figure 4**. And **Table1** shows the dimensions of the experimental section.

Condition I, II and IV to VI carry out an analysis of the effect of lengths of horizontal pipe. Condition III and VIII pay attention to the effect of shapes of upper exit of inclined pipe. Furthermore, condition VII and IX focus on the effect of shapes of bend connecting horizontal pipe with inclined pipe.

SIMULATION METHOD

The nodes division is shown in **Figure 5**. The inlet boundary, 210 and 310 components adopted the "TDV"; and the outlet boundary, 360 and 380 also adopted the "TDV". Among them, 210 was used to simulate the air injection device, 310 was used

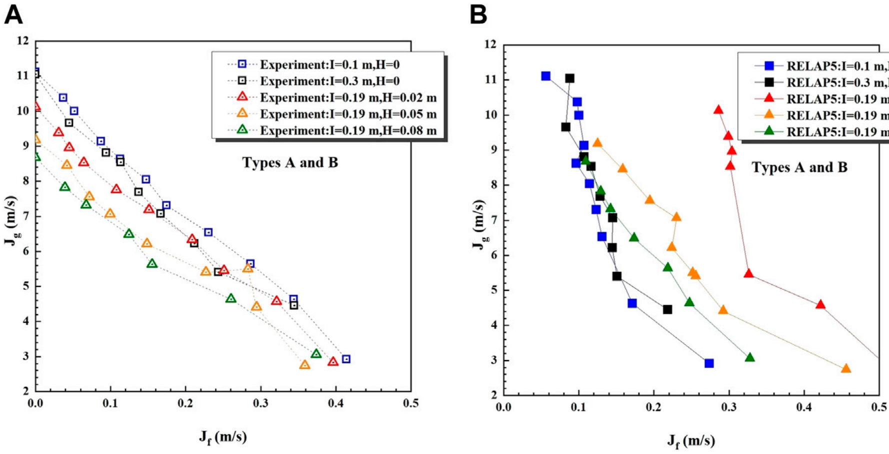

FIGURE 9 | Summary of experimental and RELAP5 data (0.19 m long inclined pipe).

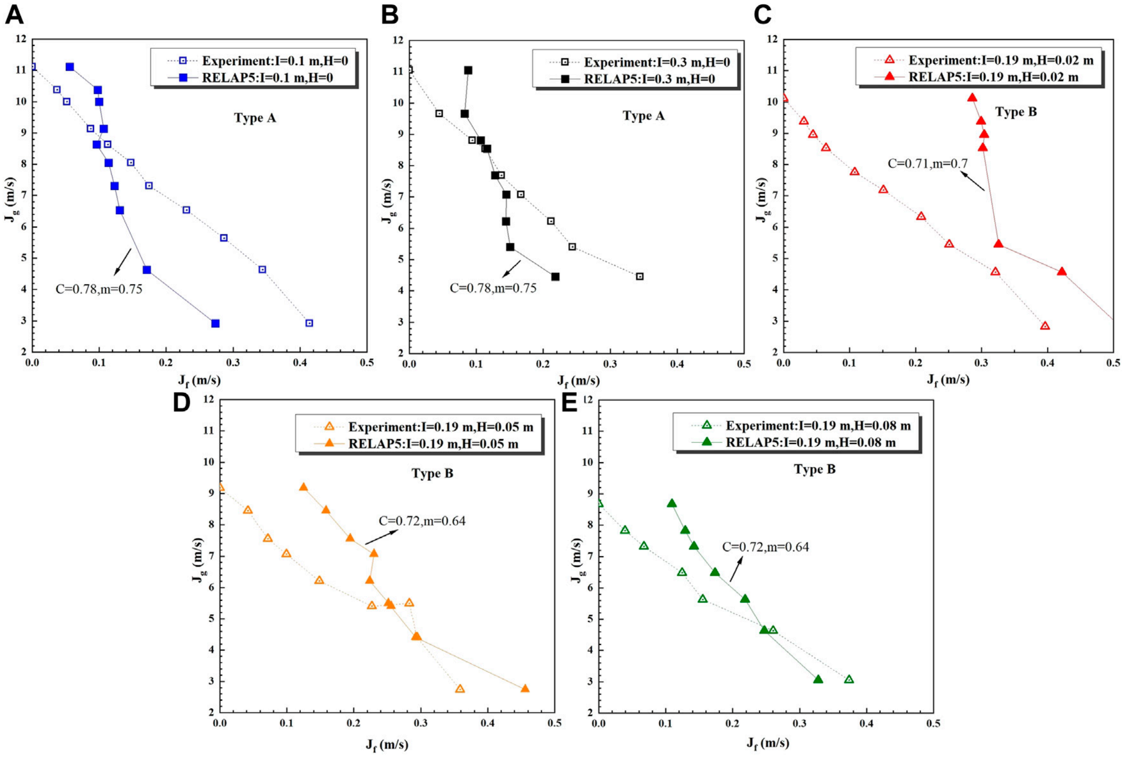

FIGURE 10 | Effect of length of horizontal pipe.

to simulate the liquid injection, 360 was the exhaust port, and the 380 was used to maintain a constant water head in the separator. The horizontal and inclined pipe were simulated by "PIPE" 100.

Noteworthily, in the modeling process, considering the difference in shapes of upper exit of inclined pipe, the simulation was carried out by changing the cross-sectional area of the exit, that was, Type A, Type B, and Type D were all calculated by elliptical area, and Type C was calculated by circular area, as shown in the **Figure 6**. As the Type D had a smooth bend connecting horizontal pipe with inclined, the nodes were refined to achieve a better simulation effect. At the same time, the influence of the coefficient of local resistance was considered at the joints of different elbows.

According to **Figure 7**, the area of the ellipse formed by the oblique cut is calculated as follows (in this study, $\theta = 40^\circ$):

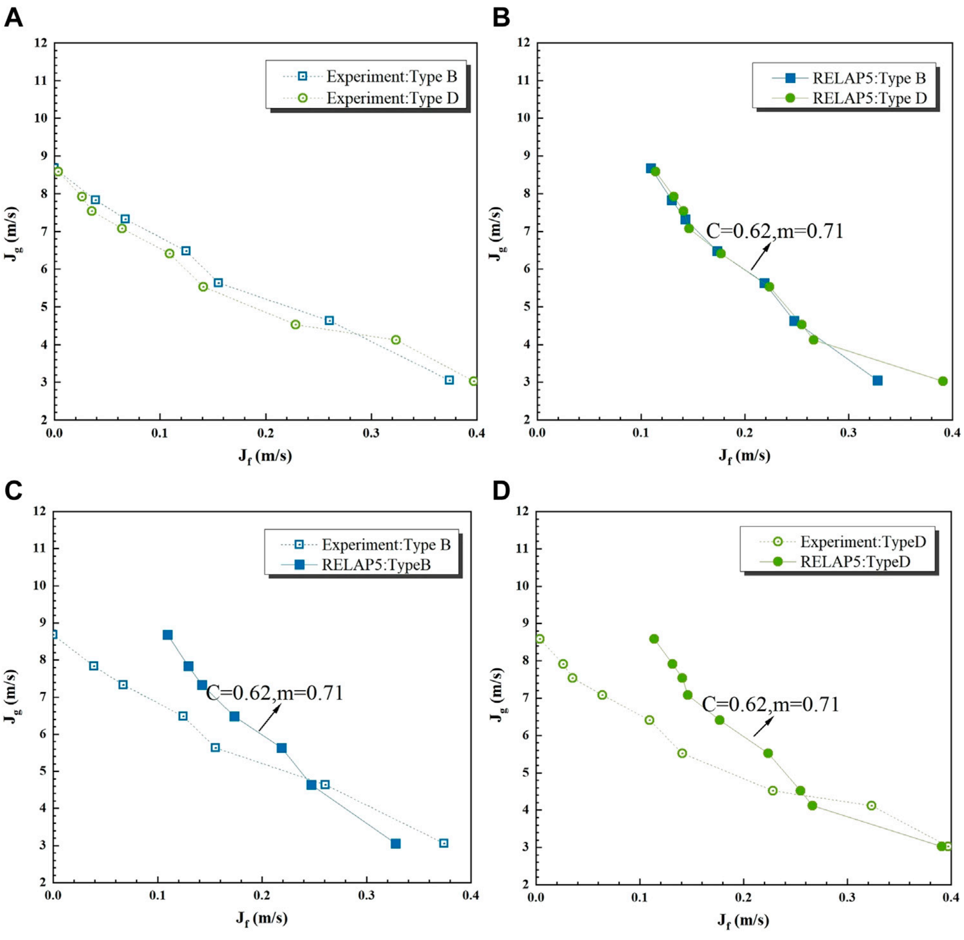

FIGURE 11 | Effect of blow shapes.

$$\frac{S}{4} = \int_0^r \frac{\sqrt{r^2 - x^2}}{\cos\theta} dx = \frac{1}{\cos\theta} \cdot \frac{\pi r^2}{4} \tag{1}$$

$$S = \frac{\pi r^2}{\cos\theta} \tag{2}$$

In the RELAP5/MOD3.3 program, if the CCFL model not turned on at the place where the gas-liquid counter current flow occurs, the "addition" and "subtraction" momentum equations are directly calculated simultaneously. Meanwhile, the program simulation do not take into consideration the effect of momentum loss caused by the instability of the liquid film; if the CCFL model turned on, this factor is considered.

The earliest Hewitt and Wallis (1963) passed the liquid down in a vertical acrylic resin tube with a diameter of 1.25 inch, and made the air flow up through the tube, in the opposite direction of the liquid, and then determined the minimum air flow rate required to cause the liquid to flow in the opposite direction upward. (that was, the flooding point), so obtain the empirical correlation related to CCFL.

Wallis number is a dimensionless number that characterizes the equilibrium relationship between momentum and static force. The following mainly analyzes the effect of the length H of the horizontal pipe, connecting the inclined pipe on the relationship between $J_g^{*1/2}$ and $J_f^{*1/2}$, where J_g^* and J_f^* parameters are based on the Wallis correlation:

$$J_g^{*1/2} + mJ_f^{*1/2} = C \tag{3}$$

where C is a geometrical parameter, the factor m and the C vary with the change of the test conditions such as the structure of the gas-liquid phase inlet and outlet of the vertical pipe, the size of the vertical pipe, and the physical properties of the fluid.

The currently developed CCFL model has three main forms in the program: Wallis correlation, Kutateladze correlation, and the form between Wallis and Kutateladze correlation (Bankoff et al., 1981).

Classical relation:

$$H_g^{1/2} + mH_f^{1/2} = C \tag{4}$$

where H_f is the dimensionless liquid flux, H_g is the dimensionless gas flux, C is the gas intercept (value of when $H_f = 0$, i.e., complete flooding), and m is the "slope", that is the gas intercept divided by the liquid intercept (the value of when $H_g = 0$).

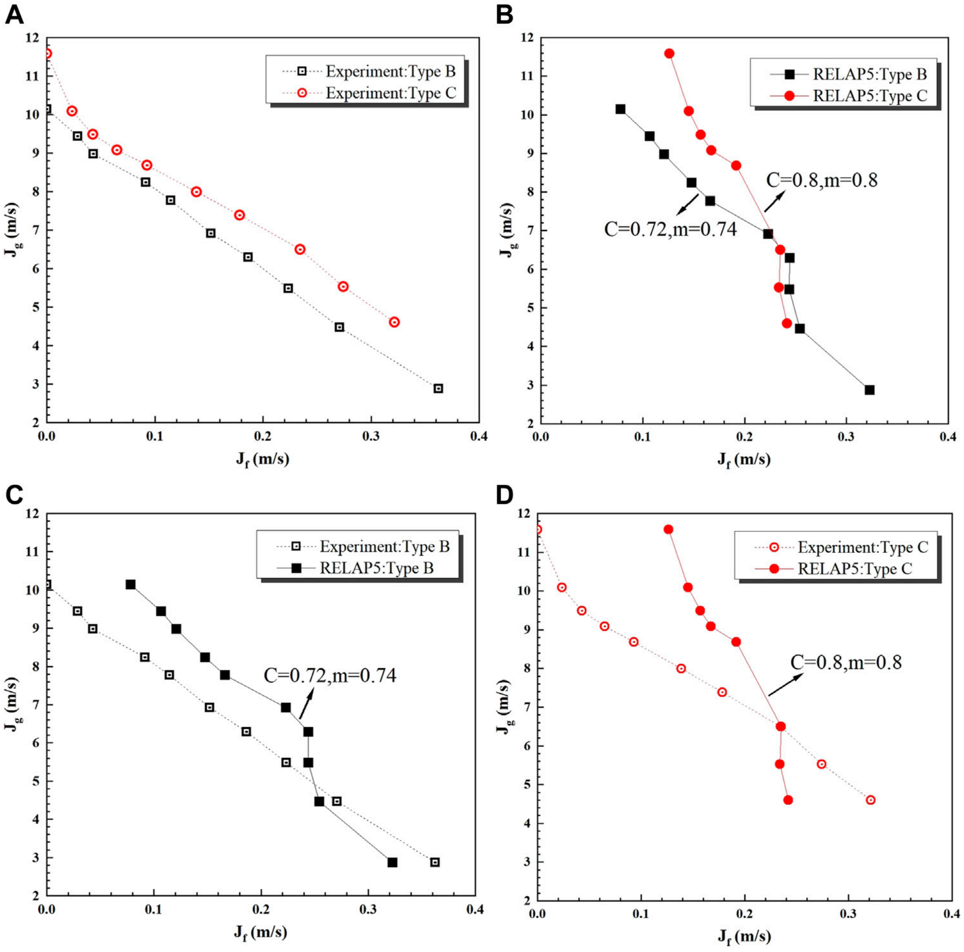

FIGURE 12 | Effect of inclined pipe upper exit shapes.

The dimensionless fluxes of gas and liquid have the following forms:

$$\boldsymbol{H}_{\mathrm{f}} = j_{\mathrm{f}}\left[\frac{\rho_{\mathrm{f}}}{gw\left(\rho_{\mathrm{f}}-\rho_{\mathrm{g}}\right)}\right]^{1/2} \tag{5}$$

$$\boldsymbol{H}_{\mathrm{g}} = j_{\mathrm{g}}\left[\frac{\rho_{\mathrm{f}}}{gw\left(\rho_{\mathrm{f}}-\rho_{\mathrm{g}}\right)}\right]^{1/2} \tag{6}$$

$$j_{\mathrm{f}} = \alpha_{\mathrm{f}}\nu_{\mathrm{f}} \tag{7}$$

$$j_{\mathrm{g}} = \alpha_{\mathrm{g}}\nu_{\mathrm{g}} \tag{8}$$

where j_{f} is the liquid superficial velocity, j_{g} is the gas superficial velocity, ρ_{f} is the liquid density, ρ_{g} is the gas density, α_{f} is the liquid volume fraction, α_{g} is the gas volume fraction, g is the gravitational acceleration.

$\boldsymbol{w}$ is the feature length, given by the following expression, (where β is a user input constant)

$$\boldsymbol{w} = \boldsymbol{D}_j^{1-\beta}\boldsymbol{L}^{\beta} \tag{9}$$

$\boldsymbol{D}_{\mathrm{j}}$ is the junction hydraulic diameter, and L is the Laplace capillary constant, given by the following form:

$$\boldsymbol{L} = \left[\frac{\sigma}{g\left(\rho_{\mathrm{f}}-\rho_{\mathrm{g}}\right)}\right]^{1/2} \tag{10}$$

where σ is the surface tension, and in **Eq. 9**, β can be a number from 0 to 1.0.

By default, the Wallis correlation is used for small diameters and the Kutateladze correlation is used for large diameters. But the study of Tien et al. (Tien et al., 1979) believed that the correlations' conditions should be more stringent and flooding data obtained from measurements of nuclear power plant geometry. Then, an appropriate CCFL model for the input cards is generated.

RESULTS AND DISCUSSION

Effect of Lengths of Horizontal Pipe

This part mainly discusses the influence of horizontal pipe length on CCFL of hot leg. It was found that the case of inclined riser without horizontal pipe, J_{f}^{*} did not depend on the length I at the same J_{g}^{*} (Ohnuki, 1986), as shown in **Figure 8**.

As follows, **Figures 9**, **10** showed the compares with the experimental data and RELAP5 simulation calculation data, respectively. It can be seen that the results calculated by RELAP5 are consistent with the change trend of the experimental data, but there are certain differences between the predicted data and the experimental data in some working conditions. If the pipe diameter and inclination angle of the inclined pipe remains constant in the hot leg, the initial flow rate keeps invariant, and the force between the gas and liquid phases and their effect maintains invariable. If the length of the horizontal pipe increases and the flow rate of the two phases remains unchanged, the action time and the distance between gas and liquid phases increases. And the gas phase consumes more energy in the liquid phase. Under the same liquid supply flow, a smaller air supply flow is required, the CCFL phenomenon occurs. It is worth noting that the "TDV" is used in the program calculation to specify the boundary conditions for the gas and liquid phase supply. In practice, if the pipe length is longer, the effect of gravity is magnified.

Effect of Shapes of Elbow

This section primarily discusses the effect of shapes of bend connecting horizontal pipe with inclined on CCFL of hot leg. **Figure 11** shows the effect of elbow shapes on the CCFL in experimental. The experimental data shows that the elbow shape had little effect on the CCFL, which is also reflected from the RELAP5 simulation results. Meanwhile, the trend of the simulated data is consistent with the experimental data, which is in good agreement. Due to the changes of the flow pattern of the two-phase flow at the junction of the horizontal pipe and the inclined pipe, the liquid in the elbow channel disturbs greatly at the junction, so it is easily carried by the gas flowing. This phenomenon becomes more obvious with the increase of liquid flow rate, which may affect the occurrence of CCFL phenomenon.

Effect of Shapes of Upper Exit of Inclined Pipe

Figure 12A shows the effect of different upper exit shapes of the inclined pipe on the CCFL experimental. Experimental data suggests that the upper exit shapes have an effect on CCFL, which are also reflected from the RELAP5 simulation results. Chung et al. (Tien et al., 1980) carried out an air-water CCFL test in a group of vertical pipes with the same pipe diameter and different outlet structures at the upper and lower ends. The lowest gas-phase flow rate occurs in the vertical pipe with the sharp-edged structure at the top; in the vertical pipe with the rounded top, the highest gas flow rate when CCFL occurs. **Figures 12B–D** have a similar situation in the inclined pipe. The J_{f}^{*} for the pipe with a circular upper exit is slightly larger than that of the sharp one at the same J_{g}^{*} .

CONCLUSION

Based on the simulation results in this paper, the following conclusions can be drawn:

1) Under the same water flow rate, the longer the horizontal pipe, the lower the gas flow rate at the beginning of the counter current flow. It should be noted that the program starts the CCFL model, nodes division in the vicinity of the connecting pipe should be as detailed as possible to reduce the program calculation error. And a single component can be added as a transition when simulating "TDV".
2) The simulation results show that the elbow has little effect on the CCFL phenomenon. But with the increase of the liquid flow rate, the liquid disturbance increases, which affects the CCFL in the elbow.
3) The results show that the upper outlet shapes have the effect on CCFL characteristics. Compared with the sharp injection method, the gentle injection method is not easy to cause the initial disturbance of the liquid phase in the exit area, and the gas flow rate required to initiate the CCFL initiation under the same conditions is larger.
4) The above simulation results show that the CCFL model in Wallis correlation has good applicability, and the influence of pipe lengths and pipe orifice shapes on the characteristics of CCFL can be considered through the parameter fitting of c and m in the CCFL model. As long as the model aims to build at different geometric structures, the CCFL characteristics of different geometric structures can be well considered, but the input data of the determined model parameters are required in advance. It should be noted that the model of Wallis parameters comes from the fitting of experimental data with a small aperture geometry, and the modeling effect of the model needs to be considered for the large aperture experimental section in the nuclear reactor accident analysis.

In order to understand the influencing factors of the CCFL phenomenon in the hot leg more clearly, this paper mainly carried out the simulation of the effect of lengths of horizontal pipe, the effect of shapes of elbow and the effect of shapes of upper exit of inclined pipe. And this paper evaluated the CCFL model in the system program and analyzed the influencing factors. Simultaneously, some special considerations and solutions for modeling hot leg segments were given.

DATA AVAILABILITY STATEMENT

The original contributions presented in the study are included in the article/Supplementary Material, further inquiries can be directed to the corresponding author.

AUTHOR CONTRIBUTIONS

XL contributed the simulation work and also contributed the original writing and revision. LG, CX and TW contributed conceptions. WS provided experimental literature surveys and contributed constructive discussions. WZ, LuZ, ZM, and LoZ contributed review and suggestions. LP contributed the supervision of the study.

FUNDING

This work is financially supported by the National Key R&D Program of China (2018YFB1900400).

REFERENCES

Ardron, K. H., and Banerjee, S. (1986). Flooding in an Elbow between a Vertical and a Horizontal or Near-Horizontal Pipe. *Int. J. Multiph. Flow* 12, 543–558. doi:10.1016/0301-9322(86)90059-5

Bankoff, S. G., Tankin, R. S., Yuen, M. C., and Hsieh, C. L. (1981). Countercurrent Flow of Air/water and Steam/water through a Horizontal Perforated Plate. *Int. J. Heat Mass Transf.* 24 (8), 1381–1395. doi:10.1016/0017-9310(81)90188-5

Chun, M. H., No, H. C., Yu, S. O., Ghyym, S-H., and Sunf, C-K. (2000). "Effect of Initial Liquid Level on the Countercurrent Flow Limitation in a Horizontal Pipe Connected to an Inclined Riser[C]," in Proceedings of NTHAS2: Second Japan-Korea symposium on nuclear thermal hydraulics and safety, Japan (IAEA).

Hewitt, G. F., and Wallis, G. B. (1963).*Flooding and Associated Phenomena in Falling Film Flow in a tube[R]. United Kingdom Atomic Energy Authority. Research Group*. Harwell Berks, England: Atomic Energy Research Establishment.

Hewitt, G. F., Lacey, P. M. C., and Nicholls, B. (1965). "Transitions in Film Flow in a Vertical Tube[C]," in Symposium on Two-phase Flow, England (Exeter).

Murase, M., Tomiyama, A., Kinoshita, I., Utanohara, Y., Yanagi, C., Takata, T., et al. (2012). VOF Calculations of Countercurrent Gas-Liquid Flow in a PWR Hot Leg[J]. *Sci. Technol. Nucl. Installations* 2012, 935391. doi:10.1155/2012/935391

Ohnuki, A. (1986). Experimental Study of Counter-current Two-phase Flow in Horizontal Tube Connected to Inclined Riser. *J. Nucl. Sci. Technol.* 23 (3), 219–232. doi:10.1080/18811248.1986.9734975

Siddiqul, H., Banerjee, S., and Ardron, K. H. (1986). Flooding in an Elbow between a Vertical and a Horizontal or Nearhorizontal Pipe, Part I; Experiment. *Int. Multiph. Flow.* 12, 531–541.

Tien, C. L., Chung, K. S., and Liu, C. P. (1979). *Flooding in Two-phase Countercurrent Flows*. EPRI.

Tien, C. L., Chung, K. S., and Liu, C. P. (1980). Flooding in Two-phase Counter Current Flows—II: Experimental Investigation[J]. *Physicochem, Hydrodyn.* 1, 209–220.

Wang, M., Wang, Y., Tian, W., Qiu, S., and Su, G. H. (2021). Recent Progress of CFD Applications in PWR Thermal Hydraulics Study and Future Directions. *Ann. Nucl. Energy* 150, 107836. doi:10.1016/j.anucene.2020.107836

Wongwises, S. (1998). Effect of Inclination Angles and Upper End Conditions on the Countercurrent Flow Limitation in Straight Circular Pipes. *Int. Commun. Heat Mass Transf.* 25 (1), 117–125. doi:10.1016/s0735-1933(97)00143-7

Conflict of Interest: Authors LG, CX and TW are employed by Nuclear Power Technology Research Institute Co., Ltd.

The remaining authors declare that the research was conducted in the absence of any commercial or financial relationships that could be construed as a potential conflict of interest.

NOMENCLATURE

g gravitational acceleration ($m{\cdot}s^{-2}$)

D pipe diameter (m)

K nondimensional group depending only on fluid properties

L length of the lower limb of the elbow (m); Laplace capillary constant

D_j junction hydraulic diameter (m)

Greek symbols

ρ_k density ($kg{\cdot}m^{-3}$)

j_k superficial velocity (m/s)

β constant

w feature length

Abbreviations

CCFL Counter current flow limitation

LOCA Loss of Coolant Accident

TDV Time Dependent Volume

RELAP Reactor Excursion and Leak Analysis Program

PWR Pressurized Water Reactor

frontiers | Frontiers in Energy Research

ORIGINAL RESEARCH
published: 09 June 2022
doi: 10.3389/fenrg.2022.914541

Experimental Research of Flow Distribution at Reactor Core Inlet of ACP100

Lei Ding, Lin Jiang, Dayu Jiang, Wenbin Zhuo, Xiao Yan and Jianjun Xu*

Nuclear Power Institute of China, Chengdu, China

A 1/3 scaled-down mock-up reactor of ACP100 was used to simulate the flow field in the prototype reactor and to carry out the experiment of core inlet flow distribution. In the mock-up reactor, the major flow path of the reactor is linearly scaled except for the core region which is replaced by 57 dummy fuel assemblies. In addition, the experiment measures core inlet flow rates by a specially designed turbine installed in each dummy fuel assembly. In the experiment, both four-loop balanced and unbalanced operating conditions are tested. The experimental results show that the flow in the major flow path of the mock-up reactor has entered the self-modeling zone and the flow field characteristics are the same as the prototype. The core inlet flow rates of different tests show similar distributions, which all meet the hydraulic performance requirements. Moreover, the effect of impeller rotation on the flow field of the core inlet has also been studied. The study indicates that the flow distribution is almost unaffected by the swirl flow.

Keywords: core inlet flow distribution, ACP100, experimental research, four-loop balanced, unbalanced operating condition, swirl flow

Edited by:
Luteng Zhang,
Chongqing University, China

Reviewed by:
Zhaoming Meng,
Harbin Engineering University, China
Yan Xiang,
Royal Institute of Technology, Sweden

****Correspondence:***
Lei Ding
ding2012014@126.com

Specialty section:
This article was submitted to
Nuclear Energy,
a section of the journal
Frontiers in Energy Research

Received: *07 April 2022*
Accepted: *03 May 2022*
Published: *09 June 2022*

Citation:
Ding L, Jiang L, Jiang D, Zhuo W, Yan X and Xu J (2022) Experimental Research of Flow Distribution at Reactor Core Inlet of ACP100. Front. Energy Res. 10:914541. doi: 10.3389/fenrg.2022.914541

1 INTRODUCTION

Nuclear energy is a clean energy source which plays an important role in achieving carbon neutrality goals. However, the promotion of traditional nuclear power plants faces many problems, such as large initial investment, long construction period, and high requirements on sitting conditions, all of which restrict the development of nuclear power. Modular small reactor (SMR) is a good solution to change this situation. SMR is a type of reactor with a single-stack electric power of less than 300 MW, which adopts new technologies like modular design, modular manufacturing, and rapid on-site assembly, thus making the reactor have a shorter construction period, better economy, and application flexibility. Furthermore, the nuclear steam supply system of SMR uses an integrated arrangement, which greatly simplifies the reactor coolant system, and can achieve higher security than the third generation of reactors.

ACP100 is a kind of SMR designed by the China National Nuclear Corporation independently. It eliminates primary loop piping by connecting steam generators and reactor coolant pumps directly to the reactor pressure vessel. The innovative design makes the internal flow field of ACP100 much different from traditional reactors. According to regulations, all the newly developed reactors are required to pass tests to verify the reliability of their safety designs. As an important factor affecting the operation of the reactor, the distribution of coolant flow at the core inlet is a significant content of verification in the design stage. Due to its importance, researchers in various countries have carried out relevant studies.

The United States was the first to carry out experiments on the hydraulic characteristics of nuclear reactors. In 1964, Hetsroni (Hestroni, 1964) carried out simulation experiments to verify the flow distribution of the reactor coolant in the Connecticut Yankee Nuclear Power Plant. Based on similarity theory, he proposed four principal parameters including geometry, relative roughness, Reynolds number, and Euler number as similarity numbers in model design. In addition, a hydraulic model with a ratio of 1:7.5 was designed and constructed representing hydraulics of the prototype reactor. Specifically, the model used 157 dummy fuel assemblies whose resistance was consistent with the prototype. The flow rate of each dummy fuel assembly was measured by an orifice flowmeter. Its experimental results show that the maximum flow distribution factor (ratio of the flow rate in one fuel assembly to the average internal flow rate of all the fuel assemblies) of the core inlet flow is 1.27 and the minimum is 0.80.

In 2006, Hensch Fabien (Hensch, 2006) from European Union set up the JULIETTE experimental facility to carry out hydraulic simulation experiments of the EPR reactor. JULIETTE was a scaled model of the four-loop reactor, consisting of four inlet pipes, a downcomer, a lower chamber with flow distribution device, an upper chamber, and the core. In the model, the flow rate was measured by a venturi arranged at the inlet of each dummy fuel assembly to investigate the flow distribution at the core inlet. Experiments showed a trend of higher flow in the middle area and lower flow in the peripheral area under rated conditions. The flow distribution factors were 0.838–1.087, and the maximum factor deviation of adjacent components was 18%. In the experiment, the effect of swirl flow at the reactor inlet and the number of operating loops were also in view. The results indicated that neither swirl flow nor the number of loop operations had obvious implications on flow distribution.

In 2012, an experimental study of System-integrated Modular Advanced Reactor (SMART) for core flow and distribution was conducted by Kim (Kim, 2012) from the Korea Atomic Energy Research Institute. A 1/5 scaled-down reactor model was constructed and the core region was replaced by 57 dummy fuel assemblies. A special venturi meter was mounted at the entrance of each dummy fuel assembly to measure the inlet flow rate. Experimental data was obtained under a 4-pump balanced condition. It was found that flow distribution factors varied from 0.952 to 1.240, and five of all dummy fuel assemblies exceeded 1.100.

In 2014, a reactor hydraulic simulation test of CAP1400 was conducted by Fang (Fang and Wang, 2014) with a 1/6 scaled-down reactor model. Fuel assemblies were replaced by 193 2 × 2 rod bundles simplified models with similar longitudinal and lateral resistance characteristics. A specially designed turbine flowmeter was mounted at the entrance of the dummy fuel assembly to measure the inlet flow rate. Experiments examined the hydraulic characteristics of the reactor coolant flow under four-pump balanced and unbalanced conditions and evaluated the influence of the flow equalizing plate. The experimental results showed that the flow equalizing plate could effectively improve the uniformity of the core inlet flow. In addition, due to the rectification of the flow equalizing plate, unbalanced flow conditions had little effect on the flow distribution characteristics.

Moreover, experimental investigations and numerical simulations have also been carried out in this field. In 2007, an open source CFD code Saturne was used to carry out the transient calculation of the flow field for EDF's four-loop PWR by Yvan Fournier (Fournier et al., 2007). The calculation results showed that there was a large-scale flow pulsation phenomenon in the flow field of the lower chamber. When the core was heated, the coolant flow rate inside the fuel assembly was severely affected, but the flow rate at the inlet of the lower plate remained basically unchanged.

In 2013, a commercial CFD code Fluent 12.0 was adopted to compute turbulence flow in the SMART reactor by Bae (Bae et al., 2013). The influence of the turbulent model, Reynolds number, and inflow condition on flow distribution was discussed in detail. It was found the maximum flow rate difference of fuel assemblies was less than 2.3%.

In 2017, another three-dimensional numerical simulation concerned with the flow field of the Qinshan Phase II Nuclear Power Plant was conducted by Chen (Chen et al., 2017) with CFX code. In the rated operating condition, the maximum deviation of the flow distribution factor between the calculated value and the experimental value was 9.8%.

Although the numerical simulation has been conducted to verify the hydraulic characteristics of various nuclear reactor types, it still could not replace experiments. Limited by the lack of computer performance, the internal structures of the reactor, especially the core region, is always being simplified, which affects the accuracy of the calculation. The scaling model experiment remains the most important testing method.

In this article, a hydraulic experimental investigation is conducted to obtain flow distribution characteristics of the ACP100 reactor under different operating conditions. The influence of flow axial rotation (swirl) and unbalanced flow conditions on flow distribution at the core inlet are also analyzed. Experimental data will be used for reactor design.

2 EXPERIMENTAL FACILITY

2.1 Similarity Theory

To recur the physical phenomena of the prototype in a mock-up reactor, the scaled-down model should be designed based on similarity theory. All the conditions of geometric similarity, flow similarity, and motion similarity between the mock-up and the prototype must be satisfied. Also, the typical similarity parameters must be the same on both sides. According to the similarity theory of fluid mechanics, the main parameters that affect the flow distribution are the flow velocity u, the density of water ρ, the structural length L, the equivalent diameter D_H, the roughness Δ, the viscosity coefficient of water μ and flow pressure drop ΔP. Keeping all the variables corresponding to scale is difficult. So the Buckingham theory is adopted here and 4 important dimensionless groups are obtained consequently, which are geometry number L/D_H, relative roughness number Δ/D_H, Reynolds number $\rho u D_H/\mu$, and Euler number $2\Delta P/\rho u^2$.

TABLE 1 | Scaling ratio of the mock-up reactor.

Parameter and Dimensionless Number	ACP100	Scaling Ratio	Model
Temperature [°C]	303	–	20
Pressure [MPa]	15	–	1
Length ratio	1	L	1/3
equivalent diameter ratio	1	L	1/3
roughness ratio	1	L	1
Velocity ratio	1	u	1
Density ratio	1	ρ	1.39
Viscosity ratio	1	μ	11.49
Re ratio	1	$\rho u^2 L/\mu$	1/24.80
ΔP ratio	1	ρu^2	1.39
Eu ratio	1	1	1

The italic values are the dimension of the parameters.

The geometrical similarity is the premise of kinematic similarity and dynamic similarity. The geometry number is mainly concerned with geometrical similarity, which means the mock-up reactor should be the same as the prototype with a constant scale factor anywhere. The determination of the scale factor needs to balance many requirements. On one hand, a large-scale factor model will be difficult to be manufactured and it requires more test facilities such as the main pump and pipes. On the other hand, a small-scale factor model is difficult for assemblage and it will also amplify the boundary layer effect and result in a different regime. Considering the dimension of the prototype, the capacity of the test rig, and cost of fabrication, a 1/3 scale factor is selected in the experiment. The geometry of the mock-up reactor will be introduced in the following sections.

Relative roughness number is important in the flow path where a large frictional pressure drop occurs. However, it can be found that pressure drops in the main flow paths of the mock-up reactor are caused by form resistance instead of frictional resistance except in the downcomer and core region. Downcomer is a large flow path, and in a large flow path relative, roughness can be ignored because it has a minor influence on the flow field. In addition, the same Euler number is adopted in the simulation of the core region, and under the premise of geometric similarity, the requirements of the flow field simulation can still be met when the surface roughness of the mock-up reactor is relaxed to the same as the prototype reactor. So the relative roughness number is strictly satisfied in the experiment.

Reynolds number is also an important parameter in hydraulic experiments. According to the similarity theory, Reynolds numbers in the model and the prototype reactor should be equal, but it is very difficult to achieve. However, it is found that if the Reynolds number is large enough, it will have little influence on the flow field and Euler number in complex construction. The flow state and velocity distribution will no longer change with the change of the Reynolds number and the resistance factor (Euler number) converges to a constant value. In hydraulics, this state is called entering the second self-modeling region. Then the similar conditions for the flow inside the model and the prototype reactor could be collated as geometrical similarity and flow entering the self-mode region. In a mock-up reactor, although the hydraulic diameter D_H is small and the temperature is low compared with the prototype, the Reynolds number is still large enough to reach the self-mode state. So Reynolds number could not be satisfied strictly and the Euler number is automatically achieved if the flow field is independent of the Reynolds number.

To sum up, in the hydraulic experiment concerns with flow distribution, geometry number must be satisfied, Reynolds number can be neglected if it is large enough, and Euler number is satisfied automatically. The scaling ratios of the key parameters and dimensionless numbers in the mock-up reactor are shown in **Table 1**.

2.2 Geometrical Model

The mock-up reactor of ACP100 simulates all the main structures of the prototype reactor, including reactor pressure vessel (internal form), flow distributor, lower core plate, core barrel, 57 fuel assemblies, upper core plate, upper internals, primary sides of 16 steam generators, and some support structures. For the structures in the front and rear end of the core have a significant effect on the flow field at the core inlet, the models there, such as flow distributor, lower core plate, and upper core plate, are strictly scaled down to 1/3 size. Upstream of the core are two flow distribution structures, the flow distributor, and the lower core baffle. The flow distributor, as the primary distribution structure, is in the shape of an ellipsoid head with a large number of holes symmetrically opened on it, and the lower core baffle also has a number of holes corresponding to each fuel assembly for secondary flow distribution. The flow distributor is directly and concentrically attached to the lower core baffle with screws. It is too difficult to simulate all the internal components, so rational simplification is necessary. For example, the prototype reactor core is a complex region consisting of 57 open lattice fuel assemblies composed of 17 ×

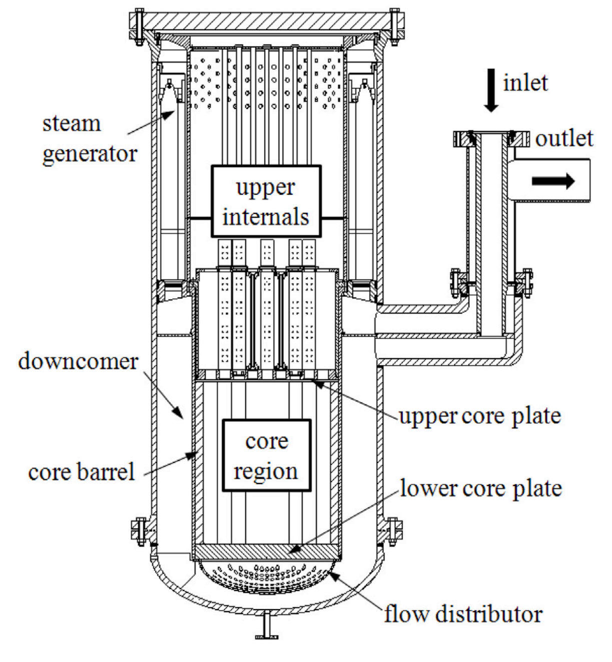

FIGURE 1 | schematic diagram of mock-up reactor (cross-section view).

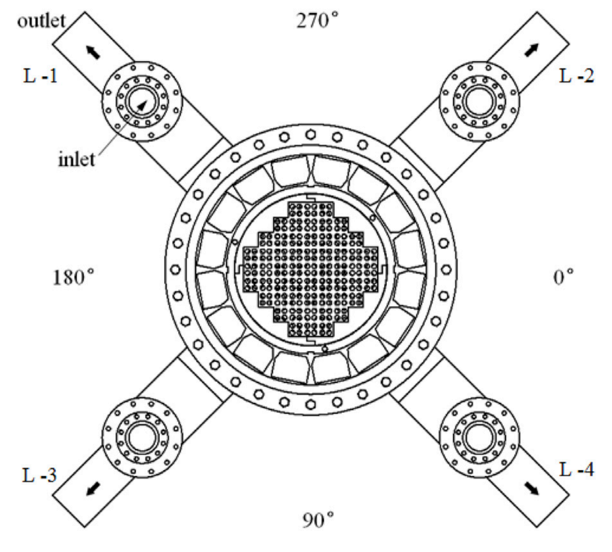

FIGURE 2 | schematic diagram of mock-up reactor (top view).

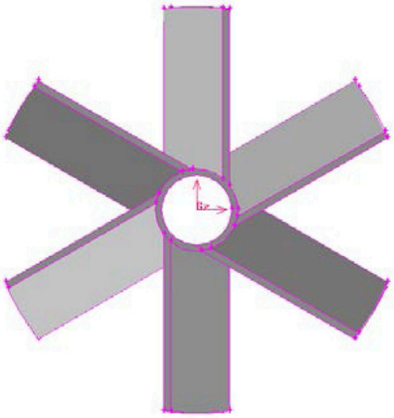

FIGURE 3 | schematic diagram of swirl generator.

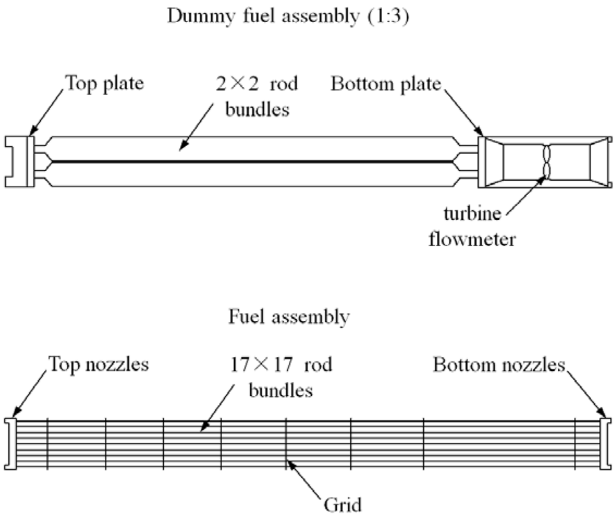

FIGURE 4 | Comparison diagram of dummy fuel assembly and prototype.

FIGURE 5 | Photograph of dummy fuel assembly.

17 fuel rods. In the mock-up reactor, the core is simplified with 57 dummy Fuel assemblies. Some guide tubes and control rods located downstream from the core are totally ignored, which have little influence on flow distribution. The elliptical head of the reactor pressure vessel is also replaced by a flat head for the space can be considered as a stagnant water area, and it should be specially explained that all the bypass flow measured by a separate bypass flow test is not taken into consideration in the experiment.

The flow characteristics in reactor nozzles also need to be concerned. In the integrated reactor, the pump is mounted directly on the vessel. However, finding a suitable small pump installed at the same site in a mock-up reactor and providing a similar flow rate is difficult. Therefore, a casing pipe is used as the inlet and outlet of the mock-up reactor, with the inlet in the center and the outlet around, to achieve the same flow rate and flow direction as the prototype. Above the casing pipe, a removable swirl generator is located to simulate the rotation caused by the pump. For the pump is too close to the reactor nozzle, the rotation of the impeller leads to significant swirling flow and it may have influence on the reactor core flow field. So it is necessary to study the effect of swirling flow. In the experiment, the swirl generator achieves the required swirl intensity by setting the inclination angle of the diversion plates.

The mock-up reactor and all internal components are all made of stainless steel. **Figure 1** and **Figure 2** show the schematic diagram of the mock-up reactor, and **Figure 3** shows the schematic diagram of the swirl generator.

In the experiment, water enters the mock-up reactor from four symmetrical inlets and flows downward in the downcomer. The flow distributor with numerous small holes in the lower plenum will break a large vortex and make flow uniform. Then the water flows through the lower core plate and enters 57 dummy Fuel assemblies. The flow distribution concerned in the experiment occurs here. Then the water flows through the upper core plate, upper internals, and 16 steam generators. Finally, water leaves the mock-up reactor from four outlets. The main flow path in the model is the same as the prototype.

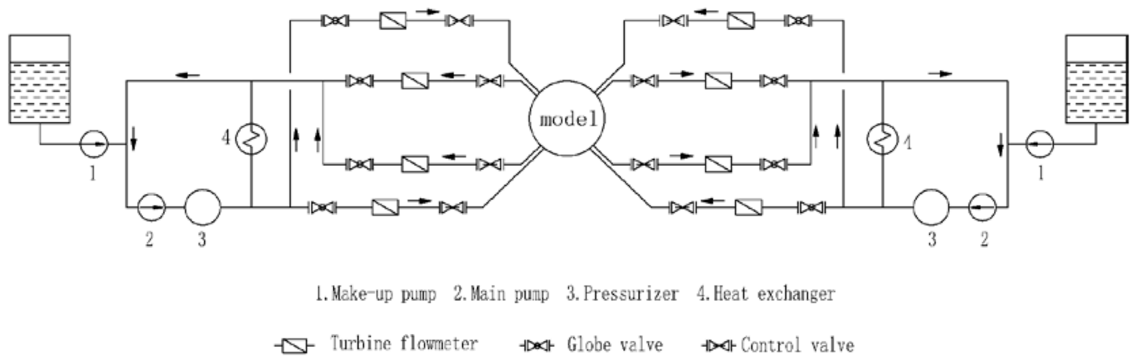

FIGURE 6 | schematic diagram of test loop.

TABLE 2 | Design parameters of test facility.

Design Parameter	Value
Design pressure	1.6 MPa
Operation pressure	1.2 MPa
Design temperature	100°C
Operation temperature	80°C
Normal mass flow rate of single pump	800 m^3/h
Pump head	119 m

2.3 Design of Dummy Fuel Assembly

Design of dummy fuel assembly is very important in experiments, which has a great influence on flow distribution. The ACP100 fuel assembly is mainly composed of top nozzles, bottom nozzles, 17 × 17 fuel rods, and different kinds of grids. For the scaled-down experimental model, from the perspective of processing and economy, the simulation of the fuel assembly can no longer be scaled down to achieve complete geometric similarity with the prototype. So fuel assembly must be simplified based on certain similarity theories with a small number of rods and a large rod diameter. A 2 × 2 open lattice dummy fuel assembly is adopted in the experiment, which has the same longitudinal resistance coefficient as a prototype. It should be mentioned that both resistance magnitude and distribution should be simulated, especially the inlet resistance characteristic of the fuel assembly, which is crucial for flow distribution. The lateral resistance characteristic of rods is also taken into consideration by the empirical formula recommended by Khan (Khan, 1972). With the same longitudinal and lateral resistance, external diameter and pitch diameter of dummy fuel rods can be determined. The diagrams of fuel assembly and dummy fuel assembly are shown in **Figure 4** and **Figure 5**.

The dummy fuel assembly is not only a resistance model, but also a flow measuring device. A specially designed turbine flowmeter is mounted at the entrance of each dummy fuel assembly to measure inlet flow rate. The measuring range of each flowmeter is from 5 m^3/h to 30 m^3/h with an accuracy of ±1%.

It should be stressed that due to manufacture and rigging errors, not only longitudinal resistance but also discharge coefficient of each dummy fuel assembly and turbine flowmeter is different from each other, so a hydraulic calibration must be carried out before the experiment. The orifice diameter of top nozzles can be sized so that the longitudinal resistance of dummy fuel assembly and prototype could be matched well. It should be mentioned here that the longitudinal resistance of fuel assembly will decrease with the increase of the Reynolds number. It will be difficult to make dummy fuel assembly that has the same resistance characteristic as the prototype due to geometrical difference. So a constant longitudinal resistance value is selected during the calibration process, which means the longitudinal resistance of fuel assembly under normal operation is chosen as reference and a deviation of ±2% is acceptable. Moreover, the discharge coefficient of each turbine flowmeter will be recorded to calculate the flow rate in the integral experiment and the accuracy of all flowmeters must meet the requirements.

2.4 Test Facility

The flow distribution experiment of ACP100 is carried out at the Nuclear Power Institute of China. A test facility with 4 loops is designed and constructed especially for this experiment. The test loop is mainly composed of 2 main pumps, 2 pressurizers, 2 heat exchangers 8 control valves, and a mock-up reactor. Each pump extends two branches connecting two entrances of the mock-up reactor. Flow rate per loop is controlled by adjusting the rotation frequency of the main pump and valve opening. When the experiment begins, de-ionized water will be transported from the water tank to the test loop. Then main pump will operate with a small flow rate until the air is totally discharged. Rotation frequency of the main pump will increase slowly until the operating condition is achieved. The pressurizer will decrease oscillation of flow rate during this process. If water temperature is high enough, the heat exchanger will work and inlet temperature of the mock-up reactor will be maintained at a constant value.

A schematic diagram of the test facility is shown in **Figure 6**, and the design parameters are shown in **Table 2**.

TABLE 3 | Measuring range and uncertainty.

Measurement	Measuring Range	Uncertainty (%)
Turbine flowmeter (loop)	90–500 m^3/h	0.5
Turbine flowmeter (dummy fuel assembly)	5–30 m^3/h	1
Thermocouple	0–100°C	0.5
Pressure transmitter	0–1.6Mpa	0.5

TABLE 4 | Test requirements and balanced conditions for the inlet flow.

Ratio to Reactor Inlet Velocity	L-1 (%)	L-2 (%)	L-3 (%)	L-4 (%)	Re[a]
Standard	100	100	100	100	1.34×10^6
Low flow	60	60	60	60	7.54×10^5
High Flow	120	120	120	120	1.64×10^6

[a] *The inlet of mock-up reactor is selected as reference cross section to calculate reference velocity.*

2.5 Measurement and Uncertainty

The parameters measured in the experiment include flow rate, fluid temperature, and system pressure. The flow rate and fluid temperature in each loop are measured by turbine flowmeters and thermocouples located at the entrance of the mock-up reactor. System pressure is monitored by a pressure transmitter and located at the entrance of the mock-up reactor too. Flow rate in each dummy fuel assembly is measured by specially designed turbine flowmeters with a total number of 57. All the instruments in the experiment are calibrated in advance. The uncertainty and measuring range are shown in **Table 3**.

3 EXPERIMENTAL RESULTS AND DISCUSSION

3.1 Experiment Data Processing

Flow rate in each dummy fuel assembly could be obtained in an experiment by a specially designed turbine flowmeter. However, it is cumbersome to evaluate the uniformity of the flow field and to distinguish the lowest flow dummy fuel assembly by comparing the measurements directly. Therefore, we introduce a dimensionless flow distribution factor to assist data processing and evaluation. The flow distribution factor is the ratio of the flow rate in each dummy fuel assembly (Q_i) to the average internal flow rate of all the 57 dummy fuel assemblies (Q_{ave}). It can be obtained by the following equations:

$$q_i = \frac{Q_i}{Q_{ave}} \tag{1}$$

$$Q_{ave} = \frac{\sum_{i=1}^{57} Q_i}{57} \tag{2}$$

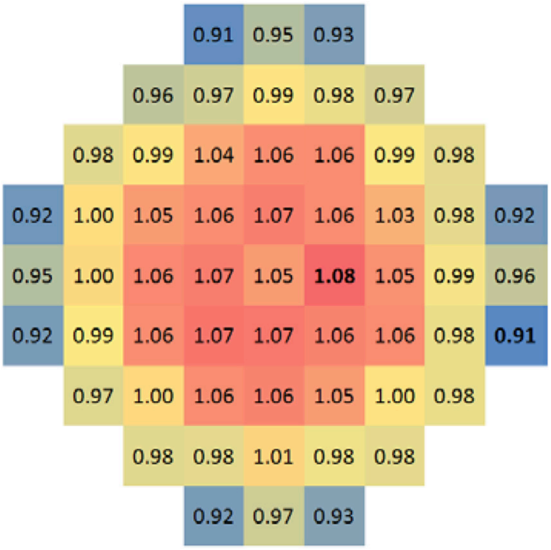

			0.91	0.95	0.93			
		0.96	0.97	0.99	0.98	0.97		
	0.98	0.99	1.04	1.06	1.06	0.99	0.98	
0.92	1.00	1.05	1.06	1.07	1.06	1.03	0.98	0.92
0.95	1.00	1.06	1.07	1.05	**1.08**	1.05	0.99	0.96
0.92	0.99	1.06	1.07	1.07	1.06	1.06	0.98	**0.91**
	0.97	1.00	1.06	1.06	1.05	1.00	0.98	
		0.98	0.98	1.01	0.98	0.98		
			0.92	0.97	0.93			

FIGURE 7 | Flow distribution map under standard condition.

3.2 Experiment Results

3.2.1 Balanced Condition Tests

The flow distribution in a mock-up reactor is measured under four-loop balanced operation conditions. **Table 4** shows the flow rate requirements for the balanced flow conditions. **Figure 7** and **Figure 8** show the results under the standard condition, low flow condition, and high flow condition.

The flow distribution factor map obtained under standard operating conditions shows that the largest internal flow of fuel assembly appears in the middle area of the core, and the distribution trend appears to be reducing from the center of the core to the periphery layer by layer. The flow rates in fuel assemblies close to the core baffle are low, and the lowest flow rate appears in the eight corners of the core baffle. However, the flow distribution at the core inlet is still homogeneous, and all the distribution factors are in the range of 0.91–1.08. Deviation within 10%, the flow distribution is homogeneous enough to meet design requirements. In addition, the flow distribution result shows obvious symmetry. Flow distribution characteristics are mainly affected by the hydro-dynamically driven convection and the structure of flow channels. The structural design of the ACP100 reactor, especially the lower chamber, has a distinct symmetry, and its four inlet nozzles are also symmetrically located at 90°. In the premise of sufficient symmetry of the structure, the uniform flow rates of the reactor inlets would create symmetrical flow characteristics at the core inlet.

In order to do further research on the effect of flow velocity on flow distribution, balanced condition experimental tests are

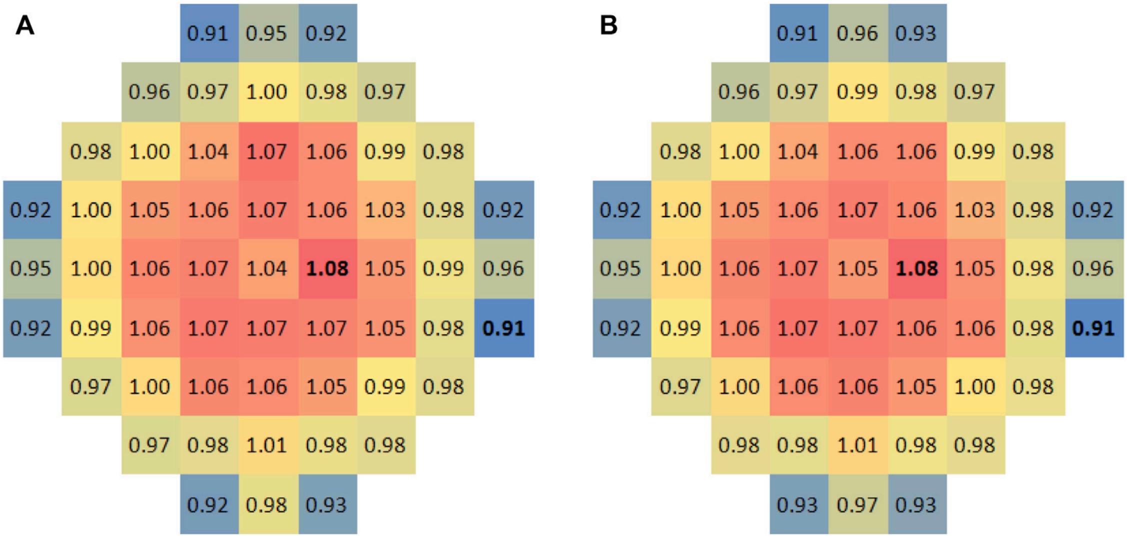

A

			0.91	0.95	0.92			
		0.96	0.97	1.00	0.98	0.97		
	0.98	1.00	1.04	1.07	1.06	0.99	0.98	
0.92	1.00	1.05	1.06	1.07	1.06	1.03	0.98	0.92
0.95	1.00	1.06	1.07	1.04	**1.08**	1.05	0.99	0.96
0.92	0.99	1.06	1.07	1.07	1.07	1.05	0.98	**0.91**
	0.97	1.00	1.06	1.06	1.05	0.99	0.98	
		0.97	0.98	1.01	0.98	0.98		
			0.92	0.98	0.93			

B

			0.91	0.96	0.93			
		0.96	0.97	0.99	0.98	0.97		
	0.98	1.00	1.04	1.06	1.06	0.99	0.98	
0.92	1.00	1.05	1.06	1.07	1.06	1.03	0.98	0.92
0.95	1.00	1.06	1.07	1.05	**1.08**	1.05	0.98	0.96
0.92	0.99	1.06	1.07	1.07	1.06	1.06	0.98	**0.91**
	0.97	1.00	1.06	1.06	1.05	1.00	0.98	
		0.98	0.98	1.01	0.98	0.98		
			0.93	0.97	0.93			

FIGURE 8 | Flow distribution factor map under non-rated condition: **(A)** 60% velocity; **(B)** 120% velocity.

TABLE 5 | Test requirements and conditions for unbalance inlet flow.

Ratio to Reactor Inlet Velocity	L-1 (%)	L-2 (%)	L-3 (%)	L-4 (%)
One-shut	0	120	120	120
5% offset	104	99	99	99

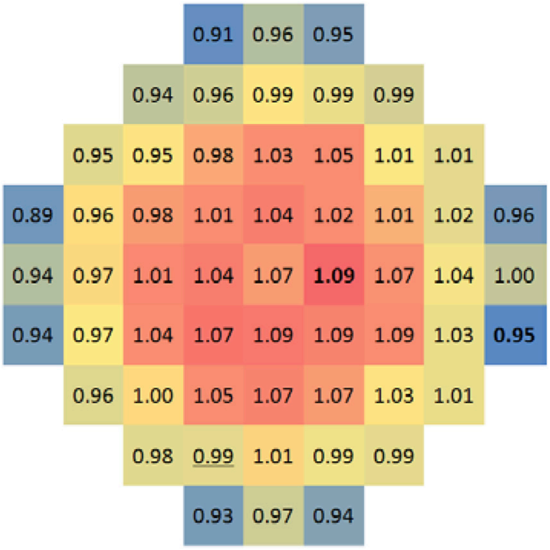

			0.91	0.96	0.95			
		0.94	0.96	0.99	0.99	0.99		
	0.95	0.95	0.98	1.03	1.05	1.01	1.01	
0.89	0.96	0.98	1.01	1.04	1.02	1.01	1.02	0.96
0.94	0.97	1.01	1.04	1.07	**1.09**	1.07	1.04	1.00
0.94	0.97	1.04	1.07	1.09	1.09	1.09	1.03	**0.95**
	0.96	1.00	1.05	1.07	1.07	1.03	1.01	
		0.98	0.99	1.01	0.99	0.99		
			0.93	0.97	0.94			

FIGURE 9 | Flow distribution map under one-shut condition.

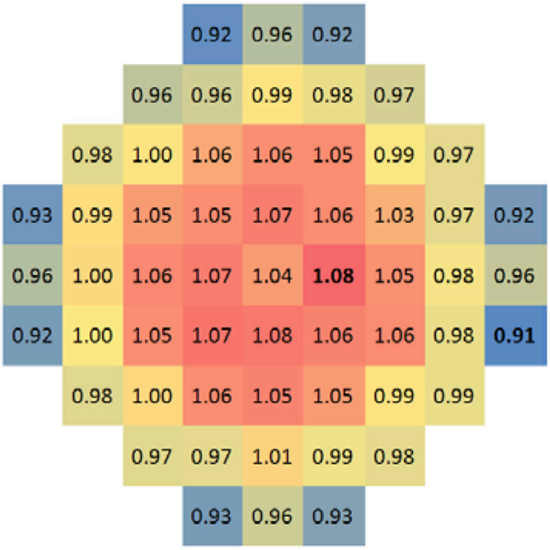

			0.92	0.96	0.92			
		0.96	0.96	0.99	0.98	0.97		
	0.98	1.00	1.06	1.06	1.05	0.99	0.97	
0.93	0.99	1.05	1.05	1.07	1.06	1.03	0.97	0.92
0.96	1.00	1.06	1.07	1.04	**1.08**	1.05	0.98	0.96
0.92	1.00	1.05	1.07	1.08	1.06	1.06	0.98	**0.91**
	0.98	1.00	1.06	1.05	1.05	0.99	0.99	
		0.97	0.97	1.01	0.99	0.98		
			0.93	0.96	0.93			

FIGURE 10 | Flow distribution map with a loop flow rate 5% higher.

carried out again under the 60% and 120% rated flow velocity of the prototype reactor. According to self-modular theory, in a complex structure such as a reactor, where the Reynolds number is large enough, the flow regime and flow velocity distribution will no longer change. The experimental results also show well agreement with each other. It means the Reynolds number is large enough that the flow velocity has little influence on the flow distribution in the experiment. Therefore, it is safe to say that the experiments yield reliable results with good repeatability.

3.2.2 Unbalance Condition Tests

Unbalance conditions may occur in accidents when the main pump stops or the steam line breaks. In the experiment, two

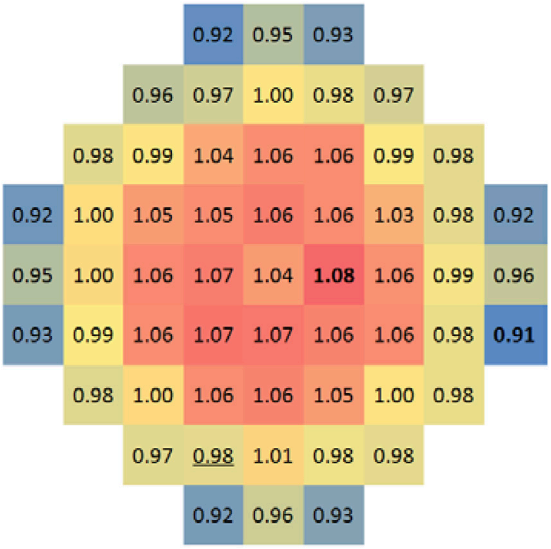

			0.92	0.95	0.93			
		0.96	0.97	1.00	0.98	0.97		
	0.98	0.99	1.04	1.06	1.06	0.99	0.98	
0.92	1.00	1.05	1.05	1.06	1.06	1.03	0.98	0.92
0.95	1.00	1.06	1.07	1.04	**1.08**	1.06	0.99	0.96
0.93	0.99	1.06	1.07	1.07	1.06	1.06	0.98	**0.91**
	0.98	1.00	1.06	1.06	1.05	1.00	0.98	
		0.97	0.98	1.01	0.98	0.98		
			0.92	0.96	0.93			

FIGURE 11 | Flow distribution map under twisted condition.

unbalance conditions as listed in **Table 5**, shutting down one loop (one-shut) and increasing the flow rate by 5% of a loop (5% offset), are selected for the simulation analysis of the two accidents. The results are shown in **Figure 9** and **Figure 10**.

Figure 9 shows that a low flow rate area appears on the closed loop side under one-shut conditions. In the test, water flow of L-1 is lost, and the flow there is whole supplemented by the other three loops, mainly relying on the lateral flow in the downcomer and the diversion effect of the flow distributor in the lower chamber. So it is undoubtedly to create a low flow area. Nevertheless, the minimum flow distribution factor still can reach 0.89, and the flow distribution factor in the low flow area is not much different from other parts, which verifies the good diversion effect of the flow distributor.

Figure 10 indicates that a 5% offset does not have a significant impact on flow distribution. It means that sufficient coolant inventory and stormy convection are enough to accommodate small flow deviations.

3.2.3 Twisted Condition Tests

The main pump of ACP100 is closer to the reactor core than in commercial reactors, and it makes the swirl of the coolant stronger. For the swirl that may have an impact on flow distribution, we adopt four removable swirl generators located at each inlet of the mock-up reactor to simulate the flow regime and measure the flow rate distribution under twisted conditions. Comparing the flow distribution data under swirl conditions showed in **Figure 11** with the aforementioned four-loop balanced experimental data, the result shows that the flow distribution characteristics do not change significantly. The variation corresponding to each fuel assembly is negligible, and the minimum and maximum flow distribution factors are both the same. This means the swirl is mitigated when passing through the downcomer and flow distributor due to the large hydraulic resistance and flow mixing at the lower plenum.

4 CONCLUSION

The objective of this study is to evaluate whether the structural design of ACP100 meets hydraulic performance requirements. We investigate flow distribution characteristics in a scaled-down mock-up reactor which has the same flow field characteristics as the prototype. Under four-loop balanced operating conditions, three different velocity tests are independently performed. The core inlet flow rates show uniform distributions with even the same maximum and minimum distribution factor. It means the flow in the major flow path of the mock-up reactor has entered the self-modeling zone and the flow distribution is the same as the prototype, and with a result of all the distribution factors in the range of 0.91–1.08, the experiment indicates the flow distribution at the core inlet is homogeneous. Unbalanced condition test results show that the reactor structures are good enough to accommodate flow deviations. In further research, the swirl produced by the pump is also proved of having little impact on flow distribution. Through different operating condition tests, we conclude that the core flow rate distribution of ACP100 has well uniformity.

DATA AVAILABILITY STATEMENT

The original contributions presented in the study are included in the article/supplementary material, and further inquiries can be directed to the corresponding author.

AUTHOR CONTRIBUTIONS

LD, WZ, XY, and JX contributed to conception and design of the study. LD conducted the data analysis and wrote the main body of the article. LJ, and DJ wrote sections of the manuscript. All authors contributed to manuscript revision, read, and approved the submitted version.

FUNDING

This work was financially supported by the Sichuan Province Youth Science and Technology Innovation Team Foundation (approved number: 2019JDTD0018).

REFERENCES

Bae, Y., Kim, Y. I., and Park, C. T. (2013). CFD Analysis of Flow Distribution at the Core Inlet of SMART. *Nucl. Eng. Des.* 258, 19–25. doi:10.1016/j.nucengdes.2013.02.003

Chen, R., Tian, M., Chen, S., Tian, W., Su, G. H., and Qiu, S. (2017). Three Dimensional Thermal Hydraulic Characteristic Analysis of Reactor Core Based on Porous Media Method. *Ann. Nucl. Energy* 104, 178–190. doi:10.1016/j.anucene.2017.02.020

Fang, Y., and Wang, S. (2014). *CAP1400 Reactor Flow Distribution Test Report [R]*. Chengdu, China: Nuclear Power Institute of China.

Fournier, Y., Vurpillot, C., and Béchaud, C. (2007). Evaluation of Fluid Flow in the Lower Core of a PWR with Code_Saturne. *Nucl. Eng. Des.* 237, 1729–1744. doi:10.1016/j.nucengdes.2007.02.025

Hensch, F. (2006). *JULIETTE Tests Interpretation Flow Rate Distribution and Characterization of the Head Losses and Pressure Fields*. Areva: Design Report NFPSDDC.

Hestroni, G. (1964). *Hydraulic Tests of the San-Onofre Reactor Model[R]*. Pittsburgh, United States: Westinghouse Electric Corporation.

Khan, E. U. (1972). Analytical Investigation and Design of a Model Hydro-Dynamically Simulating a Prototype PWR Core. *Nucl. Technol.* 16 (3), 479–496. doi:10.13182/nt72-a31217

Kim, K. M. (2012). "Hydraulic Characteristics of SMART Reactor for a Nominal Condition," in 9th International Conference on Heat Transfer, Fluid Mechanics and Thermodynamics, Malta, 16-18 July 2012 (Malta: HEFAT).

Conflict of Interest: The authors declare that the research was conducted in the absence of any commercial or financial relationships that could be construed as a potential conflict of interest.

frontiers | Frontiers in Energy Research

ORIGINAL RESEARCH
published: 07 July 2022
doi: 10.3389/fenrg.2022.925380

Numerical Investigation of Hot Helium Flow Homogenizer on Inter-Unit Flow Rate Uniformity of HTGR Once Through Steam Generator

Haiqi Qin, Xiaowei Luo, Xiaowei Li and Xinxin Wu*

Key Laboratory of Advanced Reactor Engineering and Safety of Ministry of Education, Collaborative Innovation Center of Advanced Nuclear Energy Technology, Institute of Nuclear and New Energy Technology, Tsinghua University, Beijing, China

High working temperature is a major feature of the high temperature gas-cooled reactor (HTGR). The helical tube once through steam generator (OTSG) should maintain appropriate temperature uniformity. The temperature non-uniformity of the HTGR OTSG includes the in-unit and inter-unit temperature non-uniformity, while the latter is mainly induced by the inter-unit flow rate non-uniformity of primary-side hot helium, which is significantly affected by the inlet structure. In this work, a new inlet structure with a hot helium flow homogenizer is designed, and its flow distribution characteristics are numerically investigated. Accordingly, the optimal geometrical parameters are determined, such as the circular hole diameter on the end wall, the square hole size, and arrangement on the cylinder wall. Increasing the resistance of the flow homogenizer with non-uniformly arranged square holes (NUASHs) can improve inter-unit flow rate uniformity because it decreases the effect of static pressure difference caused by dynamic pressure. Two design parameters (resistance coefficient and flow area ratio of the square hole on both sides) are introduced to evaluate the structure effect of the hot helium flow homogenizer on inter-unit flow rate distribution. They are recommended within the ranges of (7.81–22.42) and (0.53–1.64), respectively. In these recommended ranges, the suction phenomenon near the hot helium inlet can be effectively suppressed, with the critical resistance coefficient of 7.63. By coupling with 19 heat exchange units, the overall performance of the hot helium flow homogenizer is better than that of the current inlet structure with a baffle, with the maximum inter-unit flow rate deviation decreased from 2.97% to 0.30%. This one-magnitude enhancement indicates that the hot helium flow homogenizer with NUASHs is a promising solution to improve inter-unit flow rate uniformity of the HTGR OTSG.

Keywords: high temperature gas-cooled reactor, once through steam generator, inlet structure, hot helium flow homogenizer, inter-unit flow rate uniformity

Edited by:
Luteng Zhang,
Chongqing University, China

Reviewed by:
Ehsan Rafiee,
Urmia University of Technology, Iran
Kui Zhang,
Xi'an Jiaotong University, China

***Correspondence:**
Xiaowei Li
lixiaowei@tsinghua.edu.cn

Specialty section:
This article was submitted to Nuclear Energy, a section of the journal Frontiers in Energy Research

Received: *21 April 2022*
Accepted: *20 May 2022*
Published: *07 July 2022*

Citation:
Qin H, Luo X, Li X and Wu X (2022) Numerical Investigation of Hot Helium Flow Homogenizer on Inter-Unit Flow Rate Uniformity of HTGR Once Through Steam Generator. Front. Energy Res. 10:925380. doi: 10.3389/fenrg.2022.925380

1 INTRODUCTION

The high temperature gas-cooled reactor (HTGR) has the characteristics of the fourth-generation advanced nuclear power system. It has the outstanding advantages of excellent inherent safety, continuous fuel loading and discharging, high temperature and high power generation efficiency, etc. (Wu and Zhang, 2000; Wu et al., 2002; Generation-Ⅳ International Forum, 2002). HTGR can extend the nuclear energy application to high-temperature heat utilization and hydrogen production (Zhang and Sun, 2007; Zhang et al., 2009). At the Shidao Bay site in China, the world's first high-temperature gas-cooled reactor pebble-bed module (HTR-PM) demonstration power plant of 200MW$_e$ achieved criticality for the first time in September 2021, and was connected to the grid on December 20, 2021 (Zhang et al., 2016). On the basis of HTR-PM, a 600-MW$_e$ nuclear power plant has been proposed, as the next step of HTGR application in China.

The helical tube once through steam generator (OTSG) is an important equipment of the HTGR, which is characterized by its compact structure, high working temperature, and once through flow pattern. It is not only the pressure boundary of HTGR coolant but also the key heat exchanger between the primary and secondary loops. The primary-side helium absorbs fission heat from the reactor core and then heats the secondary-side water to superheated steam through the helical heat transfer tube bundles in the OTSG (Li et al., 2019a). Compared with the traditional U-tube natural circulation steam generator of the pressurized water reactor (PWR), the thermal hydraulic characteristics of the HTGR OTSG are quite different. Due to the high working temperature of 750°C, the design temperature of the helical heat transfer tube almost reaches the upper limit of the high-temperature material (Incoloy 800H) used in the HTGR OTSG. According to reference (ASME, 2015), the allowable stress of Incoloy 800H at 750°C will decrease to only one-tenth of that at normal temperature. The non-uniform temperature distribution may lead to the working temperature of certain helical heat transfer tubes above its design temperature. This will aggravate the material creep or even rupture the helical tubes. The representative examples were Heysham #1 and #2 advanced gas-cooled reactors (AGRs) built in the early 1980s in the UK. There was a large non-uniform temperature distribution among the helical heat transfer tubes of the OTSG during the commissioning. In order to ensure the maximum working temperature of the helical tube below the design temperature, the reactor operation power had to be reduced to 68% of the design value (Mathews, 1987). Therefore, the temperature non-uniformity can seriously affect the reliability and in-service lifecycle of the HTGR OTSG, which needs further detailed analysis.

The HTGR OTSG is generally composed of inlet structure and heat exchange units. The inlet structure consists of the primary-side hot helium inlet, upper chamber, main steam header, and support plate, as shown in **Figure 1A**. Moreover, there are 19 separate heat exchange units (19 helical heat transfer tube bundles) with identical geometrical parameters. Their arrangement is presented in **Figure 1B**.

Primary-side hot helium enters the upper chamber from the inlet and then flows over the helical heat transfer tube bundles from the top to the bottom. The secondary-side cold water flows into the helical heat transfer tubes from the bottom to the top. This counterflow realizes the heat exchange between the primary and secondary loops.

The temperature non-uniformity of the HTGR OTSG can be divided into two types, that is, in-unit and inter-unit non-uniformity. This temperature non-uniformity classification has been analyzed in detail in the literatures (Li, 2012; Li et al., 2016; Gao, 2020). Works have been conducted to investigate the in-unit temperature non-uniformity (among the helical heat transfer tubes). It has been reported that the wall effect, helical effect, temperature mixing effect, reverse winding of adjacent helical tube layers in the tube bundle, and geometrical parameter variations induced by the fabrication tolerance are the main reasons for in-unit temperature non-uniformity (Li and Wu, 2013; Olson et al., 2014; Li et al., 2014; Iacovides et al., 2014; Li et al., 2019b; da Silva et al., 2019; Gao et al., 2020). Furthermore,

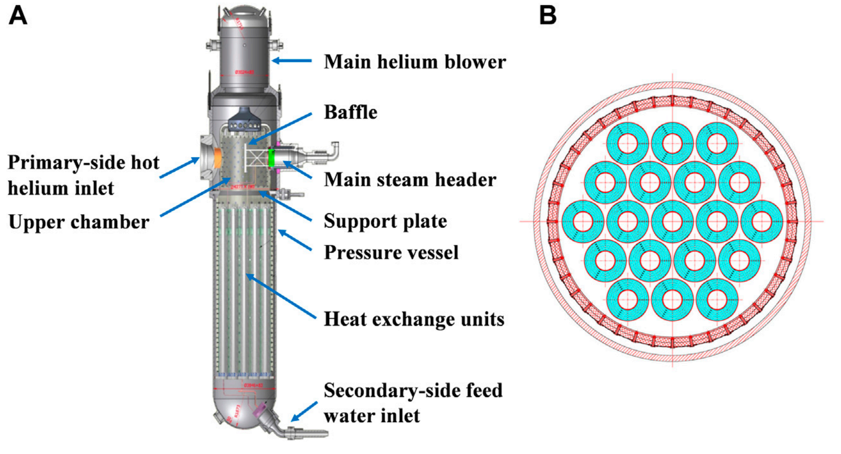

FIGURE 1 | Schematic of the HTGR OTSG Zhang et al., 2009. **(A)** Geometrical model. **(B)** Cross section.

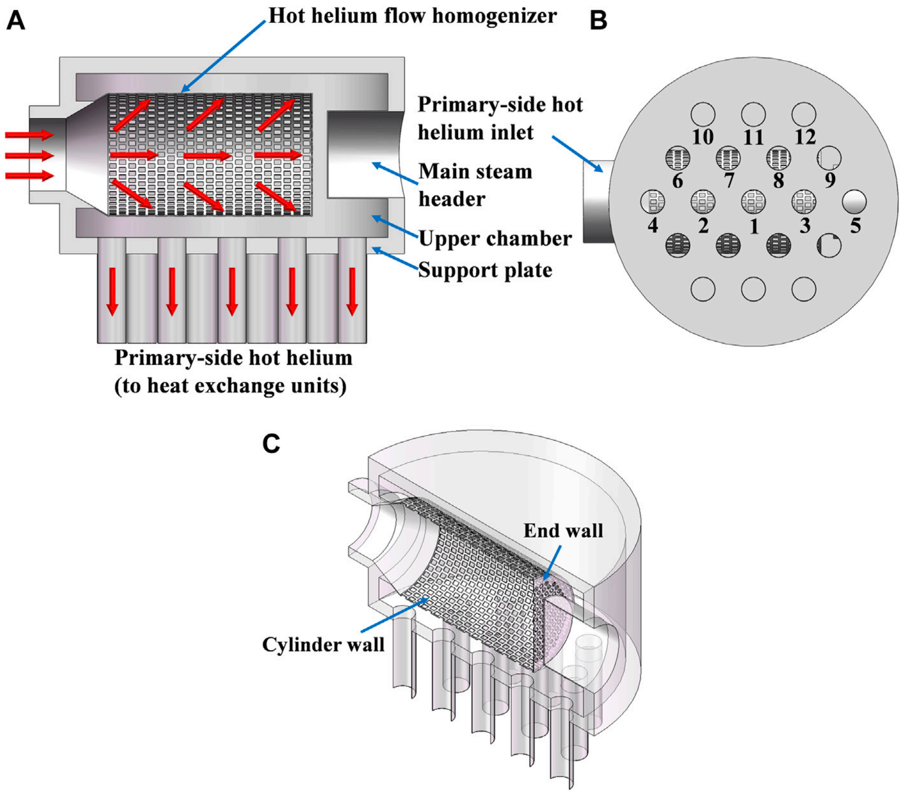

FIGURE 2 | Schematic of the hot helium flow homogenizer. **(A)** Main view. **(B)** Bottom view. **(C)** Perspective view.

the above-mentioned in-unit temperature non-uniformity has also been experimentally verified in the 10-MW engineering test facility-steam generator (ETF-SG) for the HTR-PM (Zhang et al., 2016). The inter-unit temperature non-uniformity is mainly influenced by the inlet structure and hot helium temperature uniformity at the OTSG inlet. Previous investigations have documented that the hot helium mixing structure installed at the reactor core outlet of the HTR-PM can realize the thermal mixing efficiency above 98% (Zhou et al., 2011; Zhou et al., 2016). Therefore, this study will focus on the effect of the HTGR OTSG inlet structure on inter-unit temperature non-uniformity.

In fact, the non-uniform flow rate distribution among the heat exchange units can result in significant inter-unit temperature non-uniformity. Existing research has proposed the structure with a baffle to improve inter-unit flow rate uniformity (Zhang et al., 2011). This is also the current inlet structure adopted by the HTR-PM. As a promising structure optimization, a new inlet structure (i.e., hot helium flow homogenizer) is designed in the present work. Its flow distribution characteristics are numerically investigated using the computational fluid dynamics (CFD) method. Then, the effects of different geometrical parameters on inter-unit flow rate uniformity are discussed. The optimal geometrical parameters of this newly designed hot helium flow homogenizer are proposed. Eventually, the overall flow rate distribution is simulated by coupling the inlet structure and 19 heat exchange units, to further verify the optimal geometrical parameters.

2 NUMERICAL SIMULATION

2.1 Geometrical Model of Hot Helium Flow Homogenizer

Figure 2 illustrates the geometrical model of the hot helium flow homogenizer.

In **Figure 2C**, the hot helium flow homogenizer has a cylindrical structure, where the side and bottom are defined as the cylinder wall and end wall. For the cylinder wall, there are some rectangular holes (referred to as the square holes) distributed in a certain arrangement, while some circular holes are uniformly hollowed out on the end wall. The main steam header occupies a certain space of the upper chamber and shields several heat exchange units. It causes the asymmetrical structure of the hot helium flow homogenizer, which will affect inter-unit flow rate uniformity. The main geometrical parameters of the hot helium flow homogenizer are shown in **Table 1**.

2.2 Numerical Methods

The numerical simulation is performed in two steps. First, the three-dimensional (3D) full-scale modeling is carried out for the

TABLE 1 | Geometrical parameters of the hot helium flow homogenizer.

Parameter	Value
Length (mm)	2100
Inner diameter of primary-side hot helium inlet (mm)	750
Inner diameter of upper chamber (mm)	3220
Inner diameter of flow homogenizer (mm)	1250
Flow homogenizer thickness (mm)	10

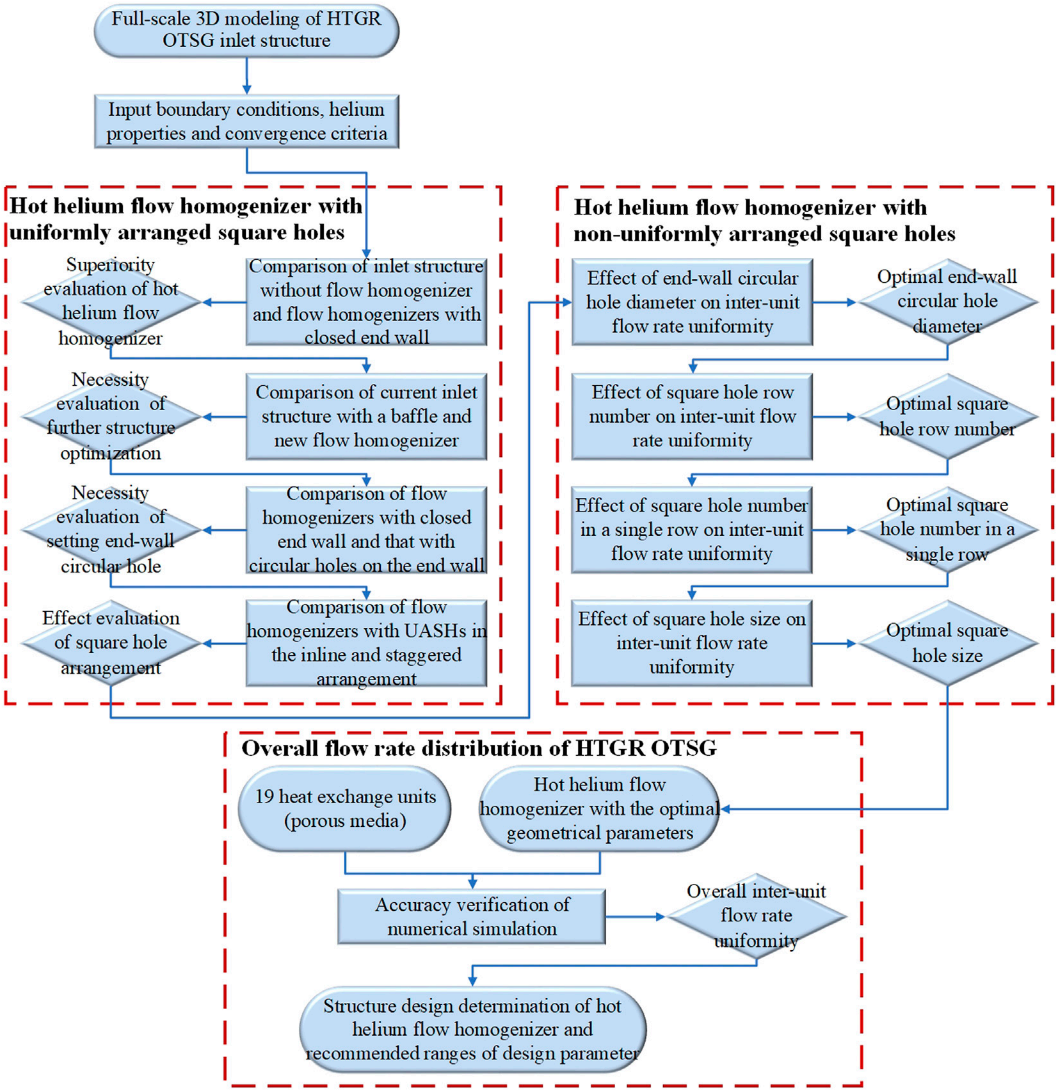

FIGURE 3 | Flow chart of the investigation.

inlet structure with the hot helium flow homogenizer. Using the commercial CFD code CFX, the inter-unit flow rate distribution is numerically simulated by solving the Reynolds Averaged Navier Stokes (RANS) governing equations together with the turbulence model (ANSYS, 2019). The superiority of the hot helium flow homogenizer, the necessity of further structure optimization, and the effects of geometrical parameter on flow rate distribution are evaluated. Second, the overall flow rate uniformity of the HTGR OTSG is further verified, considering the coupling of the inlet structure and 19 heat exchange units. As the basis, the first step is beneficial for understanding the flow distribution mechanism and independent structure design of the

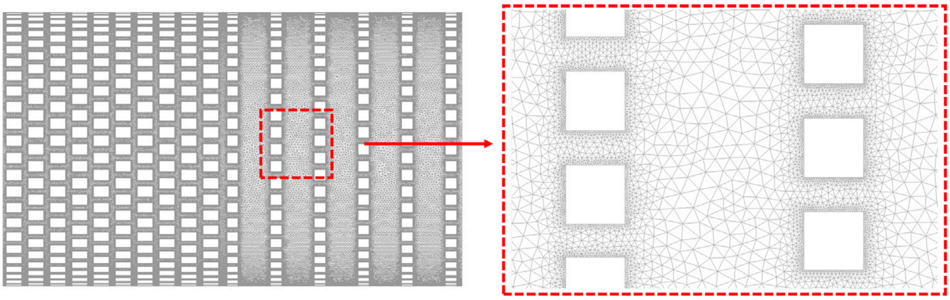

FIGURE 4 | Local mesh distribution.

hot helium flow homogenizer. The second step emphasizes the overall performance of inter-unit flow rate uniformity. **Figure 3** shows the flow chart of the steps in this investigation.

Neglecting some micro-structures such as the dead zone near the wall and grooves, the geometrical model of the inlet structure is reasonably simplified. In order to reduce the mesh element number, the porous media is used for the helical heat transfer tube bundles. Using hybrid grid technology, the computational domain is divided into two parts, including the fluid domain (the inlet structure with the hot helium flow homogenizer) and the porous media domains (19 heat exchange units). Among them, the tetrahedral unstructured mesh is automatically generated for the fluid domain and the hexahedral structured mesh is adopted for the porous media domains, respectively. These computational domains are connected by interfaces. The local mesh is refined near the square holes on the cylinder wall and circular holes on the end wall. Local mesh distribution is presented in **Figure 4**.

2.3 Physical Models

Due to the excellent thermal mixing at the reactor core outlet, the hot helium temperature is regarded as uniform at the inlet of the HTGR OTSG. Thus, all the cases in this work are 3D steady-state adiabatic simulations with helium as the working fluid. Additionally, the standard ***k-ε*** model and scalable wall treatment are selected for turbulence modeling. The reliability and stability of this turbulence model have been fully proved as a standard engineering model (Tao, 2017).

Mach number (***Ma***) reflects the influence of gas compressibility, which is used to classify whether the flow is compressible (Kong, 2014). The definition of ***Ma*** is given as **Eq. 1**.

$$Ma = \frac{v}{c} \tag{1}$$

where c is the local acoustic velocity.

When ***Ma*** is lower than 0.3, the gas compressibility has little effect on its flow characteristics, which can be considered as incompressible fluid. From **Eq. 1**, the corresponding ***Ma*** of primary-side hot helium is 0.039, so it can be treated as an incompressible viscous fluid with constant properties. Helium properties are calculated using the NIST real gas package which is a material database based on the Thermodynamic and Transport Properties of Refrigerants and Refrigerant Mixtures Database (REFPROP v9.1) provided by the National Institute of Standards and Technology (NIST) (Zhao et al., 2017; Gao et al., 2019). **Table 2** lists the helium properties, where 5 significant digits are reserved.

TABLE 2 | Helium properties.

Parameter	Unit	Value
Temperature [*T*]	°C	750
Pressure [*p*]	MPa	7
Density [*ρ*]	kg/m^3	3.2682
Dynamic viscosity [*η*]	Pa·s	4.6983×10^{-5}
Specific heat capacity at constant pressure [*C_p*]	J/kg·K	5193.1
Thermal conductivity [λ]	W/m·K	0.36983
Thermal expansivity [*γ*]	K^{-1}	9.6858×10^{-4}
Local acoustic velocity [*c*]	m/s	1895.6

Taking into account the resistance equivalence, each heat exchange unit of 8 m height is simplified into a porous media domain of 1.2 m height, to simulate the hot helium cross flow over the helical heat transfer tube bundle. Volume porosity, permeability, and the resistance coefficient are important physical properties to represent the flow characteristics of porous media. Volume porosity is the ratio of the pore volume (fluid volume) to the total geometrical volume. For a single heat exchange unit, the volume of helical heat transfer tubes acts as the solid volume, while the difference between the total geometrical volume and this solid volume is defined as the fluid volume. Permeability (K) is an inherent property of porous media, which is determined by Darcy's permeation law expressed in **Eq. 2** (Satter and Iqbal, 2016; Hayat et al., 2021).

$$K = \frac{Q_v \eta L}{A \Delta p} \tag{2}$$

where Q_v is the volume flow rate, L is the length, A is the flow area, and Δp is the pressure drop.

For cross flow over the helical tube bundle, the resistance coefficient (ξ) is calculated using the empirical correlation proposed by Idelchik, as shown in **Eq. 3** (Idelchik and Fried, 2016).

$$\xi = 0.38\left(\frac{S_1 - d}{S_2 - d} - 0.94\right)^{-0.59}\left(\frac{S_1}{d} - 1\right)^{-0.5} Re^{-0.2\left(\frac{S_1 - d}{S_2 - d}\right)^{-2}} \tag{3}$$

where S_1 is the transverse tube pitch and S_2 is the stream-wise tube pitch. In **Eq. 3**, ***Re*** and S_1-d/S_2-d are in the ranges of (3×10^3–10^5) and (1.0–8.0), respectively.

Eq. 3 is converted into **Eq. 4**, which is substituted into the geometrical parameters of the helical tube bundle.

$$\xi = 0.5338Re^{-0.0595} \tag{4}$$

The characteristic velocity and hydraulic diameter of the Reynolds number (***Re***) are considered as the maximum average flow velocity at the minimum cross section in the helical tube bundle and the outer diameter of the helical tube, respectively.

2.4 Boundary Conditions and Solution Strategy

Owing to the symmetrical structure and large size, symmetry boundary condition is assumed for the overall inlet structure of the HTGR OTSG. The inlet is specified with a constant mass flow rate of 48 kg/s and turbulence intensity of 5%. Static pressure in 0Pa is prescribed at the outlet. The smooth and non-slip wall boundary conditions are used for all the walls of the inlet structure, without considering the influence of wall roughness. The mesh connections are set as the conservative flux and general grid interface (GGI).

The convection term and turbulence equation are discretized using a high-resolution upwind scheme. Auto timescale and conservative length scale are adopted for the fluid timescale control. The convergence criteria are formulated as the root mean square residuals (RMSs) below 1×10^{-5}.

2.5 Sensitivity Analysis

The hot helium flow homogenizer with the optimal inter-unit flow rate uniformity is selected as an example to analyze the sensitivity of mesh element number. Six meshes are generated by adjusting the local mesh parameters. Their mesh qualities are all higher than 0.3, and the average y^+ is below 70, meeting the calculation accuracy requirements and the application range of the standard k-ε turbulence model and wall function.

In the current investigation, the maximum deviation and standard deviation (σ) are taken as the uniformity evaluation standards of inter-unit flow rate distribution. If the inter-unit flow rate distribution is completely uniform, the corresponding mass flow rate of each heat exchange unit should be 5.053 kg/s. The maximum inter-unit flow rate deviation is defined as the relative difference between the maximum and minimum mass flow rates among 19 heat exchange units. The standard deviation characterizes the dispersion degree of inter-unit flow rate distribution. The larger value of these uniformity evaluation parameters means a large inter-unit flow rate difference. In addition, the mass flow rate within 14 rows of square holes reveals the flow distribution characteristics of the flow homogenizer. The variation of the above uniformity evaluation parameters is shown in **Figure 5**.

On the whole, the meshes have little effect on the numerical results. From **Figure 5A**, within the mesh element number of 6.54–55.49 million, the variation amplitude of the maximum inter-unit flow rate deviation is below 0.5%. In **Figure 5B**, there are almost similar flow distribution characteristics in different meshes. Especially when the mesh element number is more than 20 million, the mass flow rate within each row of square holes tends to be consistent, with the relative error being less than 1%. Further mesh refinement has no obvious improvement on numerical results. Considering the calculation accuracy and convergence speed, the working mesh is determined as 23.75 million.

3 RESULTS AND DISCUSSION

3.1 Flow Rate Uniformity of Flow Homogenizer with Uniformly Arranged Square Holes

This group of numerical simulations is used to qualitatively evaluate the effect of the hot helium flow homogenizer on inter-unit flow rate distribution. Nevertheless, the specific structure design and geometrical parameters still need to be further explored. The inlet structure numbered 1 is not equipped with the hot helium flow homogenizer, while the previously designed inlet structure with a baffle is numbered 2. Other inlet structures numbered 3–10 are equipped with hot helium flow homogenizers, in which square holes are uniformly arranged on the cylinder wall. As for the hot helium flow homogenizer with uniformly arranged square holes (UASHs), the characteristic geometrical parameters are listed in **Table 3**.

Table 4 presents the numerical results of inter-unit flow rate distribution, where the mass flow rate retains 4 significant digits. The number of the heat exchange unit is shown in **Figure 2B**.

3.1.1 Effect of Hot Helium Flow Homogenizer on Inter-Unit Flow Rate Uniformity

Compared with the No.3 and 7 inlet structures, the standard deviation of that without the flow homogenizer (No.1) is evidently large. Blocked by the main steam header, a large amount of hot helium flows down into the heat exchange unit under it. Hence, the maximum flow rate occurs within the No.5 heat exchange unit, the farthest from the primary-side hot helium inlet. Since the hot helium flowing upward is constrained by the top of the inlet structure, an annular flow appears downward along the side wall of the upper chamber. Therefore, the hot helium flow rate distributed within the heat exchange units (Nos. 6, 9, and 12) at the edge area is relatively large. Corresponding to the inter-unit flow rate distribution, the pressure of heat exchange units at the edge area is lower than that at the center area. The above conclusions are similar to the published literature (Zhang et al., 2011). The flow homogenizer not only avoids the direct impact of primary-side hot helium on the main steam header but also helps to improve inter-unit flow rate uniformity. In

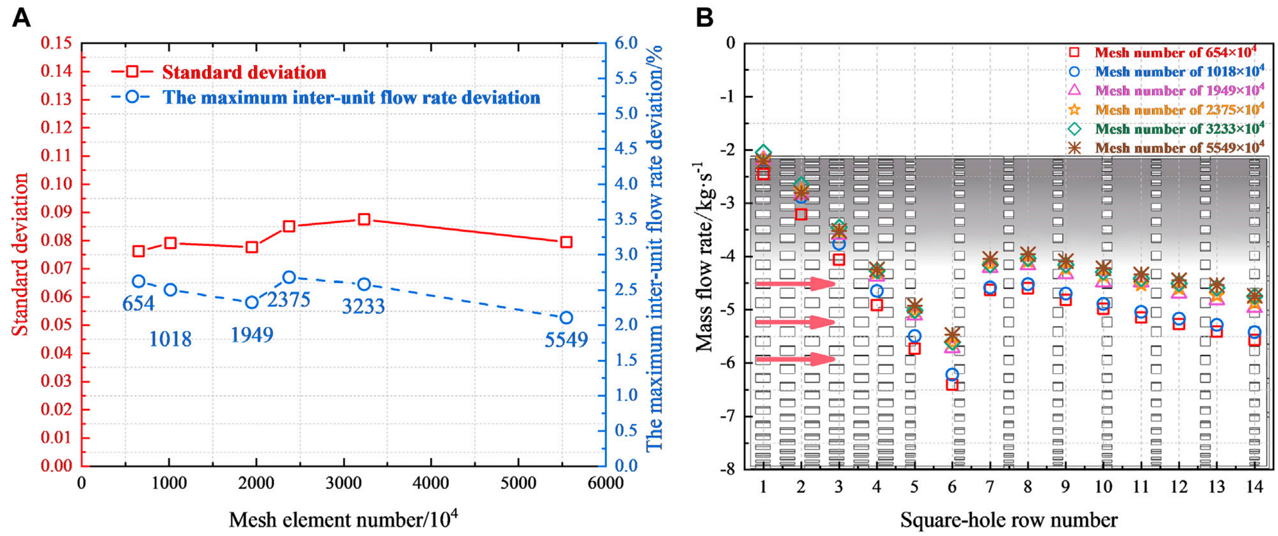

FIGURE 5 | Sensitivity analysis. **(A)** Variation with mesh element number. **(B)** Flow distribution characteristics.

TABLE 3 | Characteristic geometrical parameters of hot helium flow homogenizers with UASHs.

Case No.	Cylinder-wall square holes				End-wall circular hole diameter/mm
	Characteristic	Row	Side length/mm	Spacing/mm	
1	No flow homogenizer	--	--	--	--
2	Baffle	--	--	--	--
3	UASHs in the inline arrangement	21	70 × 50	100	Closed
4					Φ20
5					Φ50
6					Φ60
7	UASHs in the staggered arrangement				Closed
8					Φ20
9					Φ50
10					Φ60

TABLE 4 | Numerical results of inter-unit flow rate distribution of flow homogenizers with UASHs.

Case No.	Mass flow rate of heat exchange unit/kg·s^{-1}												Maximum deviation/ %	Standard deviation
	1	2	3	4	5	6	7	8	9	10	11	12		
1	4.510	4.856	5.120	5.824	6.302	4.994	4.302	4.496	5.416	5.074	4.939	5.473	39.58	0.5519
2	7.212	4.906	5.470	5.636	5.932	4.422	4.324	5.199	5.809	3.809	5.131	4.729	67.52	0.8581
3	4.776	4.952	6.172	5.424	5.518	5.096	4.515	5.048	5.100	4.861	4.708	5.251	32.79	0.4213
4	4.818	4.946	6.068	5.364	5.440	5.053	4.524	4.976	5.273	4.840	4.734	5.283	30.56	0.3914
5	4.730	4.938	5.800	5.376	5.538	5.063	4.480	4.722	5.563	4.871	4.774	5.335	26.12	0.3956
6	4.530	4.900	5.674	5.466	5.684	5.041	4.431	4.608	5.778	4.912	4.782	5.322	26.66	0.4571
7	4.790	4.926	6.160	5.424	5.520	5.099	4.520	5.050	5.101	4.857	4.701	5.263	32.46	0.4195
8	4.832	4.946	6.054	5.364	5.440	5.063	4.538	4.995	5.243	4.843	4.722	5.278	30.00	0.3850
9	4.732	4.954	5.814	5.388	5.552	5.061	4.468	4.709	5.576	4.873	4.779	5.314	26.63	0.4015
10	4.534	4.908	5.670	5.466	5.676	5.046	4.420	4.619	5.780	4.908	4.776	5.324	26.92	0.4563

consideration of the significant flow uniformization effect, the hot helium flow homogenizer designed in this work can be a potential solution to improve temperature uniformity of the HTGR OTSG.

3.1.2 Effect Comparison of Flow Homogenizer and Baffle on Inter-Unit Flow Rate Uniformity

As the current structure design, a baffle is installed between the primary-side hot helium inlet and main steam header, which also

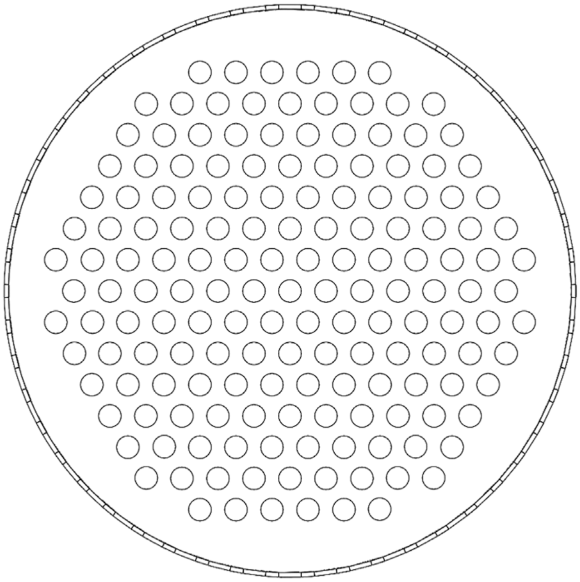

FIGURE 6 | Arrangement of circular holes on the end wall.

plays a pivotal role in improving inter-unit flow rate uniformity. By comparing with the baffle (No.2), the maximum deviations and standard deviations of hot helium flow homogenizers (No.3–10) decrease significantly. It is necessary to further optimize the current inlet structure.

3.1.3 Effect of End-Wall Circular Holes on Inter-Unit Flow Rate Uniformity

In this section, the necessity of setting circular holes on the end wall is qualitatively assessed. A total of 163 circular holes are hollowed out on the end wall with a grid pitch of 80 mm. As shown in **Figure 6**, these circular holes are arranged symmetrically.

From **Table 4**, the circular holes on the end wall have a significant impact on inter-unit flow rate distribution. The standard deviations of flow homogenizers (Nos. 4, 5, and 6 and 8, 9, and 10) with circular holes on the end wall are less than those with the closed end wall (Nos. 3 and 7). As a result, setting circular holes on the end wall is advantageous for improving inter-unit flow rate uniformity. Taking two flow homogenizers (Nos. 3 and 5) as examples, the flow fields are analyzed in detail. The surface streamlines, flow velocity, and pressure contours on the longitudinal section (stream-wise direction) are illustrated in **Figure 7**.

From **Figures 7A,B**, due to the continuous shunt flow from each row of square holes, the mainstream flow velocity decreases gradually in the flow homogenizer. The circular holes on the end wall are conductive to the smooth outflow of primary-side hot helium from the flow homogenizer. As shown in **Figures 7C,D**, corresponding to the variation of flow velocity, the static pressure gradually increases along the stream-wise direction. With the same cross-sectional area of the heat exchange unit, the streamlines can indirectly characterize inter-unit flow rate distribution. **Figure 7C** shows that the closed end wall allows hot helium to flow out only from the nearby square holes. Consequently, a lot of hot helium flows into the No.3 heat exchange unit below the end wall, while the flow rate of that at the edge area is relatively small. However, in **Figure 7D**, part of hot helium flows into the narrow gap through end-wall circular holes and then diffuses to the edge area. It increases the flow rate of heat exchange units blocked by the main steam header such as Nos. 5 and 9, which can improve inter-unit flow rate uniformity. Meanwhile, the performance of inter-unit flow rate distribution still depends on the specific circular hole diameter. When the circular holes are larger than 50 mm (Nos. 6 and 10), a further increasing diameter even aggravates inter-unit flow rate non-uniformity. In general, setting circular holes on the end wall can improve inter-unit flow rate uniformity, but the diameter should be less than 50 mm.

3.1.4 Effect of Square Hole Arrangement on Inter-Unit Flow Rate Uniformity

There are two types of square hole arrangement, that is, inline arrangement and staggered arrangement. As for the staggered arrangement, two adjacent rows of square holes on the cylinder wall are laterally staggered by 3.6°. These two arrangements are drawn in **Figure 8**.

For the hot helium flow homogenizers with the same circular holes but different square hole arrangements (Nos. 3 and 7, 4 and 8, 5 and 9, and 6 and 10 in **Table 4**, respectively), the maximum deviation and standard deviation are basically consistent with each other. As there is no change in the hot helium flow area, the square hole arrangement has little effect on inter-unit flow rate distribution. Further comparison indicates that the uniformity evaluation parameters of staggered arrangement are less than that of inline arrangement. To a certain extent, this staggered arrangement can conduce to inter-unit flow rate uniformity, which is applied in the follow-up investigations.

3.1.5 Optimization Strategy Analysis of Inter-Unit Flow Rate Uniformity

One limitation of the hot helium flow homogenizer with UASHs is that the improvement of inter-unit flow rate uniformity is still insufficient. Compared with the No.1 inlet structure, the maximum deviation of the hot helium flow homogenizer with UASHs decreases by less than 15%. Thus, its structure needs to be further optimized. Four flow homogenizers (Nos. 4 and 5 and 8 and 9, respectively) are chosen as examples, where their flow distribution characteristics are shown in **Figure 9**.

From **Figure 9**, it is found that the hot helium flow homogenizers in different square hole arrangements have almost similar flow distribution characteristics. Along the stream-wise direction, the positive mass flow rate of the first 8 rows means that hot helium flows into the flow homogenizer from the upper chamber. Subsequently, it becomes negative from the 9th row of square holes, which implies that hot helium flows out of the flow homogenizer. It is important to highlight that hot helium in some square holes near the primary-side hot helium inlet (referred to as near the inlet side) cannot outflow, whereas the helium in the upper chamber flows back into the flow homogenizer. As shown in the black dotted regions of **Figures**

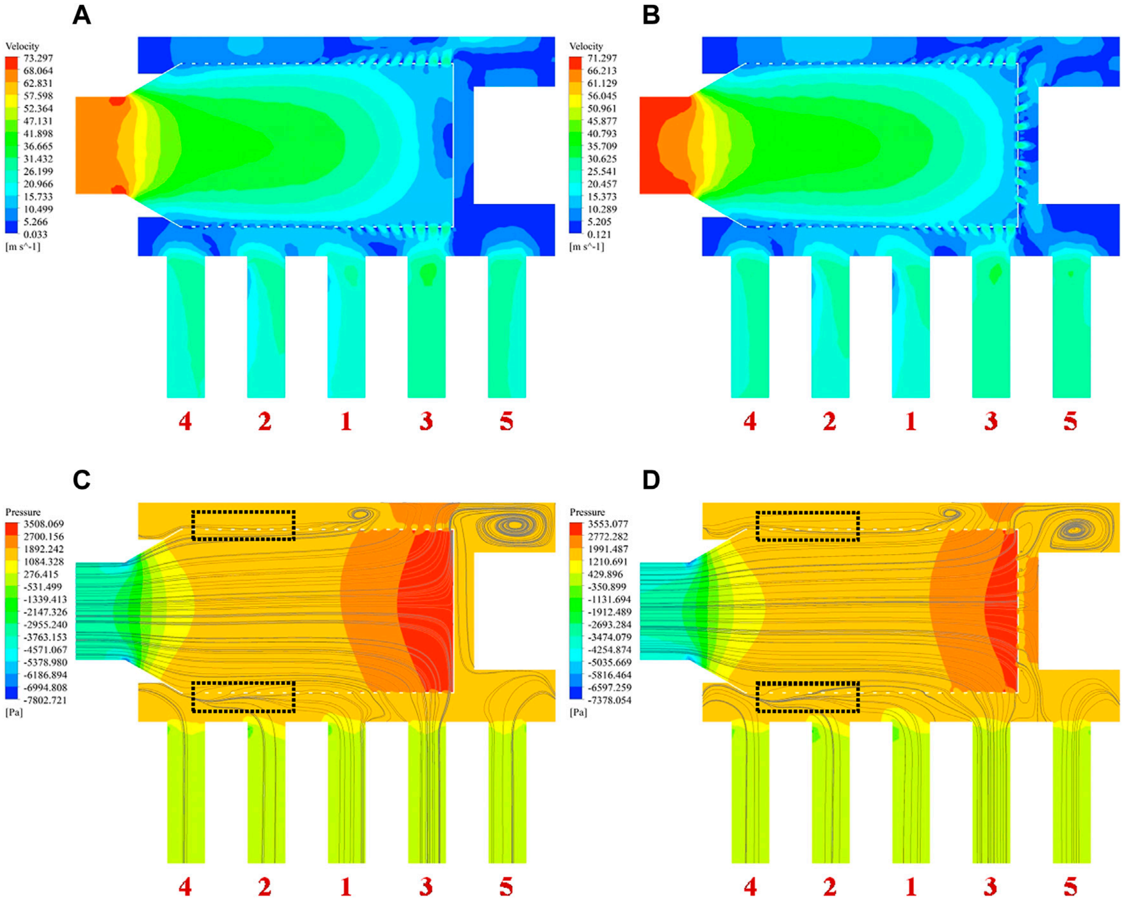

FIGURE 7 | Velocity and pressure fields. **(A)** Flow velocity contour of No.3. **(B)** Flow velocity contour of No.5. **(C)** Pressure contour of No.3. **(D)** Pressure contour of No.5.

7C,D, the streamlines also clearly exhibit this suction phenomenon. It can result in a remarkable inclination of flow distribution to the side away from the primary-side hot helium inlet (referred to as away from the inlet side), which deteriorates inter-unit flow rate uniformity. As the end-wall circular hole diameter decreases, the square holes where hot helium changes from the inflow to the outflow gradually move toward the inlet side. In brief, the effective improvement of inter-unit flow rate uniformity relies on whether hot helium can realize the outflow from all the rows of square holes. For the representative flow homogenizer (No.5), **Figure 10** presents two enlarged velocity vectors to demonstrate the flow detail of the suction phenomenon.

These vectors clearly show that the hot helium flow direction is opposite within the square holes near the inlet side and away from the inlet side. In **Figure 10A**, the velocity vectors are basically parallel to the mainstream flow direction. In the upper chamber, the hot helium near the square holes is gently sucked into the flow homogenizer. From **Figure 10B**, the velocity vectors are disordered, with the sharp change in flow velocity. A part of hot helium collides with the end wall of the flow homogenizer and reverses the flow direction. Along with the incoming flow, it flows out of the flow homogenizer through the square holes away from the inlet side.

As for the hot helium flow homogenizer with UASHs, the suction phenomenon appears at some square holes near the inlet side, resulting in the insufficient improvement of inter-unit flow rate uniformity. An acceptable explanation of the suction phenomenon is the negative static pressure difference caused by dynamic pressure. **Figures 7C,D** show that the external static pressure of the flow homogenizer is basically the same, while the internal static pressure gradually increases along the stream-wise direction. Their combined effect induces the gradual increase in static pressure difference. It is also the reason why the mass flow rate within each row of square holes gradually increases. Near the inlet side, the large dynamic pressure causes the internal static pressure to be lower than the external static pressure.

The improvement effect of the hot helium flow homogenizer on inter-unit flow rate uniformity depends on its own geometrical parameters. Further structure optimization should be carried out to suppress the suction phenomenon near the inlet side. It is a constructive

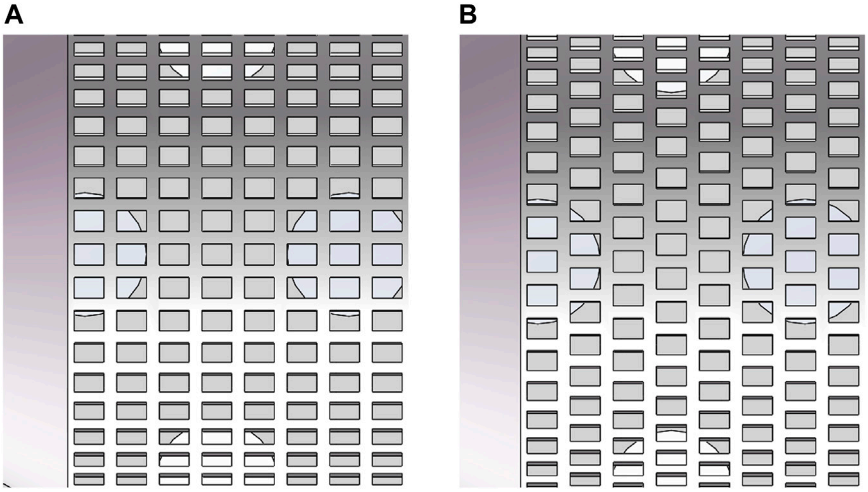

FIGURE 8 | Square hole arrangement. **(A)** Inline arrangement. **(B)** Staggered arrangement.

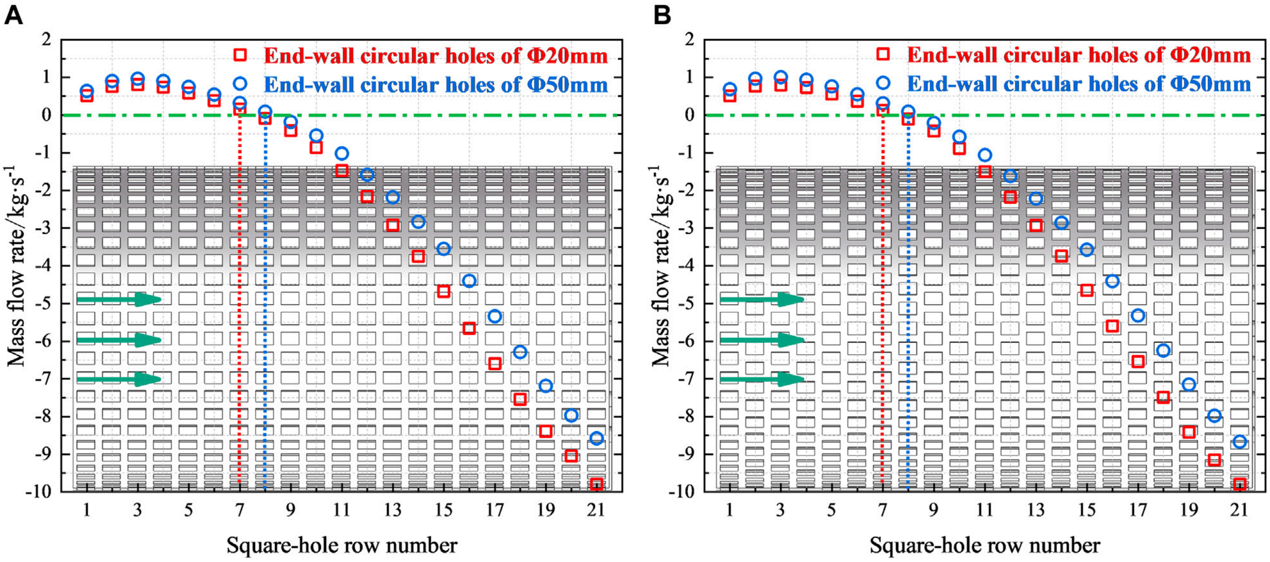

FIGURE 9 | Flow distribution characteristics of flow homogenizers with UASHs. **(A)** Inline arrangement (Nos. 4 and 5). **(B)** Staggered arrangement (Nos. 8 and 9).

optimization strategy to adjust the square holes on the cylinder wall to the non-uniform arrangement.

3.2 Flow Rate Uniformity of Flow Homogenizer with Non-Uniformly Arranged Square Holes

To address the limitation of improving inter-unit flow rate uniformity, the hot helium flow homogenizer with non-uniformly arranged square holes (NUASHs) is designed in this section. Specifically, there are more rows of square holes near the inlet side with large flow area and dense arrangement, while there are fewer rows of square holes away from the inlet side, with sparse arrangement and small flow area. In the structure design of the hot helium flow homogenizer, many geometrical parameters are coupled with each other, which cannot be completely decoupled. Therefore, the geometrical parameter effects on inter-unit flow rate uniformity are investigated in turn according to their significance.

3.2.1 Effect of End-Wall Circular Hole Diameter on Inter-Unit Flow Rate Uniformity

To avoid excessive vibration, the minimum diameter of a circular hole should be above 20 mm. The pitches between two adjacent rows of square holes near the inlet side and away from the inlet side are defined as P_{near} and P_{away}, respectively.

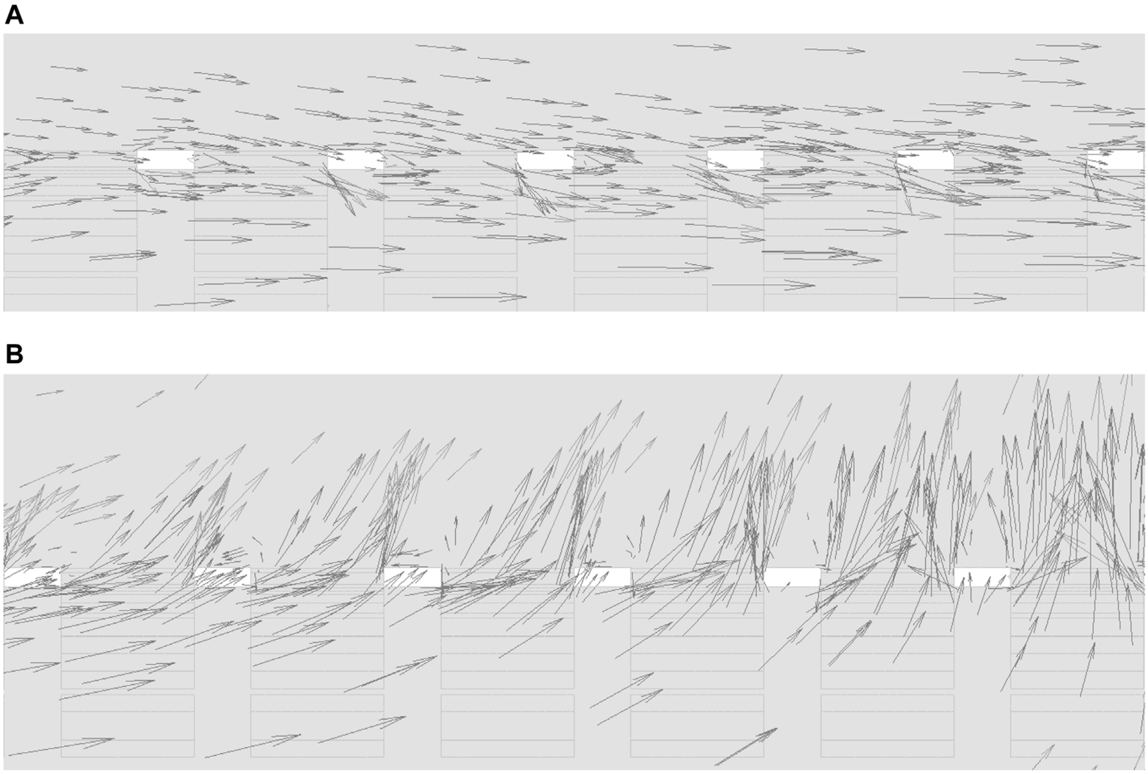

FIGURE 10 | Local velocity vector of the flow homogenizer with UASHs. **(A)** Near the inlet side. **(B)** Away from the inlet side.

TABLE 5 | Characteristic geometrical parameters of flow homogenizers with different end-wall circular hole diameters.

Case No.	Square holes near the inlet side			Square holes away from the inlet side			End-wall circular hole diameter/mm
	Row	Side length/mm	P_{near}/mm	Row	Side length/mm	P_{away}/mm	
11	10	70 × 50	100	6	50 × 50	200	Closed
12							Φ20
13							Φ25
14							Φ30
15							Φ35
16							Φ40
17							Φ45
18							Φ50

For the No.11–18 flow homogenizers, the numerical results of inter-unit flow rate distribution are shown in ***Table 6****.*

For the flow homogenizers with different end-wall circular hole diameters, the characteristic geometrical parameters are listed in **Table 5**.

By comparing **Table 4** and **Table 6**, it implicates that the hot helium flow homogenizer with NUASHs has better performance than that with UASHs in improving inter-unit flow rate uniformity. It is also confirmed that the structure optimization strategy clarified in **Section 3.1.5** is feasible. However, the relatively limited variation of standard deviation suggests that the end-wall circular hole diameter has little effect on inter-unit flow rate uniformity. In summary, the large-scale adjustment of inter-unit flow rate distribution should still be achieved by changing the geometrical parameters of square holes on the cylinder wall, while the circular hole diameter is more suitable for the fine-tuning of flow distribution. Furthermore, the effect of end-wall circular hole diameter on inter-unit flow rate uniformity reports a strong coupling with other geometrical parameters. When the diameter is larger than 40 mm (Nos. 17 and 18), its flow uniformization effect is even inferior to the No.11 flow homogenizer with the closed end wall. With the decrease in end-wall circular hole diameter, the inter-unit flow rate uniformity improves gradually. As for the No.12 flow homogenizer, the optimal diameter is determined as 20 mm, which has the smallest standard deviation. The flow

TABLE 6 | Numerical results of inter-unit flow rate distribution for flow homogenizers with different end-wall circular hole diameters.

Case No.	Mass flow rate of heat exchange unit/kg·s^{-1}												Maximum deviation/ %	Standard deviation
	1	2	3	4	5	6	7	8	9	10	11	12		
11	5.148	4.888	5.242	5.158	5.218	4.913	5.115	5.129	4.876	4.830	5.134	5.175	8.15	0.1411
12	5.044	4.878	5.198	5.098	5.240	4.898	5.048	5.121	4.990	4.890	5.135	5.189	7.16	0.1199
13	5.048	4.848	5.190	5.098	5.258	4.887	5.021	5.114	5.042	4.882	5.139	5.195	8.11	0.1270
14	5.018	4.844	5.200	5.092	5.266	4.871	4.986	5.111	5.099	4.919	5.123	5.180	8.35	0.1275
15	5.020	4.824	5.204	5.102	5.234	4.864	4.961	5.097	5.141	4.947	5.115	5.184	8.11	0.1282
16	4.988	4.816	5.146	5.106	5.236	4.861	4.930	5.080	5.208	4.941	5.095	5.239	8.37	0.1387
17	4.958	4.810	5.126	5.114	5.252	4.861	4.900	5.053	5.280	4.944	5.109	5.223	9.30	0.1507
18	4.916	4.848	5.076	5.134	5.282	4.886	4.855	5.027	5.331	4.937	5.117	5.218	9.56	0.1608

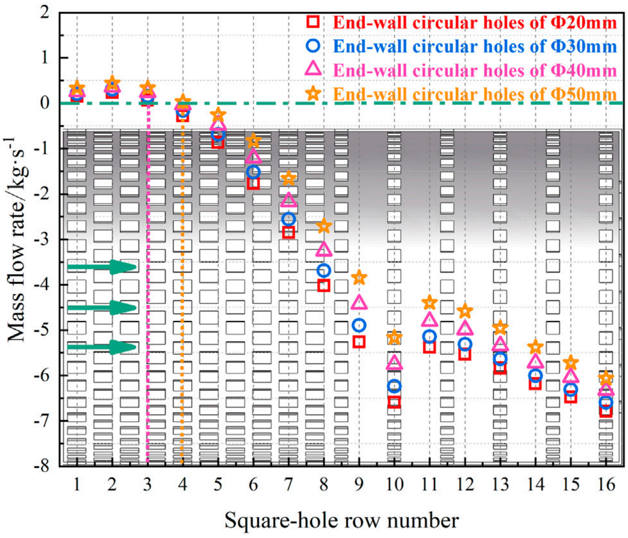

FIGURE 11 | Flow distribution characteristics of flow homogenizers with different end-wall circular hole diameters.

distribution characteristics of the above flow homogenizers with different end-wall circular hole diameters are illustrated in **Figure 11**.

As shown in **Figure 11**, these flow homogenizers with NUASHs realize the hot helium outflow from the 4th row of square holes. Compared with the flow homogenizers with UASHs, the square holes where hot helium changes from the inflow to the outflow have been obviously advanced. However, the suction phenomenon is still not effectively suppressed within the first 4 rows of square holes near the inlet side.

3.2.2 Effect of Square Hole Row Number on Inter-Unit Flow Rate Uniformity

Square holes on the cylinder wall constitute the main flow channels for hot helium outflow from the flow homogenizer, whose geometrical parameters decisively influence inter-unit flow rate uniformity. Square hole row number is the most important parameter in determining the hot helium flow area on the cylinder wall. Several hot helium flow homogenizers with different row numbers have been designed. **Table 7** shows their characteristic geometrical parameters.

From **Table 8**, the standard deviation of the No.21 flow homogenizer is below 0.1, with 6 and 8 rows of square holes near the inlet side and away from the inlet side, respectively. It is the optimal row number determined in this section. For the cases where the square holes near the inlet side are less than 6 rows, the flow area away from the inlet side is larger than the other side, which means that the square hole arrangement tends to be uniform again. As the response to this flow area variation on both sides, the inter-unit flow rate uniformity deteriorates slightly. From above discussions, one may conclude that the flow area ratio of square holes on both sides should be within an appropriate range, to improve inter-unit flow rate uniformity. Taking the flow homogenizers (Nos. 19, 12, 20, and 23) as examples, their flow distribution characteristics are shown in **Figure 12**.

Seen from **Figure 12**, with the decrease in row number near the inlet side, the square holes that realize the hot helium outflow from the flow homogenizer gradually moves forward. It implies that the suction phenomenon near the primary-side hot helium inlet tends to be sufficiently suppressed. Furthermore, the flow rate difference at the junction of square holes on both sides decreases gradually, and the curve of flow distribution characteristics also tends to be smooth. As shown in **Figure 12C**, hot helium can flow out of the No.20 flow homogenizer from all the rows of square holes. Not only is the suction phenomenon effectively suppressed but also the inter-unit flow rate distribution is more uniform. From **Figure 12D**, the No.23 flow homogenizer has the least row number (2 rows) of square holes near the inlet side, where the suction phenomenon is more significantly suppressed. There is more hot helium outflow from the first 2 rows of square holes than that of **Figure 12C**. In fact, the flow area ratio of square holes on both sides is reduced to the minimum value in this case. For the No.23 flow homogenizer, the square holes away from the inlet side are dominant, with the gradual transition of flow distribution characteristics to that with UASHs. The above analysis reveals that the suction phenomenon can be effectively suppressed within the appropriate range of the flow area ratio. This appropriate range can be approached by changing other geometrical parameters of square holes on the cylinder wall.

TABLE 7 | Characteristic geometrical parameters of flow homogenizers with different square hole row numbers.

Case No.	Square holes near the inlet side			Square holes away from the inlet side			End-wall circular hole diameter/mm
	Row	Side length/mm	P_{near}/mm	Row	Side length/mm	P_{away}/mm	
19	12	70 × 50	100	5	50 × 50	200	Φ20
12	10			6			
20	8			7			
21	6			8			
22	4			9			
23	2			10			

For the No.19–23 flow homogenizers, the numerical results of inter-unit flow rate distribution are shown in ***Table 8****.*

TABLE 8 | Numerical results of inter-unit flow rate distribution for flow homogenizers with different square hole row numbers.

Case No.	Mass flow rate of heat exchange unit/kg·s^{-1}												Maximum deviation/ %	Standard deviation
	1	2	3	4	5	6	7	8	9	10	11	12		
19	5.364	4.884	5.192	5.152	5.262	4.941	4.890	5.131	4.992	4.782	5.161	5.176	11.52	0.1684
12	5.044	4.878	5.198	5.098	5.240	4.898	5.048	5.121	4.990	4.890	5.135	5.189	7.16	0.1199
20	4.984	4.908	5.180	5.064	5.230	4.872	5.098	5.119	4.975	4.977	5.100	5.176	7.09	0.1086
21	4.966	4.936	5.178	5.064	5.216	4.904	5.032	5.129	4.988	5.002	5.102	5.163	6.18	0.0971
22	4.964	4.824	5.186	5.040	5.222	4.959	4.986	5.135	4.992	5.050	5.090	5.170	7.88	0.1101
23	4.980	4.820	5.202	5.034	5.230	4.998	4.952	5.136	4.992	5.024	5.090	5.175	8.11	0.1134

3.2.3 Effect of Square Hole Number in a Single Row on Inter-Unit Flow Rate Uniformity

Square hole number in a single row is another important parameter to determine the hot helium flow area on the cylinder wall. With the above optimal end-wall circular hole diameter and square hole row number, five flow homogenizers with different square hole numbers are shown in **Table 9**.

Table 10 shows that decreasing the square hole number is disadvantageous to inter-unit flow rate uniformity. By further comparison of flow homogenizers (Nos. 21, 24, and 25 and 21, 26, and 27, respectively), the inter-unit flow rate uniformity is more sensitive to the square hole number away from the inlet side. The single row of 50 square holes on both sides is a better choice for the structure design of the flow homogenizer. Their flow distribution characteristics are shown in **Figure 13**.

With the decrease in square hole number near the inlet side, the flow distribution characteristics of corresponding flow homogenizers (Nos. 21, 26, and 27) are roughly similar to each other, as shown by the red, green, and orange curves in **Figure 13**. However, the red, blue, and pink curves show the remarkable change in flow distribution characteristics, as the square hole number away from the inlet side decreases. These comparisons also reflect that the inter-unit flow rate distribution is more sensitive to the flow area away from the inlet side. This flow area sensitivity is attributed to the asymmetrical structure of the hot helium flow homogenizer. To increase the flow rate of heat exchange units blocked by the main steam header, the flow distribution characteristics of the flow homogenizer should still be slightly inclined to the side away from the primary-side hot helium inlet.

3.2.4 Effect of Square Hole Size on Inter-Unit Flow Rate Uniformity

The square hole size can also influence the hot helium flow area on the cylinder wall. As shown in **Table 11**, seven flow homogenizers with different square hole sizes are investigated in this section, while other geometrical parameters remain exactly the same.

Through comprehensive analysis for **Tables 8**, **10**, **12**, the square hole size can only slightly influence inter-unit flow rate distribution, compared with other geometrical parameters. The flow homogenizers (Nos. 21, 28, 30, 32, and 33) all have the excellent inter-unit flow rate uniformity, with the standard deviations below 0.1. Part of the reason is that the effect of square hole size on the hot helium flow area is much smaller than row number and square hole number. In addition, the flow area ratios corresponding to the flow homogenizers with different square hole sizes are covered within the above-mentioned appropriate range. From the view of the minimum standard deviation, the optimal size is considered as the square holes near the inlet side of 60 mm × 40 mm and that away from the inlet side of 40 mm × 40 mm, respectively. The flow distribution characteristics of the above flow homogenizers are shown in **Figure 14**.

Similar to the previous discussions in **Section 3.2.3**, the flow distribution characteristics of the flow homogenizer are more sensitive to the hot helium flow area away from the inlet side, as inferred in **Figure 14**.

3.2.5 Analysis of the Optimal Geometrical Parameters

The optimal geometrical parameters of the hot helium flow homogenizer are summarized. A total of 163 circular holes are symmetrically arranged on the end wall with a grid pitch of

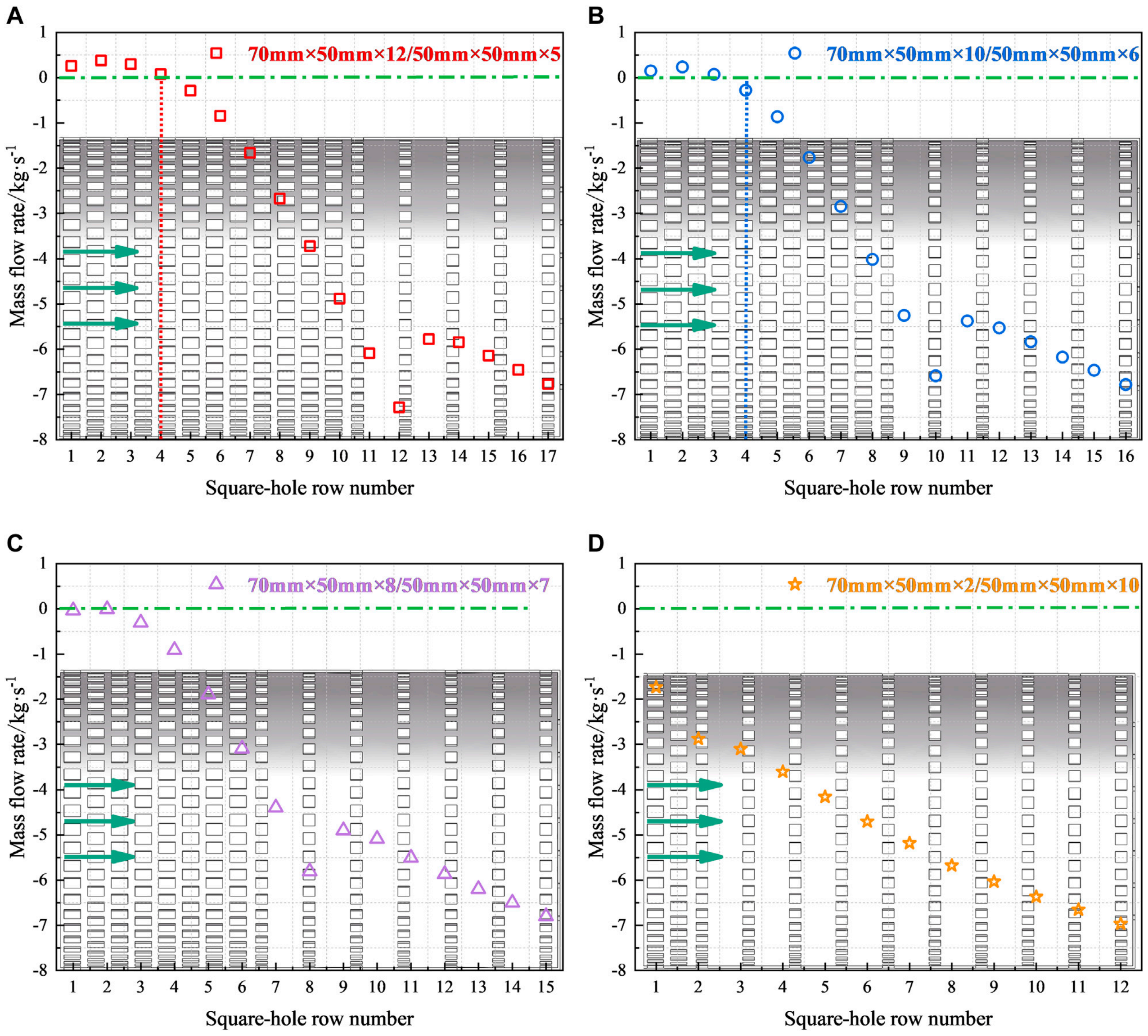

FIGURE 12 | Flow distribution characteristics of flow homogenizers with different square hole row numbers. **(A)** Flow homogenizer No.19. **(B)** Flow homogenizer No.12. **(C)** Flow homogenizer No.20. **(D)** Flow homogenizer No.23.

TABLE 9 | Characteristic geometrical parameters of flow homogenizers with different square hole numbers in a single row.

Case No.	Square holes near the inlet side				Square holes away from the inlet side				End-wall circular hole diameter/mm
	Row	Side length/mm	P_{near}/mm	Hole number	Row	Side length/mm	P_{away}/mm	Hole number	
21	6	70 × 50	100	50	8	50 × 50	200	50	Φ20
24				50				30	
25				50				25	
26				30				50	
27				25				50	

For the No.24–27 flow homogenizers, the numerical results of inter-unit flow rate distribution are shown in ***Table 10****.*

TABLE 10 | Numerical results of inter-unit flow rate distribution for flow homogenizers with different square hole numbers in a single row.

Case No.	Mass flow rate of heat exchange unit/kg·s^{-1}												Maximum deviation/%	Standard deviation
	1	2	3	4	5	6	7	8	9	10	11	12		
21	4.966	4.936	5.178	5.064	5.216	4.904	5.032	5.129	4.988	5.002	5.102	5.163	6.18	0.0971
24	4.932	5.248	4.954	4.998	5.166	5.101	4.917	5.049	4.906	5.154	5.061	5.162	6.73	0.1053
25	4.884	5.224	4.984	5.030	5.146	5.037	4.970	5.046	4.887	5.144	5.106	5.177	6.77	0.1091
26	4.972	4.884	5.184	5.056	5.222	4.967	5.009	5.130	4.982	4.994	5.093	5.167	6.69	0.0997
27	4.970	4.904	5.192	5.048	5.228	4.977	4.998	5.129	4.978	4.992	5.087	5.168	6.41	0.0989

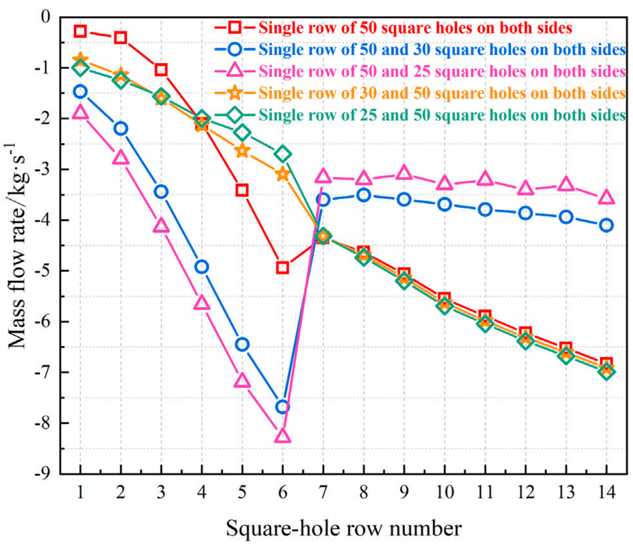

FIGURE 13 | Flow distribution characteristics of flow homogenizers with different square hole numbers in a single row.

80 mm and diameter of 20 mm. On the cylinder wall, the square holes should be arranged non-uniformly, including 6 rows near the inlet side with a pitch of 100 mm and side length of 60 mm × 40 mm and 8 rows away from the inlet side with a pitch of 200 mm and side length of 40 mm × 40 mm, respectively. Moreover, the optimal square hole number should be 50 in each row. As for this hot helium flow homogenizer, the standard deviation of inter-unit flow rate distribution is only 0.0850, with the maximum inter-unit flow rate deviation being below 5.50%. **Figure 15** presents the flow characteristics of the No.30 flow homogenizer with the optimal geometrical parameters.

From **Figure 15A**, the suction phenomenon is effectively suppressed, and the streamlines in **Figure 15C** also clearly show that hot helium realizes the outflow from all the rows of square holes. Meanwhile, the streamlines are uniformly distributed within each heat exchange unit, demonstrating the uniform inter-unit flow rate distribution. In terms of this flow homogenizer, the distributions of flow velocity and pressure provide a key link to the sufficient improvement of inter-unit flow rate uniformity. Thanks to the increased resistance through a specific structure design, the reduction of flow velocity within the flow homogenizer increases the internal static pressure. It ensures that the internal static pressure is always greater than the external static pressure, thereby reducing the effect of static pressure difference caused by dynamic pressure.

The inter-unit flow rate distribution is strongly associated with the geometrical parameters of the hot helium flow homogenizer, which directly determine its resistance coefficient. Therefore, the inter-unit flow rate uniformity can be viewed as the function of the resistance coefficient. The suction phenomenon is widely presented in the Nos. 3–19 hot helium flow homogenizers, while it can be effectively suppressed within other flow homogenizers (Nos. 20–33). In fact, the effective suppression of the suction phenomenon has a direct correlation with the resistance coefficient of the flow homogenizer.

According to the different mechanisms, the energy loss of viscous fluid can be divided into the friction and local resistance

TABLE 11 | Characteristic geometrical parameters of flow homogenizers with different square hole sizes.

Case No.	Square holes near the inlet side			Square holes away from the inlet side			End-wall circular hole diameter/mm
	Row	Side length/mm	P_{near}/mm	Row	Side length/mm	P_{away}/mm	
21	6	70 × 50	100	8	50 × 50	200	Φ20
28		70 × 50			40 × 40		
29		70 × 50			30 × 30		
30		60 × 40			40 × 40		
31		60 × 40			30 × 30		
32		50 × 30			40 × 40		
33		50 × 30			30 × 30		

For the No.28–33 flow homogenizers, the numerical results of inter-unit flow rate distribution are shown in ***Table 12****.*

TABLE 12 | Numerical results of inter-unit flow rate distribution for flow homogenizers with different square hole sizes.

Case No.	Mass flow rate of heat exchange unit/kg·s^{-1}												Maximum deviation/ %	Standard deviation
	1	2	3	4	5	6	7	8	9	10	11	12		
21	4.966	4.936	5.178	5.064	5.216	4.904	5.032	5.129	4.988	5.002	5.102	5.163	6.18	0.0971
28	4.900	5.206	4.994	5.026	5.142	4.995	4.996	5.058	4.911	5.121	5.133	5.151	6.06	0.0942
29	4.828	5.238	4.928	5.024	5.230	5.226	4.893	5.018	5.022	5.175	5.017	5.022	8.11	0.1315
30	4.910	5.086	5.010	5.004	5.150	5.019	5.007	5.066	4.912	5.075	5.188	5.152	5.50	0.0850
31	4.848	5.112	4.946	5.036	5.188	5.219	4.907	5.040	4.978	5.127	5.046	5.119	7.34	0.1079
32	4.932	4.978	5.056	4.974	5.180	5.001	5.028	5.095	4.922	5.063	5.179	5.150	5.11	0.0865
33	4.870	5.026	4.974	4.948	5.154	5.153	4.951	5.063	4.947	5.120	5.103	5.177	6.08	0.0974

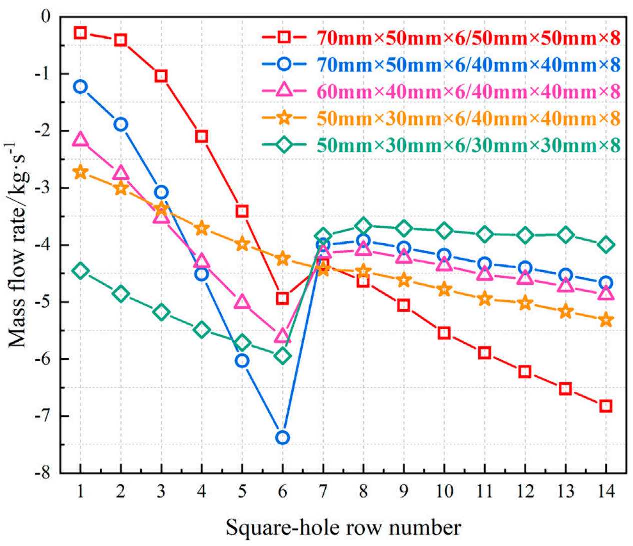

FIGURE 14 | Flow distribution characteristics of flow homogenizers with different square hole sizes.

loss, where the pressure drop and resistance coefficient satisfy the following Darcy–Visbach formula (Darcy, 1857). The hot helium flow homogenizer is simplified as a throttle based on the idea of equivalent substitution, so its resistance coefficient can be calculated by local energy loss (Qin et al., 2019; Qin et al., 2020).

The Darcy–Visbach formula of local energy loss is as follows:

$$\Delta p = \xi \frac{\rho v^2}{2} \tag{5}$$

The resistance coefficient represents the overall flow characteristics of the flow homogenizer, but it cannot reflect the non-uniform arrangement of square holes on the cylinder wall. As a vital design parameter of the hot helium flow homogenizer with NUASHs, the flow area ratio of square holes on both sides (k) is introduced to depict the geometrical parameter effects on inter-unit flow rate uniformity, as calculated by **Eq. 6**.

$$k = \frac{F_{near}}{F_{away}} = \frac{\sum f_{near}}{\sum f_{away}} \tag{6}$$

where F_{near} and F_{away} are the hot helium flow area of square holes near the inlet side and away from the inlet side, respectively. Similarly, f_{near} and f_{away} are the flow area of a single square hole on both sides.

The inter-unit flow rate uniformity is principally evaluated based on the standard deviation, taking into account the maximum deviation. Considering the overall thermal hydraulic performance of the HTGR OTSG, the uniformity design requirement is established as the standard deviation below 0.1. The design parameters of the hot helium flow homogenizer which meets this uniformity design requirement are listed in **Table 13**.

From **Table 13**, the critical resistance coefficient is 7.63 for effective suppression of the suction phenomenon. As the optimized design of the new inlet structure, the hot helium flow homogenizer with NUASHs should be adopted to improve inter-unit flow rate uniformity of the HTGR OTSG. Meanwhile, it is recommended that the resistance coefficient and flow area ratio need to be controlled within the ranges of (7.81–22.42) and (0.53–1.64), respectively.

3.3 Overall Flow Rate Uniformity of HTGR OTSG

The resistance of the heat exchange unit is much greater than that of the inlet structure. It is necessary to verify the overall flow rate distribution of the full-scale HTGR OTSG. In these simulations, 19 heat exchange units are coupled with the inlet structure. The geometrical models of overall numerical simulation are shown in **Figure 16**.

Engineering verification experiment of the HTR-PM shows that the measured pressure drop of the heat exchange unit is 45 kPa, at a rated mass flow rate of 5.053 kg/s (Li et al., 2021). As for overall numerical simulation, the average pressure drop of 19 heat exchange units is 45.35 kPa, with a relative error of 0.77%. It is evident that the numerical results are in good agreement with previous experiment data. The reliability of numerical methods adopted in the current investigation is also validated. **Table 14** shows the numerical results of overall flow rate distribution.

As shown in **Table 14**, the flow uniformization effect of the hot helium flow homogenizer is much more excellent than that of the current inlet structure with a baffle, with the maximum deviation decreased from 2.97% to 0.30%. It proves the feasibility of this new inlet structure of the hot helium flow homogenizer designed in this work.

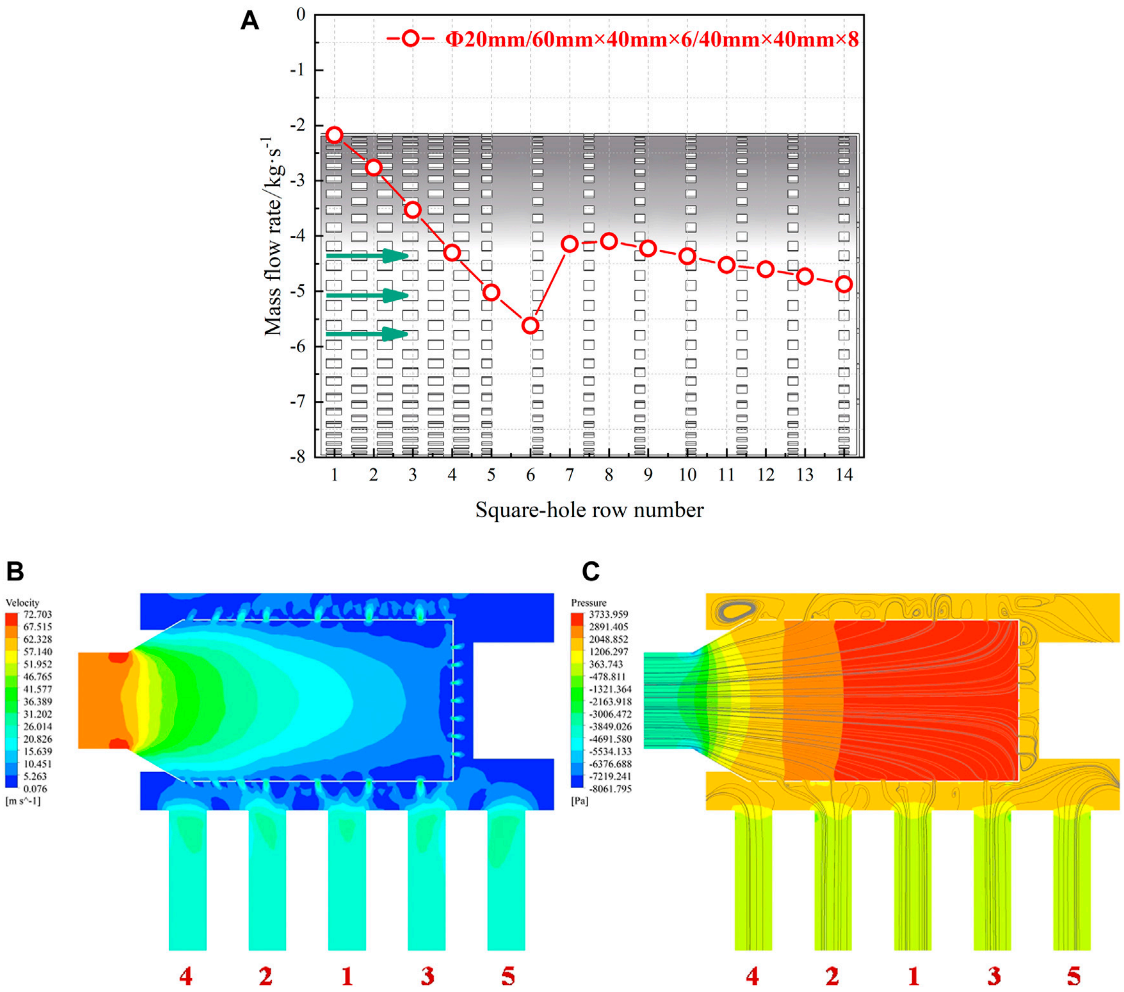

FIGURE 15 | Flow characteristics of the optimal hot helium flow homogenizer (No.30). **(A)** Flow distribution. **(B)** Flow velocity contour. **(C)** Pressure contour.

TABLE 13 | Design parameters of the hot helium flow homogenizer.

Case No.	Standard deviation	Maximum deviation/%	Resistance coefficient	Flow area ratio of square holes on both sides
20	0.1086	7.09	7.63	1.60
21	0.0971	6.18	7.81	1.05
26	0.0997	6.69	7.97	0.63
27	0.0989	6.41	8.14	0.53
28	0.0942	6.06	9.50	1.64
30	0.0850	5.50	10.92	1.13
32	0.0865	5.11	13.61	0.70
33	0.0974	6.08	22.42	1.25

4 CONCLUSION

Due to the high working temperature of the HTGR OTSG, large temperature non-uniformity should be avoided during operation. The primary-side helium flow rate distribution among the heat exchange units induced by the inlet structure is important for inter-unit temperature uniformity. A new inlet structure design with the hot helium flow homogenizer is proposed to improve inter-unit flow rate uniformity. Its flow distribution characteristics and mechanism are numerically investigated. Finally, the overall flow rate distribution of the HTGR OTSG is further evaluated by coupling the inlet structure and 19 heat exchange units. The main conclusions are as follows:

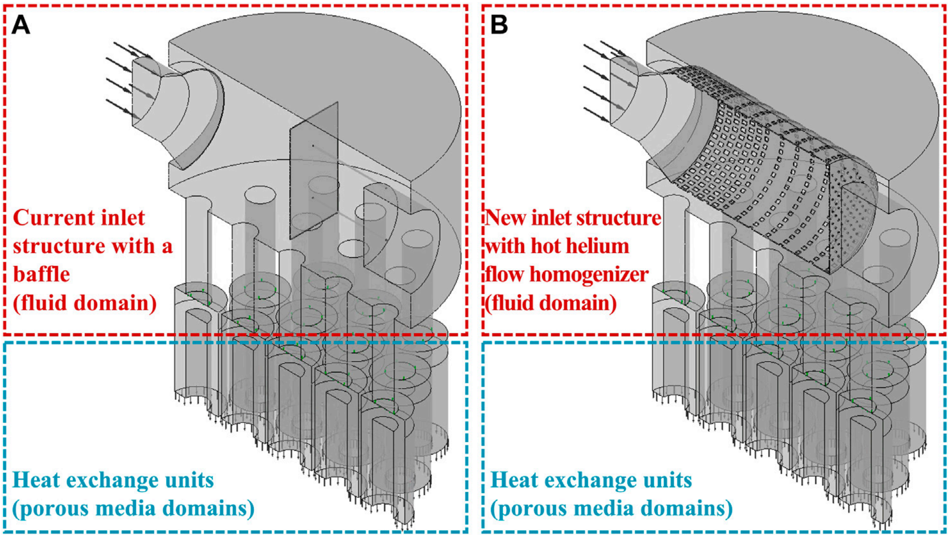

FIGURE 16 | Geometrical model of the HTGR OTSG. **(A)** Current inlet structure with a baffle. **(B)** New inlet structure with the flow homogenizer.

TABLE 14 | Numerical results of overall flow rate distribution for the HTGR OTSG.

Case No.	Mass flow rate of heat exchange unit/kg·s^{-1}												Maximum deviation/ %	Standard deviation
	1	2	3	4	5	6	7	8	9	10	11	12		
2	7.212	4.906	5.470	5.636	5.932	4.422	4.324	5.199	5.809	3.809	5.131	4.729	67.52	0.8581
Couple	5.150	5.050	5.072	5.080	5.098	5.027	5.026	5.057	5.075	5.000	5.056	5.033	2.97	0.0377
30	4.910	5.086	5.010	5.004	5.150	5.019	5.007	5.066	4.912	5.075	5.188	5.152	5.50	0.0850
Couple	5.048	5.052	5.050	5.054	5.060	5.051	5.047	5.053	5.047	5.052	5.062	5.056	0.30	0.0046

(1) Setting circular holes on the end wall can increase the flow rate of heat exchange units blocked by the main steam header, which can improve inter-unit flow rate uniformity.
(2) Flow distribution characteristics are strongly related with the geometrical parameters of square holes on the cylinder wall. The non-uniform arrangement is a more superior design for improving inter-unit flow rate uniformity, which can reduce the effect of static pressure difference caused by dynamic pressure.
(3) Increasing the resistance of the hot helium flow homogenizer can make the internal pressure greater than the external pressure, and the suction phenomenon near the inlet side can be effectively suppressed. The critical resistance coefficient is 7.63. Moreover, the resistance coefficient and flow area ratio are recommended to be within the ranges of (7.81–22.42) and (0.53–1.64), respectively.
(4) Compared with the previous baffle design, the hot helium flow homogenizer with NUASHs can reduce the maximum deviation from 2.97% to 0.30%, which is a promising design to further optimize the inlet structure of the HTGR OTSG.

DATA AVAILABILITY STATEMENT

The raw data supporting the conclusion of this article will be made available by the authors, without undue reservation.

AUTHOR CONTRIBUTIONS

HQ: methodology, software, design, validation, investigation, data curation, writing—original draft, and writing—review and editing. XLu: design, project administration, and supervision. XLi: methodology, design, theorization, writing—review and editing, and resources. XW: supervision and resources.

FUNDING

This work was financially supported by the National Key Research and Development Program of China (2020YFB1901600), the National Natural Science Foundation of China (51576103), and the National S&T Major Project (Grant No. ZX06901).

REFERENCES

Mathews, A. J. 1987. “The Early Operation of the Helical Once-Through Boilers at Heysham 1 and Hartlepool,” In Proceeding of specialists' meeting on technology of steam generator for gas-cooled reactors, Switzerland.

ANSYS (2019). ANSYS CFX-Solver Modeling Guide. Release 19.2. Available at: http://www.ansys.com (Accessed November 8, 2011).

ASME (2015). *ASME Boiler and Pressure Vessel Code Section Ⅲ: Rules for Construction of Nuclear Facility Components*. New York: ASME.

da Silva, B. L., Luciano, R. D., Utzig, J., and Meier, H. F. (2019). Analysis of Flow Behavior and Fluid Forces in Large Cylinder Bundles by Numerical Simulations. *Int. J. Heat Fluid Flow* 75, 209–226. doi:10.1016/j.ijheatfluidflow.2019.01.006

Darcy, H. (1857). *Researches Experimentales Relatives Au Mouvement De L'eau Dans Les Tuyaux*. Paris, France: Mallet-Bachelier 1857

Gao, W. K. (2020). *Numerical and Experimental Investigation on the Flow and Heat Transfer Non-uniformity of Cross Flow over Tube Bundles (Doctor Thesis)*. Beijing, PR China: Tsinghua University.

Gao, W., Li, X., Wu, X., Zhao, J., and Luo, X. (2020). Influences of Fabrication Tolerance on Thermal Hydraulic Performance of HTGR Helical Tube once through Steam Generator. *Nucl. Eng. Des.* 363, 110665. doi:10.1016/j.nucengdes.2020.110665

Gao, W., Zhao, J., Li, X., Zhao, H., Zhang, Y., and Wu, X. (2019). Heat Transfer Characteristics of Carbon Dioxide Cross Flow over Tube Bundles at Supercritical Pressures. *Appl. Therm. Eng.* 158, 113786. doi:10.1016/j.applthermaleng.2019.113786

Generation-Ⅳ International Forum (2002). A Technology Roadmap for Generation Ⅳ Nuclear Energy Systems. Report No.: GIF-002-00. Available at: https://www.hsdl.org/?view&did=894 (Accessed December 12, 2002).

Hayat, T., Haider, F., Alsaedi, A., and Ahmad, B. (2021). Entropy Generation Analysis of Carreau Fluid with Entire New Concepts of Modified Darcy's Law and Variable Characteristics. *Int. Commun. Heat Mass Transf.* 120, 105073. doi:10.1016/j.icheatmasstransfer.2020.105073

Iacovides, H., Launder, B., and West, A. (2014). A Comparison and Assessment of Approaches for Modelling Flow over In-Line Tube Banks. *Int. J. Heat Fluid Flow* 49, 69–79. doi:10.1016/j.ijheatfluidflow.2014.05.011

Idelchik, I. E., and Fried, E. (2016). *Handbook of Hydraulic Resistance*. New York: Begell House Inc.

Kong, L. (2014). *Engineering Fluid Mechanics*. 4th Edn. Beijing, PR China: China Electric Power Press.

Li, X., Gao, W., Su, Y., and Wu, X. (2019b). Thermal Analysis of HTGR Helical Tube once through Steam Generators Using 1D and 2D Methods. *Nucl. Eng. Des.* 355, 110352.doi:10.1016/j.nucengdes.2019.110352

Li, X. W. (2012). *Thermal-hydraulic and Temperature Sensitivity Analysis of the HTR-PM once through Steam Generator*. Beijing, China: Institute of Nuclear and New Energy Technology. (internal report).

Li, X., Wu, X., and He, S. (2014). Numerical Investigation of the Turbulent Cross Flow and Heat Transfer in a Wall Bounded Tube Bundle. *Int. J. Therm. Sci.* 75, 127–139. doi:10.1016/j.ijthermalsci.2013.08.001

Li, X., and Wu, X. (2013). Thermal Mixing of the Cross Flow over Tube Bundles. *Int. J. Heat Mass Transf.* 67, 352–361. doi:10.1016/j.ijheatmasstransfer.2013.08.031

Li, X. W., Wu, X. X., and Luo, X. W. (2016). “Thermal Hydraulic Issues of HTGR Helical Tube once through Steam Generator: Methods and Application,” in *The 8th International Topical Meeting on High Temperature Reactor Technology (HTR-2016)* (NV: Las Vegas).

Li, X. W., Wu, X. X., Zhang, Z. Y., Zhao, J., and Luo, X. (2021). Engineering Test of HTR-PM Helical Tube once through Steam Generator. *J. Tsinghua Univ. Sci. Technol.* 61, 329–337. (in Chinese).

Li, X. W., Wu, X. X., and Zhang, Z. Y. (2019a). Thermal Hydraulics of HTGR Helical Tube once through Steam Generator. *Atomic Energy Sci. Technol.* 53, 1906–1917. (in Chinese). doi:10.7538/yzk.2019.53.10.1906

Olson, J. T., Li, X., and Wu, X. (2014). Tube and Shell Side Coupled Thermal Analysis of an HTGR Helical Tube once through Steam Generator Using Porous Media Method. *Ann. Nucl. Energy* 64, 67–77. doi:10.1016/j.anucene.2013.09.036

Qin, H., Lu, D., Liu, S., Tang, J., Wang, Y., and Zhong, D. (2019). Hydraulic Experiment Investigation on the Plate-Throttle Entry Tube Flow Characteristics of Fast Reactor Fuel Assembly. *Nucl. Eng. Des.* 352, 110172. doi:10.1016/j.nucengdes.2019.110172

Qin, H., Lu, D., Zhong, D., Wang, Y., and Song, Y. (2020). Experimental and Numerical Investigation for the Geometrical Parameters Effect on the Labyrinth-Seal Flow Characteristics of Fast Reactor Fuel Assembly. *Ann. Nucl. Energy* 135, 106964. doi:10.1016/j.anucene.2019.106964

Satter, A., and Iqbal, G. M. (2016). Fundamentals of Fluid Flow through Porous Media. *Reserv. Eng.*, 155–169. doi:10.1016/b978-0-12-800219-3.00009-7

Tao, W. Q. (2017). *Numerical Heat Transfer*. 2nd Edn. Xi'an, PR China: Xi'an Jiaotong University Press.

Wu, Z., Lin, D., and Zhong, D. (2002). The Design Features of the HTR-10. *Nucl. Eng. Des.* 218, 25–32. doi:10.1016/s0029-5493(02)00182-6

Wu, Z. X., and Zhang, Z. Y. (2000). World Development of Nuclear Power System and High Temperature Gas-Cooled Reactor. *Chin. J. Nucl. Sci. Eng.* 20 (3), 211–219. (in Chinese). doi:10.3321/j.issn:0258-0918.2000.03.004

Zhang, J., Li, X. W., and Wu, X. X. (2011). Numerical Investigation of the HTR-PM Steam Generator Entrance Structure Influence to the Flow Distribution. *Chin. High. Technol. Lett.* 21, 652–656. (in Chinese). doi:10.3772/j.issn.1002-0470.2011.06.016

Zhang, Z., Dong, Y., Li, F., Zhang, Z., Wang, H., Huang, X., et al. (2016). The Shandong Shidao Bay 200 MW e High-Temperature Gas-Cooled Reactor Pebble-Bed Module (HTR-PM) Demonstration Power Plant: An Engineering and Technological Innovation. *Engineering* 2, 112–118. doi:10.1016/j.eng.2016.01.020

Zhang, Z., and Sun, Y. (2007). Economic Potential of Modular Reactor Nuclear Power Plants Based on the Chinese HTR-PM Project. *Nucl. Eng. Des.* 237, 2265–2274. doi:10.1016/j.nucengdes.2007.04.001

Zhang, Z., Wu, Z., Wang, D., Xu, Y., Sun, Y., Li, F., et al. (2009). Current Status and Technical Description of Chinese 2×250MWth HTR-PM Demonstration Plant. *Nucl. Eng. Des.* 239, 1212–1219. doi:10.1016/j.nucengdes.2009.02.023

Zhao, H., Li, X., and Wu, X. (2017). Numerical Investigation of Supercritical Water Turbulent Flow and Heat Transfer Characteristics in Vertical Helical Tubes. *J. Supercrit. Fluids* 127, 48–61. doi:10.1016/j.supflu.2017.03.016

Zhou, Y., Hao, P., Li, F., Shi, L., He, F., Dong, Y., et al. (2016). Experiment Study on Thermal Mixing Performance of HTR-PM Reactor Outlet. *Nucl. Eng. Des.* 306, 186–191. doi:10.1016/j.nucengdes.2016.03.009

Zhou, Y. P., Li, F., Hao, P. F., and He, F. (2011). Similarity Analysis for Hot Gas Mixing Experiment of Outlet of HTR-PM Reactor Core. *Atomic Energy Sci. Technol.* 45, 1208–1214. (in Chinese).

Conflict of Interest: The authors declare that the research was conducted in the absence of any commercial or financial relationships that could be construed as a potential conflict of interest.

NOMENCLATURE

A cross-sectional area (m^2)

c local acoustic velocity (m/s)

C_p specific heat capacity at constant pressure (J/(kg·K))

d helical tube outer diameter (m)

f hot helium flow area of a single hole (m^2)

F hot helium flow area (m^2)

k flow area ratio of square holes on both sides, dimensionless

K permeability (m^2)

L length (m)

Ma Mach number, dimensionless

p pressure (Pa)

Δp pressure drop (Pa)

P pitch (m)

Q_v volume flow rate (m^3/s)

Re Reynolds number, dimensionless

S_1 transverse tube pitch (m)

S_2 stream-wise tube pitch (m)

T temperature (°C)

v flow velocity (m/s)

y^+ dimensionless wall distance

Greek Symbols

γ thermal expansivity (/K)

η dynamic viscosity (Pa·s)

λ thermal conductivity (W/(m·K))

ξ resistance coefficient, dimensionless

ρ density (kg/m^3)

σ standard deviation, variable unit

Subscript

away away from the inlet side

near near the inlet side

Advantages of publishing in Frontiers

OPEN ACCESS
Articles are free to read
for greatest visibility
and readership

FAST PUBLICATION
Around 90 days
from submission
to decision

HIGH QUALITY PEER-REVIEW
Rigorous, collaborative,
and constructive
peer-review

TRANSPARENT PEER-REVIEW
Editors and reviewers
acknowledged by name
on published articles

Frontiers
Avenue du Tribunal-Fédéral 34
1005 Lausanne | Switzerland

Visit us: www.frontiersin.org
Contact us: frontiersin.org/about/contact

REPRODUCIBILITY OF RESEARCH
Support open data
and methods to enhance
research reproducibility

DIGITAL PUBLISHING
Articles designed
for optimal readership
across devices

FOLLOW US
@frontiersin

IMPACT METRICS
Advanced article metrics
track visibility across
digital media

EXTENSIVE PROMOTION
Marketing
and promotion
of impactful research

LOOP RESEARCH NETWORK
Our network
increases your
article's readership